

**Measurements of 1st, 2nd and 3rd azimuthal
anisotropy in $\sqrt{s_{\text{NN}}} = 200$ GeV Cu+Au collisions at
RHIC-PHENIX**

Hiroshi NAKAGOMI

December 2016

**Measurements of 1st, 2nd and 3rd azimuthal
anisotropy in $\sqrt{s_{NN}} = 200$ GeV Cu+Au collisions at
RHIC-PHENIX**

**Hiroshi NAKAGOMI
Doctoral Program in Physics**

**Submitted to the Graduate School of
Pure and Applied Sciences
in Partial Fulfillment of the Requirements
for the Degree of Doctor of Philosophy in
Science**

**at the
University of Tsukuba**

Abstract

Relativistic high energy heavy ion collision is a unique tool in the laboratory to create a new state of nuclear matter composed of de-confined quarks and gluons, "Quark Gluon Plasma (QGP)", which is predicted to exist under extreme high temperature and/or high density by lattice Quantum Chromodynamics. Azimuthal anisotropies of particle production, defined as Fourier coefficients v_n , in relativistic heavy ion collisions have proven the importance of the initial condition and the bulk property of the QGP, because the azimuthal anisotropies originate from the initial spatial geometry ε_n and develops during the entire evolution of the expanding system. In spite of many experimental results and theoretical calculations, there are still uncertainties of the initial geometry and the viscosity of QGP.

In 2012, Cu+Au collisions, which are the first asymmetric heavy ion collisions at collider energy, were delivered at the Relativistic Heavy Ion Collider (RHIC) to study the influence of asymmetric initial condition on azimuthal anisotropy of produced particles. In Cu+Au collisions, the large directed azimuthal anisotropy of produced particles at mid-rapidity $\eta \sim 0$ is observed in transverse plane, where η describes the angle of a particle with respect to the beam axis. Large absolute values of η correspond to the angles close to the beam axis. The forward/backward asymmetry of produced particle multiplicity and azimuthal anisotropy, which have not been observed in the symmetric collisions, are observed. These observations could be due to the sideward asymmetric shape at the mid-rapidity and the forward/backward asymmetry in number of participants and eccentricity ε_n . In this dissertation, the directed, elliptic and triangular flow in Cu+Au collisions at $\sqrt{s_{NN}} = 200\text{GeV}$ have been measured at mid-rapidity ($|\eta| < 0.35$) for charged hadrons, π^\pm, K^\pm, p and \bar{p} and forward/backward-rapidity ($3 < |\eta| < 3.9$) for charged hadrons via event plane technique by using the PHENIX detectors at the RHIC.

At mid-rapidity region, the elliptic flow v_2 and the triangular flow v_3 in asymmetric Cu+Au collisions show similar transverse momentum p_T dependence and collision centrality dependence as seen in symmetric Au+Au and Cu+Cu collisions. The p_T integrated v_2 in Cu+Au collisions is always between those in Au+Au and Cu+Cu collisions. On the other hand, the values of Cu+Au v_3 is almost same as the Au+Au results. The system size dependence of v_2 is expected from the initial spatial ellipticity ε_2 calculated in Monte Carlo Glauber model which is commonly used in heavy ion field as the initial geometry model. On the other hand, the system size dependence of v_3 is not ordered according to the initial spatial triangularity ε_3 in Monte Carlo Glauber model. The large directed flow v_1 is observed at mid-rapidity and indicates that large number of high p_T particles are emitted toward the hemisphere of Au spectator. By studying Monte Carlo Glauber simulation and Blast wave model, the largest pressure gradient in Au hemisphere side pushes more particles to higher p_T , which leads the larger v_1 for high p_T particles at mid-rapidity. For identified hadron v_n , mass ordering is observed for all three harmonics at low p_T region and baryon/meson splitting is observed for the v_2 and v_3 measurements but not for the v_1 measurements. At forward/backward rapidity region, the Au-going ($-3.9 < \eta < -3$) v_2 and v_3 in Cu+Au collisions have larger values than the Cu-going ($3 < \eta < 3.9$) results. Like the mid-rapidity v_2 measurements, we found that the forward/backward Cu+Au v_2 is always between the Au+Au and Cu+Cu results. The Au-going v_3 in Cu+Au collisions shows larger values than those in Au+Au collisions.

Since the v_n originates from the ε_n , we studied the influence of the initial condition on v_n

by scaling the v_n with ε_n in Monte Carlo Glauber model. For the mid-rapidity v_n measurements, the scaled v_2 with ε_2 in Cu+Au collisions are good agreement with those in Au+Au and Cu+Cu collisions, while the difference of the scaled v_3 between Au+Au and Cu+Au collisions is observed. These results suggest that the Glauber model is not favored for describing the initial geometry because ε_2 and ε_3 have to be described simultaneously by one model. Although one might expect in model calculations that the forward/backward asymmetry of v_n is caused by the forward/backward asymmetry of ε_n , we conclude that the forward/backward asymmetry of v_n arises from the forward/backward asymmetry of initial energy density by testing various different eccentricity assumptions as well as different energy density assumptions.

The charged hadron v_n is compared to event by event hydrodynamical and the combined parton cascade and hadron cascade model (AMPT) calculations. The hydrodynamical calculations reproduce v_n at mid-rapidity reasonably. Although the AMPT model calculations reproduce mid-rapidity v_2 and v_3 well, the sign of mid-rapidity v_1 is found to be opposite with respect to the experimental data. The forward/backward v_n measurements are also compared to the predictions from the hydrodynamical and the AMPT model calculations. Although the hydrodynamical calculation predicts the larger values of v_n than those of the measured v_n , the hydrodynamical calculations reproduce the forward/backward asymmetry of v_2 except for peripheral collisions but underpredict the forward/backward asymmetry of v_3 . The AMPT model reproduces the magnitude of measured v_n reasonably. However, the AMPT model calculations overpredict the forward/backward asymmetry of v_2 and v_3 . The longitudinal fluctuation has been naturally embedded in AMPT model, which is based on the *Hijing* (pythia pp superpositions), while smooth longitudinal profile is assumed in the hydrodynamical model. Therefore this comparison has shed light on the importance of longitudinal initial condition and longitudinal dynamics.

Contents

1	Introduction	1
1.1	Quark Gluon Plasma	1
1.2	Relativistic Heavy Ion Collisions	3
1.2.1	Participant Spectator Picture	5
1.2.2	Nuclear stopping power	6
1.2.3	Space-Time Evolution of Collisions	8
1.3	Major Features of Experimental Observables	9
1.3.1	Energy Density	9
1.3.2	Particle Production	11
1.3.3	Azimuthal anisotropy	14
	Event by event fluctuation	17
	Identified hadron $v_n(p_T)$	18
	Pseudorapidity dependence of v_n	20
1.4	Cu+Au collision and thesis motivation	24
2	Experimental Apparatus	26
2.1	Relativist Heavy Ion Collider(RHIC)	26
2.2	PHENIX Detectors	28
2.2.1	Magnet systems	29
	PHENIX Magnet system	29
2.2.2	Global detector	29
	Beam-Beam Counter	30
	Zero Degree Calorimeter(ZDC)	30
	Shower Max Detector(SMD)	31
2.2.3	Central arm detector	32
	Drift Chamber	32
	Pad chamber	33
	Time of flight	36
	Time of flight East(TOF.E)	36
	Time of flight West	36
	Electro Magnetic Calorimeter(EMCal)	37
	Pb scintillator sampling calorimeter	37
	Pb glass Cherenkov calorimeter	38
	Reaction Plane Detector(RXNP)	39

2.2.4	Data acquisition(DAQ)	39
3	Analysis	42
3.1	Event selection	42
	Centrality Determination	42
3.2	Track selection	43
3.2.1	Track reconstruction	43
3.2.2	Momentum determination	45
3.2.3	Track Quality	45
	Track Matching	45
3.2.4	Particle Identification	46
3.3	Event Plane	50
3.3.1	Azimuthal anisotropy	50
3.3.2	Event Plane Determination	51
3.3.3	Event Plane Calibration	52
3.3.4	Re-centering Calibration	52
3.3.5	Flattening Calibration	52
3.3.6	Event Plane QA	53
3.3.7	Event Plane Resolution	53
3.4	Measurements of charged hadron v_n at mid-rapidity	58
3.5	Measurements of particle identified v_n at mid-rapidity	58
3.6	Measurements of hadron v_n at forward/backward-rapidity	59
3.6.1	Single particle simulation for forward/Backward-rapidity v_n measurements	62
3.7	Measurements of charged hadron $dN_{ch}/d\eta$ at forward/backward-rapidity	63
3.7.1	Single particle simulation for forward/backward-rapidity charged particle multiplicity $dN_{ch}/d\eta$ measurements	63
3.8	Initial spatial anisotropy	63
3.8.1	Glauber model Monte Carlo simulation	65
3.8.2	Initial spatial anisotropy	65
3.9	Systematic Uncertainty	66
3.9.1	Systematic Uncertainties at mid-rapidity v_n	66
	Uncertainty from Event plane determination	66
	Uncertainty from East and West	68
	Uncertainty from hadron misidentification	69
3.9.2	Systematic Uncertainties of forward/backward v_n measurements	71
	Uncertainty from Event plane determination	71
	Uncertainty from Input p_T spectra in Single particle simulation	71
	Uncertainty from input η probability distribution in Single particle simulation	72
	Uncertainty from input $v_n(\eta)$ shape in Single particle simulation	73
	Uncertainty from magnitude of $v_n(p_T)$	74
	Uncertainty from the shape of $v_n(p_T)$	75
3.9.3	Systematic Uncertainties of forward/backward $dN_{ch}/d\eta$ measurements	78
3.9.4	Summary of systematic uncertainties	78

4 Results	82
4.1 Charged hadron v_n at mid-rapidity	82
4.2 π^\pm, K^\pm, p and \bar{p} v_n results	89
4.3 Charged hadron v_n at forward/backward rapidity	90
4.4 Charged hadron $dN/d\eta$	92
5 Discussions	96
5.1 Interpretation of sign of $v_1(p_T)$	96
5.1.1 Approach with Monte Carlo Glauber model	96
5.1.2 Approach with Blast wave model	99
5.2 Interpretation of forward/backward asymmetry of $dN_{ch}/d\eta$ with Monte Carlo Glauber model	102
5.3 Eccentricity scaling of v_n	106
5.3.1 Mid-rapidity v_n/ε_n	106
5.3.2 Forward/Backward-rapidity v_n/ε_n	109
5.4 Theory comparison	119
6 Conclusion	125
A Intrinsic triangularity	127
A.1 $v_3(\Psi_1)$ at mid-rapidity	127
B Initial geometry model	131
B.1 Initial geometry model dependence	131
C Eccentricity and N_{part} scaling	136
C.1 Weighted eccentricity and N_{part} scaling of forward/backward v_n	136

List of Figures

1.1	Summary of measurement of α_s as a function of momentum transfer Q [4]	2
1.2	(2 + 1) flavor lattice QCD prediction of the potential energy between a pair of quark and anti-quark as a function of the distance[5]	2
1.3	(2 + 1) flavor lattice QCD prediction on pressure, energy density and entropy density normalized by $\frac{1}{T^4}$ as a function of temperature. The dark tree lines are the results of hadron resonance gas model. The ideal gas limit for the energy density is shown as a horizontal line at $95\pi^2/60$ [6]	3
1.4	Schematic view of the colliding nuclei before(left) and after(right) collision.	6
1.5	Net proton $dN/d\eta$ distribution at 5(AGS), 17(SPS) and 200(RHIC) GeV.	7
1.6	A sketch for the space time history of a relativistic heavy ion collision in the beam direction z and the time t	9
1.7	Geometry for the initial state of a central collision in nucleus-nucleus collisions[8].	10
1.8	Bjorken energy density as a function of number of participants at mid-rapidity in Au+Au collisions observed by PHENIX[9]	10
1.9	Charged hadron p_T spectrum for different multiplicity class in Au+Au collisions at $\sqrt{s_{NN}} = 200$ GeV [16]	11
1.10	π^\pm , K^\pm , p and \bar{p} transverse mass spectra at mid-rapidity for different multiplicity class in Au+Au collisions at $\sqrt{s_{NN}} = 200$ GeV [18]	12
1.11	Inverse slope parameters for π , K and p m_T distributions in Pb+Pb 17.2 GeV, S+S 19.4 GeV and p+p 23 GeV collisions[17]	13
1.12	Inverse slope parameters for different multiplicity class in Au+Au 200 GeV collisions[18]	13
1.13	Charged particle $dN/d\eta$ in central Au+Au collisions at $\sqrt{s_{NN}} = 200, 130, 62.4$ and 19.6 GeV[13]	13
1.14	Overlap region in beam direction and transverse plane	14
1.15	Overlap region in transverse plane	15
1.16	The proper time dependence of spatial eccentricity ϵ_x and momentum eccentricity ϵ_p in Au+Au collisions for two different sets of EOS [19]	16
1.17	parton v_2 as a function of proper time calculated by parton transport model for several parton cross sections in Au+Au collisions at $\sqrt{s_{NN}} = 200$ GeV [20]	16
1.18	Sketches of heavy ion collisions for directed, elliptic and triangular flow	17
1.19	Transverse momentum dependence of charged hadron v_n at mid-rapidity for different multiplicity class in Au+Au 200GeV measured by the PHENIX collaboration	18
1.20	Multiplicity dependence of charged hadron v_n at mid-rapidity for two transverse momentum intervals in Au+Au 200GeV measured by the PHENIX collaboration	19

1.21 Charge combined pion, kaon and proton v_n at mid-rapidity in Au+Au collisions at $\sqrt{s_{NN}} = 200\text{GeV}$	21
1.22 Pseudo-rapidity dependence of charge hadron v_2 in Au+Au collisions at $\sqrt{s_{NN}} = 200\text{GeV}$ in comparison to the hydrodynamic calculations. Left:Glauber Monte Carlo model(nucleon base) initial condition. Right:KLN model(gluon base) initial condition	22
1.23 Pseudo-rapidity dependence of charge hadron v_n in Pb+Pb collisions at $\sqrt{s_{NN}} = 200\text{GeV}$	23
1.24 Pseudo-rapidity dependence of charge hadron v_n in Au+Au collisions at $\sqrt{s_{NN}} = 200\text{GeV}$	23
1.25 Cu+Au collisions in longitudinal direction(a) and transverse direction(b)	25
2.1 RHIC accelerator complex	27
2.2 Schematic of procedure of Au ion injection.	27
2.3 Schematic view of the PHENIX subsystems. Top panel:Beam View, Bottom panel:Side View	28
2.4 Schematic view of Central and Muon magnets.	29
2.5 Left:One BBC counter composed of 64 elements. Right:Single BBC element composed of PMT equipped with quartz	31
2.6 Schematic view of the colliding nuclei before(left) and after(right) collision.	31
2.7 Schematic view of the colliding nuclei before(left) and after(right) collision.	32
2.8 Schematic view of the colliding nuclei before(left) and after(right) collision.	34
2.9 Schematic view of the colliding nuclei before(left) and after(right) collision.	34
2.10 A plane cutting through by a Pad chamber	35
2.11 Left:The pad and pixel geometry. Right:A cell made of three pixels is at center of this picture	35
2.12 TOF.E installed at PHENIX Central Arm East Arm	36
2.13 TOF.E each panel composed of scintillator slats and PMTs	36
2.14 Schematic view of MRPC	37
2.15 Schematic view of each Pb-Schintilator tower	38
2.16 Schematic view of each Lead Glass tower	39
2.17 Schematic view of Reaction plane detector	40
2.18 Schematic design of PHENIX DAQ system	40
3.1 A schematic of the correlation between measured charged particles and N_{part} and b calculated by Glauber Monte Carlo. The plotted distribution is not actual measurements.[7]	43
3.2 The total bbc charge distribution in Cu+Au collisions at $\sqrt{s_{NN}} = 200\text{GeV}$ from combined South and North Bbc detectors	43
3.3 A cartoon of the ϕ and α for the DC track reconstruction. The dashed lines represent DC West arm. The small circles are DC hits along the track	44
3.4 A cartoon of the track in r and z plane. The red line corresponds to the reference radius of the DC	44

3.5	Left figure:Simulated hit informations in a central Au+Au collisions with HIJING for a small region of the DC. Right figure:The Hough transform feature space(ϕ - α plane) for this small DC region. The peaks corresponds to tracks.	44
3.6	The squared mass distributions as functions of p_T . In each plot, the lowest horizontal band corresponds to pions, the second bad are kaons and the third and forth bands are protons and deuterons. Top Left: Positive and TOF.E tracks. Bottom Left:Negative and TOF.E tracks. Top Right:Positive and TOF.W tracks. Bottom Right:Negative and TOF.W tracks.	47
3.7	Squared mass distribution for medium p_T bin and positive particles in TOF.W. The fitted functions are for pions, kaons and protons.	48
3.8	The mean values of squared mass distributions for p_T bins and positive particles in TOF.W.	48
3.9	The width of squared mass distributions for p_T bins and positive particles in TOF.W.	48
3.10	The squared mass distributions as functions of p_T after the PID cuts(2σ from the peaks and 2σ veto cuts from their adjacent species peaks). In each plot, the lowest horizontal band corresponds to pions, the second bad are kaons and the third and forth bands are protons and deuterons. Top Left: Positive and TOF.E tracks. Bottom Left:Negative and TOF.E tracks. Top Right:Positive and TOF.W tracks. Bottom Right:Negative and TOF.W tracks.	49
3.11	The Qvector distribution determined the combined South and North Bbc detectors before and after the Re-centring correction. Left:Raw Qvector. Right:Corrected Qvector	53
3.12	The 2nd harmonic event plane determined by the combined South and North Bbc detectors for the no correction, only the Re-centering correction and the Re-centering and the Flattening corrections in Cu+Au collisions at $\sqrt{s_{NN}} = 200\text{GeV}$	54
3.13	The 2_{nd} order event plane resolutions of South and North side of Bbc and Cnt as functions of centrality in CuCu collisions at 200GeV. The resolutions are determined by BbcS-Cnt-BbcN 3-subevent combination.	55
3.14	The 2_{nd} and 3_{rd} order event plane resolutions of the South and North side of Bbc, the South and North side of Rxn and the Cnt as functions of centrality in Au+Au collisions at 200GeV. The event plane resolution of the Rxn is determined from 2-subevent method. The others are determined from BbcS-Cnt-BbcN 3-subevent combination. Left panel: 2_{nd} order event plane. Righ panel: 3_{rd} order event plane.	56
3.15	The 1_{st} , 2_{nd} and 3_{rd} order event plane resolutions as functions of centrality. Left panel:The 1_s event plane for the South side of Smd determined from 3-subevent combinations, SmdS-BbcS-SmdN and SmdS-BbcN-SmdN. Middle panel:The 2_{nd} order event plane for the South, North and combined South and North Bbc and the Cnt. Right panel: 3_{rd} order event plane for the Bbc and Cnt. The 2_{nd} and 3_{rd} order event plane resolutions for the Bbc and the Cnt are determined from BbcS-Cnt-BbcN 3-subevent combination.	57
3.16	Charged hadron v_1 as a function of p_T in Cu+Au collisions for different centrality bins	58

3.17 Charged hadron v_2 as a function of p_T in Cu+Au collisions for different centrality bins	59
3.18 Charged hadron v_3 as a function of p_T in Cu+Au collisions for different centrality bins	59
3.19 PID v_2 as a function of p_T in Cu+Au collisions	60
3.20 PID v_3 as a function of p_T in Cu+Au collisions for different centrality bins	60
3.21 PID v_1 as a function of p_T in Cu+Au collisions	60
3.22 Charged hadron v_2 as a function of η in Cu+Au collisions for different centrality bins	61
3.23 Charged hadron v_3 as a function of η in Cu+Au collisions for different centrality bins	61
3.24 Bbc charge sum as a function of centrality in Au+Au, Cu+Au and Cu+Cu collisions. In Cu+Au collisions, BbcS and BbcN indicate Au-going side and Cu-going side respectively	64
3.25 Left:Impact parameter distribution in Monte Carlo Glauber model. Right: N_{part} distribution estimated from Monte Carlo Glauber model.	66
3.26 2nd and 3rd order eccentricity ε_2 in Monte Carlo Glauber model as a function of centrality for Au+Au, Cu+Au and Cu+Cu collisions	67
3.27 v_1 as a function of p_T with respect to SMD S for different centrality bins	67
3.28 v_2 as a function of p_T with respect to BBC S, BBC N and BBC S and N combined event plane for different centrality bins	68
3.29 v_3 as a function of p_T with respect to BBC S, BBC N and BBC S and N combined event plane for different centrality bins	68
3.30 v_1 as a function of p_T with respect to SMD S for different centrality bins	69
3.31 v_2 as a function of p_T with respect to BBC S and N combined event plane for different track matching cuts and centrality bins	69
3.32 v_3 as a function of p_T with respect to BBC S and N combined event plane for different track matching cuts and centrality bins	69
3.33 v_1 as a function of p_T with East, West and East and West combined central arms for different centrality bins	70
3.34 v_2 as a function of p_T with East, West and East and West combined central arms for different centrality bins	70
3.35 v_3 as a function of p_T with East, West and East and West combined central arms for different centrality bins	70
3.36 Integrated p_T v_2 as a function of η for different event plane selections in Au+Au collisions at $\sqrt{s_{NN}} = 200\text{GeV}$	71
3.37 Integrated p_T v_3 as a function of η for different event plane selections in Au+Au collisions at $\sqrt{s_{NN}} = 200\text{GeV}$	72
3.38 Input p_T spectra for three inverse parameters	72
3.39 Input η probability distribution. The blue data points represent central Au+Au collisions case and the red data points corresponds to peripheral Cu+Cu collisions case.	73
3.40 Input v_n as a function of η for four type slopes	74
3.41 Input $v_n(\eta)$ probability distribution	75

3.42 Input $v_n(\eta)$ probability distribution	76
3.43 Input $v_n(\eta)$ probability distribution	76
3.44 Input $v_n(\eta)$ probability distribution	77
4.1 Charged hadron v_1 at mid-rapidity ($ \eta < 0.35$) as a function of p_T in Cu+Au collisions	83
4.2 Charged hadron v_2 at mid-rapidity ($ \eta < 0.35$) as a function of p_T in Cu+Au collisions	83
4.3 Charged hadron v_3 at mid-rapidity ($ \eta < 0.35$) as a function of p_T in Cu+Au collisions	84
4.4 Charged hadron v_2 at mid-rapidity ($ \eta < 0.35$) as a function of p_T in Au+Au, Cu+Au and Cu+Cu collisions for different centrality classes	84
4.5 Charged hadron v_3 at mid-rapidity ($ \eta < 0.35$) as a function of p_T in Au+Au and Cu+Au collisions for different centrality classes	85
4.6 Charged hadron v_2 with polynomial fitting functions at mid rapidity in Au+Au, Cu+Au and Cu+Cu collisions	86
4.7 Charged hadron v_3 with polynomial fitting functions at mid rapidity in Au+Au and Cu+Au collisions	86
4.8 Charged hadron p_T spectra at mid rapidity in Au+Au collisions [16]	87
4.9 Parameters A , p_0 and n of fitting function $f(p_T) = A \frac{p_0}{p_0 + p_T}^n$ for charged hadron p_T spectra at mid rapidity in Au+Au collisions [16]	88
4.10 p_T integrated $v_2(0 < p_T < 3\text{GeV}/c)$ at mid rapidity Au+Au, Cu+Cu and Cu+Au collisions	88
4.11 PID v_2 as a function of p_T in Cu+Au collisions	89
4.12 PID v_3 as a function of p_T in Cu+Au collisions for different centrality bins	90
4.13 PID v_1 as a function of p_T in Cu+Au collisions	90
4.14 The v_2 measurements for $0 \sim 40\%$ centrality class in Au+Au and Cu+Cu compared to the PHOBOS results	91
4.15 The v_2 measurements for different centrality classes in Au+Au and Cu+Cu compared to the PHOBOS results	91
4.16 v_2 at BBC rapidity in the three collision systems for different centrality classes	92
4.17 Left: p_T integrated v_2 as a function of N_{part} at forward/backward rapidity in Au+Au, Cu+Au and Cu+Cu collisions at $\sqrt{s_{NN}} = 200\text{GeV}$. Right: ε_2 in Monte Carlo Glauber model as a function of N_{part} in Au+Au, Cu+Au and Cu+Cu collisions	93
4.18 v_3 at BBC rapidity in the two collision systems for different centrality classes	93
4.19 Left: p_T integrated v_3 as a function of N_{part} at forward/backward rapidity in Au+Au and Cu+Au collisions at $\sqrt{s_{NN}} = 200\text{GeV}$. Right: ε_3 in Monte Carlo Glauber model as a function of N_{part} in Au+Au and Cu+Au collisions at $\sqrt{s_{NN}} = 200\text{GeV}$	94
4.20 The measurements of charged particle multiplicity $dN/d\eta$ at $3 < \eta < 3.9$ in Au+Au and Cu+Cu collisions at $\sqrt{s_{NN}} = 200\text{GeV}$ in comparison to PHOBOS results[12],[53]	94
4.21 Charged particle multiplicity $dN/d\eta$ as a function of η in Au+Au, Cu+Au and Cu+Cu collisions at $\sqrt{s_{NN}} = 200\text{GeV}$	95

5.1	Participant nucleon distribution in Cu+Au collisions for 20-30 % centrality class	97
5.2	Number of participant distribution and density gradient distribution in x direction in Cu+Au collisions for 20-30% centrality class. Left:Number of participant distribution. Right:Density gradient distribution	97
5.3	Azimuthal correlation between 1st order participant plane $\Psi_{1,PP}$ and impact parameter Ψ_{imp} . Negative sign indicates the highest density gradient is Au nucleus side.	98
5.4	Identified charged hadron v_1 at mid-rapidity fitted with the Blast wave model for 10-50 % centrality class in Cu+Au collisions	100
5.5	The Blast wave model parameters for identified charged hadron v_1 at mid-rapidity for 10-50 % centrality class in Cu+Au collisions. Top left: Freeze-out temperature T_f , Top right: Averaged radial velocity $\langle \rho \rangle$, Bottom left:Directed anisotropy of radial velocity ρ_1 , Bottom right:Directed anisotropy of spatial density s_1 . The parameters T_f and $\langle \rho \rangle$ are obtained from the PHENIX Au+Au publication [24]. The anisotropy parameters ρ_1 and s_1 are extrapolated from the fitting.	101
5.6	Total charged particle multiplicity per participant nucleon in Au+Au collisions at $\sqrt{s_{NN}} = 200, 130, 62.4$ and 19.6 GeV measured by PHOBOS [48]	102
5.7	The comparison of the charged particle multiplicity distributions $dN_{ch}/d\eta$ among Au+Au, Cu+Au(Cu-going) and Cu+Cu collisions	104
5.8	The comparison of the charged particle multiplicity distributions $dN_{ch}/d\eta$ among Au+Au, Cu+Au(Au-going) and Cu+Cu collisions	104
5.9	The χ^2/NDF distributions for the comparison of $dN_{ch}/d\eta$ among Au+Au, Cu+Au and Cu+Cu collisions	105
5.10	Left: p_T integrated v_2 as a function of N_{part} at mid-rapidity in Au+Au, Cu+Au and Cu+Cu collisions at $\sqrt{s_{NN}} = 200$ GeV. The integrated p_T range is from 0 to 3 GeV. Right: ε_2 in Monte Carlo Glauber model as a function of N_{part} in Au+Au, Cu+Au and Cu+Cu collisions	107
5.11	v_2/ε_2 at mid-rapidity as a function of N_{part} in Au+Au, Cu+Au and Cu+Cu collisions	107
5.12	Left: p_T integrated v_3 as a function of N_{part} at mid-rapidity in Au+Au and Cu+Au collisions at $\sqrt{s_{NN}} = 200$ GeV. The integrated p_T range is from 0 to 3 GeV. Right: ε_3 in Monte Carlo Glauber model as a function of N_{part} in Au+Au and Cu+Au collisions	108
5.13	v_3/ε_3 as a function of N_{part} in Au+Au and Cu+Au collisions	108
5.14	Forward/backward-rapidity v_2 for charged hadrons as a function of $dN_{ch}/d\eta$ measured at forward/backward rapidity($3 < \eta < 3.9$) in Au+Au, Cu+Au and Cu+Cu collisions.	111
5.15	$\varepsilon_{2,A(B)}$, $\varepsilon_{2,A+B}$ and $\varepsilon_{2,B(A)}$ as a function of forward/backward $dN_{ch}/d\eta$ at $\sqrt{s_{NN}} = 200$ GeV in Au+Au, Cu+Au and Cu+Cu collisions.	111
5.16	$v_2/\varepsilon_{2,A(B)}$ (Left), $v_2/\varepsilon_{2,A+B}$ (Middle) $v_2/\varepsilon_{2,B(A)}$ (Right) as a function of $dN/d\eta$ at forward/backward rapidity($3 < \eta < 3.9$) in Au+Au, Cu+Au and Cu+Cu collisions at $\sqrt{s_{NN}} = 200$ GeV	112
5.17	v_2/ε_2 as a function of $dN_{ch}/d\eta$ at measured rapidity region ($3 < dN_{ch}/d\eta < 3.9$) in Au+Au, Cu+Au(Cu-going, Au-going) and Cu+Cu collisions. ε_2 for Cu+Au collisions is defined as $\varepsilon_{2,Au(Cu)-going} = w_{Au(Cu)-going}\varepsilon_{2,Au} + (1 - w_{Au(Cu)-going})\varepsilon_{2,Cu}$	113

5.18	χ^2/NDF contour distribution for $w_{\text{Cu-going}}$ vs $w_{\text{Cu-going}}$. χ^2/NDF is obtained from the difference between the Cu-going and the Au-going side v_2	114
5.19	χ^2/NDF as a function of weight for the Au-going and the Cu-going side. χ^2/NDF is obtained from the difference between Cu+Au and Au+Au collisions	114
5.20	Forward/backward-rapidity v_3 for charged hadrons as a function of $dN_{\text{ch}}/d\eta$ measured at forward/backward rapidity($3 < \eta < 3.9$) in Au+Au and Cu+Au collisions.	115
5.21	$\varepsilon_{3,\text{A(B)}}$, $\varepsilon_{3,\text{A+B}}$ and $\varepsilon_{3,\text{B(A)}}$ as a function of forward/backward $dN_{\text{ch}}/d\eta$ at $\sqrt{s_{NN}} = 200\text{GeV}$ in Au+Au and Cu+Au collisions.	115
5.22	$v_3/\varepsilon_{3,\text{A(B)}}$ (Left), $v_3/\varepsilon_{3,\text{A+B}}$ (Middle) $v_3/\varepsilon_{3,\text{B(A)}}$ (Right) as a function of $dN/d\eta$ at forward/backward rapidity($3 < \eta < 3.9$) in Au+Au, Cu+Au and Cu+Cu collisions at $\sqrt{s_{NN}} = 200\text{GeV}$	116
5.23	v_3/ε_3 as a function of $dN_{\text{ch}}/d\eta$ at measured rapidity region ($3 < dN_{\text{ch}}/d\eta < 3.9$) in Au+Au and Cu+Au(Cu-going, Au-going) collisions. ε_3 for Cu+Au collisions is defined as $\varepsilon_{3,\text{Au(Cu)-going}} = w_{\text{Au(Cu)-going}}\varepsilon_{3,\text{Au}} + (1 - w_{\text{Au(Cu)-going}})\varepsilon_{3,\text{Cu}}$	117
5.24	χ^2/NDF contour distribution for $w_{\text{Cu-going}}$ vs $w_{\text{Au-going}}$. χ^2/NDF is obtained from the consistency between the Cu-going and the Au-going side v_3	118
5.25	χ^2/NDF as a function of weight for the Au-going and the Cu-going side. χ^2/NDF is obtained from the consistency between Cu+Au and Au+Au collisions	118
5.26	Structure of AMPT model	119
5.27	Charged hadron $v_1(p_T)$ measured at mid-rapidity in Cu+Au collisions at $\sqrt{s_{NN}} = 200\text{GeV}$ in comparison to theory calculations for 20-30% centrality class. The theory calculations shown in this figure are viscous hydrodynamic calculation with $\eta/s = 0.08$ (Bozek et al[51]), ideal hydrodynamic calculation(Hirano et al[52]) and AMPT model with $\sigma = 3\text{mb}$ parton cross section[50]	120
5.28	Charged hadron $v_2(p_T)$ measured at mid-rapidity in Cu+Au collisions at $\sqrt{s_{NN}} = 200\text{GeV}$ in comparison to theory calculations for different % centrality classes. The theory calculations shown in this figure are the ideal hydrodynamic calculation(Hirano et al[52]) and the AMPT model with $\sigma = 3\text{mb}$ parton cross section[50].	121
5.29	Charged hadron $v_3(p_T)$ measured at mid-rapidity in Cu+Au collisions at $\sqrt{s_{NN}} = 200\text{GeV}$ in comparison to theory calculations for different % centrality classes. The theory calculations shown in this figure are the ideal hydrodynamic calculation(Hirano et al[52]) and the AMPT model with $\sigma = 3\text{mb}$ parton cross section[50].	121
5.30	Charged hadron $v_2(p_T)$ measured at mid-rapidity in Cu+Au collisions at $\sqrt{s_{NN}} = 200\text{GeV}$ in comparison to theory calculation for 0-5% and 20-30%centrality classes. The theory calculation shown in this figure is the viscous hydrodynamic calculation(Bozek et al[51])	122
5.31	Charged hadron $v_3(p_T)$ measured at mid-rapidity in Cu+Au collisions at $\sqrt{s_{NN}} = 200\text{GeV}$ in comparison to theory calculation for 0-5% and 20-30%centrality classes. The theory calculation shown in this figure is the viscous hydrodynamic calculation(Bozek et al[51])	122
5.32	Charged hadron $v_2(\eta)$ measured in Cu+Au collisions at $\sqrt{s_{NN}} = 200\text{GeV}$ in comparison to theory calculations for different % centrality classes. The theory calculations shown in this figure are ideal hydrodynamic calculation(Hirano et al[52]) and AMPT model with $\sigma = 3\text{mb}$ parton cross section[50].	123

5.33 Charged hadron $v_3(\eta)$ measured in Cu+Au collisions at $\sqrt{s_{NN}} = 200\text{GeV}$ in comparison to theory calculations for different % centrality classes. The theory calculations shown in this figure are ideal hydrodynamic calculation(Hirano et al[52]) and AMPT model with $\sigma = 3\text{mb}$ parton cross section[50].	123
5.34 The ratio of forward/backward v_2 values as a function of centrality in Cu+Au collisions at $\sqrt{s_{NN}} = 200\text{GeV}$ in comparison to the theory calculations. The theory calculations shown in this figure are ideal hydrodynamic calculation(Hirano et al[52]) and AMPT model with $\sigma = 3\text{mb}$ parton cross section[50].	124
5.35 The ratio of forward/backward v_3 values as a function of centrality in Cu+Au collisions at $\sqrt{s_{NN}} = 200\text{GeV}$ in comparison to the theory calculations. The theory calculations shown in this figure are ideal hydrodynamic calculation(Hirano et al[52]) and AMPT model with $\sigma = 3\text{mb}$ parton cross section[50].	124
A.1 Participant nucleon distributions for the impact parameter range $4 < b < 5$ in Au+Au and Cu+Au collisions at $\sqrt{s_{NN}} = 200\text{GeV}$ simulated by Monte Carlo Glauber model	128
A.2 Participant plane correlations between $\Psi_{3,PP}$ and the impact parameter $\Psi_{1,imp}$ in Au+Au and Cu+Au collisions	129
A.3 $v_3(\Psi_{1,Imp})$ at mid-rapidity as a function of p_T in Au+Au and Cu+Au collisions at $\sqrt{s_{NN}} = 200\text{GeV}$ calculated from the ideal hydrodynamics and the AMPT.	129
A.4 $v_3(\Psi_{1,SMDS})$ as a function of p_T measured without the resolution correction at mid-rapidity ($ \eta < 0.35$) in Au+Au and Cu+Au collisions at $\sqrt{s_{NN}} = 200\text{GeV}$	130
B.1 Initial energy density in transverse plane for nucleon base Monte Carlo Glauber model and IPGlasma model. Left:nucleon base Monte Carlo Glauber model. Right:IPGlasma model [55]	132
B.2 ϵ_2 for Au+Au, Cu+Au and Cu+Cu collisions at 200GeV in nucleon base Glauber Monte Carlo, quark base Glauber Monte Carlo and IPGlasma models	133
B.3 ϵ_3 for Au+Au and Cu+Au collisions at 200GeV in nucleon base Glauber Monte Carlo, quark base Glauber Monte Carlo and IPGlasma models	133
B.4 Scaled v_2 for charged hadrons at mid-rapidity with ϵ_2 estimated in the three initial condition models in Au+Au, Cu+Au and Cu+Cu collisions at $\sqrt{s_{NN}} = 200\text{GeV}$. Left:Nucleon base Monte Carlo Glauber model, Middle:Quark base Monte Carlo Glauber model and Right:IPGlasma model	134
B.5 Scaled v_3 for charged hadrons at mid-rapidity with ϵ_3 estimated in the three initial condition models in Au+Au and Cu+Au collisions at $\sqrt{s_{NN}} = 200\text{GeV}$. Left:Nucleon base Monte Carlo Glauber model, Middle:Quark base Monte Carlo Glauber model and Right:IPGlasma mode	134
B.6 Scaled v_2 for charged hadrons at forward/backward-rapidity with ϵ_2 estimated in the three initial condition models in Au+Au, Cu+Au and Cu+Cu collisions at $\sqrt{s_{NN}} = 200\text{GeV}$. Left:Nucleon base Monte Carlo Glauber model, Middle:Quark base Monte Carlo Glauber model and Right:IPGlasma mode	135

B.7 Scaled v_3 for charged hadrons at forward/backward-rapidity with ϵ_3 estimated in the three initial condition models in Au+Au and Cu+Au collisions at $\sqrt{s_{NN}} = 200\text{GeV}$. Left:Nucleon base Monte Carlo Glauber model, Middle:Quark base Monte Carlo Glauber model and Right:IPGlasma mode	135
C.1 Weighted eccentricity scaling of v_2 as a function of weighted N_{part} for Au-going side in Cu+Au collisions compared to the Au+Au and Cu+Cu results.	137
C.2 Weighted eccentricity scaling of v_2 as a function of weighted N_{part} for Cu-going side in Cu+Au collisions compared to the Au+Au and Cu+Cu results.	138
C.3 Weighted eccentricity scaling of v_3 as a function of weighted N_{part} for Au-going side in Cu+Au collisions compared to the Au+Au result.	139
C.4 Weighted eccentricity scaling of v_3 as a function of weighted N_{part} for Cu-going side in Cu+Au collisions compared to the Au+Au result.	140

List of Tables

1.1	Summary of heavy ion program. Accelerators, Locations of the accelerators, Collision species, Energy and operation years are written.	4
3.1	Default setting for single particle simulation	62
3.2	Nuclear density parameters used in Glauber model	65
3.3	Systematic uncertainties in the v_1 measurements at mid rapidity	78
3.4	Systematic uncertainties given in percent on the v_2 measurements at mid rapidity	79
3.5	Systematic uncertainties given in percent on the v_3 measurements at mid rapidity	79
3.6	Systematic uncertainties in the measured v_1 for identified particles at mid rapidity	79
3.7	Systematic uncertainties in percent on the measured v_2 and v_3 for identified particles at mid rapidity	79
3.8	Event Plane systematic uncertainties given in percent on the v_2 measurements at forward/backward rapidity.	80
3.9	Event Plane systematic uncertainties given in percent on the v_3 measurements at forward/backward rapidity.	81
3.10	Correction factors and Systematic uncertainties given in percent on the simulated v_n (n=2,3) at forward/backward rapidity	81
3.11	Correction factors and Systematic uncertainties given in percent on the simulated $dN_{ch}/d\eta$ at forward/backward rapidity	81

Acknowledgements

First of all, I would like to express my gratitude to Prof. Y. Miake for giving me an opportunity to study heavy ion physics and have great experience in this field. He gave me essential and important suggestions and advises. His crucial comments led improvement of my research and this dissertation. I also would like to acknowledge Prof. S. Esumi. My dissertation would never been finished without him. He always gave me a great deal of comments and advices, discussed with me and kindly answered my questions. When I talked at PHENIX physics working group meeting, he always attended at the meeting till night. I learned many things from him, the knowledge on the heavy ion physics, experimental technique and analysis of experimental data. I am thankful to the staff at our laboratory. Prof. T. Chujo, Prof. M. Inaba, Prof. S. Sakai and Mr. S. Kato for giving me comments, advices and suggestions and supporting me to develop the comfortable research environment.

I would like to acknowledge my colleagues at our laboratory. Especially, I would like to thank Dr. S. Mizuno, Mr. N. Tanaka, Mr. S. Horiuchi, Dr. D. Watanabe, Ms. K. Gunji and Ms. T. Nakajima. I enjoyed my student life with them. I would like to thank Mr. H. Yokoyama, Mr. R. Hosokawa, Mr. N. Toshihiro, Mr. R. Aoyama, Mr. L. Joonil, Mr. T. Sugiura, Mr. Y. Fukuda, Mr. K. Ito, Mr. B. Kim, Mr. R. Koyama, Ms. S. Kudo, Mr. K. Matsunaga, Mr. K. Sato, Mr. Y. Rebaza, Mr. T. Ichisawa, Mr. H. Kato, Mr. D. Taichi, Mr. Y. Kawamura, Mr. T. Suzuki, Mr. K. Nakagawa, Mr. T. Nishimatsu and Mr. H. Jeong for their friendship and discussions.

I would like to acknowledge RIKEN Radiation Laboratory members, Dr. H. En'yo, Dr. Y. Akiba, Dr. I. Nakagawa, Dr. T. Hachiya, Dr. Y. Yamaguchi, Ms. K. Suzuki, Dr. C. Kim, Dr. I. Yoon, Mr. T. Moon, Ms. S. Han, Ms. M. Kim and the other members for their support, many useful comments and discussions.

I am very grateful to Prof. M. Shimomura, Dr. M. Kurosawa, Dr. Y. Ikeda, Dr. T. Niida and Dr. T. Todoroki for their useful comments, discussions and friendship.

I would like to acknowledge the students of Hiroshima University, Mr. T. Hoshino, Mr. K. Nagashima and Mr. Y. Ueda for their friendship at BNL.

I would express my many thanks to PHENIX collaborator, Prof. J. Nagle, Dr. D. Morrison, Prof. J. Velkovska, Dr. T. Sakaguchi, Dr. P. Stankus, Prof. R. Seto, Prof. V. Riavov, Dr. J. Haggerty, Dr. Mickey Chiu, Dr. S. Huang, Dr. B. Schaefer and Dr. Y. Haiwang for many advises and comments.

Finally, I would like to express my deepest appreciation to my family, Keiichi Nakagomi, Toshie Nakagomi and Miku Nakagomi for their understanding, continuous support and encouragements.

Chapter 1

Introduction

1.1 Quark Gluon Plasma

An atom consists of electrons and a nucleus that is composed of protons and neutrons. The electrons are considered to be point like particles and the protons and neutrons are composed of three fundamental particles, so called quarks. The quarks have the flavor degrees of freedom (up, down, strange, charm, bottom and top) and color degrees of freedom (red, blue and green). Experimentally, quarks have been never observed in isolation, because they are always combined to form composite particles "hadrons" that are white or neutral in terms of color charges. Hadrons are categorized into two familiar groups, baryons and mesons. Baryons are fermions such as protons and neutrons and compose of three quarks. On the other hand mesons are bosons, such as pions and kaons, and are formed by a pair of quark and anti-quark.

The interaction(strong interaction) acting among quarks are called the strong interaction and described by quantum chromodynamics (QCD). QCD is the gauge field theory based on color charge in analogous to quantum electrodynamics (QED). In QCD (QED) theory, the gluons (photons) as gauge bosons that carry the strong force (electromagnetic force) between quarks (charged particles). Although QCD is similar to QED, QCD has $SU(3)$ algebra and QED has $U(1)$ algebra. This is because gluons are not neutral in color charge. Gluons interact with each other as well as with quarks. On the other hand, photons do not interact with each other due to no electric charge.

QCD has two important characteristics. One is "Asymptotic freedom" [1, 2] and the other is "Color confinement" [3]. In QCD, the asymptotic freedom describes the interaction between quarks and gluons to become asymptotically weaker at large energy (short distance) and larger at small energy (large distance). Fig. 1.1[4] shows the (running) coupling constant of QCD as a function of momentum transfer Q . At the small Q region, the coupling constant becomes larger and is described in non-perturbative way. On the other hand, the coupling constant become smaller at the high Q region and is described pertubatively.

As described at the beginning of this section, the quarks that compose a hadron can not be separated from the hadron. This phenomena is called Color confinement. Due to asymptotic freedom, the interaction becomes stronger at long distance. Although there is no analytic proof of the confinement, the potential energy between quark and anti-quark pair is calculated in

lattice QCD. Figure 1.2[5] shows the potential energy as a function of the distance of a quark and anti-quark pair r . The potential energy $V(r)$ is fitted with

$$V(r) = V_0 - \frac{\alpha}{r} + \sigma_0 r \quad (1.1)$$

where V_0 , α and σ are unknown parameters (free parameters). As a pair of constituent quark and anti-quark are separated from each other, the potential energy increases linearly. If the distance between them is beyond some critical distance, energetically it is favorable to create a new quark and anti-quark pair. Then, the original pair is divided into two pair. Thus quarks are always bound together and are inside hadrons.

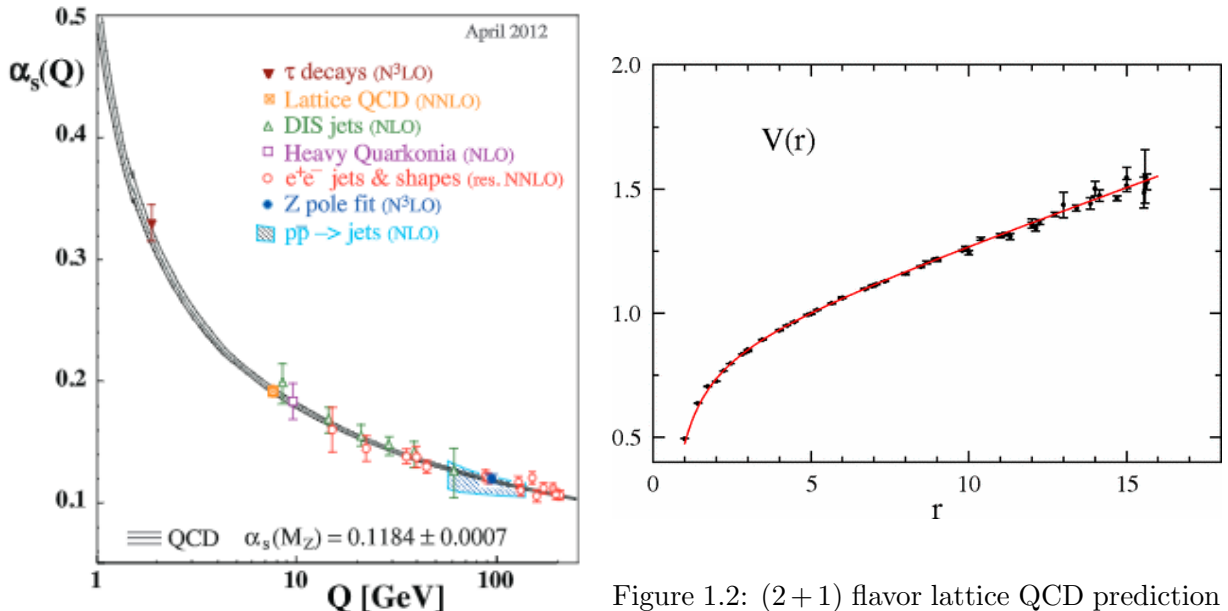


Figure 1.1: Summary of measurement of α_s as a function of momentum transfer Q [4]

Figure 1.2: (2 + 1) flavor lattice QCD prediction of the potential energy between a pair of quark and anti-quark as a function of the distance[5]

Quark-Gluon-Plasma(QGP) is a new state of nuclear matter that is formed by asymptotically free quarks and gluons. Due to asymptotic freedom, a phase transition from normal nuclear matter to the QGP should occur at high temperature(high energy). Indeed, lattice QCD theory predicts the QCD phase transition at high temperature and zero-baryon density by computing from first principles[6]. Fig. 1.3 shows the temperature dependences of pressure, energy density and entropy density normalized by $\frac{1}{T^4}$ calculated by (2 + 1) flavor lattice QCD. These thermodynamic variables are smoothly changed when increasing the temperature, which means the phase transition from hadronic matter to the QGP state is a crossover. The critical temperature $T_c = 154 \pm 9$ is shown as a yellow vertical band in Figure 1.3. At the critical temperature, the corresponding energy density is $\epsilon = 0.18 - 0.5$ GeV.

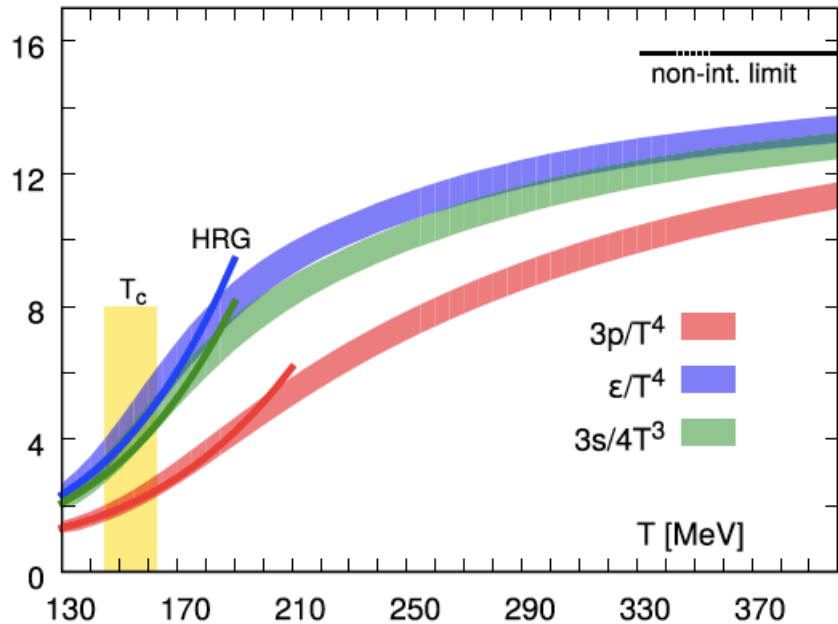


Figure 1.3: $(2+1)$ flavor lattice QCD prediction on pressure, energy density and entropy density normalized by $\frac{1}{T^4}$ as a function of temperature. The dark tree lines are the results of hadron resonance gas model. The ideal gas limit for the energy density is shown as a horizontal line at $95\pi^2/60$ [6]

1.2 Relativistic Heavy Ion Collisions

As described in previous chapter, Lattice QCD calculation predicts the existence of new state of nuclear matter called Quark-Gluon-Plasma(QGP) which is composed of de-confined quarks and gluons under extremely high and/or dense. Experimentally to create such a hot and/or dense matter, relativistic heavy ion collisions is considered a unique tool on the earth. By heavy ion collisions, longitudinal kinetic energies of incoming nuclei are deposited into the region between the receding nuclei. If the released energy is highly enough, the QGP state can be formed.

Historically, some high energy heavy ion accelerators have been built to create QGP state. From the middle of 1970's to the end of 1980's, BEVALAC accelerator at Lawrence Berkeley Laboratory in United States of America was operated. In the middle of 1980's, Alternating Gradient Synchrotron(AGS) at Brookhaven National Laboratory(BNL) in USA and Super Proton Synchrotron(SPS) at European Organization for Nuclear Research (CERN) in Switzerland were operated. In 2000, Relativistic Heavy Ion Collider(RHIC) at BNL began operation. And Large Hadron Collider(LHC) at CERN started its first run in 2010. Table 1.1 is the summary of the accelerators, heavy ion collision species, energies and operation years.

Table 1.1: Summary of heavy ion program. Accelerators, Locations of the accelerators, Collision species, Energy and operation years are written.

Accelerators	Location	Species	Energies (GeV)	Year
AGS	BNL	^{16}O , ^{28}Si	5.4	1986
		^{197}Au	4.8	1992
SPS	CERN	^{16}O , ^{32}S	19.4	1986
		^{208}Pb	17.4	1994
RHIC	BNL	^{197}Au	130	2000
		^{197}Au	200	2001
		d+ ^{197}Au	200	2003
		^{197}Au	200,62.4	2004
		^{63}Cu	200,62.4,22.4	2005
		^{197}Au	200	2007
		d+ ^{197}Au	200,62.4	2008
		^{197}Au	200,62.4,39,11.5, 7.7	2010
		^{197}Au	200,19.6, 27	2011
		^{238}U	193	2012
		$^{63}\text{Cu} + ^{197}\text{Au}$	200	2012
		^{197}Au	200,14.6	2014
		He+ ^{197}Au	200	2014
		p+ ^{197}Au	200	2015
LHC	CERN	p+ ^{27}Al	200	2015
		^{197}Au	200	2016
		d+ ^{197}Au	200,62.4,19.6,39	2016
		^{208}Pb	2760	2010
		^{208}Pb	2760	2011
		p+ ^{208}Pb	5020	2013
		^{208}Pb	5500	2015

1.2.1 Participant Spectator Picture

In a heavy ion collision, the initial collision geometry play a important role to understand the collision dynamics. In relativistic heavy ion collisions, nuclei collide at nearly the speed of light. Because they move at relativistic speed, they are Lorentz-contracted. The longitudinal thickness of nuclei becomes $2R/\gamma$ where R is radius of nuclei and γ is Lorentz factor. γ is expressed as $\gamma = E/M$ using colliding energy E and nuclei mass M .

In high energy nucleus-nucleus collisions, "participant-spectator model" is established and experimentally observed features are described well using this model. In relativistic heavy ion collisions, the speed of colliding nuclei is much faster than fermi motion of nucleons. Therefore nucleons do not approximately move in transverse direction. Fig. 1.4 is a schematic picture of the colliding nuclei before and after a collision. Then the overlap region can be described using impact parameter b . Impact parameter b is defined as the distance between the centers of two colliding nuclei. If b is less than $2R$ where R is a radius of the nucleus, inelastic collisions occur. As impact parameter decreases, overlap region increases. If $b \simeq 0$, almost all particles participate in a collision. Such a collision is called a central collision. If $b \simeq 2R$, the overlap region of two nuclei is small. Such collision is called a peripheral collision. In nucleus-nucleus collisions, the collision systems consist of two components. One is "participant", which is the overlapped region shown by elliptical region in Fig. 1.4 and the other is "spectator", which is the region other than "participant" shown in Fig. 1.4. Glauber model described below can successfully evaluate the number of nucleons which participate collisions[7].

In order to describe high energy nuclear reactions, the Glauber model has been employed. By using the Glauber model, the total reaction cross-sections and the number of nucleons which participate in collisions, the number of nucleon-nucleon binary collisions can be evaluated. In the Glauber model, the nucleus-nucleus collision are treated as the multiple nucleon-nucleon collisions and nucleons are assumed to go through in straight lines without any deflection. In Au+Au collisions at $\sqrt{s_{NN}} = 200\text{GeV}$, this approximation works well because the nucleon can move 0.12 fm at maximum in transverse plane during the beam crossing time 0.12 fm/c. Compared to the radius of Au nuclear 6.38 fm, this moving distance is relatively small. In this model, secondary particle production and possible excitation of nucleons are not included. For the simplest type of the Glauber model, a nucleon-nucleon collision occurs when the distance of the two nucleons d is less than,

$$d \leq \sqrt{\sigma_{NN}/\pi} \quad (1.2)$$

where σ_{NN} is the total inelastic nucleon-nucleon cross section. The nucleus A sickness function $T_{AB}(\mathbf{b})$ with impact parameter \mathbf{b} is given by,

$$T_A(\mathbf{s}) = \int dz \rho_A(z, \mathbf{s}) \quad (1.3)$$

where $\rho_A(\mathbf{s}, z)$ is the probability per unit volume for the nucleon at (\mathbf{s}, z) . The product of $T_A(\mathbf{s})T_B(\mathbf{s} - \mathbf{b})d^2s$ provides the probability per unit area ds^2 of target nuclear A and projectile nuclear B. Then the overlap thickness function of A and B nuclei defined by integrating the product over all \mathbf{s} is given by,

$$T_{AB}(\mathbf{b}) = \int d^2s T_A(\mathbf{s})T_B(\mathbf{s} - \mathbf{b}) \quad (1.4)$$

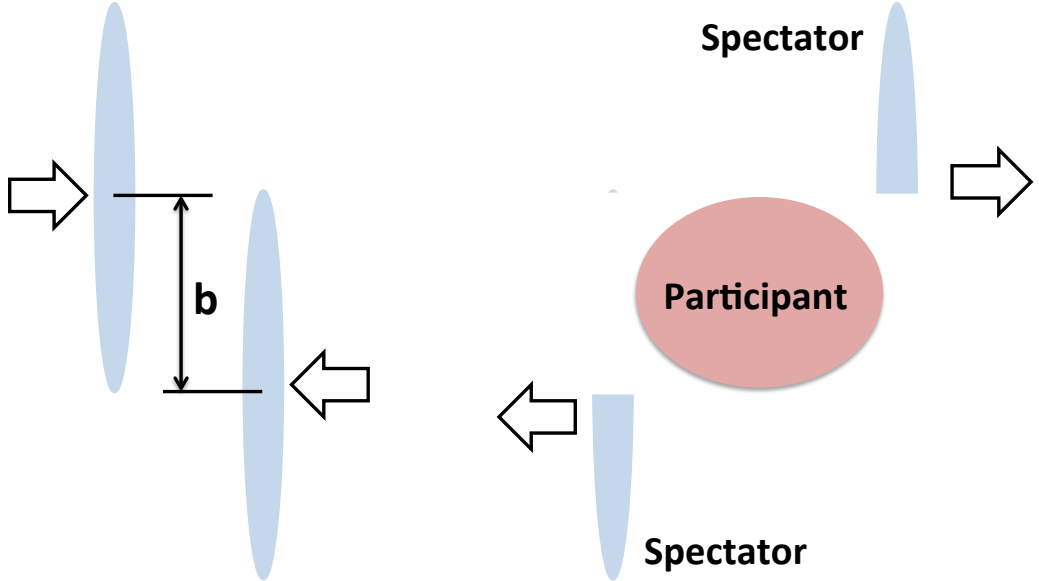


Figure 1.4: Schematic view of the colliding nuclei before(left) and after(right) collision.

The number of participant nucleons N_{part} and the number of binary collisions N_{coll} are expressed as,

$$N_{\text{part}}(b) = \int ds^2 T_A(s) (1 - e^{-\sigma_{NN} T_B(s)}) + \int d^2 s (T_B(s - b) (1 - e^{-\sigma_{NN} T_A(s)})) \quad (1.5)$$

$$N_{\text{coll}}(b) = \int d^2 s \sigma_{NN} T_A(s) T_B(s - b) \quad (1.6)$$

1.2.2 Nuclear stopping power

In heavy ion collisions, the energy deposition of colliding two nuclei is a fundamental quantity that is converted into particle production. For the QGP formation, the colliding nuclei have to loss sufficient kinetic energy. Since the baryon number is conserved, the energy deposition could be estimated by the measured net-baryon rapidity distribution(the baryon rapidity distribution is subtracted by the anti-baryon rapidity distribution). The rapidity is defined as

$$y = \frac{1}{2} \ln \frac{E + p_z}{E - p_z} \quad (1.7)$$

where E and p_x are energy and momentum in beam direction respectively. The energy deposition

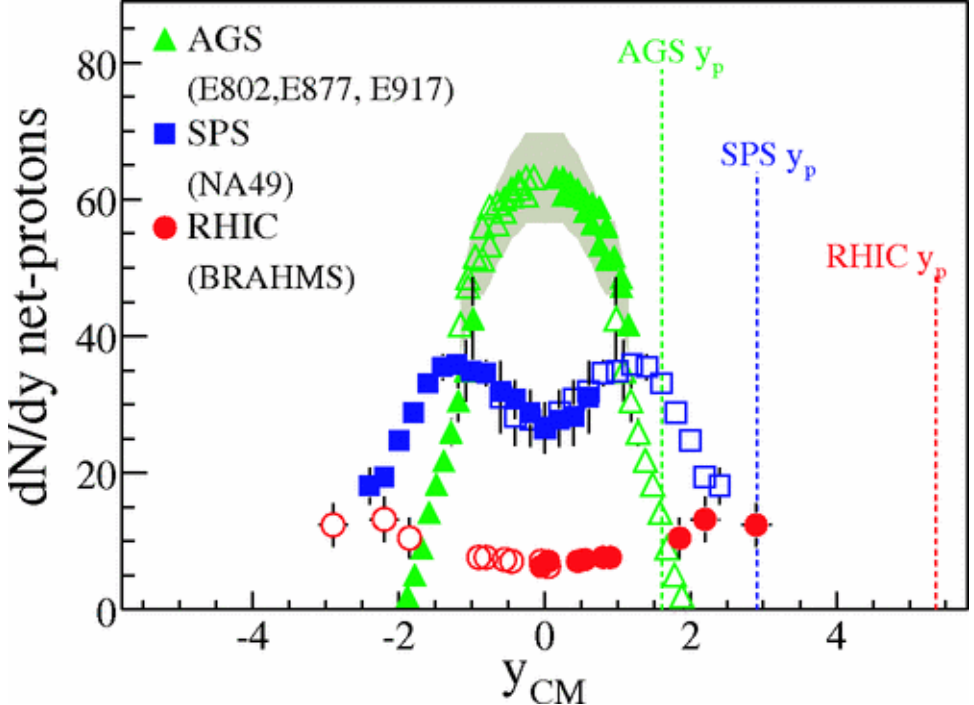


Figure 1.5: Net proton dN/dy distribution at 5(AGS), 17(SPS) and 200(RHIC) GeV.

is quantified by the average net-baryon rapidity loss. The average rapidity $\langle y \rangle$ after the collision is expressed as

$$\langle y \rangle = \int_0^{y_p} y \frac{dN}{dy} dy / \int_0^{y_p} \frac{dN}{dy} dy \quad (1.8)$$

where y_p is rapidity of the incoming projectile particles(incident particles) and $\frac{dN}{dy}$ is the number of net-baryons per rapidity unit. The average rapidity loss is $\langle \delta y \rangle = y_p - \langle y \rangle$. If the incident particles loss all their energy, $\delta \langle y \rangle = 0$.

Fig. 1.5 shows the net-proton rapidity distribution (the p rapidity distribution is subtracted by the \bar{p} rapidity distribution) for central Pb+Pb and Au+Au collisions at AGS($\sqrt{s_{NN}} = 5$ GeV), SPS($\sqrt{s_{NN}} = 17$ GeV) and RHIC $\sqrt{s_{NN}} = 200$ GeV. The distributions have strong beam energy dependence. At AGS energy, the central peak is seen at mid-rapidity. But at SPS and RHIC energies, the dip and plateau structures are seen at mid-rapidity and the central peak as seen at AGS energy is changed into a double hump structure. This energy dependence implies that the nuclear collision dynamics is changed from "stopping" to "transparent". Nuclear stopping power is considered to saturate in these energies, namely the incident particles don't lose all their kinetic energy but pass through each other.

The BRAHMS collaboration estimated the rapidity loss in central Au+Au collisions at $\sqrt{s_{NN}}=200$ GeV. The rapidity loss is $\langle \delta y \rangle = 2.0 \pm 0.4$. The corresponding energy loss is around 70 GeV per nucleon. The total kinetic energy deposition in central Au+Au collision at $\sqrt{s_{NN}}=200$ GeV is about 28 TeV ($70 \times 197 \times 2$).

1.2.3 Space-Time Evolution of Collisions

The time history of the hot and dense matter formed in relativistic heavy ion collisions is categorized into following stages. Fig. 1.6 is a sketch for the space time history of a relativistic heavy ion collision in the beam direction z and the time t .

–**Parton cascade stage(pre-equilibrium stage) : $0 < \tau < \tau_0$**

After the collisions, a large amount of energy is deposited in the overlap region. The energy density is expected to be high. Many free partons are produced because of huge energy density and frequently parton-parton scattering occurs.

–**QGP phase(thermal equilibrium)**

After multi parton scattering occurs, local thermal equilibrium is achieved. Once the local thermal equilibrium is achieved, relativistic hydrodynamics could describe the evolution of the interaction region. In the relativistic hydrodynamics, the equation of motion are given by conservation laws for the energy-momentum tensor $T^{\mu\nu}$ and the i -th conserved charge currents j_i^μ (in heavy ion collisions, there are some conserved charges, for example baryon number and strangeness.)

$$\partial_\mu T^{\mu\nu} = 0 \quad (1.9)$$

$$\partial j_i^\mu = 0 \quad (1.10)$$

When the fluid achieve the local thermal equilibrium, in the perfect fluid approximation, the momentum-energy tensor and the conserved charge current are given by

$$T^{\mu\nu} = (\epsilon + P)u^\mu u^\nu - Pg^{\nu\mu} \quad (1.11)$$

$$j_i^\mu = n_i u^\nu \quad (1.12)$$

where ϵ and P are the energy and the thermodynamic pressure in the local rest frame of the fluid, $g^{\nu\mu}$ is the Minkowski metric tensor, n_i is the charge density and u^ν is the fluid flow four-velocity. The perfect fluid approximation reduces the number of unknown variables to $5+n$. The unknown $5+n$ variables are the energy density, pressure, the charge density for n types and three component of four-velocity v_x, v_y, v_z . Eq. 1.10 contain $4+n$ equation. If the equation of state $P = P(\epsilon, \{n_i\})$ is provided, the total unknown variables and equations will be same, then one can solve these equations with boundary conditions (initial conditions).

–**Mixed state between QGP and hadrons**

As the medium expands, the temperature becomes low. If the temperature reaches the critical temperature T_c , the medium starts to hadronize. The medium consists of free partons and hadrons. If the phase transition is first order transition, this state would exist.

–**Chemical Freeze-out and thermal Freeze-out**

While the medium hadronize, inelastic scattering among hadrons is kept until the temperature become below T_{ch} , inelastic scattering is terminated and hadron yield is determined. We call this temperature T_{ch} "Chemical Freeze-out". Finally hadron elastic scattering is also terminated and hadrons stream out at temperature T_{th} . This temperature is called "Thermal freeze-out".

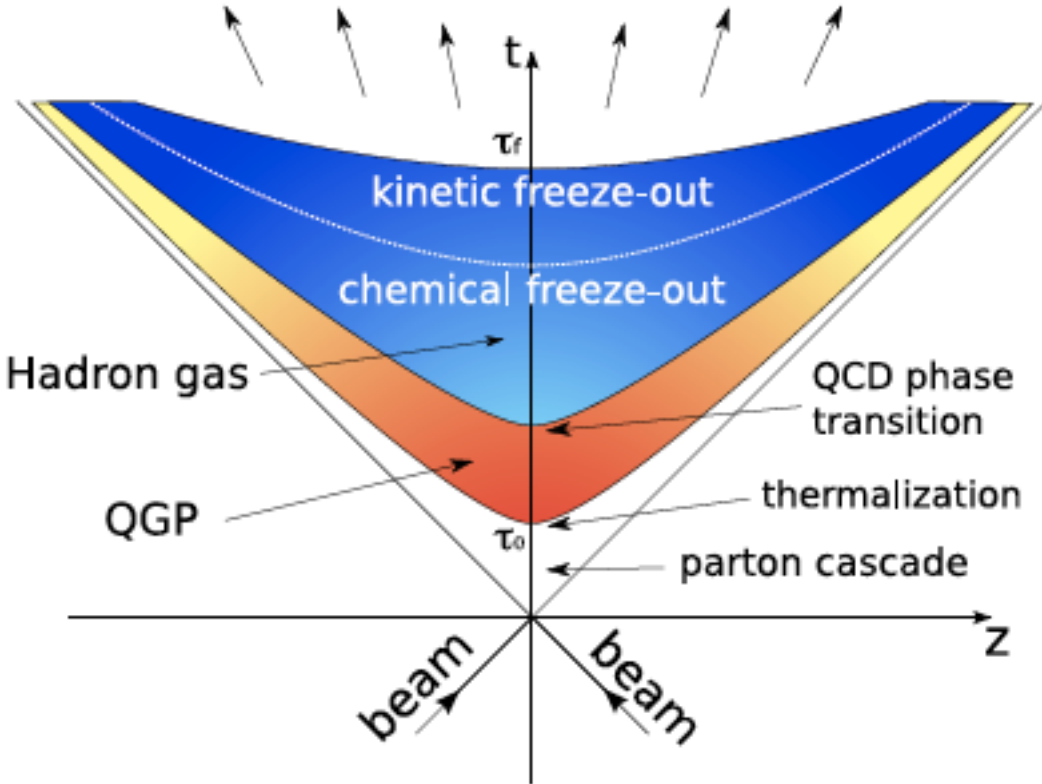


Figure 1.6: A sketch for the space time history of a relativistic heavy ion collision in the beam direction z and the time t

1.3 Major Features of Experimental Observables

1.3.1 Energy Density

Bjorken gave a prescription for the initial energy density estimation in [8]. In Fig. 1.7, the original diagram in his paper is shown. Once the two pancakes recede from the collision points, particles are produced and occupy the region between two pancakes. At time t after the collision, the volume that contains all of the produced particles will be longitudinal thickness dz with the nuclear-nuclear overlap region A . The number of produced particles in this volume can be written

$$dN = \frac{dz}{\tau} \frac{dN}{d\beta} \quad (1.13)$$

If the produced particles have an average total energy $\langle m_T \rangle$ ($m_T = \sqrt{p_T^2 + m^2}$ no longitudinal velocity), the energy density is calculated by the total volume at time τ from the collision and

the total energy

$$\begin{aligned}
 \langle \epsilon(\tau) \rangle &= \frac{dN \langle m_T \rangle}{dzA} \\
 &= \frac{dN \langle m_T \rangle}{dy} \frac{c\tau A}{c\tau A} \\
 &= \frac{1}{\tau A} \frac{dE_T}{dy}
 \end{aligned} \tag{1.14}$$

where $\frac{dE_T}{dy} = \langle m_T \rangle \frac{dN}{dy}$. This equation is referred to as Bjorken energy density ϵ_{Bj} . The PHENIX experiment measured the ϵ_{Bj} in Au+Au collisions at three collision energies as shown in Fig. 1.8 [9]. In the estimation of ϵ_{Bj} , the time τ is used 1 fm/c at the thermalization time from the collision and the overlap zone A is calculated by the Monte Carlo Glauber model simulation. As described in Section 1.1, the energy density for the phase transition is expected to be approximately $\epsilon = 0.18 - 0.5 \text{ GeV/fm}^3$ by the Lattice QCD. Except peripheral collisions, the ϵ_{Bj} are larger than the predicted energy density.

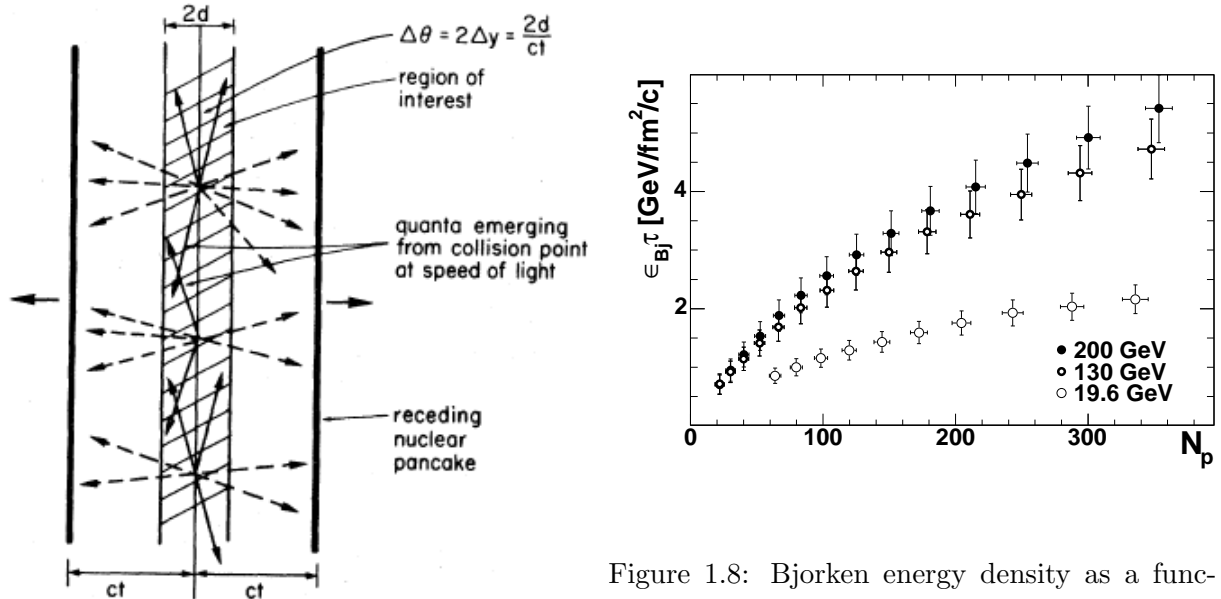


Figure 1.7: Geometry for the initial state of a central collision in nucleus-nucleus collisions[8].

Figure 1.8: Bjorken energy density as a function of number of participants at mid-rapidity in Au+Au collisions observed by PHENIX[9]

1.3.2 Particle Production

Measurement of single particle transverse momentum $p_T = \sqrt{p_x^2 + p_y^2}$ distribution is one of the useful tools in studying collision dynamics because the transverse motion of produced particles is generated during the collisions and hence the produced particles carries informations of the collision dynamics. The transverse momentum spectra have been measured in several collision systems and at several energies. The charged hadron transverse spectra at mid-rapidity for different centrality in Au+Au collisions at $\sqrt{s_{NN}} = 200$ GeV are shown in Fig. 1.9 [16]. It is known that the p_T spectra are described by an exponential function at $p_T \leq 2$ and power law function at higher p_T range. This trend implies the transition of particle production mechanism from soft production at low p_T to hard particle production hight p_T . It is also known that the

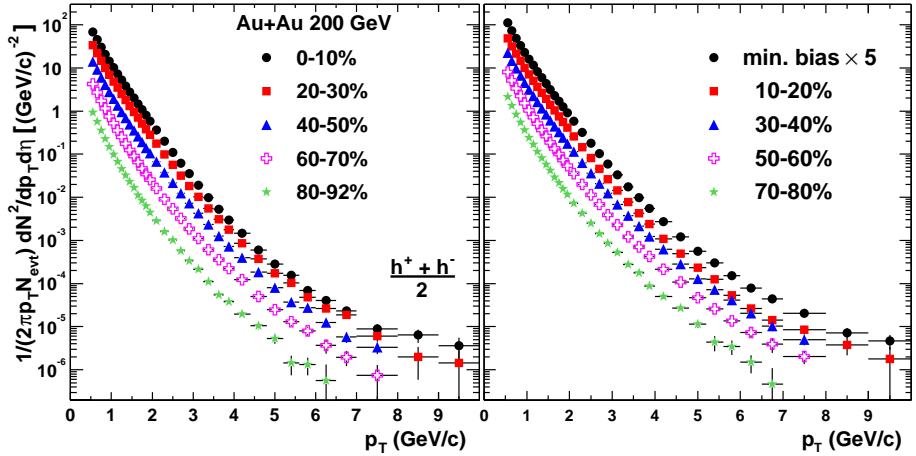


Figure 1.9: Charged hadron p_T spectrum for different multiplicity class in Au+Au collisions at $\sqrt{s_{NN}} = 200$ GeV [16]

single particle spectra of transverse mass $m_T = \sqrt{p_T^2 + m_0^2}$ (m_0 is particle mass) are expressed as an exponential function at low p_T region.

$$E \frac{d^3\sigma}{dp^3} \frac{1}{2\pi m_T} \frac{d^2\sigma}{dm_T dy} \propto \exp(-m_T/T) \quad (1.15)$$

where the inverse slope parameter T . The inverse slope parameter is called effective temperature which increases with increasing collision energy and depend on system size. In high energy nucleon-nucleon collisions above $\sqrt{s_{NN}} \geq 5$ GeV, the inverse slope parameters are common for particle species. This scaling is called m_T scaling. In Fig.1.10, the π^\pm , K^\pm , p and \bar{p} transverse mass spectra at mid-rapidity for different multiplicity class in Au+Au collisions at $\sqrt{s_{NN}} = 200$ GeV[18]. The overlaid solid lines are the exponential fitting functions. The fitting ranges are 0.2 – 1.0GeV for π and 0.1 – 1.0 GeV for K and p . The inverse slope parameters for π , K and p m_T distributions at mid-rapidity for different energies and collision species are shown in Fig. 1.11 and 1.12. In Fig.1.11, the parameters are measured by NA44 collaboration at SPS accelellator and compared among Pb+Pb $\sqrt{s_{NN}} = 17.2$ GeV, S+S $\sqrt{s_{NN}} = 19.4$ GeV and p + p $\sqrt{s_{NN}} = 23$ GeV. The parameters in p+p collisions case are almost same for the particles species as referred to above. Whereas the parameters for the nucleus - nucleus collisions increase

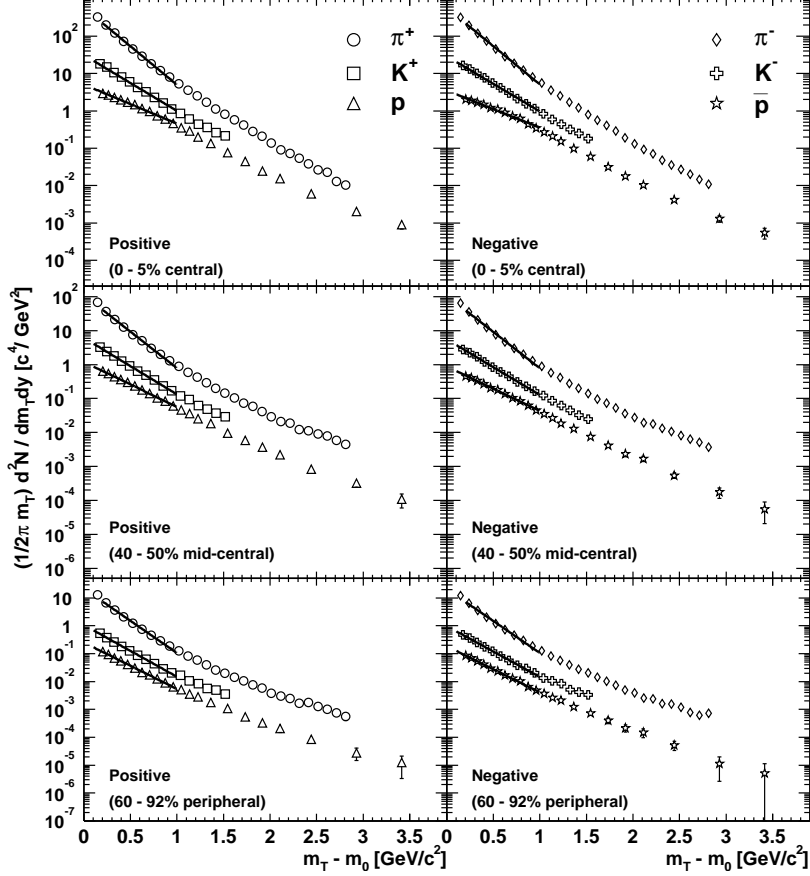


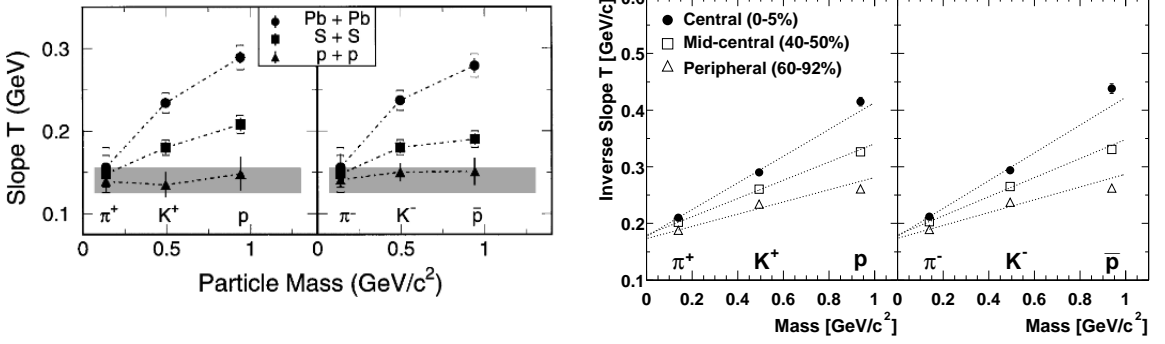
Figure 1.10: π^\pm , K^\pm , p and \bar{p} transverse mass spectra at mid-rapidity for different multiplicity class in Au+Au collisions at $\sqrt{s_{NN}} = 200\text{GeV}$ [18]

with increasing particle mass and the size of colliding system. In Fig. 1.12, the parameters extracted from the fitting functions in Fig.1.10[18] are shown. The parameters at RHIC energy have particle mass dependence as seen at SPS energy in Fig.1.11. This particle mass dependence has been considered as the influence of a common radial velocity field directed outward. This radial flow is caused by the strong interaction among the produced particles and described by hydrodynamics. In the low p_T , the inverse slope parameter is written as

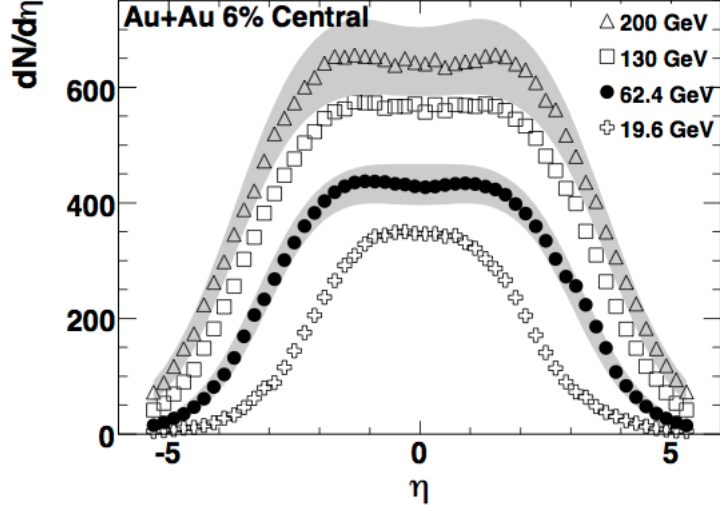
$$T_{\text{eff}} \simeq T_f + \frac{1}{2}m_0 \langle \beta^2 \rangle, p_T \leq 2\text{GeV} \quad (1.16)$$

where T_f is the temperature at thermal freeze out, m_0 is a particle mass and $\langle \beta \rangle$ is the average radical velocity. Eq. 1.16 shows the effective temperature becomes higher for the heavier particles and the larger effective temperature for the higher collision energy and the larger system size imply the stronger radial flow.

Bjorken proposed the collision reaction picture based on the parton model of hadrons for relativistic high energy collision. By the deep inelastic lepton-hadron scattering experiments, the nucleon is considered to consist of three valence quark(proton:uud,neutron:udd) and the wee partons (gluons and sea quarks). Compared to the valence quarks, most of wee partons have much smaller momentum fraction of the colliding nucleon. Thus the two incoming nuclei

Figure 1.11: Inverse slope parameters for π , K

and p m_T distributions in $\text{Pb} + \text{Pb}$ 17.2 GeV, Figure 1.12: Inverse slope parameters for different multiplicity class in $\text{Au} + \text{Au}$ 200 GeV collisions[17]

Figure 1.13: Charged particle $dN/d\eta$ in central $\text{Au} + \text{Au}$ collisions at $\sqrt{s_{NN}} = 200, 130, 62.4$ and 19.6 GeV[13]

before the collision wear the "fur coat of wee partons". When the two nuclei collide, the valence quarks punch through each other because On the other hand, the wee partons scattering take place. After head-on collisions, the region between the two nuclei is supposed to achieve the local thermal equilibrium within the time scale $1 \text{ fm}/c$ though the multiple scattering of the wee partons. Fig. 1.13 shows the pseudo-rapidity distributions of charged particles for different multiplicity classes for $-5.4 < \eta < 5.4$ in $\text{Au} + \text{Au}$ collisions at $\sqrt{s_{NN}} = 200, 130, 62.4$ and 19.6 GeV measured by the PHOBOS collaboration. Since the PHOBOS detectors have large acceptance in η direction, $\frac{dN}{d\eta}$ is measured over the almost all η region. The number of produced particle at central plateau (mid-rapidity) is about 650. The distributions become larger density and wider at central plateau with increasing collision energy.

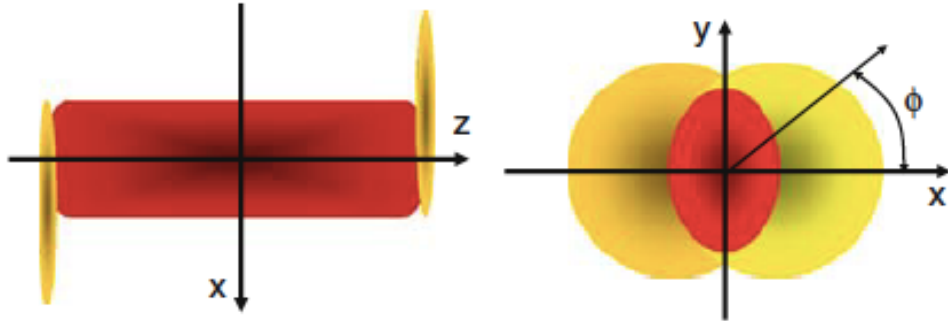


Figure 1.14: Overlap region in beam direction and transverse plane

1.3.3 Azimuthal anisotropy

In relativistic heavy ion collisions, measurements of azimuthal anisotropies of particle emission is a strong tool for investigating initial spatial condition and bulk property of the QGP. The origin of this phenomena is considered to be the initial spatial participant geometry. Fig.1.14 shows a nucleus - nucleus collision in beam direction and transverse plane. In such a collision, the overlap region has a rugby ball shape. If the overlap region rapidly reaches local thermal equilibrium state while keeping the initial geometry, the final particle distribution could be proportional to the initial spatial geometry as described below. Strengths of these anisotropies are evaluated by the coefficients of the Fourier expansion of the produced particle distribution in azimuthal plane with respect to event plane Ψ_n .

$$\frac{dN}{d\phi} \propto 1 + 2 \sum_{n=1} v_n \cos(n[\phi - \Psi_n]) \quad (1.17)$$

where n is the order of the harmonics, ϕ denotes the azimuthal angle of produced particle and Ψ_n is the event plane for the n_{th} order. The event plane is the azimuthal angle of n_{th} order event plane where the particles emission become largest and determined for each order of the harmonics on event by event basis. Mainly measurements of the second harmonic coefficient which corresponds to the magnitude of the second harmonic flow so-called "Elliptic flow" have been studied. Elliptic flow is considered to arise from initial elliptical participant shape in nucleus - nucleus overlap zone. If the mean free path of produced particles l is much larger than system size R , $l \gg R$, the produced particles are emitted radially without any interactions. In this case, the azimuthal distribution of produced particles does not have azimuthal angle dependence. In the other case, when the mean free path is much smaller than the system size $l \ll R$, multi particle interaction occurs and leads to the thermalization of the medium. After the medium achieve the thermalization, the medium expands by the pressure gradient. The pressure gradient toward the minor axis is larger than the major axis due to the elliptic geometry. The azimuthal dependence of the pressure gradient leads to that the particle production toward the minor axis is enhanced rather than toward the major axis. Thus the azimuthal distribution of produced particles has azimuthal angle dependence and its oscillation amplitude corresponds to the elliptic flow v_2 .

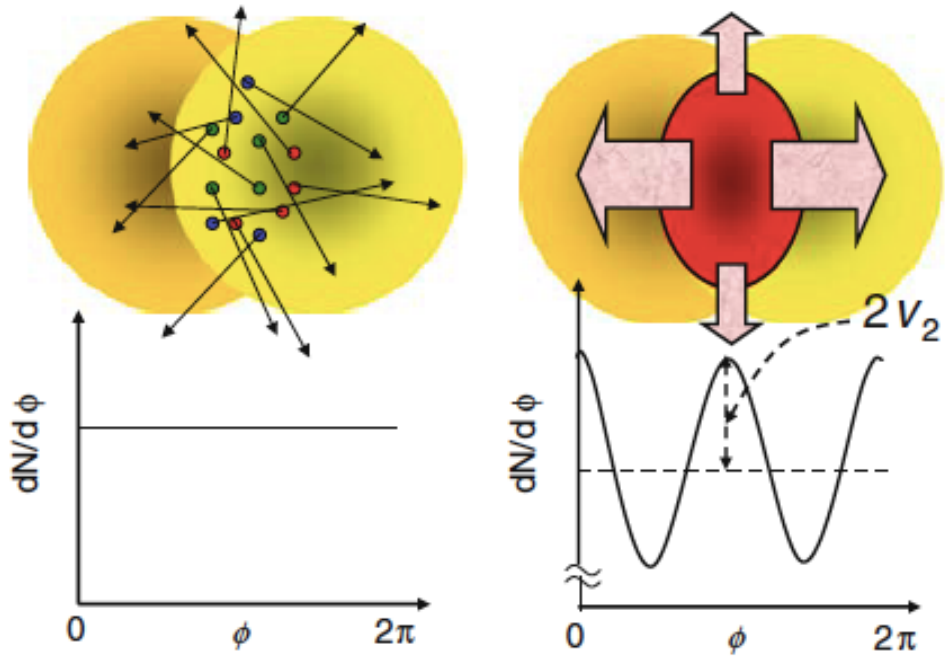


Figure 1.15: Overlap region in transverse plane

The hydrodynamic/transport simulation demonstrate the important property of elliptic flow. Fig.1.16 shows the spatial anisotropy of the participant geometry ε_x and the participant momentum ε_p as a function of the proper time from hydrodynamic simulations for different sets of the equation of state in non central Au+Au collisions. The spacial eccentricity decrease and the momentum eccentricity increase with expanding the medium. Therefore the spacial anisotropy is converted into the anisotropy in momentum space though the hydrodynamic expansion. Since the momentum anisotropy is created at the beginning and saturate at the first few fm/c, the v_2 is a sensitive observable to the early stage of the hydrodynamic evolution.

In Fig.1.17, a parton transport theory based on the Boltzmann equation for undergoing elastic scattering process of gluons only shows parton v_2 as a function of proper time in Au+Au collisions at $\sqrt{s_{NN}} = 200$ GeV. At the beginning, the multi gluon medium has an rugby ball spacial geometry in transverse plane and thermal parton distribution in momentum space. The medium with several gluon-gluon scattering cross section expands as the proper time goes by. For free streaming case(without any parton scattering) v_2 are consistent with zero, so that secondary collisions are necessary to generate azimuthal anisotropy. The v_2 for the all three parton cross sections is generated at the early stage of collisions and saturate at around 2 fm/c. The v_2 for larger parton cross section is larger than that for smaller parton cross section. The parton cross section is proportional to

$$\sigma \propto \frac{1}{\lambda} \propto \frac{1}{\eta} \quad (1.18)$$

where λ is the mean free path and η is the shear viscosity calculated in the kinetic theory of gases. The v_2 values with the finite parton cross section are smaller than the ideal hydrodynamic limit ($\eta \sim 0$).

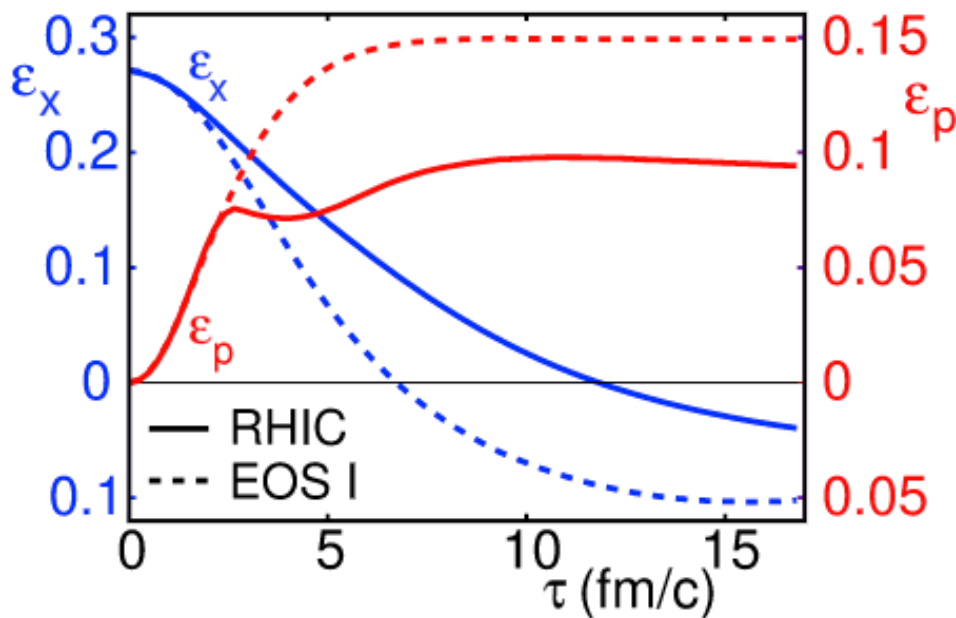


Figure 1.16: The proper time dependence of spatial eccentricity ϵ_x and momentum eccentricity ϵ_p in Au+Au collisions for two different sets of EOS [19]

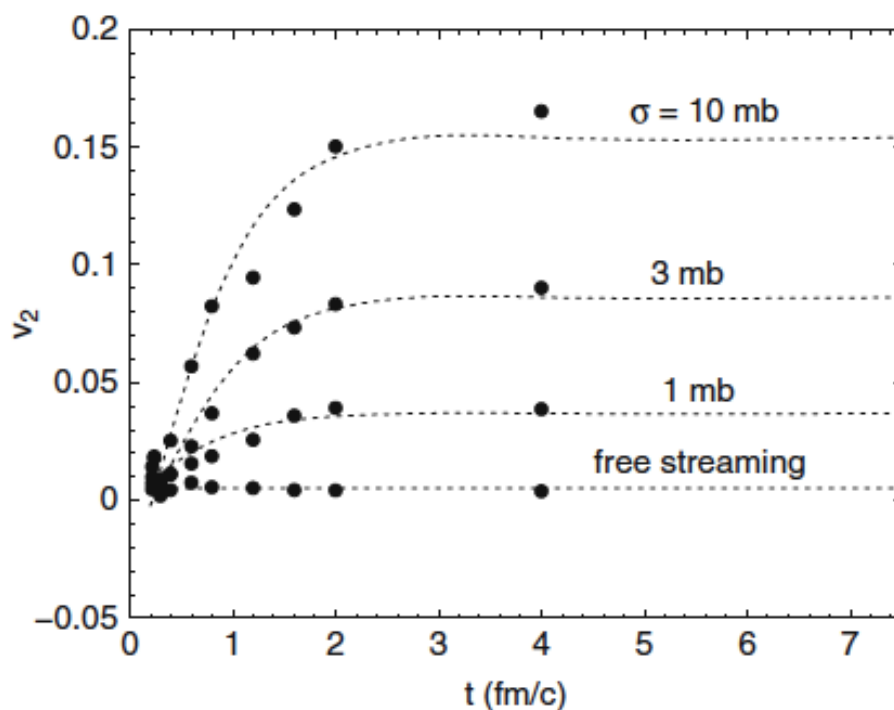


Figure 1.17: parton v_2 as a function of proper time calculated by parton transport model for several parton cross sections in Au+Au collisions at $\sqrt{s_{NN}} = 200$ GeV [20]

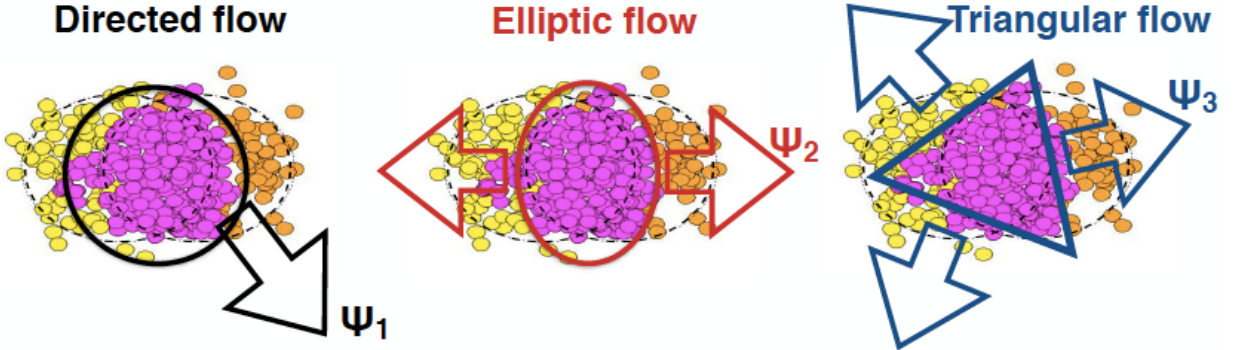


Figure 1.18: Sketches of heavy ion collisions for directed, elliptic and triangular flow

Event by event fluctuation

Lately significant attention from both of experimentalists and theorists have been attracted for studying the initial geometry fluctuation. If the colliding nuclei have smooth density distributions, the participant region in the symmetric nuclear-nuclear collisions is always almond shape. Such a participant geometry does not make odd harmonics at mid-rapidity. However, in actual fact, the event by event fluctuations of participant nucleons lead to odd harmonic anisotropies at mid-rapidity. Figure 1.18 shows the cartoons of the initial geometries for directed flow, elliptic flow and triangular flow. The violet small circles denote the participant nucleons and the other small circles are the spectator nucleons. The first order eccentricity implies the center of mass, the second order eccentricity is an almond shape of the overlapping region with the participants fluctuations and the third order eccentricity is the triangular shape caused by the participant fluctuations alone. Indeed, sizeable odd harmonics have been observed at RHIC and LHC [21, 22, 23]. Figure 1.19 shows the p_T dependence of charged hadron v_n at mid-rapidity for different multiplicity classes in Au+Au 200GeV collisions measured by the PHENIX collaboration. The values of v_n increase with transverse momentum for all event classes. As observed before, the values of the v_2 increase from central collision event(left side panel) to peripheral collision event (right side panel). On the other hand, the v_3 has weak multiplicity dependence. These observed trend in v_2 and v_3 measurements are expected by the eccentricity ε_n [14]. In Fig. 1.20, the PHENIX collaboration compared the multiplicity dependence of v_n for two transverse momentum range to several theoretical predictions. The black data points denote the results from the PHENIX collaboration and the other symbols are the theoretical predictions. The purpose of this comparison with theoretical models is to constrain the initial conditions and the viscosity (shear viscosity over entropy density ratio η/s of QGP) because these model presented in this Fig.1.20 employed the different initial conditions and the values of the viscosity. The initial conditions are introduced from Glauber Monte Carlo simulation and MC-KLN model. In the Glauber Monte Carlo simulation, the participant geometry in transverse plane is determined by the nucleon positions. On the other hand, the MC-KLN model describes the participant geometry by the transverse gluon positions based on the Color Glass Condensate(CGC). Since ε_2 in MC-Glauber is smaller than that in MC-KLN, MC-Glauber is combined with the value of viscosity $4\pi\eta/s = 1$ and MC-KLN is paired with the value $4\pi\eta/s = 2$ to reproduce the v_2 . The values of ε_3 from the two models are similar for reproduction of the v_2 and therefore the larger viscous

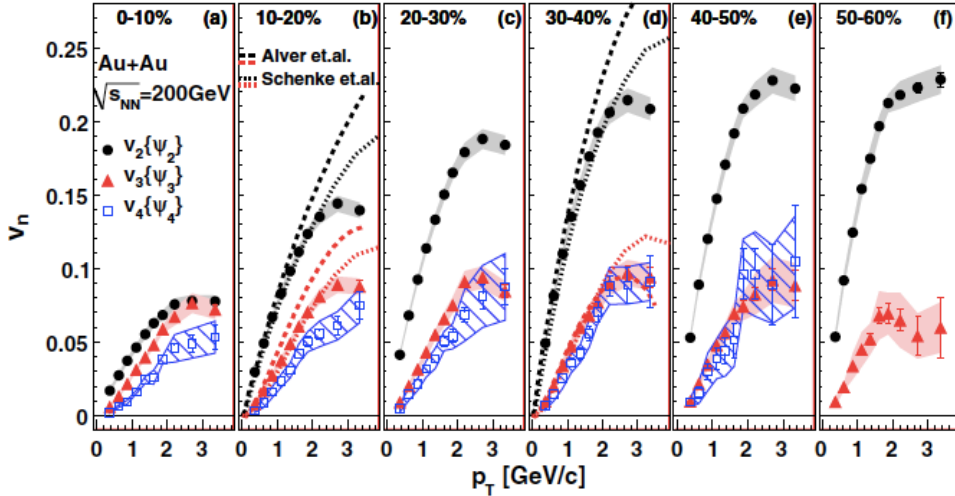


Figure 1.19: Transverse momentum dependence of charged hadron v_n at mid-rapidity for different multiplicity class in Au+Au 200GeV measured by the PHENIX collaboration

correction makes smaller v_3 in MC-KLN model. Additionally, the calculation from the transport model "UrQMD+ $4\pi/s = 0$ " is shown in Fig.1.20. That model employ MC-Glauber with the UrQMD transport model for reproducing the pre-equilibrium combined as the initial condition and the ideal hydrodynamics ($4\pi\eta/s = 0$). Because the ideal hydrodynamics reproduces the highest value of v_2 and v_3 due to no viscous correction, the ideal hydrodynamics provides the upper limit of v_2 and v_3 . All theoretical predictions describe the v_2 in both of the p_T range except for the low multiplicity bins. However in the lower panel for the v_3 comparison, "KLN + $4\pi\eta/s = 2$ " shows the smaller value of the v_3 compared to the PHENIX experimental results. Although MC-KLN model with $4\pi\eta/s = 2$ combination is disfavored by the v_3 measurements, this comparison does not imply the initial condition is not CGC. Thus the v_n measurements could constrain the initial condition and the value of viscosity of the QGP.

Identified hadron $v_n(p_T)$

Measurements of azimuthal anisotropies for pions, kaons and protons provide further insight into the property of the QGP. Figure 1.21 shows the charge combined pion, kaon and proton v_n at mid-rapidity in Au+Au collisions at $\sqrt{s_{NN}} = 200$ GeV collisions [24]. All v_n coefficients seen in Fig.1.21 have two common trends that are referred to as "mass ordering" and "baryon and meson splitting". First, the feature of the mass ordering is seen in the low p_T region. The anisotropies of the lighter hadrons are larger than those of heavier hadrons. This trend reflects the mass dependence from the radial flow effect as described in the previous section. Second, baryon and meson splitting appears at the higher p_T region. The anisotropy for baryons becomes larger than that for mesons. This behaviour is explained by quark coalescence hadronization mechanism.

Quark coalescence model starts from the idea that the invariant spectra for emitted particles is proportional to the product of the invariant spectra of constituent quarks. In the quark

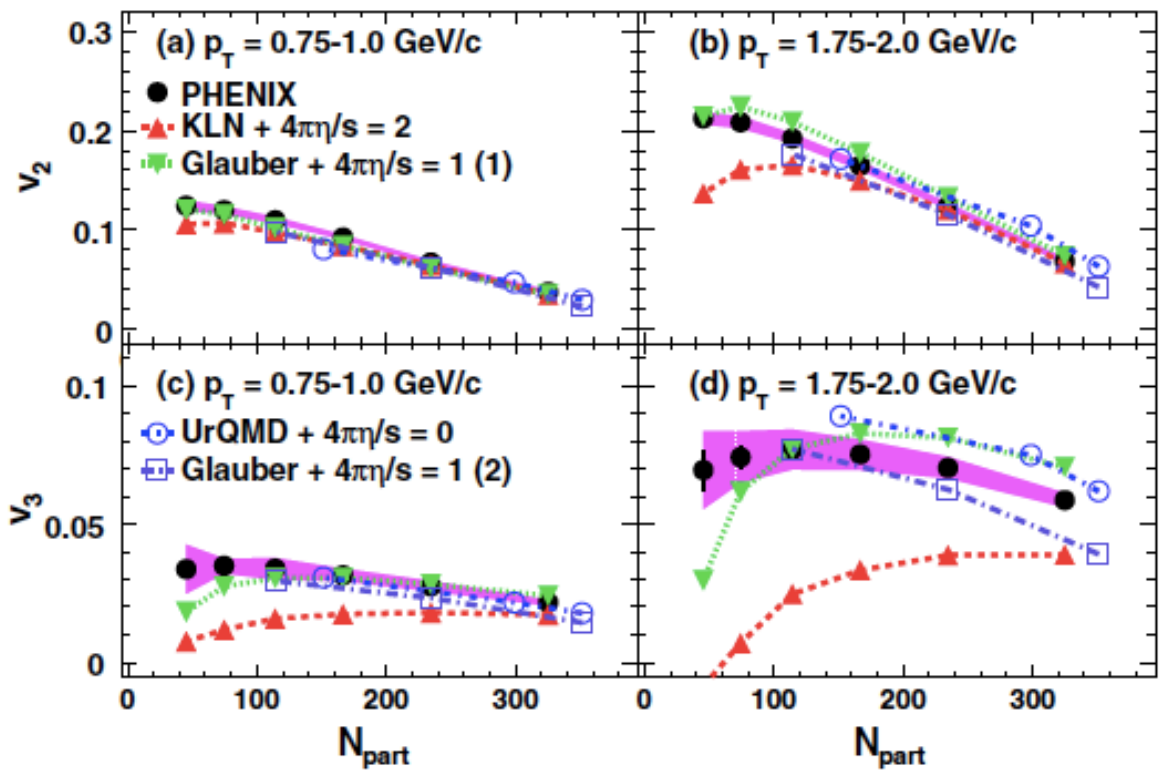


Figure 1.20: Multiplicity dependence of charged hadron v_n at mid-rapidity for two transverse momentum intervals in Au+Au 200GeV measured by the PHENIX collaboration

coalescence model, the meson and baryon spectra are given by those of constituent quarks

$$\frac{dN_M}{d^2p_T}(p_T) = C_M(p_T) \left(\frac{dN_q}{d^2p_T} \left(\frac{p_T}{2} \right) \right)^2 \quad (1.19)$$

$$\frac{dN_B}{d^2p_T}(p_T) = C_B(p_T) \left(\frac{dN_q}{d^2p_T} \left(\frac{p_T}{3} \right) \right)^3 \quad (1.20)$$

where N_M , N_B and N_q are the number of mesons, baryons and quarks. The $C_M(p_T)$ and $C_B(p_T)$ are the probability for $q\bar{q} \rightarrow$ meson and $qqq \rightarrow$ baryon respectively. These relations are valid at intermediate p_T region, which is moderate constituent phase space density. In the intermediate p_T region, anisotropies of produced hadrons are given by parton anisotropies,

$$v_{n,M} \approx 2v_{n,q} \left(\frac{p_T}{2} \right) \quad (1.21)$$

$$v_{n,B} \approx 3v_{n,q} \left(\frac{p_T}{3} \right) \quad (1.22)$$

$$(1.23)$$

where $v_{n,M}$, $v_{n,B}$ and $v_{q,n}$ are meson, baryon and parton v_n respectively.

Pseudorapidity dependence of v_n

At RHIC, pseud-rapidity dependence of v_n in Au+Au collisions is measured by the PHOBOS Collaboration and STAR Collaboration[25] and [26]. Figure 1.22 shows rapidity dependence of charged hadron v_2 for three different multiplicity classes measured by the PHOBOS Collaboration. The black squares represent the experimental results. The v_2 for entire rapidity region increases from the high multiplicity class (top panel) to the low multiplicity class (bottom panel). For all multiplicity classes, the v_2 at mid-rapidity is largest and decreases with increasing absolute value of rapidity. In Fig.1.22, several hydrodynamics calculations for two different initial conditions are compared to the experimental results. In left panel, the Glauber type initial condition is employed and the KLN initial condition is used in right panel. For both of the panels, the pure ideal hydrodynamic simulation with freeze out(kinetic decoupling) temperature $T_{dec} = 100$ MeV shows weak rapidity dependence of v_2 and overpredicts the experimental data at entire rapidity region except for most central collisions for the Glauber initial condition case. On the other hand, the pure hydrodynamic simulation with freeze out temperature $T_{dec} = 169$ MeV underpredicts the data at entire rapidity region for the Glauber initial condition case and overpredicts the peripheral collision data at $|\eta| < 2$ for the KLN initial condition case. In these pure hydrodynamic calculations, the phase transition temperature from the QGP to hadron phase is $T_c = 170$ MeV. Thus the hydrodynamics calculations with $T_{dec} = 100$ MeV and $T_{dec} = 169$ MeV correspond to "QGP+hadron fluid" and "only QGP" state, respectively. The red circles shown between the two theory curves represent "QGP + hadron cascade". Compared to "QGP+hadron fluid", hadron cascade phase makes smaller v_2 value. Especially this dissipative effect is seen at forward and backward rapidity region. The hydrodynamics with the KLN initial condition is always higher than that with the Glauber initial condition for all three multiplicity classes. The PHOBOS results prefer the calculation from the "QGP+hadronic cascade" with the KLN initial condition for highest multiplicity class. In the lowest multiplicity class, the "QGP+hadronic cascade" with the Glauber initial condition model agrees with the PHOBOS data.

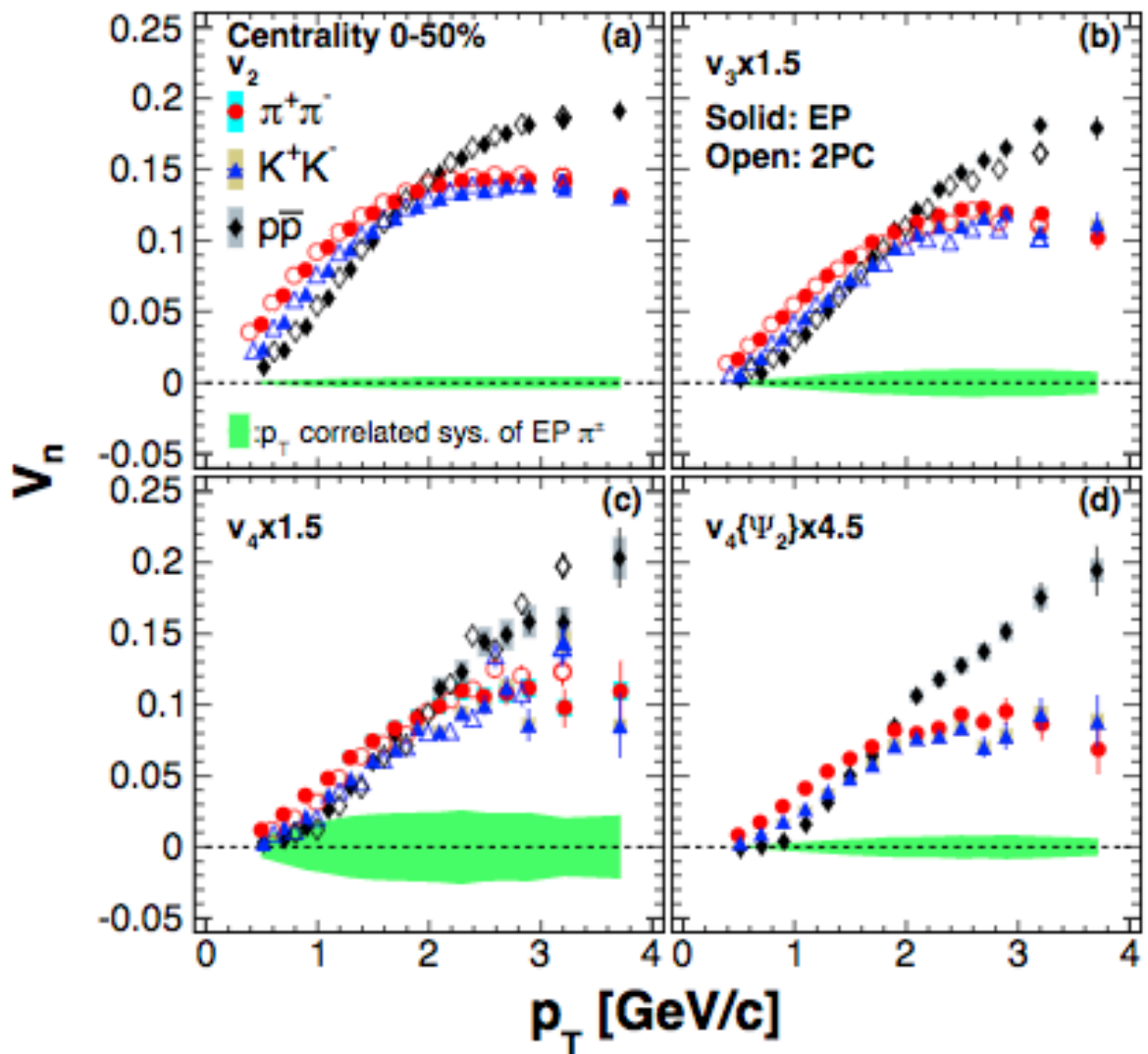


Figure 1.21: Charge combined pion, kaon and proton v_n at mid-rapidity in Au+Au collisions at $\sqrt{s_{NN}} = 200$ GeV

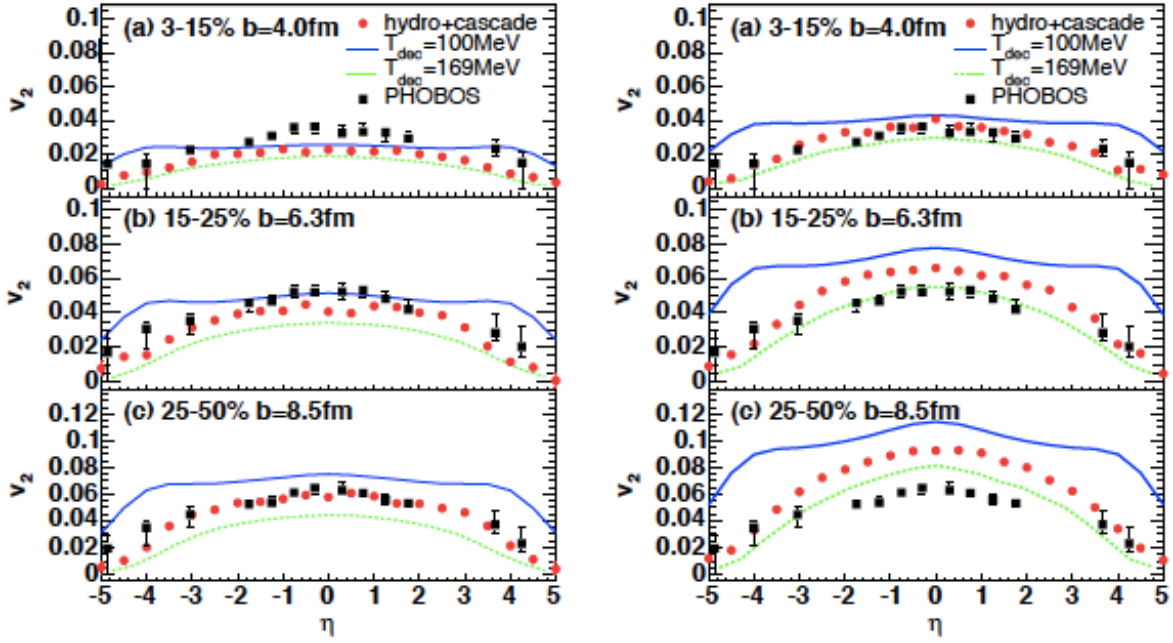


Figure 1.22: Pseudo-rapidity dependence of charge hadron v_2 in Au+Au collisions at $\sqrt{s_{NN}} = 200\text{GeV}$ in comparison to the hydrodynamic calculations. Left:Glauber Monte Carlo model(nucleon base) initial condition. Right:KLN model(gluon base) initial condition

Although the event averaged longitudinal multiplicity distribution in A+A collisions is symmetric and boost invariance at $|\eta| < 2$ (plateau region), the event by event distribution is not necessarily a symmetric shape. The particle production at the forward(backward) rapidity is influenced by the participant nucleons moving toward the forward(backward) rapidity. Thus the different number of forward going and backward going participant nucleons, $N_{\text{part}}^F \neq N_{\text{part}}^B$, would lead to the forward/backward asymmetric rapidity distribution. Indeed, the experimental results from the PHOBOS and STAR collaboration reveal a forward/backward asymmetric particle production in rapidity[27],[28].

Jia and Huo[29] predict forward/backward asymmetry of azimuthal anisotropies of particle production in Pb+Pb collisions at $\sqrt{s_{NN}} = 2.76\text{TeV}$ using a multiphase transport model(AMPT) [50], which is frequently used for the study of azimuthal anisotropies in relativistic heavy ion collisions. In order to study forward/backward asymmetry in azimuthal anisotropies, initial participant eccentricities of forward going and backward going participant nucleons, $\epsilon_n^F, \epsilon_n^B$, are defined separately on event by event basis in their study. In each event, they calculate the difference of forward and backward eccentricity, $\Delta\epsilon_n = \epsilon_n^F - \epsilon_n^B$. Fig. 1.23 shows the simulated rapidity dependence of v_2 and v_3 for selecting similar forward and backward eccentricities event, $|\delta\epsilon_n| < 0.02$. The flow harmonics are calculated with respect to the three event planes Ψ_n defined by the three rapidity region, $4 < \eta < 6, -6 < \eta < -4$ and $-1 < \eta < 1$ and the participant plane, Φ_n^* , that is the reference axis for the ϵ_n . The participant plane is calculated by all the participant nucleons at the thermalization time before the collective expansion. The deviations among the three event planes and the participant plane selections are observed in Fig. 1.23 and are mainly contributed from non-flow effect In Fig. 1.24, the simulated rapidity dependence of v_2 and v_3 for

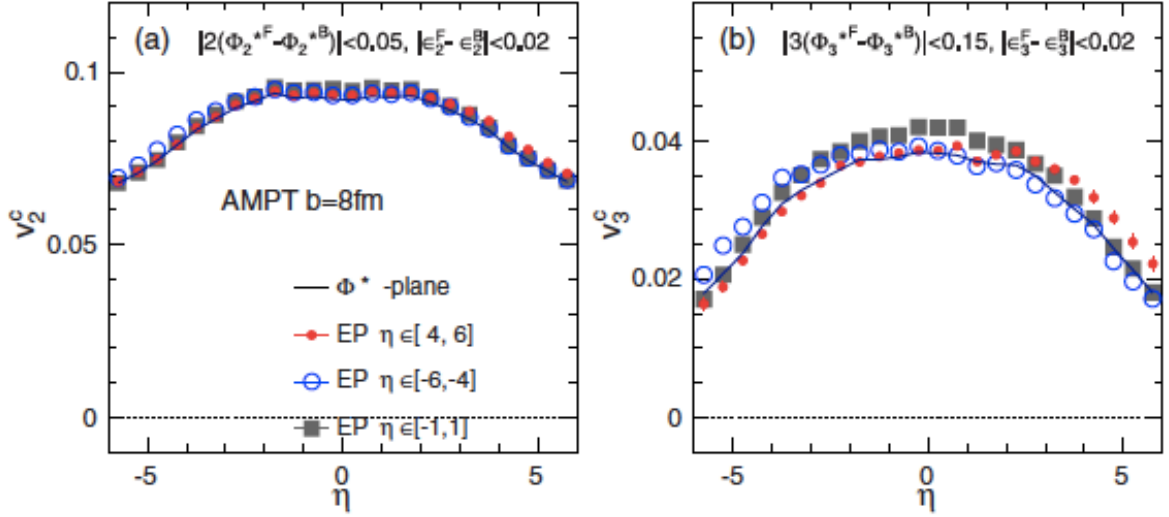


Figure 1.23: Pseudo-rapidity dependence of charge hadron v_n in Pb+Pb collisions at $\sqrt{s_{NN}} = 200\text{GeV}$

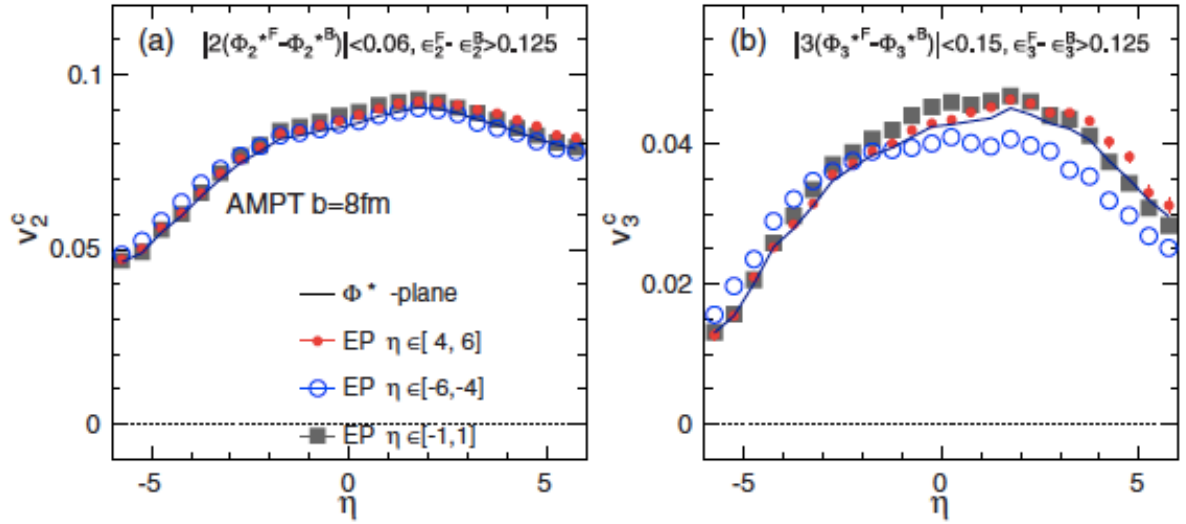


Figure 1.24: Pseudo-rapidity dependence of charge hadron v_n in Au+Au collisions at $\sqrt{s_{NN}} = 200\text{GeV}$

$|\delta\epsilon_n| > 0.125$ event are shown. Significantly the values of v_2 and v_3 are larger at forward rapidity(positive rapidity) than at backward rapidity(negative rapidity). These asymmetric rapidity dependences are attributed to the event selection of $\epsilon_n^F > \epsilon_n^B$. Thus this rapidity asymmetry of v_n implies the independent fluctuations of the participant nucleons in the two colliding nuclei survive even after the collective expansion and the initial geometry would not be boost invariant but have a strong rapidity dependence.

1.4 Cu+Au collision and thesis motivation

As it is introduced in the previous sections, the azimuthal anisotropies are strong tool to understand the initial condition and the bulk property of the QGP. Until now, many experimentalists and theorists have concentrated on studying the azimuthal anisotropies in high energy heavy ion collisions and concluded the QGP formed at RHIC behaves nearly perfect fluid. However, in spite of the many experimental observables and theoretical predictions, the uncertainties of the initial condition and the viscosity of the QGP still remain. The understanding of the initial condition in heavy ion collisions is crucial for the subsequent hydrodynamic expansion. Thus the determination of the initial condition help us to quantify the viscosity of the QGP.

In 2012, Cu+Au collisions at $\sqrt{s_{NN}} = 200\text{GeV}$ were operated at RHIC for controlling the initial geometry. Until now, symmetric collision systems such as Au+Au collisions, have been operated at high energy collisions so that this is the first test to collide different heavy nuclei. Since the size of Au nucleus ($A=197$, the radius of Au is 7fm) is larger by factor about 3 than Cu nucleus ($A=63$ and the radius of Cu is 4.5fm), the participant geometry would be asymmetric in transverse and longitudinal directions. The asymmetric initial geometry provides different geometry situations from symmetric collision systems such as Au+Au collisions. Thus the asymmetric collisions provide opportunities to investigate the influence of the initial geometry on the collective dynamics and particle production.

In this dissertation, we present the measurements of the azimuthal anisotropies of charged particles at mid- and forward/backward-rapidities in Cu+Au collisions at $\sqrt{s_{NN}} = 200\text{ GeV}$ using PHENIX detectors. As it is noted in the above paragraph, the initial geometry of Cu+Au collisions has two features, sideward asymmetry and longitudinal asymmetry. In non-central collisions, the participant geometry has sideward asymmetry in transverse plane as shown in Figure 1.25 (b). The sideward asymmetry of initial geometry would lead directed flow at mid-rapidity. Therefore we examine the v_1 measurements at mid-rapidity with model calculations and discuss about the influence of the initial sideward asymmetry on the directed flow.

Until now, the longitudinal structure is considered to be boost invariant. However, lately some experimental results which indicate breaking boost invariant longitudinal structure are observed and there are some theoretical calculations which predict longitudinal dependence of initial condition. In the asymmetric collisions, longitudinally, the forward (Cu-going side) and backward (Au-going side) different collective dynamics and particle production are expected, because the participant geometry and number of participants in Au nucleus and those in Cu nucleus influence Au-going side and Cu-going side, respectively. Therefore the measurements of v_n and particle multiplicity in Cu+Au collisions will provide us further insight into the initial condition. By introducing weighted ε_n and N_{part} scalings, we discuss about longitudinal initial geometry and density in Cu+Au collisions.

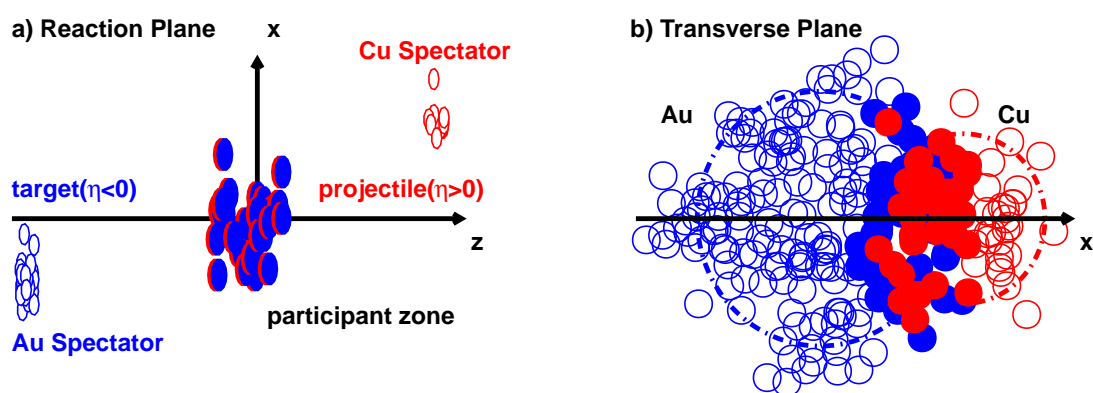


Figure 1.25: Cu+Au collisions in longitudinal direction(a) and transverse direction(b)

Chapter 2

Experimental Apparatus

2.1 Relativist Heavy Ion Collider(RHIC)

Relativistic Heavy Ion Collider(RHIC) was built as the first heavy ion collider at Brookhaven National Laboratory in Upton New York the United State of America and is the second highest energy heavy ion collider in the world at present. RHIC is composed of two 3.834km long rings which circulate in opposite directions. One ring is called “Blue ring” which is clock-wise and the other is “Yellow ring” which is anti-clock-wise. The length of circumference of RHIC is 3.8km. At RHIC, a wide variety of particle species can be operated from $A = 1$ (proton) to $A = 238$ (uranium) at present and nuclei are collided at several energies. In heavy ion experiment, heavy ions are accelerated in several stages to achieve relativistic speed. Thus several accelerators are needed. At BNL, five accelerators are used before the injection to RHIC, Electron Beam Ion Source (EBIS), Radio Frequency Quadrupole (RFQ) accelerator, Linear accelerator (LINAC), the Booster Synchrotron, the Alternating Gradient Synchrotron(AGS). The accelerator complex is shown in Fig. 2.1. In Fig 2.2, the procedure for accelerating gold ions is shown. At the first step, heavy nuclei are created and accelerated by EBIS. In the gold ions case, the ions are accelerated to 2A MeV through EBIS, RFQ and LINAC before the Booster accelerator. At the second stage, the Booster Synchrotron accelerate ions to 70A MeV and the ions are grouped into three bunches by a RF electric field. At the exit of the Booster, all of atomic electrons are stripped off by the foil. These positive gold ions are injected into the AGS. At the AGS, the three bunches of gold ions are further accelerated to 9A GeV and then injected to RHIC ring. The two RHIC rings are rounded hexangular concentric superconducting magnet rings and have six intersection locations where collisions occur. At the present, two experiments records collisions data at two intersection points. To guide and focus ion beam, each beam pipe uses 396 superconducting dipole magnets and 492 superconducting quadrupole magnets. In total, there are 1740 magnets including other correction magnets. The magnets are cooled less than 4.6 K by supercritical helium. In the two RHIC rings, RF cavities are implemented. The injected bunches are accelerated by electric filed in RF cavities. As increasing collision energy, the magnitude of magnetic filed are increased accordingly up to 3.5 T which corresponds to Au-Au collisions at 200 GeV case and p+p collisions at 500 GeV case. The ions are stored in the rings for a period of 6 to 12 hours and collided at six intersection points. For the description of the performance of

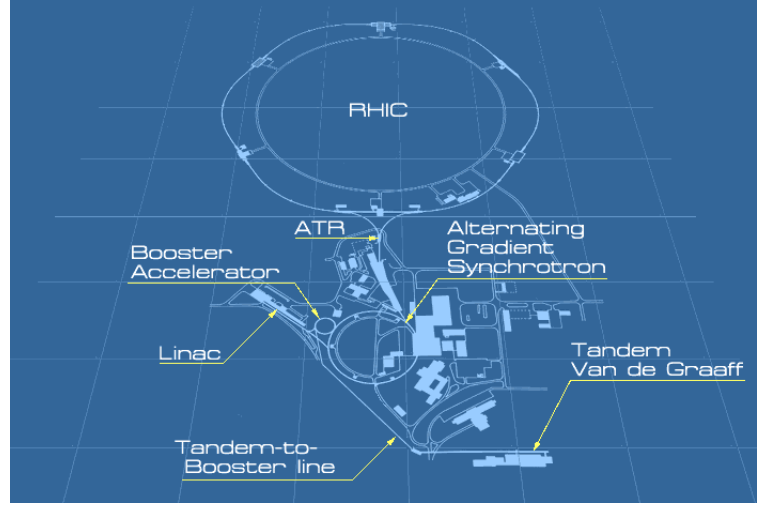


Figure 2.1: RHIC accelerator complex

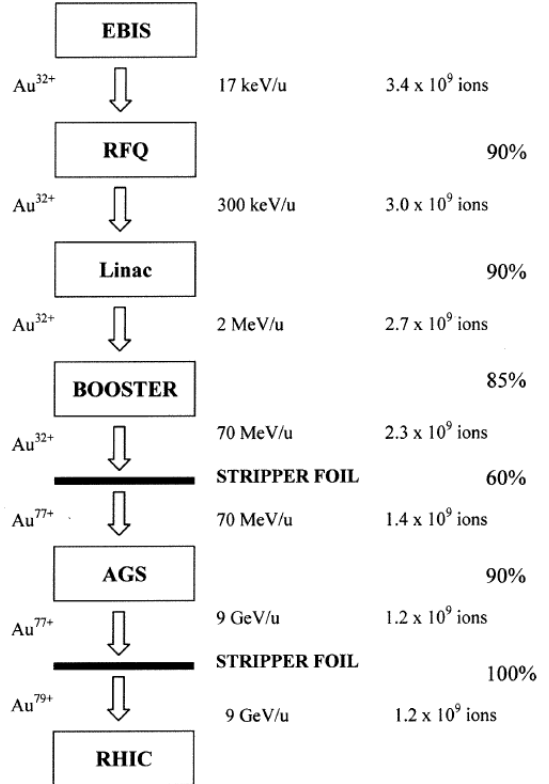


Figure 2.2: Schematic of procedure of Au ion injection.

the accelerator, the parameter of collisions rate is important. The luminosity L is the parameters which is used for the description of the collisions rate. The number of events N are expressed as follows using L and a cross section σ

$$N = L\sigma \quad (2.1)$$

2.2 PHENIX Detectors

PHENIX (the Pioneering High Energy Nuclear Interaction eXperiment) is one of the two experiments at BNL. PHENIX is located at 8 o'clock, if the injection point of the beam pipe from AGS is 6 o'clock. Fig.2.3 is the schematic view of the PHENIX subsystems. PHENIX is designed to measure hadrons, leptons and photons in high rate events and high multiplicity events. PHENIX consists of 4 spectrometers. The two spectrometers at mid-rapidity are instrumented to measure electrons, photons and hadrons and the two spectrometers at forward/backward rapidity are instrumented to measure muons.

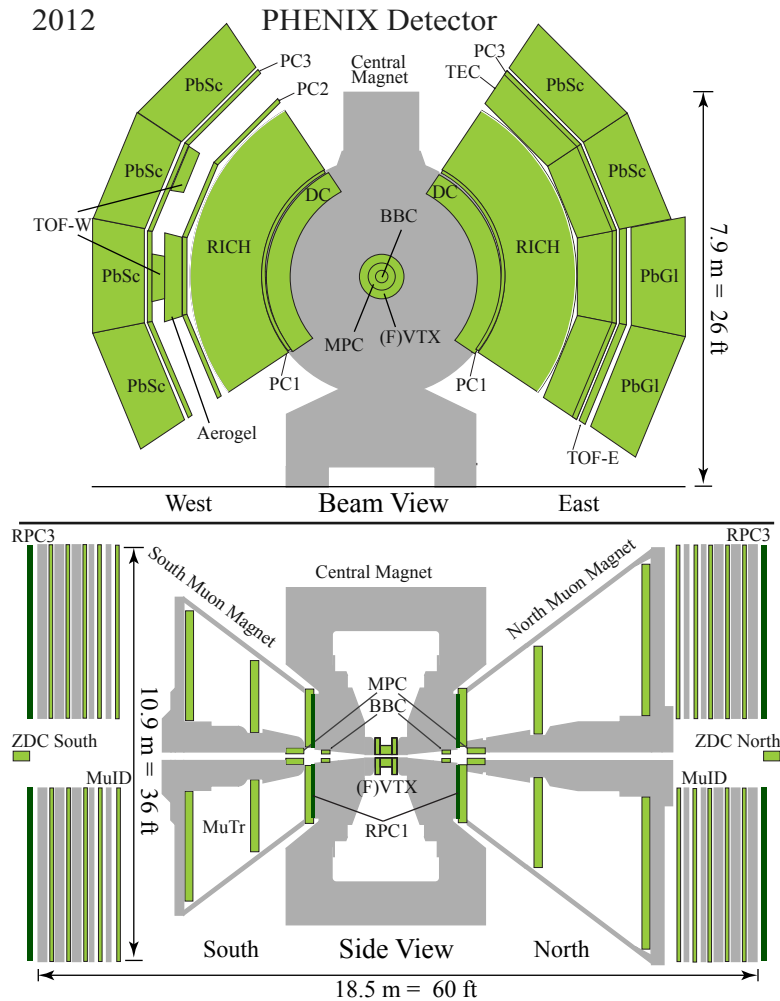


Figure 2.3: Schematic view of the PHENIX subsystems. Top panel: Beam View, Bottom panel: Side View

2.2.1 Magnet systems

PHENIX Magnet system

At PHENIX, the magnet systems is composed of three spectrometer magnets which are made of warn iron yokes and water-cooled copper coils. One is the Central Magnet (CM) and the others are the North and South Muon Magnets. The CM use concentric coil and provide magnetic field around the collision vertex position which is parallel to the beam axis for measurements of charged particle tracks. The Muon Magnets use solenoid coils produce radial magnetic filed for muon analysis. Each of three magnets produce about 0.8 Tesla-meters. The design of CM for the physics-driven requirements

- To minimize multiple scattering and interactions of particles from primary vertex, there is no mass in the apertures of the central spectrometer arms.
- To create a "zero-filed" region near $R=0$, the radial magnetic field has to be controlled.
- The magnitude of magnetic field for the region $R>200$ cm is required to be minimum. As described, CM uses two sets of circular coils as shown in Fig.2.4. These "inner" and "outer" coils produce the "++" configuration and the "-+" configuration.

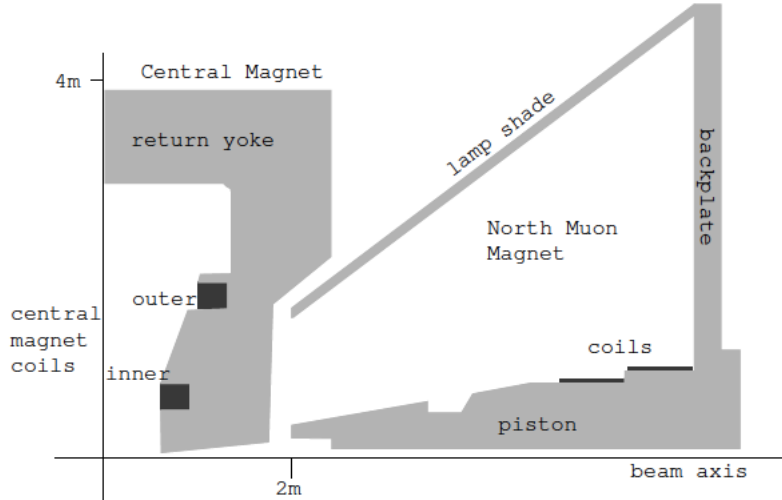


Figure 2.4: Schematic view of Central and Muon magnets.

2.2.2 Global detector

For the event categorization, Beam - Beam counters(BBC) installed at forward/backward rapidity is employed. A pair of BBCs provides time of flight of particles emitted to forward/backward rapidity for the determination of the collision time and position. The BBCs

provides multiplicity at forward/backward rapidity to determine centrality. At this subsection these detectors are explained.

Beam-Beam Counter

The main role of Beam-Beam counter (BBC) is to provide the vertex position along with beam axis and the multiplicity of produced particles at forward/backward rapidity region for the event categorization, to provide the collisions time for the time of flight of particles for particle identification using TOF and EMCAL detectors and to trigger the PHENIX LVL1 trigger. The BBC is composed of two identical counters installed on South side and North side of collision point along with beam pipe. One installed on the South side and the other installed on the North side are named BBC S and BBC N respectively. The both of counter are placed at the distance of 144cm from the center of interaction point and surround the beam pipe. The BBC S and BBC N cover full azimuthal angle and pseudo-rapidity range from 3 to 3.9. The BBC is required to satisfy the following conditions:

- (i) The BBC has a capability to function the dynamic range from 1MIP to 30 MIPs. Because the number of particles generated in central Au+Au collision at 200GeV is about few thousands at BBC rapidity and BBC has to operate p+p collisions case.
- (ii) BBC has to be radiation hard. The place where BBC is installed is around beam pipe near the collision point. At the place, a very high level radiation is expected.
- (iii) Since BBC is placed behind the PHENIX central magnet, BBC has to work under high a high magnetic filed environment.

Each detector consist of 64 Cherenkov radiators. Each radiator is composed of one-inch diameter mesh-dynode photomultiplier tubes(Hamamatsu R6178) attached with 3cm quartz on the top of PMT. In Fig.2.5, each BBC counter is shown on left side picture and each individual element is shown on right side picture. The outer diameter is 30cm and the inner diameter is 10cm. In central AuAu collisions at 200GeV, 15 particles per each element are expected for this configuration.

Zero Degree Calorimeter(ZDC)

Zero Degree Calorimeter(ZDC) is installed to detect spectator neutrons and to measure the total energy of them. The purpose of ZDC is to detect spectator neutrons and measurement of the total energy of them. ZDC is also used as a event trigger and a luminosity monitor. Because of this reason, identical detectors are installed in all RHIC experiments. ZDC systems are composed of two identical calorimeters. ZDC systems are placed at a distance of 18m from interaction point along the beam line for South and North side separately and the coverage of pseudo-rapidity range is $|\eta| > 6.5$. Since ZDC systems are placed at DX magnets, the charged particles are bended and swept away and only neutral particles are detected at ZDC. The some of charged particles may hit beam pipe and induce showers. The induced shower may hit the

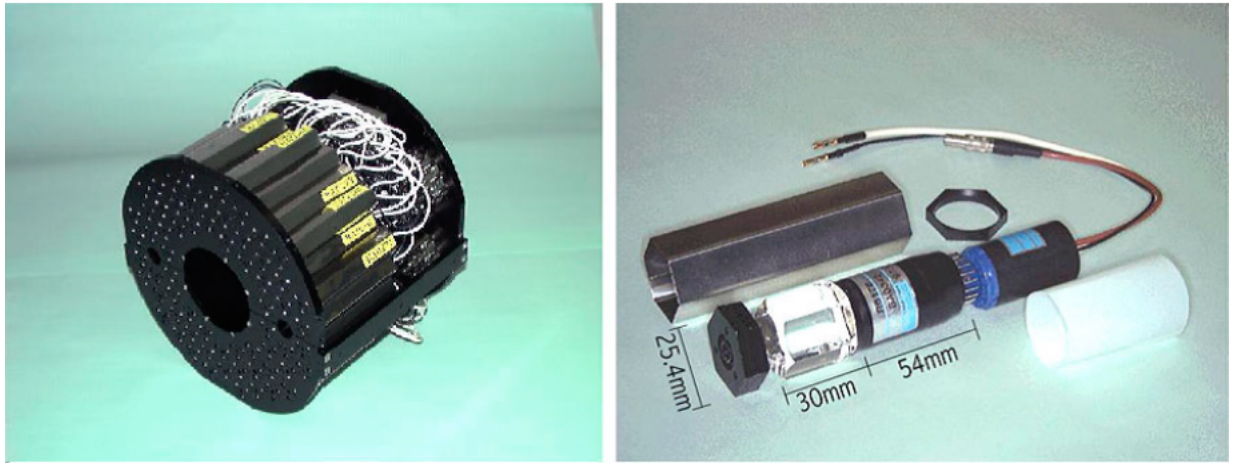


Figure 2.5: Left:One BBC counter composed of 64 elements. Right:Single BBC element composed of PMT equipped with quartz

ZDC. A scintillation counter is placed in front of ZDC for charged particle veto. ZDC is a hadronic sampling calorimeter. Each ZDC system consists of three ZDC modules. Each module is composed of 27 Tungsten absorber layer and polymethylmethacrylate fiber layers(PMMA). In Fig 2.7, the schematic view of fiber layer and the schematic view of single ZDC module are shown. The fiber ribbons were impregnated with a low viscosity silicone rubber glue. The active region of the fibers are covered and the surface of fibers in the fiber and absorber sandwich region are protected by the glue. The one side of fibers are connected to PMT and the other side of fibers were left untreated.

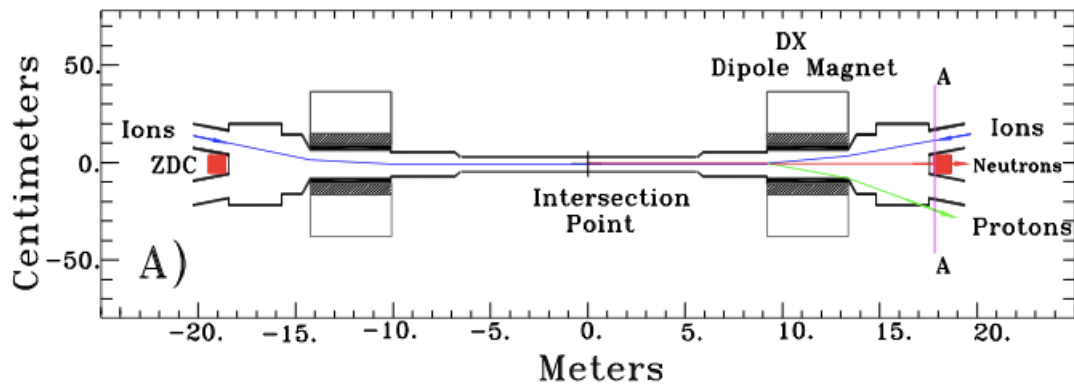


Figure 2.6: Schematic view of the colliding nuclei before(left) and after(right) collision.

Shower Max Detector(SMD)

Shower Max Detector is installed to measure the center of neutron induced neutron shower.

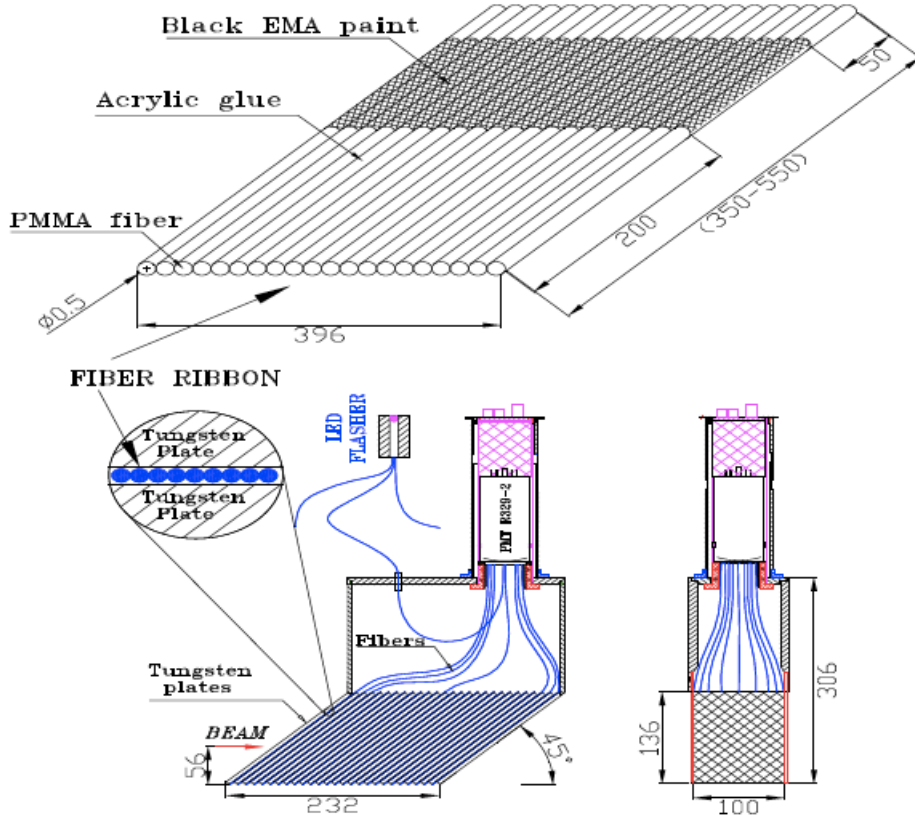


Figure 2.7: Schematic view of the colliding nuclei before(left) and after(right) collision.

The SMD is composed of 7 scintillator strips for the determination of x-coordinate of center of neutron induced shower and 8 scintillator strips for the determination of y-coordinate of center of neutron induced shower. The SMD is placed between first and second ZDC modules where the maximum energy of neutron induced shower is reached. The position resolution is about 1mm for neutrons at 100GeV energy.

2.2.3 Central arm detector

Central magnet provide magnetic field parallel to the beam axis and the magnetic field bend the tracks of emitted charged particles. Central arm is composed of two hybrid tracking detectors for charged particles and photons. They are installed in East and West side respectively. On the central arm, electro magnetic calorimeters are installed in both side for electron and photon measurement. For charged particles tracking, Pad and Drift chamber are employed. In this section, each subsystem at Central Arm are explained.

Drift Chamber

Drift Chamber(DC) systems provide, measurement of charged particle trajectories and determine transverse momentum of charged particles. DC is composed of two identical detectors located East and West side of Central arm spectrometers respectively. DC are inner most detector of Central arm subsystems and placed at the region from 2 to 2.4 m from the beam pipe. The magnetic field is applied in the region where DC is placed to bend charged particle tracks for the determination the transverse momentum. In heavy ion simulation study, the requirement of the transverse momentum resolution and double track spatial resolution are specified for the measurement of ϕ mass with a resolution better than 4.4 MeV and good tracking efficiency for the highest multiplicities. The drift chamber is imposed the following requirements,

- Resolution of single wire is better than $150 \mu\text{m}$ in $r\phi$ plane
- Two track separation of single wire is better than 1.5 mm.
- Efficiency of single wire is better than 99%.
- Spatial resolution in the z direction is better than 2 mm

Each detectors are divided 20 sectors which cover 4.5° in ϕ . In each sector, there are six different types of wire modules. The six modules are called X1,U1,V1,X2,U2 and V2. Each module has 4 cathode planes and 4 anode planes. The X1 and X2 are placed in the direction parallel to the beam to measure trajectories of charged particles precisely in transverse plane. The U and V are used for the track pattern recognition and determine the z coordinate of the track. The U1(2) and V1(2) are placed at 6° relative to X1(2) plane.

Pad chamber

Pad chamber(PC) provides three dimensional coordinate of charged particle track, especially precise measurement of z-coordinate. Since PC systems are located outside of magnetic field, the hit points are along the straight line particle trajectories. The charged particle track coordinates at PC are used for tagging charged particle and track matching to reduce background from decays and γ conversions. The PC is Multi Wire Proportional Chambers which consists of 3 separated layers(PC1, PC2, PC3). PC1 is most inner layer of 3 PC layers. PC1 is located at radial distance of 2.5m and is present behind DC for East and West both side. PC2 is the second inner layer. The radial distance of PC2 from beam pipe is 4.2m. PC2 is present behind Ring Image Cherenkov counter(RICH) in West arm only. PC3 is installed between RICH and Electro Magnetic Calorimeter(EMCAL) in East and West arms and the radial distance from beam pipe is 4.9m. Each layer consists of a signal plate of anode and field wires inside a gas bounded by two cathode plates as shown in Fig. 2.10. Each cathode plate is segmented into an array of pixels as shown in Fig.2.11. The inside gas was composed of 50% Argon and 50% of Ethan under atmospheric pressure.

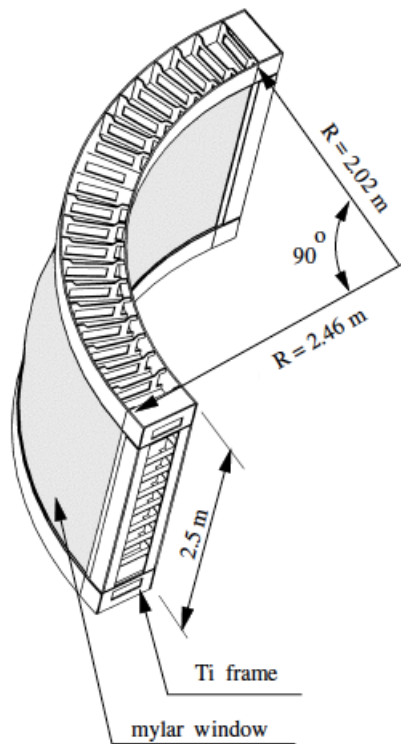


Figure 2.8: Schematic view of the colliding nuclei before(left) and after(right) collision.

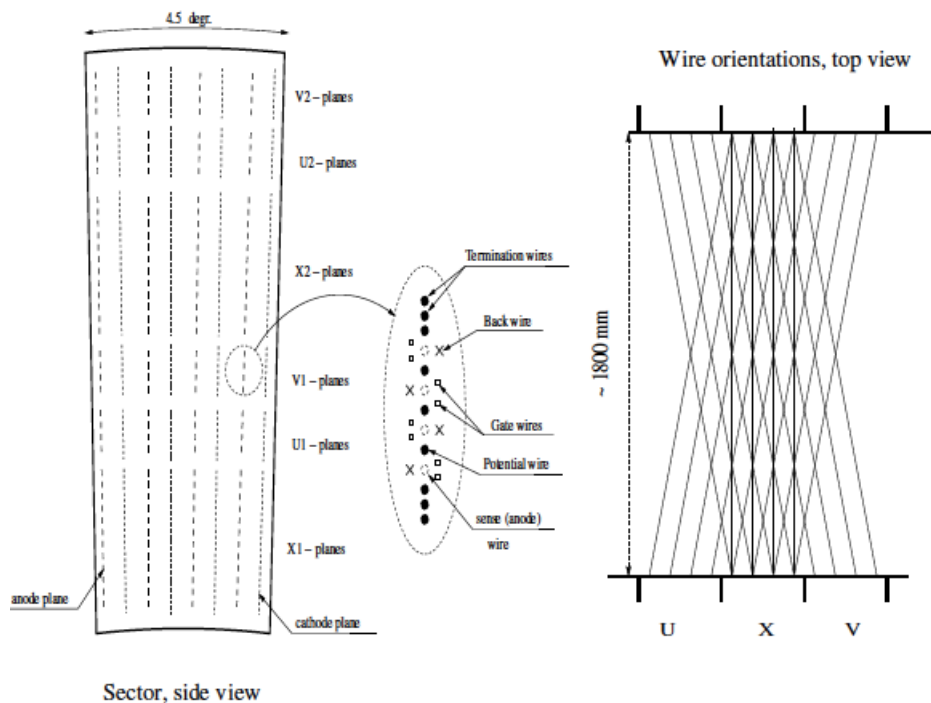


Figure 2.9: Schematic view of the colliding nuclei before(left) and after(right) collision.

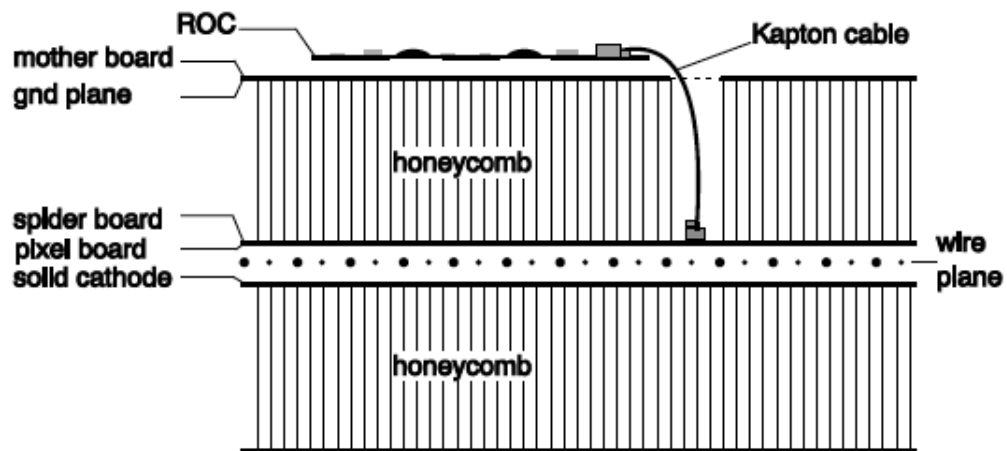


Figure 2.10: A plane cutting through by a Pad chamber

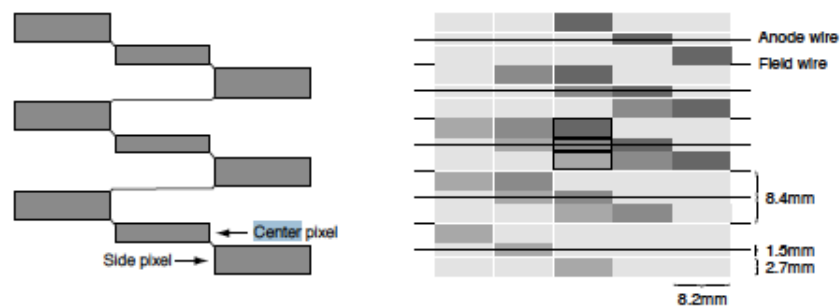


Figure 2.11: Left:The pad and pixel geometry. Right:A cell made of three pixels is at center of this picture

Time of flight

Time of flight detectors provides charged particle identification. For particle identification, Time of flight detectors measure charged particle time of flight from collision vertex. Time of flight detectors are composed of two different detectors which are installed in Central arm detectors for East and West side separately.

Time of flight East(TOF.E)

Time of flight East(TOF.E) detector is a scintillator detector and placed at a distance of 5.1m from beam pipe, in between PC3 and EMCAL in Central arm East side. TOF.E covers $70^\circ \leq \theta \leq 110^\circ$ in azimuth. The TOF.E consists of 960 scintillator slats and 1920 PMTs. Scintillator slats are oriented along $r\phi$ and parallel to z -axis. Each scintillator slat is equipped with two PMTs which are attached at the both side edge of a scintillator slat. The designed timing resolution is about 100ps. π and K could be separated up to 2.4 GeV/c and K and proton separation could be up to 4 GeV/c.

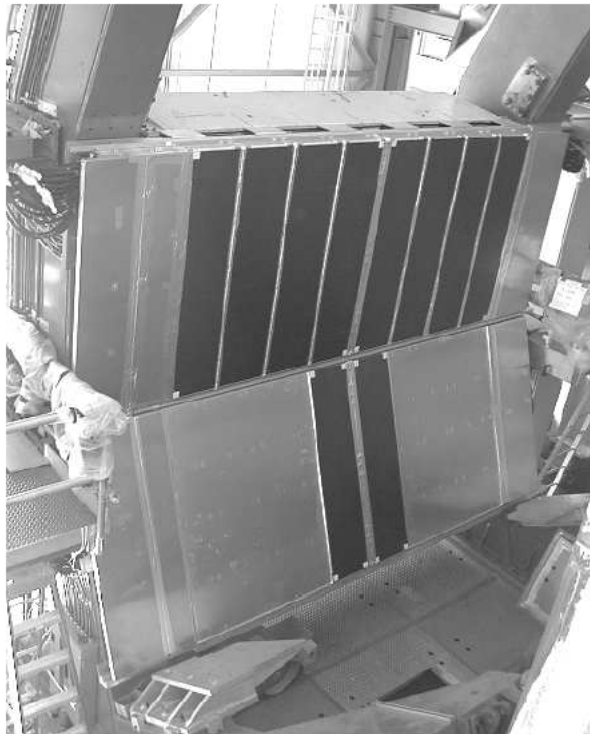


Figure 2.12: TOF.E installed at PHENIX Central Arm East Arm

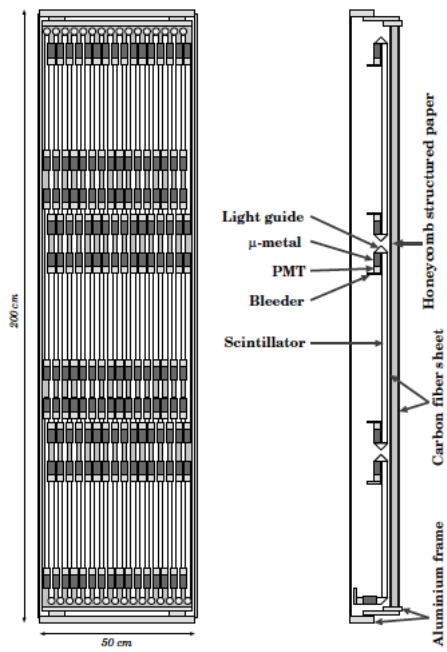


Figure 2.13: TOF.E each panel composed of scintillator slats and PMTs

Time of flight West

Time of flight West(TOF.W) detector is a Multi-Gap Resistive Plate Chamber(MRPC) which is a gas chamber with multi-layers and multi-gas gaps. TOF.W is composed of two identical counters which are placed at a radial distance of 4.81 m from collision point in Central Arm West side separately. The TOF.W covers pseudo-rapidity acceptance of $|\eta| < 0.35$ and azimuth acceptance of 22° in two separated counters. Each counter is composed of 6 0.23mm gas gaps separated by 5 0.55mm glass layers in between anode and cathode plates. If charged particles pass through the MRPC, the charged particles ionize the gas between glass layers. The image charge is collected at both top and bottom side of chamber on copper readout strips. Since the readout strips are placed at top and bottom side of chamber, the hit position is determined from the time difference between top and bottom readout chips. The timing resolution is achieved 90 ps for the transverse momentum range of $1.3 \leq p_T \leq 1.7$.

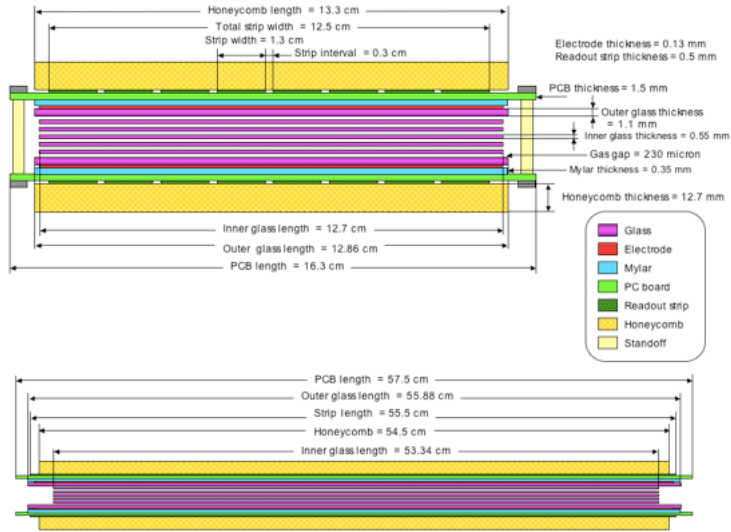


Figure 2.14: Schematic view of MRPC

Electro Magnetic Calorimeter(EMCal)

Electromagnetic Calorimeter(EMCal) [32]system provides the hit position of particles and energy of photons and electrons. EMCal systems are placed at most outer layer of Central arm and covers pseudo-rapidity range of $|\eta| < 0.35$ and azimuthal range of $70^\circ \leq \theta \leq 110^\circ$. EMCal systems is composed of two walls which are installed in Central arm East side and West side separately. West side wall comprised four Pb scintillator sampling calorimeters. East side wall comprises two Pb scintillator sampling calorimeters and two Pb glass Cherenkov calorimeters. Pb scintillator and Pb glass have different properties. From following the properties are explained.

Pb scintillator sampling calorimeter

The PHENIX Pb scintillator calorimeter consists of 15552 individual towers which are made of a pile of alternating tiles of Pb and scintillator. This type of calorimeter is referred to shashlik type sampling calorimeter. Each tower contains 66 cells made of alternating tiles of Pb and scintillator. At the edge of tiles, Al tiles are placed. For light collection, 36 longitudinally penetrating wavelength shifting fibers are inserted into each tower and at the back of the towers, light is read out by 30mm phototubes. Mechanically four tower form together one module which is a single structural entity. Thirty six modules are grouped into super-module and eighteen super-module form one sector. The Pb scintillator has a energy resolution of $8.1\%/\sqrt{E}(GeV) \oplus 2.1\%$ and a timing resolution is better than 200 ps.

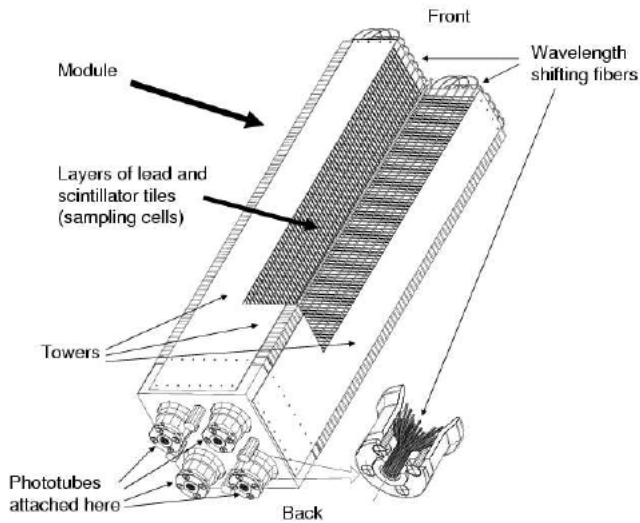


Figure 2.15: Schematic view of each Pb-Schintilator tower

Pb glass Cherenkov calorimeter

The Pb glass Cherenkov calorimeter is most outer layer of Central arm and placed at lower sectors of East side. Each sector contains 192 super-modules arranged widthwise 16 super-modules and heightwise 12 super-modules as shown in Fig. Each super-module contains twenty four modules arranged widthwise 6 modules and heightwise 4 modules. The size of each module is widthwise 40mm and heightwise 40 mm and depthwise 400mm. Each module are wrapped with aluminized mylar and shrink tube. To form super-module, twenty four modules are glued with carbon fiber and epoxy resin. For Cherenkov radiation collection, FEU-84 photomultiplier is used at the back of module. At the front of super-module, LED light is attached for gain monitoring and a polystyrene reflective dome is also attached to enclose the LED system. The Pb glass calorimeter has energy resolution of $6\%/\sqrt{E}(GeV)$. The timing resolution is better than 300ps.

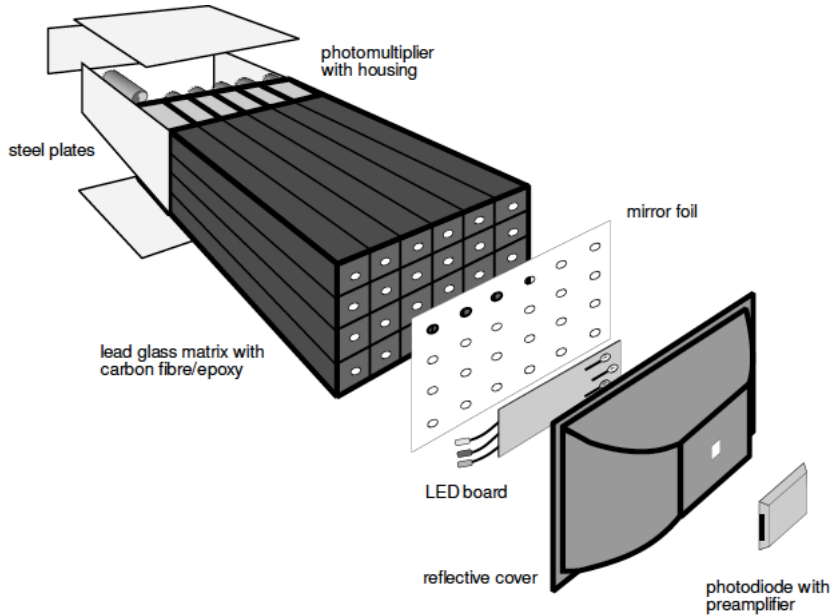


Figure 2.16: Schematic view of each Lead Glass tower

Reaction Plane Detector(RXNP)

Reaction Plane Detector(RXNP) system is composed of two identical detectors which are installed at a distance of 39 cm from the nominal interaction point along with beam pipe in South and North side of PHENIX respectively. Each detector is composed of concentric inner and outer rings and contains 24 scintillators in these rings. Each ring has twelve equally sized segment scintillator arranged perpendicular to beam pipe and azimuthal acceptance of 2π , pseudo-rapidity acceptance of $1 < \eta < 2.8$. Each scintillator is trapezoidal shape with 2cm thickness and wrapped with aluminized mylar inner layer and black plastic outer layer. A schematic view of RXNP is shown in Fig.2.17. The inner segments cover from 5cm to 18 cm from the beam pipe and outer segments cover from 18cm to 33cm. These radial acceptance corresponds to $1.5 < |\eta| < 2.8$ and $1 < |\eta| < 1.5$. The inner segment has 2cm inner and 9cm outer edges respectively. The outer segment has 17cm outer edge.

2.2.4 Data acquisition(DAQ)

The PHENIX data acquisition(DAQ) system is designed to collect the event data in a wide range of colliding systems and the interaction rate at design luminosity. The number of produced particles within PHENIX acceptance is from a few tracks in p+p and several hundred tracks in central Au+Au collisions. The collision rate at RHIC varies from approximately 500kHz for minimum bias p+p collisions to a few kHz for Au+Au collisions at design beam luminosity. The PHENIX DAQ system is able to seamlessly accommodate the variety of event size and event rate through the dead timeless and pipelined features of the detector front ends and the ability to

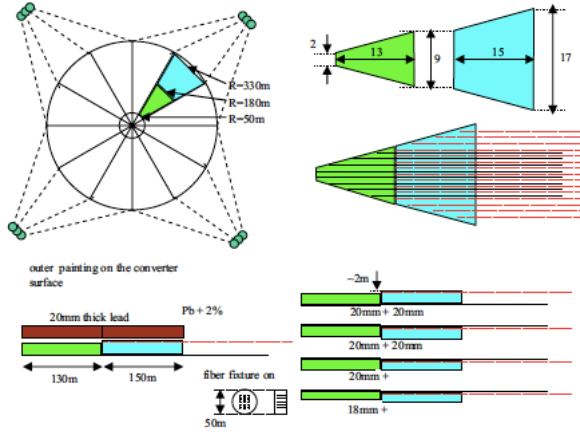


Figure 2.17: Schematic view of Reaction plane detector

accommodate higher level trigger. Fig 2.18 represent the general schematic for PHENIX DAQ flow. At PHENIX, the Master Timing Module(MTM), the Global Level-1 Trigger System(GL1)

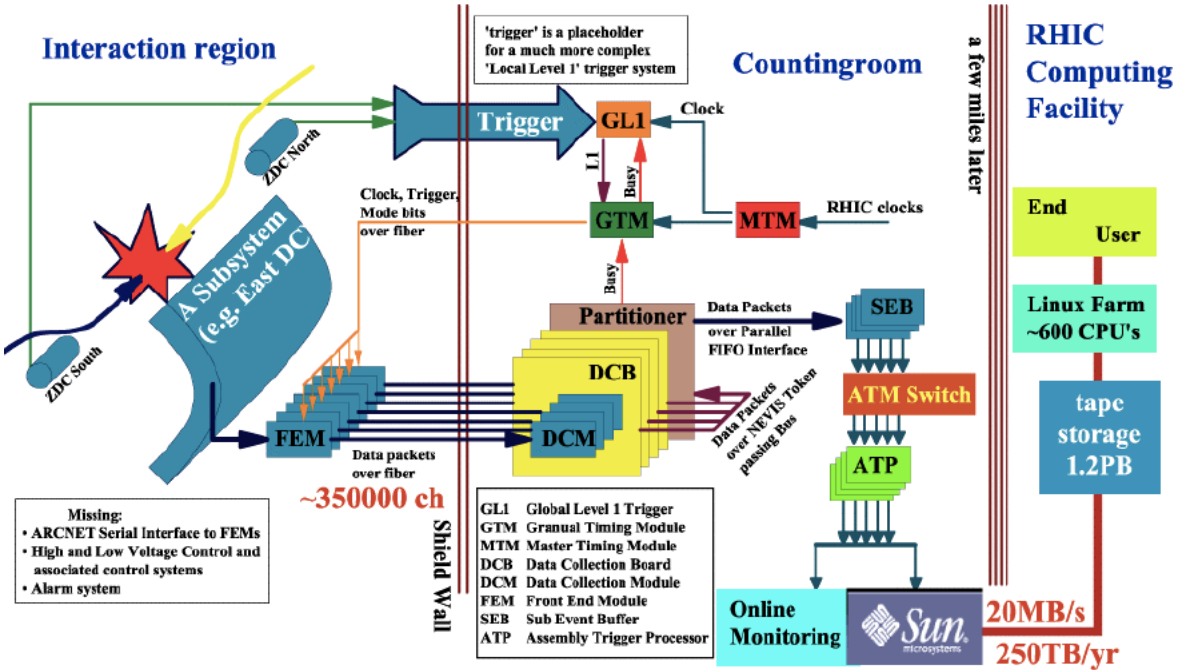


Figure 2.18: Schematic design of PHENIX DAQ system

and the Granule Timing Module(GTM) control overall data acquisition. The MTM receive RHIC beam clock and distribute it to GL1 and GTM. The GL1 receive and combine the data to provide the first Level-1(LVL1) trigger decision. In addition, the GL1 also manages busy signals. The GTM deliver the RHIC clock, trigger information and event accepts to the Front End Modules which convert detector analog signal into digitized signal. While the GL1 is making the decision, where the event data is recorded or not, temporally the event data is stored in AMU. After FEM's

receive the accept decision, the digitization of the analog signals are started. The digitized data are collected by Data Collection Modules(DCM) which communicate with rest the rest of the DAQ system. via G-LINK. The DCM is able to receive 100 Gbytes/sec of uncompressed event data and perform zero suppression, error checking and data reformation. From DCM's, many parallel informations are sent to Event Builder(EvB) which is the final stage of data collection. The EvB also provides an environment for the LVL2 trigger to operate. In order to record interesting events, it is necessary to discard the number of events. The LVL2 trigger provides a second filter for uninteresting events to assemble interesting events. Then EvB sends the accepted event data to the PHENIX Online Control System(ONCS) to log and monitor the data. The Common Object Request Broker Architecture(CORBA) system is the technology used to handle the many components. Throughout the network, the CORBA access to the object on the remote computers. The Run Control(RC) is the main control process. The role of the RC is access and communication with remote object that handle each of the hardware. The configuration of DAQ is determined by RC system for example the trigger, the subsystems and run type and so on.

Chapter 3

Analysis

In this thesis, the data sets used are Minimum-bias triggered Cu+Au, Au+Au and Cu+Cu collisions at $\sqrt{s_{NN}} = 200$ GeV recorded by PHENIX experiment in 2012(Run12), 2007(Run7) and 2005(Run5). In this chapter, we describe the data reduction and the analysis method performed in this study.

3.1 Event selection

As described above, minimum bias data set is used in this study. The minimum bias event is defined as more than two PMTs fired in each BBC counter. In Cu+Au collision case, the MB sample covers $93 \pm 3\%$ of total inelastic collision cross-section simulated by a comparison of BBC multiplicity distribution to Monte Carlo Glauber model. Z vertex position is determined by the average hit time difference between BBCS and BBCN. Moreover Z vertex region within ± 30 cm is required.

Centrality Determination

In order to classify event geometry, “centrality” is introduced. The centrality is the degree of overlap region in two nuclei, which is related to impact parameter b . The centrality from 0 % to 100 % corresponds to impact parameter from 0 fm to $R + R'$ fm (R, R' are radius of different nuclei). The centrality 0 % and 100 % corresponds to the most central and the most peripheral collisions respectively. Under the assumption that impact parameter b is related to emitted particle multiplicity, experimentally centrality class is determined by comparing the measured particle distribution and the simulated particle distribution by Monte Carlo Glauber [7]. Figure 3.1 shows the total emitted charged particles as a function of N_{part} or b calculated by Glauber Monte Carlo. In the PHENIX experiment, centrality is defined as a percentile of the total charge distribution on combined BBC S and N side, which corresponds to charged particle multiplicities at forward/backward rapidity. Fig.3.2 shows BBCS and N combined charge sum distribution with the boundary lines which represent centrality classes in Cu+Au collisions.

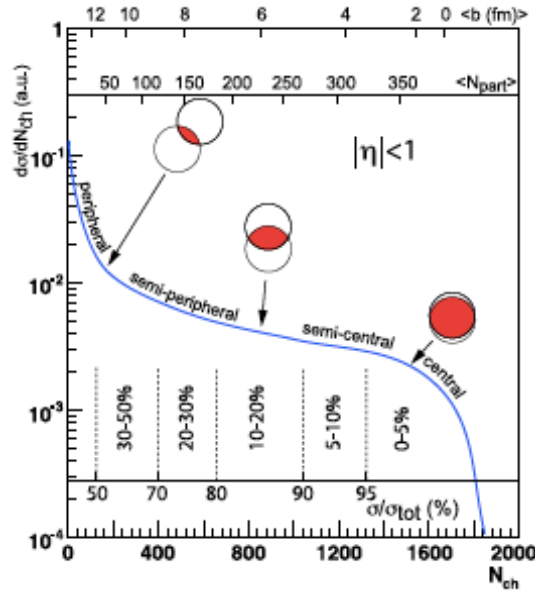


Figure 3.1: A schematic of the correlation between measured charged particles and N_{part} and b calculated by Glauber Monte Carlo. The plotted distribution is not actual measurements.[7]

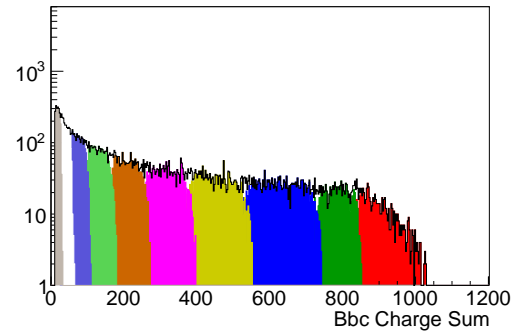


Figure 3.2: The total bbc charge distribution in Cu+Au collisions at $\sqrt{s_{NN}} = 200\text{GeV}$ from combined South and North Bbc detectors

3.2 Track selection

3.2.1 Track reconstruction

In each event, a lot of number of particles are emitted and pass through PHENIX detectors. At the Central Arm spectrometer, charged particle tracks can be reconstructed on event by even basis. For data analysis, the track reconstruction is important for momentum determination, identification of particle and background estimation, and so on. In order to reconstruct the trajectories of charged particles, the hit informations on the Central Arm subsystems have to be combined. Mainly the DC and the PC1-3 reconstruct track from collision vertex. The other detectors, such as TOF.E, TOF.W and EMCAL are employed for particle identification and additional background removal.

The track reconstruction is performed in the $r - \phi$ plane and the $r - z$ plane of the DC and the PC1 respectively. Fig. 3.3 and 3.4 show the typical tracks in these planes. The variables illustrated in Fig. 3.3 and 3.4 are used for the track reconstruction with the DC and the PC1, of which definitions are summarized below

- ϕ : The azimuthal angle of the intersection of the track with the reference radius at mid-point of the DC
- α : The azimuthal inclination angle of the track at the intersection point.
- zed : z coordinate of the intersection point

- β : The inclination angle of the intersection point in the $r - z$ plane.

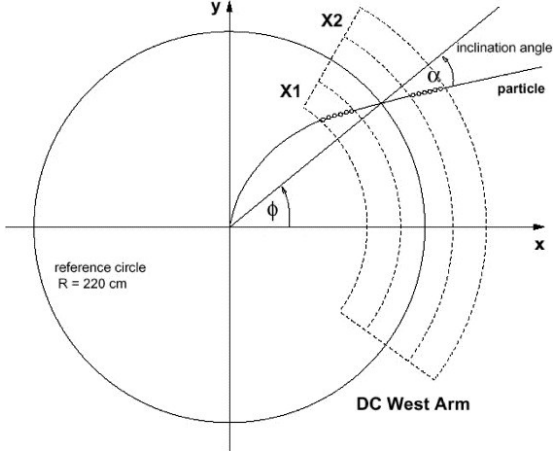


Figure 3.3: A cartoon of the ϕ and α for the DC track reconstruction. The dashed lines represent DC West arm. The small circles are DC hits along the track

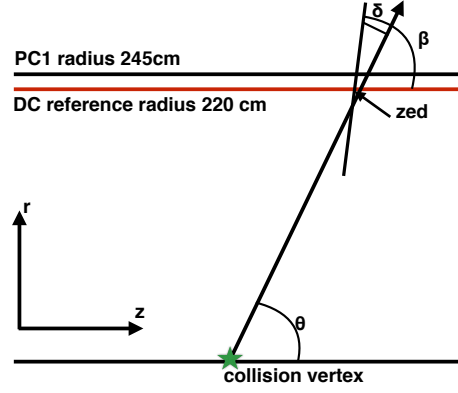


Figure 3.4: A cartoon of the track in r and z plane. The red line corresponds to the reference radius of the DC

The reconstruction of tracks within the DC is based on combinatorial Hough transform technique[31]. Fig. 3.5 shows HIJING simulation results in central Au+Au collisions at RHIC energy for the small region of the DC x-y plane and the associated feature space. After a track is reconstructed in the magnetic field, two parameters ϕ and α specify the direction of the track. In the non-bend plane, track reconstruction is first attempted by information of PC1 hits have z coordinate information. The non-bend vector is determined from z coordinate from PC1 and Z vertex position information from the BBC.

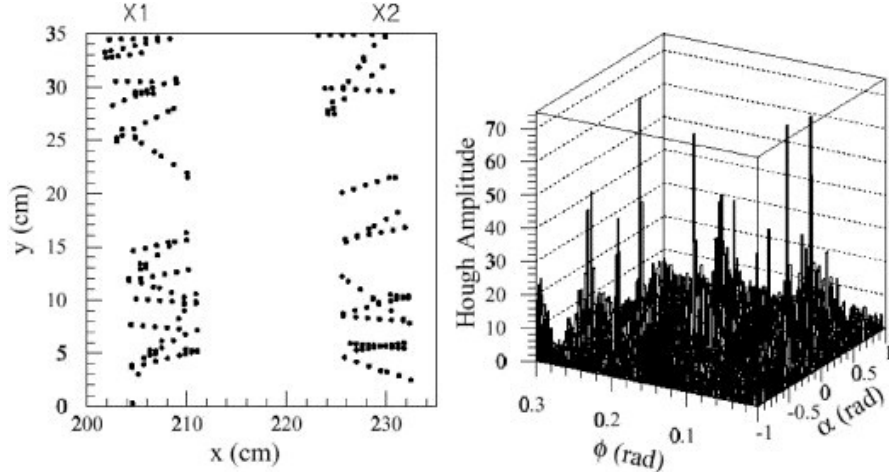


Figure 3.5: Left figure: Simulated hit informations in a central Au+Au collisions with HIJING for a small region of the DC. Right figure: The Hough transform feature space(ϕ - α plane) for this small DC region. The peaks corresponds to tracks.

3.2.2 Momentum determination

In the magnetic field which is parallel to the beam axis, the transverse momentum of charged particles can be determined from the curvature of track trajectory. In the PHENIX experiment, the transverse momentum of charged particles are obtained from the inclination of the track at the reference radius of the DC, α , as described in the previous section. The relation between p_T and α is expressed as

$$\alpha \simeq \frac{K}{p_T}, \quad (3.1)$$

where $K=101$ mrad GeV/c is the effective field integral. One can derive the relation between the momentum resolution and the angular resolution using Eq. (3.1),

$$\begin{aligned} \frac{\delta p}{p} &= \frac{\delta \alpha}{\alpha} \\ &= \frac{1}{K} \sqrt{\left(\frac{\sigma_{ms}}{\beta}\right)^2 + (\sigma_\alpha p)^2} \end{aligned} \quad (3.2)$$

where $\delta\alpha$ is the measured angular spread, σ_{ms} is the contribution from multiple scattering and σ_α is the contribution from angular resolution of the DC respectively.

3.2.3 Track Quality

The tracks reconstructed by the DC and the PC1 have quality parameter which represents track hit pattern recognition of the DC wires and the PC1 and are expressed as 6 bit number from 17 to 63. In this analysis, we select the quality values of 31 and 63 as the good tracks. Good track, 31 and 63, require a hit in both X1 and X2 wires, the unique hit in the UV layers and the (unique) hit in the PC1. For the quality value of 31 case, there are multiple hits in PC1 and for the quality value of 63 case, the unique hit in PC1 is required.

Track Matching

Track model projects a charged track trajectory reconstructed by the DC and the PC1 to the outer layer subsystems, such as PC3 and EMCAL and find candidates of real hit within a fixed $\phi - z$ window around real hit in the each outer layer subsystem. The hit associated with the track is identified by the closest distance to the projection point. Since the track model assume the track is from primary vertex, the background track from non-primary vertex could be removed by the distance between the projection point and the real hit. The track matching residual distribution which is the distribution of the differences between the projection points and real hits is approximately Gaussian distribution with a width of

$$\sigma_{match} = \sqrt{\sigma_{detector}^2 + \left(\frac{\sigma_{ms}}{p\beta}\right)^2}, \quad (3.3)$$

where $\sigma_{detector}$ is the position resolution of the detector and σ_{ms} is the contribution from multiple scattering. The contribution of multiple scattering becomes large at low p_T and small and negligible compared to the position resolution at high p_T . If the mean of the residual distribution is non-zero value, this is considered to be imperfect detector alignment calibration or the magnetic field parameters in the track model. For the analysis, the track matching distributions are normalized by the width of the distribution and the mean of the distribution is shifted towards zero such that the standard deviation is one and the mean is zero in azimuthal($r - \phi$) and longitudinal(z) directions respectively.

3.2.4 Particle Identification

Particle identification for π , K , p is performed via Time of flight method using Time of flight East and West detectors. In the time of flight method, particles are identified by squared mass distribution. The squared mass and the time of flight relation is expressed as,

$$\begin{aligned} m^2 &= p^2 \left(\frac{1}{\beta^2 - 1} \right) \\ &= p^2 \left(\left(\frac{ct}{L} \right)^2 - 1 \right), \end{aligned} \quad (3.4)$$

where p is the particle momentum and β is particle velocity expressed as a ratio relative to the speed of light c , the time of flight of particle t and flight path length L . The particle momentum is measured by the DC and the time of flight of particle is measured by TOF.E and W. The particle flight path length corresponds to the distance between the interaction point and projection point at TOF.E and W. Fig. 3.6 shows the squared mass distribution in Cu+Au collisions for positive and negative, TOF.E and TOF.W separately. In each plot, the lowest horizontal band corresponds to pions, the second band is kaons and the third and forth bands are protons and deuterons

The particle identification cuts are determined based on the distance from the peaks of particle species in the squared mass distribution. The values of peaks and σ for pions, kaons and protons are extracted from fits. For the pions and kaons identification, one fitting function that has two “Crystal Ball” functions is used and for the protons case, a single Crystal Ball function is used. The Crystal Ball function has five parameters, three parameters from a Gaussian function(height, mean and σ) and two parameters from a power function which reproduce tail. The fitting are performed for every 100 MeV/ cpt bin, charge and TOF.E and TOF.W separately. Fig. 3.7 represents squared mass distribution for the positive pions, kaons and protons at inter-mediate p_T bin in the TOF.W fitted with the Crystal Ball functions and three single Gaussian function of which the parameters are fixed by the Crystal Ball functions(height, mean and σ). Once the means and σ are determined, the values of them are plotted as functions of p_T , then they are fit with polynomials. The polynomials used in our analysis are the following formula,

$$\langle m_i^2 \rangle(p_T) = a_{0,i} + a_{1,i}p_T + a_{2,i}p_T^2 + a_{3,i}p_T^3 + \frac{a_{4,i}}{\sqrt{p_T}} + \frac{a_{5,i}}{p_T} \quad (3.5)$$

$$\sigma_i(p_T) = b_{0,i} + b_{1,i}p_T + \frac{b_{2,i}}{p_T} + b_{3,i}p_T^2 + b_{4,i}p_T^3 + \frac{b_{5,i}}{\sqrt{p_T}} \quad (3.6)$$

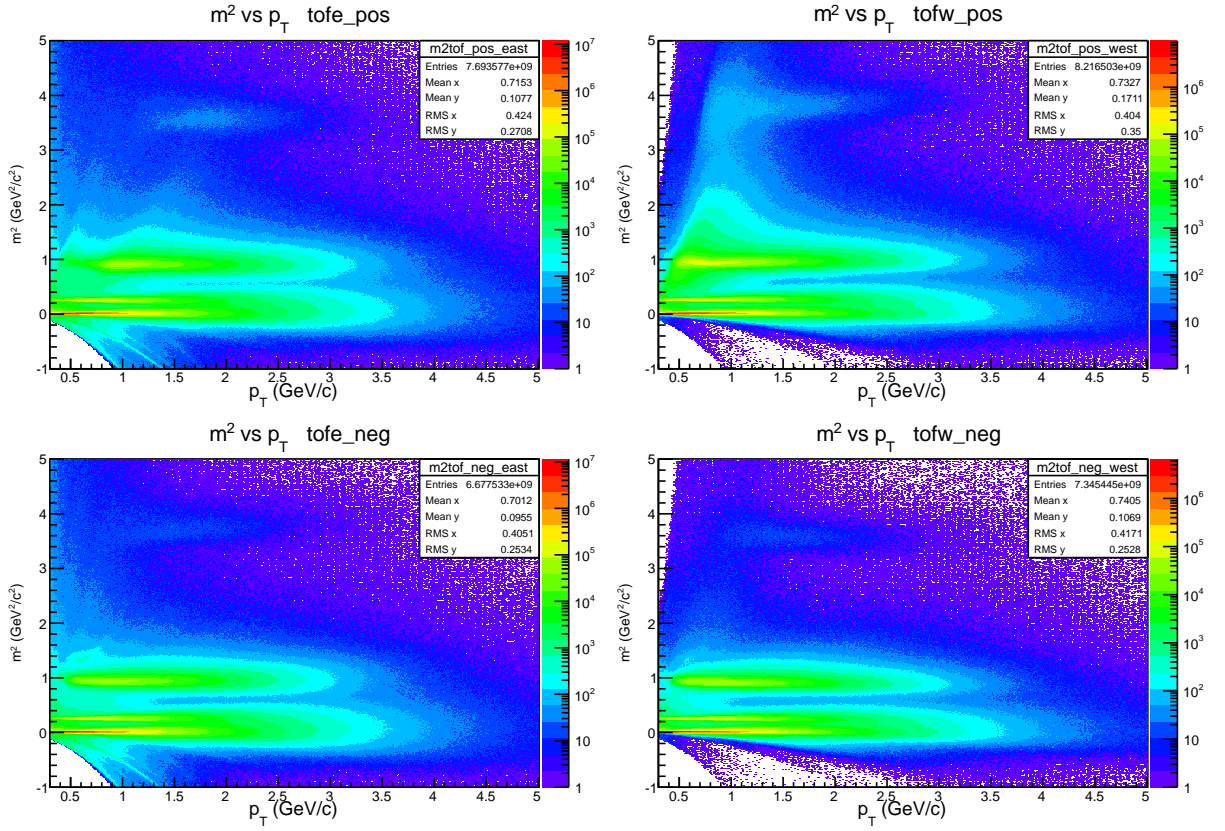


Figure 3.6: The squared mass distributions as functions of p_T . In each plot, the lowest horizontal band corresponds to pions, the second band are kaons and the third and forth bands are protons and deuterons. Top Left: Positive and TOF.E tracks. Bottom Left:Negative and TOF.E tracks. Top Right:Positive and TOF.W tracks. Bottom Right:Negative and TOF.W tracks.

where i corresponds to pions, kaons and protons.

In Fig. 3.8 and 3.9, the mean and width values for positive and TOF.W tracks as functions of p_T with the fitting functions are shown.

In our analysis, the 2σ from the mean values cuts are applied to identify particle species. Additionally to maintain good signal to background ratio, we used a veto cut which require 2σ away from the adjacent species peak. The squared mass distribution after the PID cuts are shown in Fig. 3.10. Although deuterons are identified using the PID functions, we do not use them in any measurements.

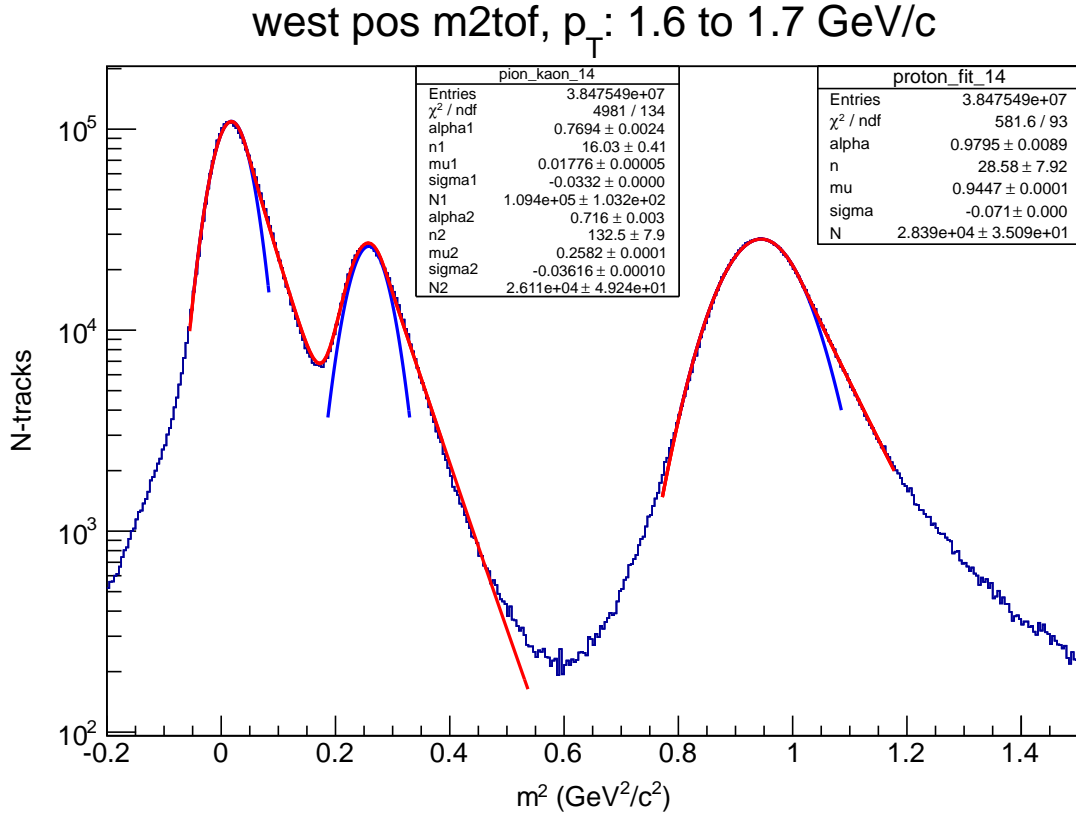


Figure 3.7: Squared mass distribution for medium p_T bin and positive particles in TOF.W. The fitted functions are for pions, kaons and protons.

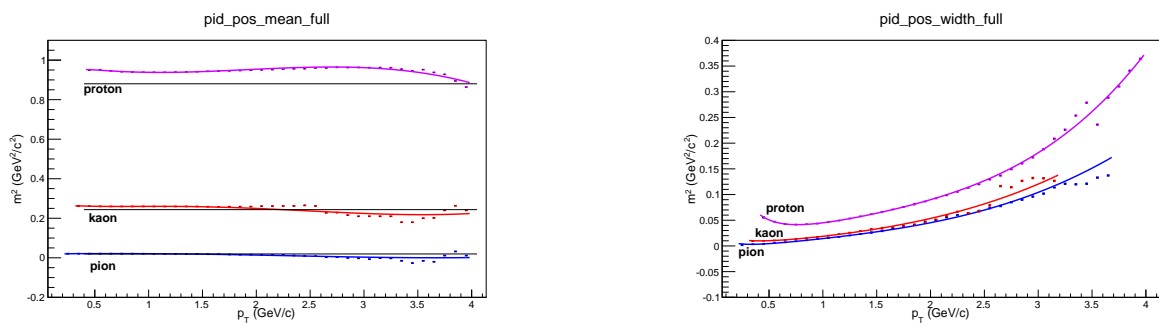


Figure 3.8: The mean values of squared mass distributions for p_T bins and positive particles in TOF.W.

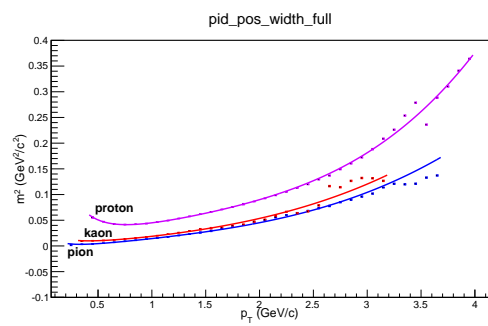


Figure 3.9: The width of squared mass distributions for p_T bins and positive particles in TOF.W.

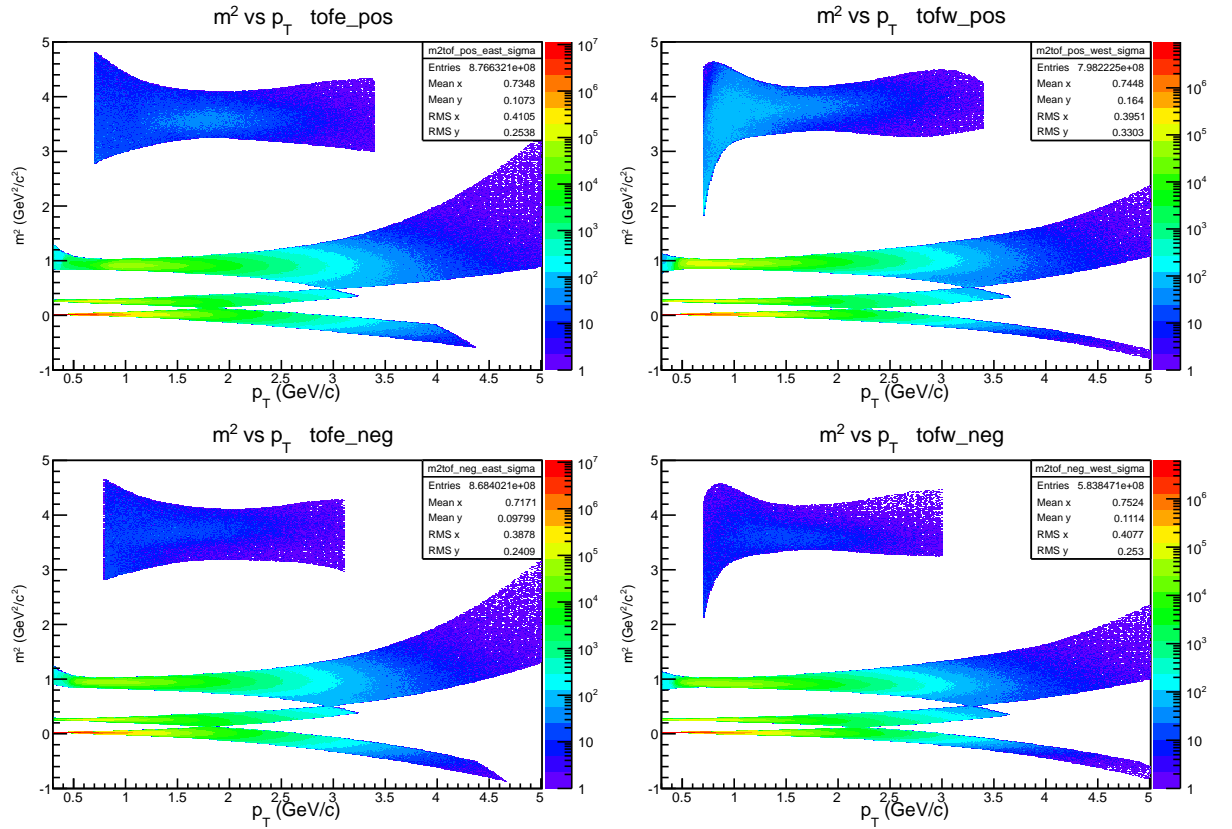


Figure 3.10: The squared mass distributions as functions of p_T after the PID cuts(2σ from the peaks and 2σ veto cuts from their adjacent species peaks). In each plot, the lowest horizontal band corresponds to pions, the second bad are kaons and the third and forth bands are protons and deuterons. Top Left: Positive and TOF.E tracks. Bottom Left:Negative and TOF.E tracks. Top Right:Positive and TOF.W tracks. Bottom Right:Negative and TOF.W tracks.

3.3 Event Plane

3.3.1 Azimuthal anisotropy

Azimuthal distribution of emitted particle $dN/d\phi$ is written in the form of Fourier expansion with 2π period,

$$\frac{dN}{d\phi} = \frac{x_0}{2\pi} + \frac{1}{\pi} \sum_{n=1} [x_n \cos(n\phi) + y_n \sin(n\phi)], \quad (3.7)$$

The coefficients x_n and y_n are obtained by integrating $\cos(n\phi)$ and $\sin(n\phi)$ with the azimuthal probability distribution $r(\phi)$ or by counting cosine and sine of each particle with normalized weight r

$$x_n = \int_{-\pi}^{\pi} r(\phi) \cos(n\phi) d\phi \quad (3.8)$$

$$= \sum_{\nu} r_{\nu} \cos(n\phi_{\nu}) \quad (3.9)$$

$$y_n = \int_{-\pi}^{\pi} r(\phi) \sin(n\phi) d\phi \quad (3.10)$$

$$= \sum_{\nu} r_{\nu} \sin(n\phi_{\nu}) \quad (3.11)$$

where $\int r(\phi) = 1$ and $\sum_{\nu} r_{\nu} = 1$, ν represents particle number and runs all particles, ϕ_{ν} is the azimuthal angle of ν -th particle. If there are no azimuthal anisotropic flow effect, $r(\phi)$ is constant, $r(\phi) = 1/(2\pi)$. The Fourier coefficients x_n and y_n give the corresponding harmonic component, defined as $v_n = \sqrt{x_n^2 + y_n^2}/x_0$, and the n -th harmonic order event plane angle Ψ_n ($-\pi/n \leq \Psi_n \leq \pi/n$).

$$\frac{x_n}{x_0} = v_n \cos(n\Psi_n) \quad (3.12)$$

$$\frac{y_n}{x_0} = v_n \sin(n\Psi_n) \quad (3.13)$$

$$\Psi_n = \tan^{-1}(y_n/x_n)/n \quad (3.14)$$

Eq. 3.7 can be re-written using v_n and Ψ_n ,

$$\frac{dN}{d\phi} = \frac{x_0}{2\pi} + \frac{1}{\pi} \sum_{n=1} [v_n \cos(n\Psi_n) \cos(n\phi) + v_n \sin(n\Psi_n) \sin(n\phi)] \quad (3.15)$$

$$= \frac{x_0}{2\pi} + \frac{1}{\pi} \sum_{n=1} [v_n \cos(n\Psi_n) \cos(n\phi) + v_n \sin(n\Psi_n) \sin(n\phi)] \quad (3.16)$$

$$= \frac{x_0}{2\pi} + \frac{1}{\pi} \sum_{n=1} [v_n \cos(n[\phi - \Psi_n])] \quad (3.17)$$

In experimentally, the real azimuthal anisotropy v_n^{true} is obtained from following relation between

the observed anisotropy and the real anisotropy in enough number of events,

$$v_n^{\text{obs}} = \langle \cos(n[\phi - \Psi_n^{\text{obs}}]) \rangle \quad (3.18)$$

$$= \langle \cos(n[\phi - \Psi_n + \Psi_n - \Psi_n^{\text{obs}}]) \rangle \quad (3.19)$$

$$= \langle \cos(n[\phi - \Psi_n]) \rangle \langle \cos(n[\Psi_n - \Psi_n^{\text{obs}}]) \rangle + \langle \sin(n[\phi - \Psi_n]) \rangle \langle \sin(n[\Psi_n - \Psi_n^{\text{obs}}]) \rangle \quad (3.20)$$

$$= \langle \cos(n[\phi - \Psi_n]) \rangle \langle \cos(n[\Psi_n - \Psi_n^{\text{obs}}]) \rangle \quad (3.21)$$

$$= v_n^{\text{true}} \text{Res}\{\Psi_n^{\text{obs}}\} \quad (3.22)$$

$$v_n^{\text{true}} = \frac{v_n^{\text{obs}}}{\text{Res}\{\Psi_n^{\text{obs}}\}} \quad (3.23)$$

where $\text{Res}\{\Psi_n^{\text{obs}}\} = \langle \cos(n[\Psi_n - \Psi_n^{\text{obs}}]) \rangle$ is the resolution of the observed event plane determination. This equation is given under the assumption that sine terms of $\phi - \Psi_n$ and $\Psi_n^{\text{obs}} - \Psi_n$ vanish because the distributions of ϕ and Ψ_n^{obs} with respect to Ψ_n become symmetric distribution in enough number of events.

3.3.2 Event Plane Determination

The event plane is defined as the average angle of emitted particles and reconstructed on event by event basis. Since the azimuthal angle of the impact parameter can not be controlled by the beam, the azimuthal angle of the impact parameter is distributed randomly. Thus in enough number of events, the azimuthal distribution in the event plane angle should be flat. The event plane is reconstructed using flow vector(Q-vector),

$$Q_{xn} = \sum_i w_i \cos(n\phi_i) \quad (3.24)$$

$$Q_{yn} = \sum_i w_i \sin(n\phi_i) \quad (3.25)$$

where i is the index for the reconstructed particles, ϕ_i and w_i correspond to azimuthal angle and weight of the i -th particle respectively. If the Q-vector is reconstructed using a detector which can not reconstruct charged particle tracks, such as BBC, i -th particle is changed to i -th segment in the detector. In this analysis, BBC, RXN, SMD and CNT detectors are employed for Q-vector i.e. event plane determination. The BBC is located at $3 < |\eta| < 4$ and has 64 PMTs for South and North side respectively. The charge information in each PMT is used as weight and the azimuthal angle of each PMT is used as ϕ_i for Q-vector calculation. The RXN sits on $1 < |\eta| < 2.8$ and has 24 PMTs in each side of North and South. The weight for RXN Q-vector calculation is ADC value in each PMT. The SMD provide the centroid of spectator neutrons, which corresponds to Q-vector. The CNT is located at $-0.35 < |\eta| < 0.35$ and can reconstruct charged tracks. The weight of CNT is p_T of each charged track and $p_T < 2 \text{ GeV}/c$ is used due to reduction of the high p_T particle contribution which has non flow correlates with event plane angle, such as jet. Ideally, the azimuthal angle of event plane is flat distribution. However normally the reconstructed event plane distribution is not always flat because imperfect azimuthal acceptance of detector, the shifted beam line and the dead area effect and so on. In order to correct these effects, we perform two step calibrations. One is “Re-centering collection” and the other is “Fourier Flattening collection”.

3.3.3 Event Plane Calibration

In this section, we describe two steps for event plane calibration mentioned in previous section.

3.3.4 Re-centering Calibration

At the first step, we calibrate Qvector distribution of X component and Y component respectively. We perform Re-centering procedure to correct beam shift and non-uniform detector acceptance. This correction method is used to obtain isotropic distribution of Qvector in laboratory frame. The event by event Qvector X and Y components Q_x, Q_y are subtracted by Qvector X and Y components $\langle Q_{nx} \rangle, \langle Q_{ny} \rangle$ averaged over all event and divided by the standard deviations of Qvector X and Y distributions, σ_{nx}, σ_{ny} . With this correction, the corrected Qvector components become,

$$Q_{nx}^{corr} = \frac{Q_{nx} - \langle Q_{nx} \rangle}{\sigma_{nx}} \quad (3.26)$$

$$Q_{ny}^{corr} = \frac{Q_{ny} - \langle Q_{ny} \rangle}{\sigma_{ny}} \quad (3.27)$$

In practice, this correction is applied for each centrality and Z vertex class. After applying the Re-centering correction, the event plane angle is given from

$$\Psi_n^{\text{Re-centered}} = \tan^{-1}(Q_{ny}^{\text{Re-centered}}, Q_{nx}^{\text{Re-centered}})/n \quad (3.28)$$

Fig.3.11 shows the Qvector distributions determined the combined South and North Bbc detectors before and after the Re-centring correction. In both plots, the horizontal and vertical axes are the x and y components of the Qvector. In the raw Qvector plot, the mean are slightly shifted from the center due to the shifted beam position and non-uniform azimuthal acceptance. After the Re-centering correction, the corrected Qvector distribution is centered and has RMS = 1. If the event plane corrected by Re-centering is non-flat distribution, additional calibration step is needed. In our analysis, we apply “Flattening” calibration to the corrected event plane.

3.3.5 Flattening Calibration

For the second additional event plane correction, we perform Flattening procedure. Basically, the Re-centering procedure remove almost all beam shift bias and detector acceptance bias. However there are the residual non-flat components which can not be removed by the Re-centering procedure. The Flattening calibration is defined as,

$$\begin{aligned} n\Psi_n &= n\Psi_n^{corr} + n\Delta\Psi_n^{\text{Re-centered}} \\ n\Delta\Psi_n^{\text{Re-centered}} &= \sum_{k=1} [A_k \cos(kn\Psi_n^{\text{Re-centered}}) + B_k \sin(kn\Psi_n^{\text{Re-centered}})]. \end{aligned} \quad (3.29)$$

Since the performance of EP detectors and the beam condition are changed run by run, we generate the Re-centering and the Flattening calibration parameters for each centrality class and

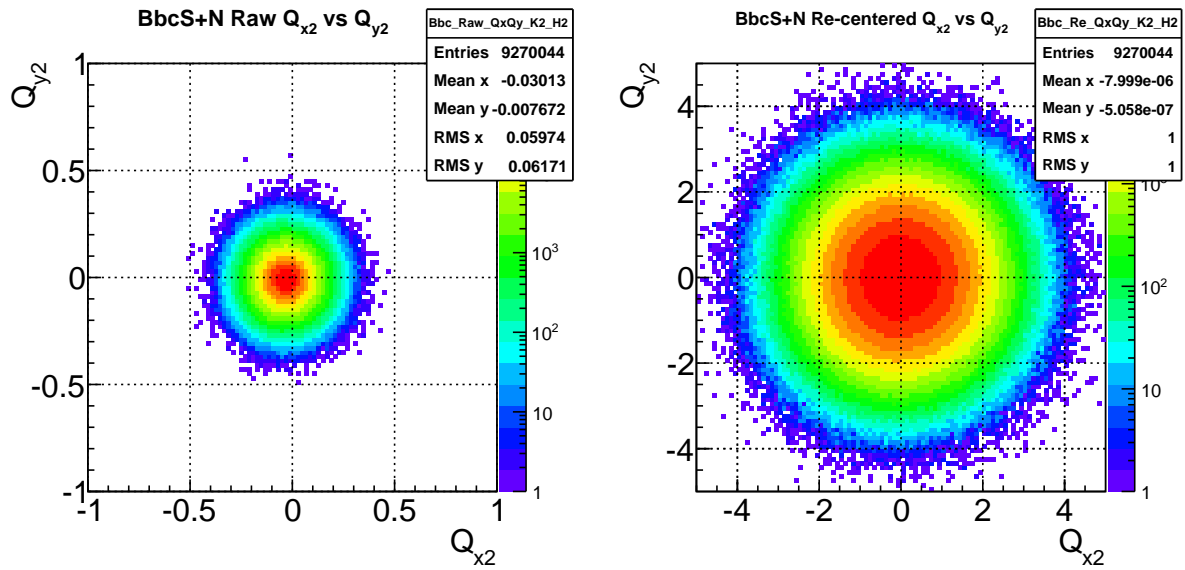


Figure 3.11: The Qvector distribution determined the combined South and North Bbc detectors before and after the Re-centring correction. Left:Raw Qvector. Right:Corrected Qvector

Z vertex class in each run. Figure 3.12 shows the 2nd harmonic event plane determined the combined South and North Bbc detectors for the no correction, only the Re-centring correction and the Re-centring and the Flattening corrections. The red line is no correction case, the blue line is the application of Re-centring and the green line is the application of Re-centring and Flattening. Although the Re-centring correction could be enough for the Bbc detector, the additional Flattening correction make flatter event plane distribution as shown in the insert box in Fig 3.12.

3.3.6 Event Plane QA

After applying the two step calibration, the event plane distribution for different centrality class, Zvertex class and detectors should be flat in each run. We check the flatness of the event plane distribution in each run. In order to check the flatness of the event plane distribution, we fit the distribution with a constant function and the extract χ^2/NDF . The χ^2/NDF value is selected below 3.

3.3.7 Event Plane Resolution

Since the finite number of emitted particles make the azimuthal angle resolution of the event plane $\text{Res}\{\Psi_n\}$, the observed Fourier coefficients v_n^{obs} with respect to the event plane have to be corrected by the event plane resolution. If the number of emitted particles that determine the event plane is large enough, the correction is done by dividing the observed v_n^{obs} by the event plane resolution $v_n = v_n^{\text{obs}}/\text{Res}\{\Psi_n\}$. This correction is analytically introduced in Eq.(3.18). The event plane resolution is obtained from the correlation of the two event planes $\langle \cos[n(\Psi_{n,A} -$

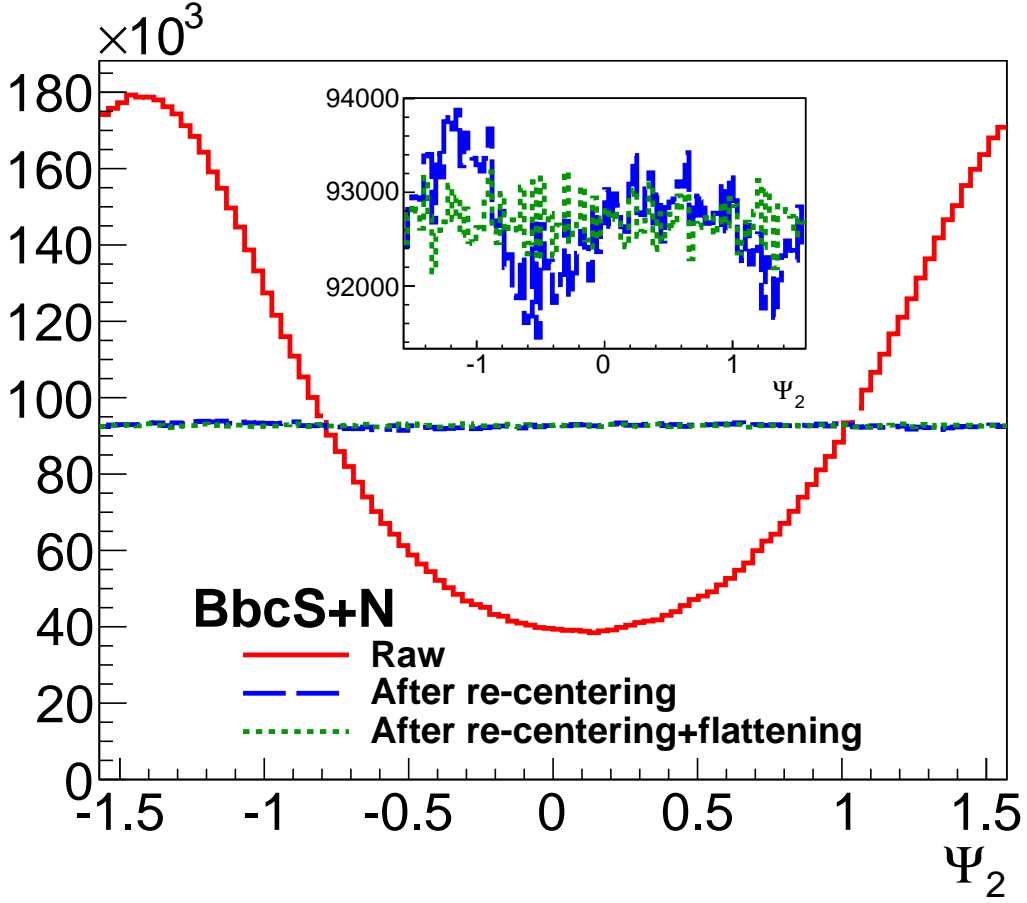


Figure 3.12: The 2nd harmonic event plane determined by the combined South and North Bbc detectors for the no correction, only the Re-centering correction and the Re-centering and the Flattening corrections in Cu+Au collisions at $\sqrt{s_{NN}} = 200\text{GeV}$.

$\Psi_{n,B})] \rangle$ determined by independent rapidity windows A, B. When the distance of the two rapidity windows A and B is large, the event plane correlation of the two subevents could be expressed as the product of the event plane resolutions of the two subevents. If the distance of the two subevents is close, other corrections from non-flow effect such as multi-particle correlations from resonance decay and jets, make the stronger event plane correlation.

$$\begin{aligned}
 \langle \cos[n(\Psi_{n,A} - \Psi_{n,B})] \rangle &= \langle \cos[n(\Psi_{n,A} - \Psi_n - (\Psi_{n,B} - \Psi_n))] \rangle \\
 &= \langle \cos[n(\Psi_{n,A} - \Psi_n)] \rangle \langle \cos[n(\Psi_{n,B} - \Psi_n)] \rangle \\
 &\quad + \langle \sin[n(\Psi_{n,A} - \Psi_n)] \rangle \langle \sin[n(\Psi_{n,B} - \Psi_n)] \rangle \\
 &= \langle \cos[n(\Psi_{n,A} - \Psi_n)] \rangle \langle \cos[n(\Psi_{n,B} - \Psi_n)] \rangle \\
 &= \text{Res}\{\Psi_{n,A}\} \text{Res}\{\Psi_{n,B}\}
 \end{aligned} \tag{3.30}$$

where Ψ_n is the true event plane and \sin term (odd function) should vanish because the observed event plane distributions with respect to the true event plane are symmetric. If the two subevents

are symmetric in rapidity and have same multiplicity, the resolution of each of them becomes,

$$\text{Res}\{\Psi_{n,A}\} = \text{Res}\{\Psi_{n,B}\} = \sqrt{\langle \cos[n(\Psi_{n,A} - \Psi_{n,B})] \rangle}. \quad (3.31)$$

This method is so-called “2-subevent method” and can be performed in symmetric collision cases. For asymmetric collision cases or asymmetric rapidity window cases, “3-subevent method” is generally used. In the 3-subevent method, the 3 event plane correlations from 3 independent subevents A,B and C are used to determine the event plane resolution of each of them. The relation of the resolution and the correlations are

$$\text{Res}\{\Psi_{n,A}\} = \sqrt{\frac{\langle \cos[n(\Psi_{n,A} - \Psi_{n,B})] \rangle \langle \cos[n(\Psi_{n,A} - \Psi_{n,C})] \rangle}{\langle \cos[n(\Psi_{n,B} - \Psi_{n,C})] \rangle}}. \quad (3.32)$$

In Cu+Cu collisions, the 2_{nd} order event plane is measured by the BbcS, the BbcN and the Cnt. Each of the event plane resolutions are determined by the 3-subevent combination BbcS-Cnt-BbcN. Fig. 3.13 shows the 2_{nd} order event plane resolutions as functions of centrality for the BbcS, the BbcN and the Cnt.

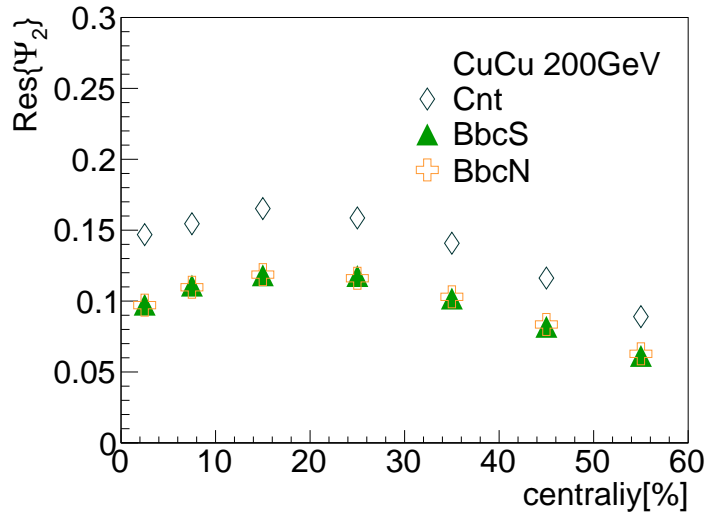


Figure 3.13: The 2_{nd} order event plane resolutions of South and North side of Bbc and Cnt as functions of centrality in CuCu collisions at 200GeV. The resolutions are determined by BbcS-Cnt-BbcN 3-subevent combination.

In Au+Au collisions, the 2_{nd} order and 3_{rd} order event planes are measured by the RxnS, the RxnN, the BbcS, the BbcN and the Cnt. The RxnS and the RxnN event plane resolutions are determined by the 2-subevent combination RxnS-RxnN. Therefore the resolutions for the RxnS and the RxnN are identical. The other event plane resolutions are determined by the 3-subevent combination BbcS-Cnt-BbcN. Fig. 3.14 shows the 2_{nd} order and 3_{rd} order event plane resolutions as functions of centrality for the RxnS, the RxnN, the BbcS, the BbcN and the Cnt.

In Cu+Au collisions, the 1_{st} order coefficient is measured with respect to the Au spectator neutrons measured by the SmdS on the Au-going side. The event plane resolution for SmdS is

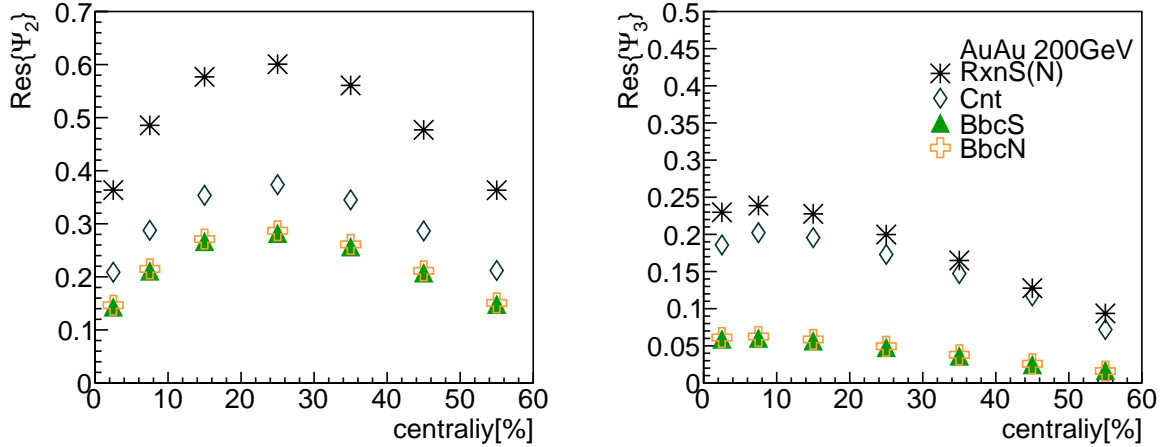


Figure 3.14: The 2_{nd} and 3_{rd} order event plane resolutions of the South and North side of Bbc, the South and North side of Rxn and the Cnt as functions of centrality in Au+Au collisions at 200GeV. The event plane resolution of the Rxn is determined from 2-subevent method. The others are determined from BbcS-Cnt-BbcN 3-subevent combination. Left panel: 2_{nd} order event plane. Right panel: 3_{rd} order event plane.

estimated by the 3-subevent combinations, the Cu spectator neutrons measured by the SmdN on the Cu-going side and the 1_{st} order participant event plane determined the South side of Bbc, SmdS-BbcS-SmdN. Event by event fluctuations in the participants and spectators will make difference between the 1_{st} order participant event plane and the 1_{st} order spectator plane. To cover this uncertainty, the resolution of SmdS is also estimated by the 3-subevent combinations including the participant event plane observed by the BbcN, SmdS-BbcN-SmdN.

For the 2_{nd} and 3_{rd} harmonics, the event plane resolutions for the BbcS, the BbcN and the Cnt are estimated by the 3-subevent combinations of them, BbcS-Cnt-BbcN. The combined South and North side of Bbc event plane resolution is calculated by dividing the correlation of the BbcSN $\Psi_{n,BbcSN}$ and the Cnt $\Psi_{n,Cnt}$ with the Cnt resolution $\text{Res}\{\Psi_{n,Cnt}\}$, $\text{Res}\{\Psi_{n,BbcSN}\} = \langle \cos(n[\Psi_{n,BbcSN} - \Psi_{n,Cnt}]) \rangle / \text{Res}\{\Psi_{n,Cnt}\}$. In Fig. 3.15, the 1_{st} , 2_{nd} and 3_{rd} order event plane resolutions as functions of centrality are shown.

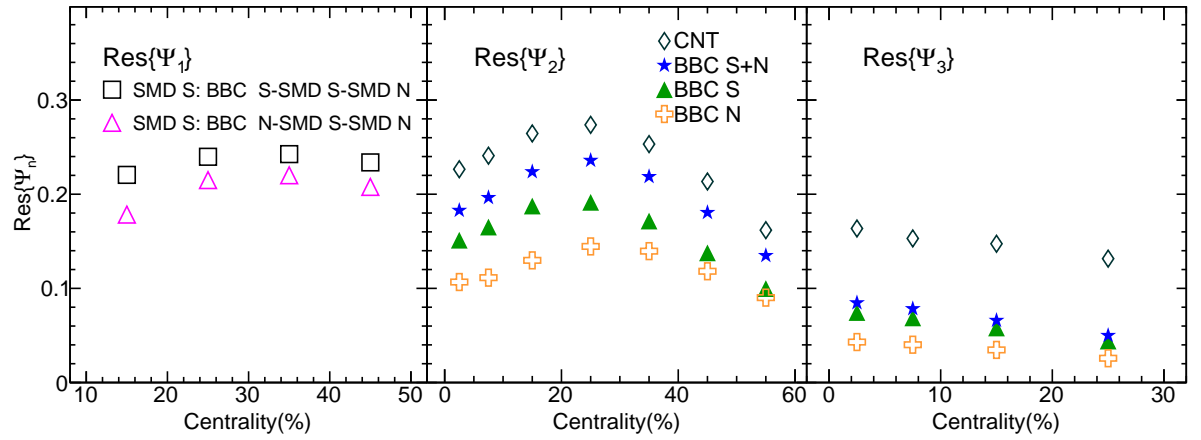


Figure 3.15: The 1_{st} , 2_{nd} and 3_{rd} order event plane resolutions as functions of centrality. Left panel: The 1_s event plane for the South side of Smd determined from 3-subevent combinations, SmdS-BbcS-SmdN and SmdS-BbcN-SmdN. Middle panel: The 2_{nd} order event plane for the South, North and combined South and North Bbc and the Cnt. Right panel: 3_{rd} order event plane for the Bbc and the Cnt. The 2_{nd} and 3_{rd} order event plane resolutions for the Bbc and the Cnt are determined from BbcS-Cnt-BbcN 3-subevent combination.

3.4 Measurements of charged hadron v_n at mid-rapidity

The charged hadron v_n is measured via the Event Plane method as described at the previous section. Experimentally, the magnitude of v_n are obtained from following formula as shown at previous section,

$$v_n^{\text{true}} = \frac{v_n^{\text{obs}}}{\text{Res}\{\Psi_n\}} \quad (3.33)$$

$$= \frac{\langle \cos(n[\phi - \Psi_n^{\text{obs}}]) \rangle}{\langle \cos(n[\Psi_n^{\text{obs}} - \Psi_n^{\text{true}}]) \rangle} \quad (3.34)$$

where ϕ is the azimuthal angle of the track and Ψ_n^{true} are true Event plane azimuthal angle and Ψ_n^{obs} are the observed Event plane azimuthal angle. At the mid-rapidity, inclusive charged hadron and π, K, p v_n (n=1 3) are measured for different centrality classes. The azimuthal angle ϕ are determined by Central Arm detector and the Event plane is estimated by BBC detector. In this analysis, $\langle \cos(n[\phi - \Psi_n^{\text{obs}}]) \rangle$ are the average of the observed event by event $\cos(n[\phi - \Psi_n^{\text{obs}}])$ and the resolution of Ψ_n^{obs} are estimated from 2-subevent or 3-subevent method. Inclusive charged hadron v_n (n=1 3) are measured for each centrality bin and π, K and *proton* v_n are measured. π, K and p v_2 are measured for each 10% centrality class and v_1 and v_3 are measured for one wider centrality class.

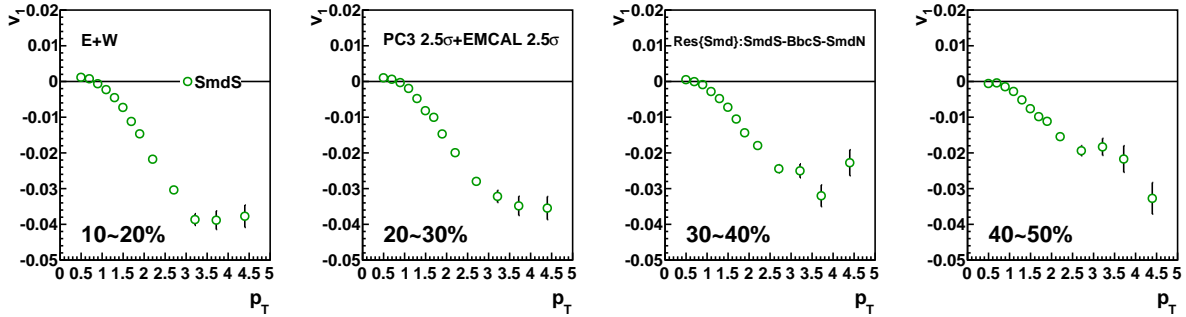


Figure 3.16: Charged hadron v_1 as a function of p_T in Cu+Au collisions for different centrality bins

3.5 Measurements of particle identified v_n at mid-rapidity

The identified particle v_n (PID v_n) at the Cnt region are also measured via the event plane technique. The used event planes are observed by the SmdS for the 1_{st} order and the BbcSN for the 2_{nd} and 3_{rd} order flow harmonics. For the PID v_n measurements, the azimuthal angles ϕ in the observed PID $v_n^{\text{obs}} = \langle \cos(n[\phi - \Psi_n^{\text{obs}}]) \rangle$ are used for the each particle species. The particle species are determined on track by track basis with the PID functions. Fig. 3.19, 3.20 and 3.21 show the PID v_2, v_3 and v_1 with PID 2 sigma cut in Cu+Au collisions separately.

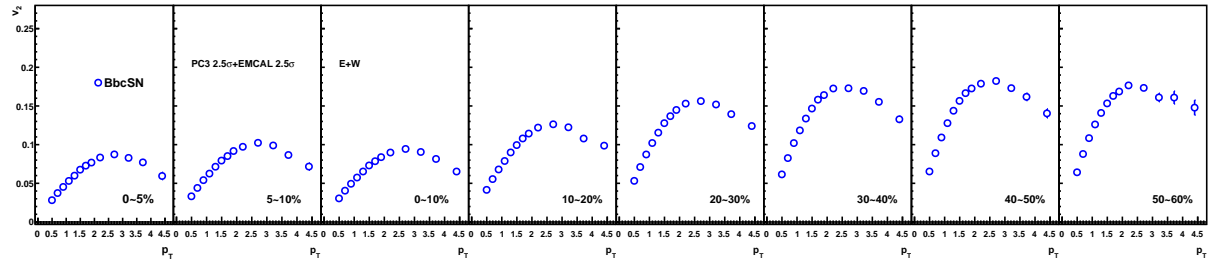


Figure 3.17: Charged hadron v_2 as a function of p_T in Cu+Au collisions for different centrality bins

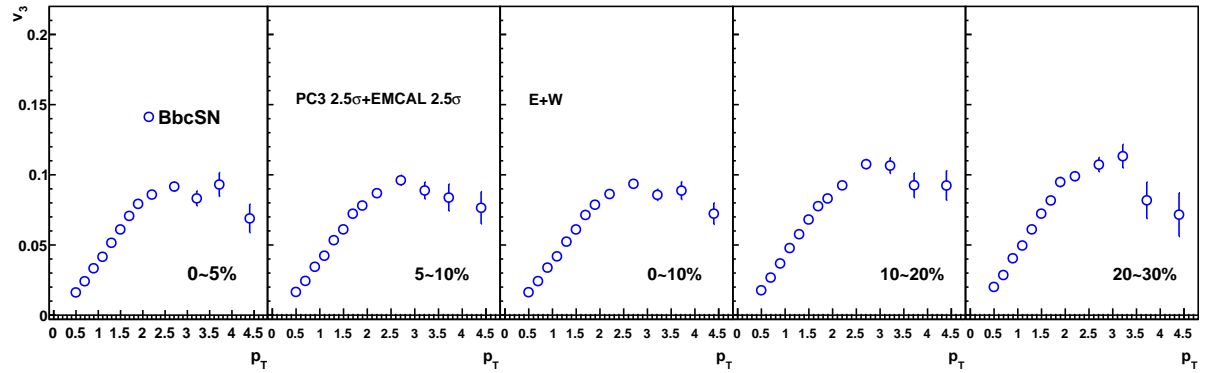
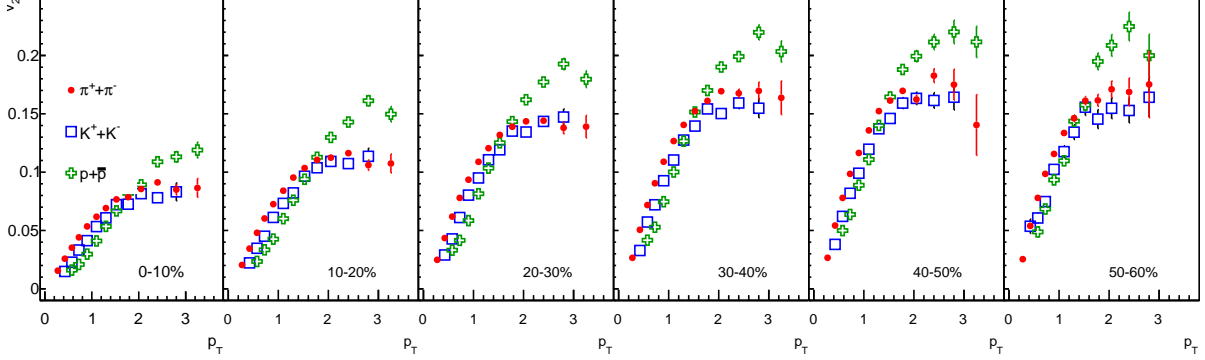
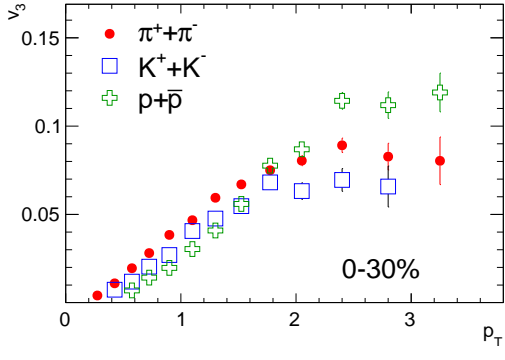
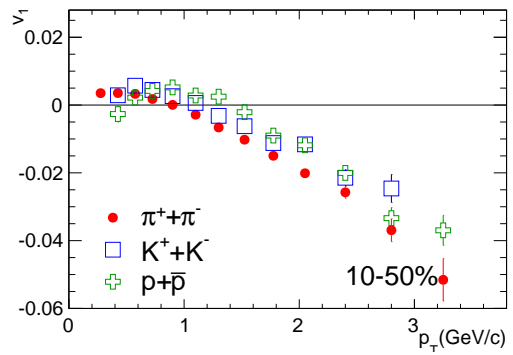


Figure 3.18: Charged hadron v_3 as a function of p_T in Cu+Au collisions for different centrality bins

3.6 Measurements of hadron v_n at forward/backward-rapidity

At the forward/backward rapidity, v_2 and v_3 are measured using the BBC PMTs for each 10% centrality class. Since the BBC can not reconstruct charged hadron tracks, the statistical uncertainty of v_n can not be calculated single particle basis. Thus we extract v_n coefficients by fitting the azimuthal PMT angle distribution with respect to the Event Plane, $\Delta\phi_{PMT}(n) = \phi_{PMT} - \Psi_n$ with a Fourier expansion serious formula. The $\Delta\phi_{PMT}(n)$ distribution is measured for each Fourier harmonic. In the $\Delta\phi_{PMT}(n)$ distribution, the charge information from single PMT is used as weight for the $\Delta\phi_{PMT}(n)$ bin which corresponds to the azimuthal angle of that PMT, because each PMT charge information is proportional to the number of particles detected at the PMT. Since each BBC counter has 64 PMTs, the azimuthal coverage of the BBC is not uniform. Although the calibrated event plane can reduce such detector acceptance effects, we apply an additional acceptance correction that is event mixing method. In the event mixing method, the $\Delta\phi_{PMT}(n)$ is corrected by being divided by the product of one PMT and the event

Figure 3.19: PID v_2 as a function of p_T in Cu+Au collisionsFigure 3.20: PID v_3 as a function of p_T in Cu+Au collisions for different centrality binsFigure 3.21: PID v_1 as a function of p_T in Cu+Au collisions

plane probability distributions.

$$C(\Delta\phi)_n = \frac{P(\phi_{PMT}, \Psi_n)}{P(\phi_{PMT})P(\Psi_n)} \quad (3.35)$$

Since PMTs fired by emitted charged particles and the Event Plane preserve physical correlation in real (same) event, the measurement of the azimuthal angle of fired PMTs with respect to the Event Plane become the pair of one fired PMT and the Event Plane probability distribution. If those pair is measured in mixed (different) events, the pair distribution corresponds to the product of one fired PMT and the Event Plane probability distributions because there is no physical correlation between fired PMTs and the Event plane in different event. Because the limited acceptance effect is included in real event and mixed event, the limited acceptance effect is canceled by taking ration of real event and mixed event. As described before, v_n coefficients

are extracted by fitting the above correlation function with following Fourier function,

$$r(\Delta\phi)_n = 1 + 2v_n^{\text{obs,pmt}} \cos(n[\phi_{\text{pmt}} - \Psi_n^{\text{obs}}]) \quad (3.36)$$

$$v_n^{\text{pmt}} = \langle \cos(n[\phi_{\text{pmt}} - \Psi_n^{\text{obs}}]) \rangle \quad (3.37)$$

$$v_n^{\text{corr,pmt}} = \frac{v_n^{\text{obs,pmt}}}{\text{Res}\{\Psi_n\}} \quad (3.38)$$

where ϕ_{pmt} is the azimuthal angle of PMT and $v_n^{\text{obs,pmt}}$ is free parameter in $r(\Delta\phi)_n$ function. The v_n coefficient extracted from fitting function is divided by the Event plane resolution to correct the uncertainty of the estimated Event Plane. The v_n coefficients measured with BBC PMTs have to be converted to track based v_n , since BBC can not reconstruct charged particle track. In order to obtain track based v_n at BBC rapidity, we run Single Monte Carlo simulation to produce correction parameters which translate PMT based v_n to track based v_n . To remove non-flow effect, we employ the Event Plane estimated from the detector placed at opposite rapidity side of v_n measurement rapidity region.

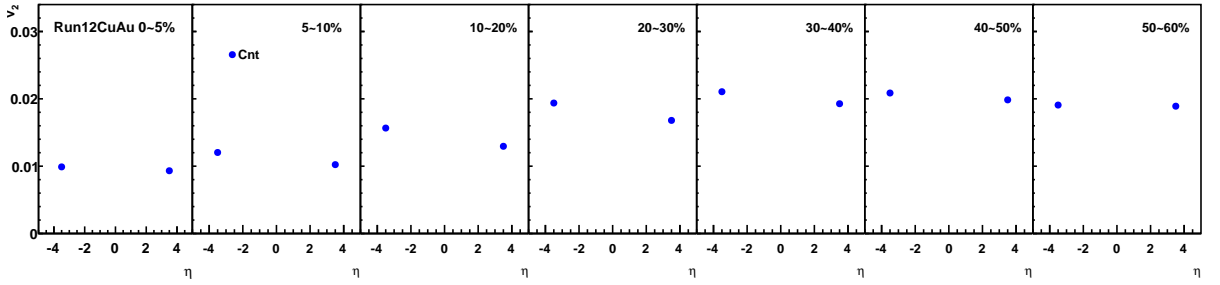


Figure 3.22: Charged hadron v_2 as a function of η in Cu+Au collisions for different centrality bins

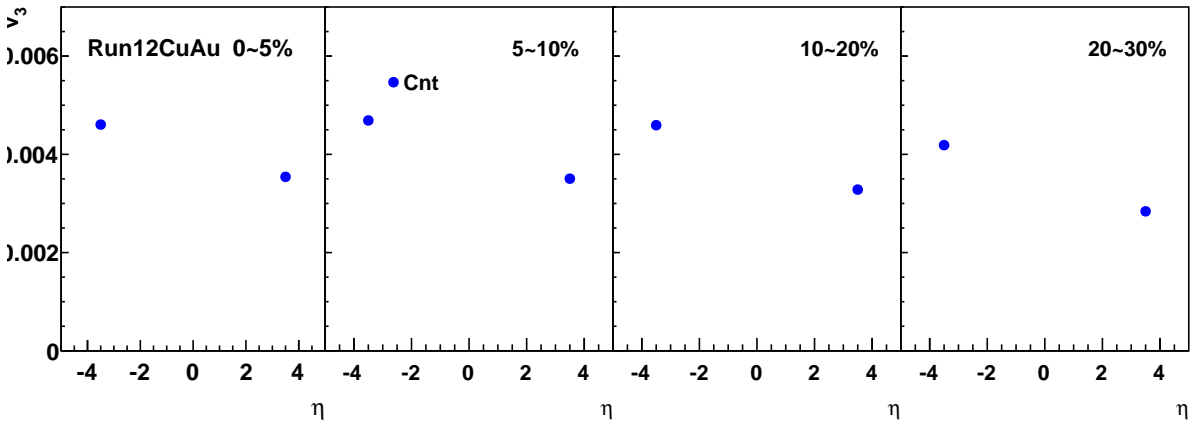


Figure 3.23: Charged hadron v_3 as a function of η in Cu+Au collisions for different centrality bins

3.6.1 Single particle simulation for forward/Backward-rapidity v_n measurements

Since the BBC detector can not reconstruct charged hadron tracks, the measurements of the PMT based v_n include the background effect such as γ conversion. In order to estimate the background contribution, we run single particle Monte Carlo simulation with PISA which is the PHENIX simulation software based on the GEANT libraries. The PMT based v_n including background contribution is corrected by following steps

1. Single particle Monte Carlo simulation (input)
2. Single particle Monte Carlo simulation with the PISA to evaluate material interactions and secondary particle generation
3. Reconstruct Bbc information from the PISA hits(output)
4. Measure v_n using the reconstructed Bbc information
5. Estimate the correction factor

The correction factor R_n is estimated by comparing the input v_n and the output v_n from the PISA simulation.

$$R_n = \frac{v_n^{\text{input}}}{v_n^{\text{output}}} \quad (3.39)$$

where v_n^{input} and v_n^{output} are the v_n estimated by the single particle simulation without and with the PISA respectively. We obtain the corrected v_n as

$$v_n = R_n v_n^{\text{pmt}} \quad (3.40)$$

The default set-up of single particle simulation is summarized in Table 3.1.

Table 3.1: Default setting for single particle simulation

Parameter	Value
Event type	Single particle
Species	π^\pm and π_0
p_T distribution	$p_T \exp\left(\frac{-p_T}{T}\right)$
p_T range	$0 < p_T < 5 \text{ GeV}/c$
η distribution	Trapezoidal
η range	$-5 < \eta < 5$
azimuth range	$-\pi/2 < \phi < \pi/2$

3.7 Measurements of charged hadron $dN_{ch}/d\eta$ at forward/backward-rapidity

Measurements of $dN/d\eta$ at forward/backward-rapidity ($3 < |\eta| < 3.9$) is also performed in Au+Au, Cu+Au and Cu+Cu collisions at $\sqrt{s_{NN}} = 200$ GeV using Bbc detectors. As noted in the previous section about the v_n measurements at forward/backward-rapidity, Bbc can not reconstruct charged particle tracks. Thus the Bbc can not remove the background contribution and count the number of charged particles directly. Figure. 3.24 shows the Bbc charge sum which is ADC information corresponding the charged particle multiplicity as a function of centrality in Au+Au, Cu+Au and Cu+Cu collisions. In Cu+Au collisions, BbcS and BbcN indicate Au-going side and Cu-going side respectively. The Bbc charge sum become the largest in the central collisions and the smallest in the peripheral collisions, because the charged particle multiplicity and the background particles increase from the peripheral to the central collisions. In the next subsection, we will explain how to remove the background contribution using simulation study.

3.7.1 Single particle simulation for forward/backward-rapidity charged particle multiplicity $dN_{ch}/d\eta$ measurements

In order to measure the number of charged particles correctly, the ADC in Bbc for charged particles is converted into the number of charged particles with the correction factor R . For estimating the correction factor R , we perform the single particle simulation which is used for the correction in the forward/backward v_n measurements described in the previous section. The simulation set up is completely same as the v_n simulation listed in Table 3.1. Both of correction factors R for the multiplicity measurements and R_n for azimuthal measurements are obtained simultaneously in the same simulation run. The correction factor R is defined as following,

$$R = \frac{2}{3} \frac{1}{ADC_{output}^{\text{sim}}}, \quad (3.41)$$

where $\frac{2}{3}$ is the fraction of charged π and 1 is the number of emitted particle in each event. $ADC_{output}^{\text{sim}}$ is the ADC for 1 particle passing through Bbc. Once the correction factor R is estimated, the charge particle multiplicity is given by following formula,

$$\frac{dN_{ch}}{d\eta} = R \times ADC^{\text{obs}}, \quad (3.42)$$

where ADC^{obs} is the ADC for charged particles and backgrounds measured at Bbc.

3.8 Initial spatial anisotropy

In this study, the initial spatial anisotropy ε_n are estimated from the Glauber model Monte Carlo simulation[7]. The Glauber model Monte Carlo simulation is the simplest approach to describe the initial collision geometry as described. This simulation model is widely used for determination of centrality and the initial conditions in hydrodynamical models and event generators.

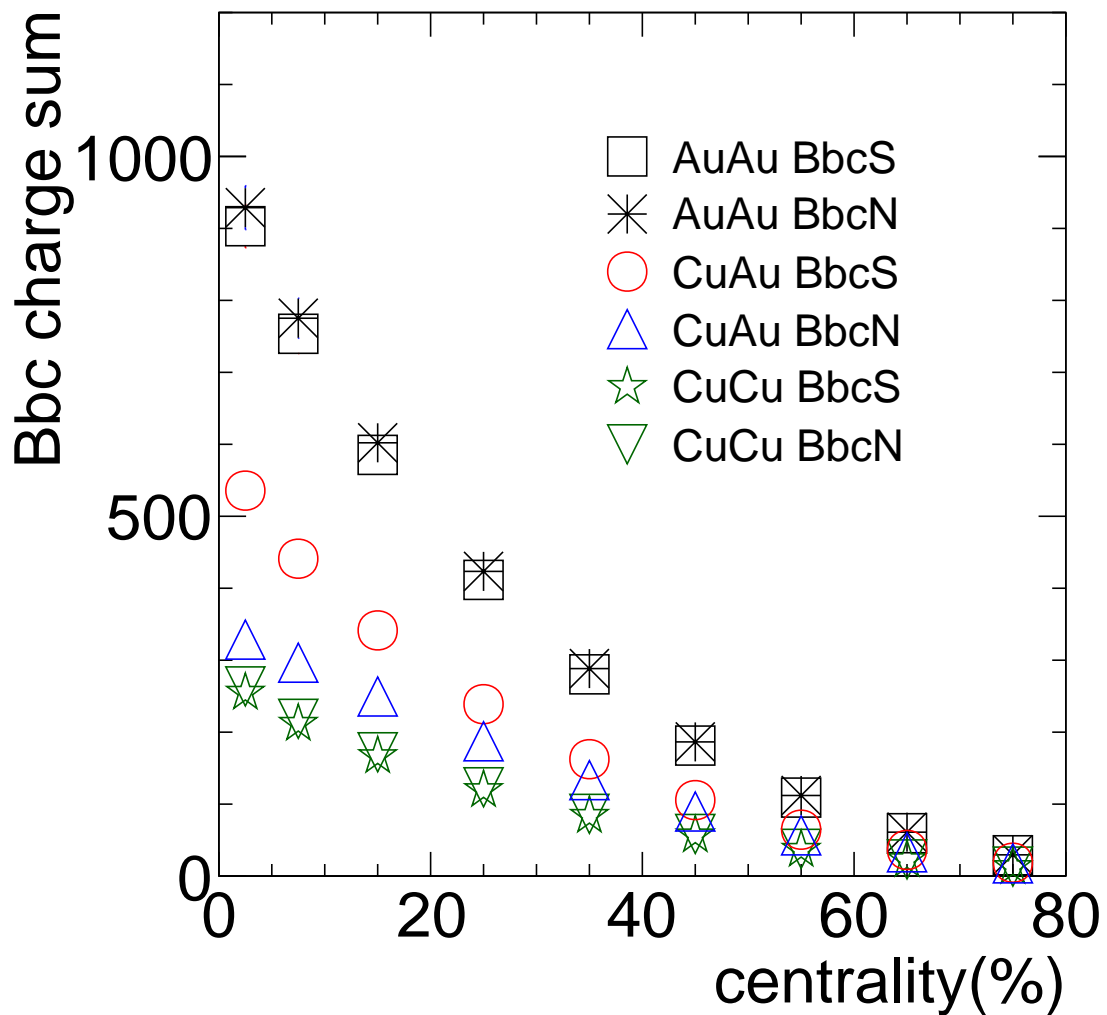


Figure 3.24: Bbc charge sum as a function of centrality in Au+Au, Cu+Au and Cu+Cu collisions. In Cu+Au collisions, BbcS and BbcN indicate Au-going side and Cu-going side respectively

Table 3.2: Nuclear density parameters used in Glauber model

Species	R[fm]	a[fm]	$\sigma_{NN}[\text{mb}]$
Au	6.38	0.535	42
Cu	4.20	0.5960	42

3.8.1 Glauber model Monte Carlo simulation

In the Glauber model Monte Carlo simulation, the nucleons of nucleus A and the nucleons of nucleus B are distributed inside A and B respectively according to the Woods-Saxon distribution.

$$\rho(r) = \frac{1}{1 + \exp(\frac{r-R}{a})} \quad (3.43)$$

where r is the distance of each nucleon from the center of nucleus, R is the nuclear radius and a is the skin depth. The Glauber model assumes that the nucleons travel on straight line trajectories and the inelastic nucleon-nucleon cross section is independent of the number of collisions. Under these assumptions, an A-B collision is treated as independent binary nucleon-nucleons collisions. The impact parameter b is randomly sampled. A nucleon-nucleon collision occur if the distance of two nucleons d in the transverse plane(x-y plane) becomes less than

$$d \leq \sqrt{\sigma_{NN}/\pi} \quad (3.44)$$

where σ_{NN} is the total inelastic nucleon-nucleon cross section. The value of R , a and σ_{NN} are listed in Table 3.2. The nucleons participating in collisions provide the number of binary collisions $\langle N_{\text{coll}} \rangle$, the number of participant nucleons $\langle N_{\text{part}} \rangle$ and the initial spatial anisotropy ε_n . The impact parameter and $\langle N_{\text{part}} \rangle$ distribution in Cu+Au collisions are shown in Fig.3.25. The centrality class for this simulation is determined by $\langle N_{\text{part}} \rangle$ distribution.

3.8.2 Initial spatial anisotropy

The origin of the azimuthal anisotropy of produced particles with respect to the event plane is considered to be the initial spatial anisotropy. The initial spatial anisotropy is converted to the anisotropy in the momentum space through the pressure gradient. Thus it is important to characterize the initial geometry. The initial spatial anisotropy is defined as the following formula [34],

$$\varepsilon_n = \frac{\sqrt{\langle r^n \cos(n\phi) \rangle^2 + \langle r^n \sin(n\phi) \rangle^2}}{\langle r^n \rangle} \quad (3.45)$$

$$= -\frac{\langle r^n \cos(n[\phi - \Psi_{n,PP}]) \rangle}{\langle r^n \rangle}, \quad (3.46)$$

where r and ϕ are the distance and azimuthal angle of participant nucleon in the polar coordinate where the center of participant nucleons is the origin and $\Psi_{n,PP}$ is the average angle of over all

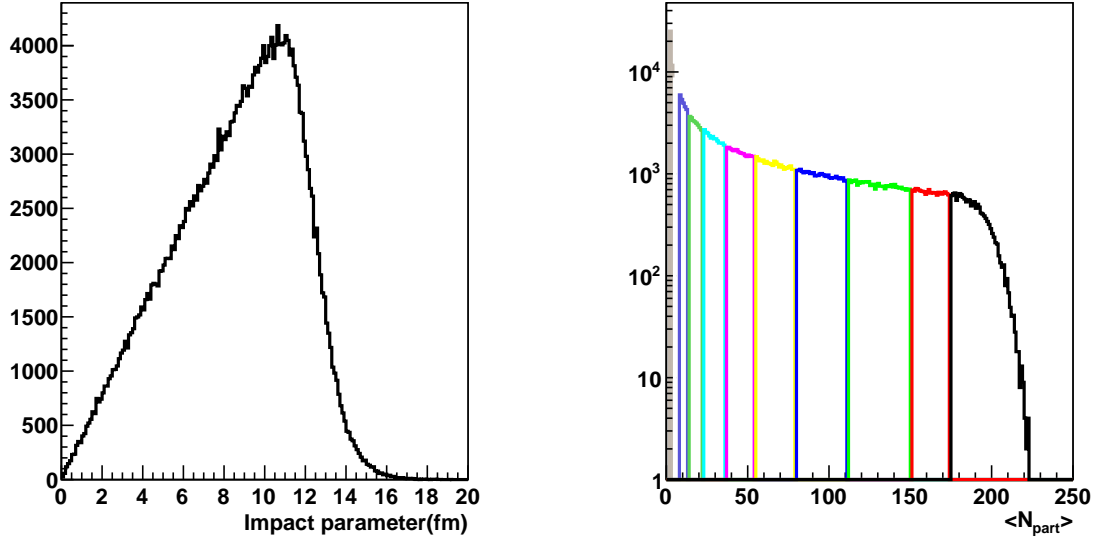


Figure 3.25: Left:Impact parameter distribution in Monte Carlo Glauber model. Right: N_{part} distribution estimated from Monte Carlo Glauber model.

participant nucleons so called the participant plane. The participant plane is determined for each harmonic

$$\Psi_{n,PP} = \frac{\tan^{-1}[\langle r^n \sin(n\phi) \rangle, \langle r^n \cos(n\phi) \rangle]}{n} + \frac{\pi}{n}. \quad (3.47)$$

Figure 3.26 shows 2nd and 3rd order eccentricities in Monte Carlo Glauber model as a function of centrality for Au+Au, Cu+Au and Cu+Cu collisions at $\sqrt{s_{NN}} = 200\text{GeV}$.

3.9 Systematic Uncertainty

3.9.1 Systematic Uncertainties at mid-rapidity v_n

Contributions to systematic uncertainties of mid-rapidity v_n are from the following sources

- Event plane
- Background contribution to v_n measurement
- East and West arm acceptance difference
- Particle identification purity

Uncertainty from Event plane determination

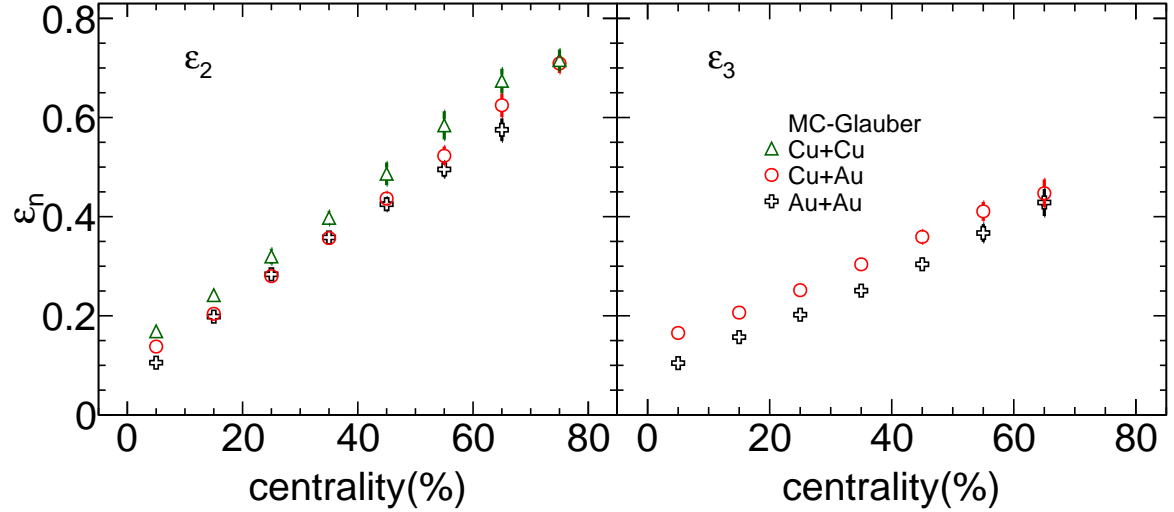


Figure 3.26: 2nd and 3rd order eccentricity ε_2 in Monte Carlo Glauber model as a function of centrality for Au+Au, Cu+Au and Cu+Cu collisions

The systematic uncertainties from the event plane measurements using the different detectors are considered not to depend on p_T . For the v_1 measurement, the uncertainties are estimated by comparing the v_1 with respect to SMD S with alternately BBC N or BBC S used for the estimation of SMDS event plane resolution. For the v_2 and v_3 measurements, the uncertainties are obtained by comparing the v_2 and v_3 measured with respect to BBC S and BBC N. Figure 3.28 and 3.29 show the v_2 and v_3 measured with respect to BBC S and BBC N separately as a function of p_T for different centrality bins.

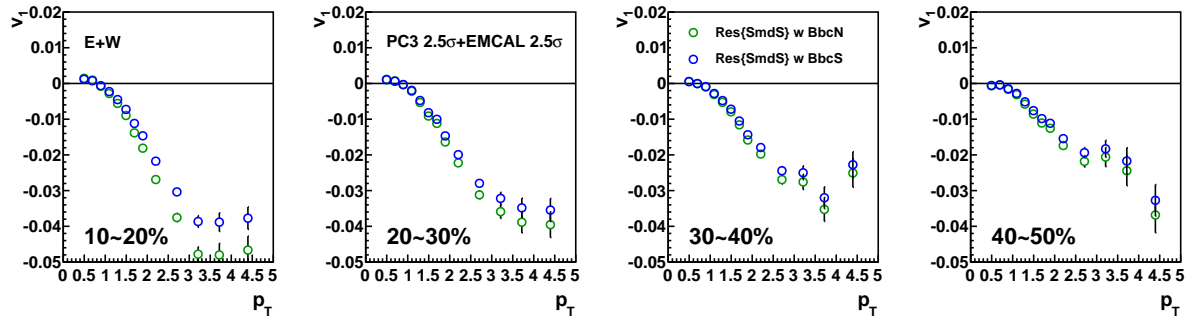


Figure 3.27: v_1 as a function of p_T with respect to SMD S for different centrality bins

The tracking selection can not remove all of background tracks which may distort the magnitude of v_n . The background is caused by γ conversion, particle decay and track mis-reconstruction. The systematic uncertainties from the background contribution is obtained by varying the different PC3 and EMCAL matching width cut. The following are the different PC3

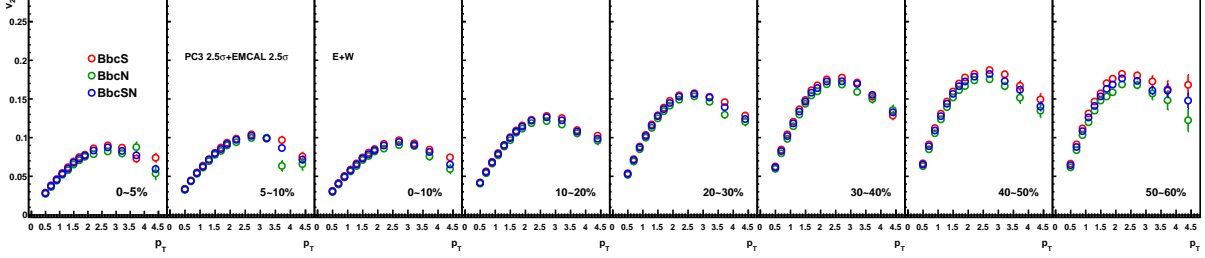


Figure 3.28: v_2 as a function of p_T with respect to BBC S, BBC N and BBC S and N combined event plane for different centrality bins

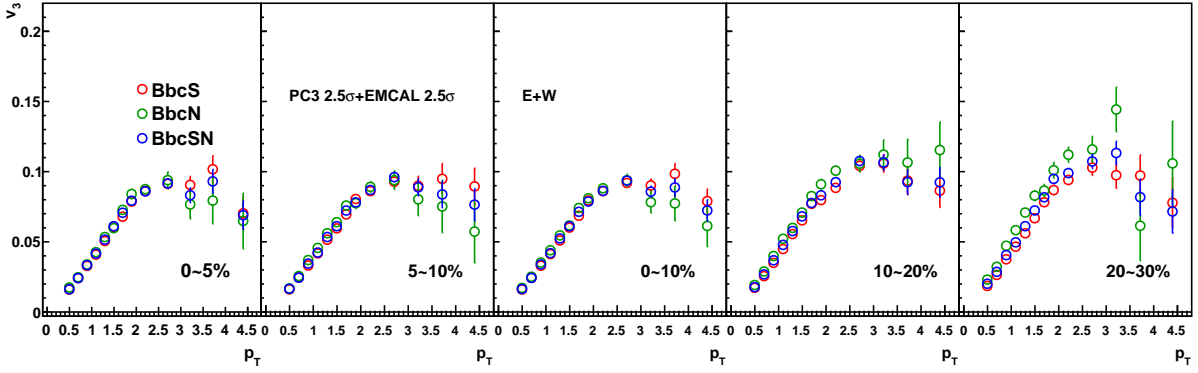


Figure 3.29: v_3 as a function of p_T with respect to BBC S, BBC N and BBC S and N combined event plane for different centrality bins

and EMCAL matching width cut.

- $|\text{pc3}| < 2.5 \sigma, |\text{emcal}| < 2 \sigma$
- $|\text{pc3}| < 2.5 \sigma, |\text{emcal}| < 3 \sigma$
- $|\text{pc3}| < 2 \sigma, |\text{emcal}| < 2.5 \sigma$
- $|\text{pc3}| < 3 \sigma, |\text{emcal}| < 2.5 \sigma$

Figure 3.30, 3.31 and 3.32 show the v_1 , v_2 and v_3 measured with the different PC3 and EMCAL matching width cut as a function of p_T for different centrality bins.

Uncertainty from East and West

Systematic uncertainties from acceptance were obtained from the measurements using East and West separately. The differences in the v_n measurements using East and West arm are caused by different alignment and performance. Figure 3.33, 3.34 and 3.35 show the v_1 , v_2 and v_3 measured with East and West separately as a function of p_T for different centrality bins.

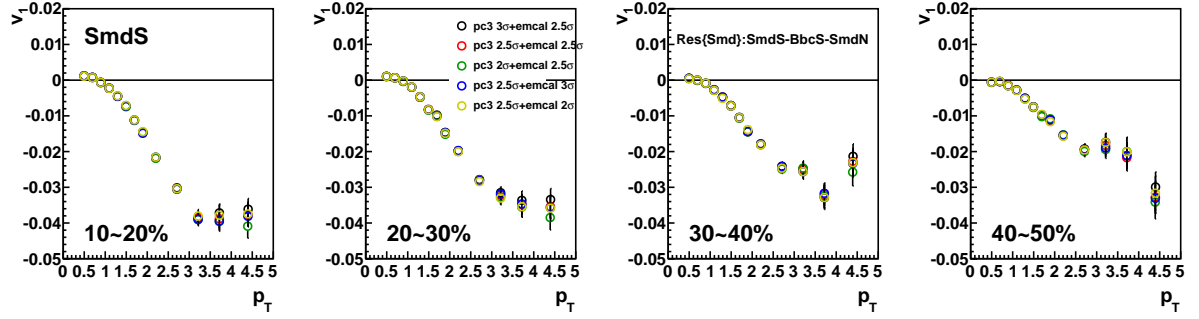


Figure 3.30: v_1 as a function of p_T with respect to SMD S for different centrality bins

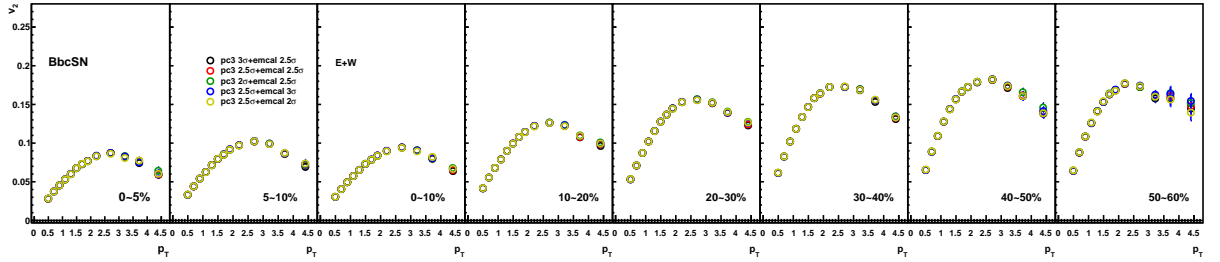


Figure 3.31: v_2 as a function of p_T with respect to BBC S and N combined event plane for different track matching cuts and centrality bins

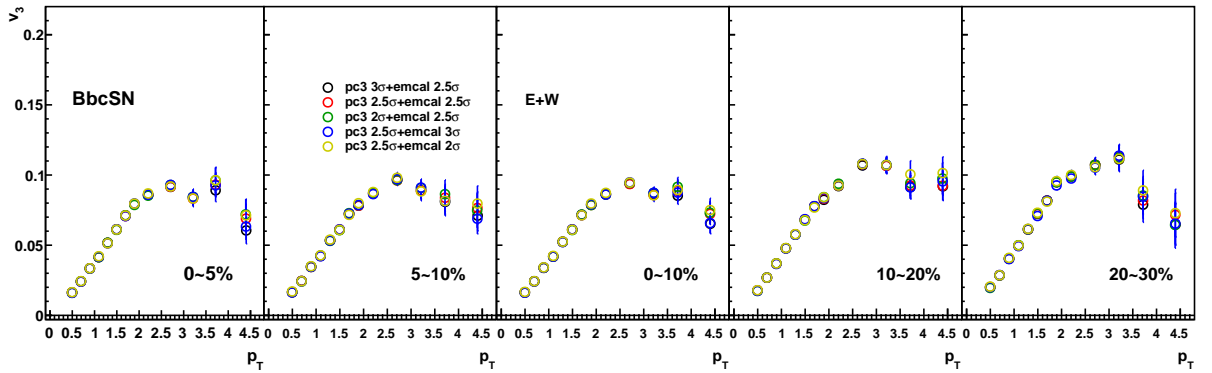


Figure 3.32: v_3 as a function of p_T with respect to BBC S and N combined event plane for different track matching cuts and centrality bins

Uncertainty from hadron misidentification

For the PID v_n measurements, an additional systematic uncertainty from the purity of particle species needs to be considered. The purity of particle species is affected by the particle mass square distribution width cut. This uncertainty is estimated from the difference among PID v_n with the different PID cuts. Veto cut is also applied to establish boundaries between particle species. The different PID cuts with the veto cut are following

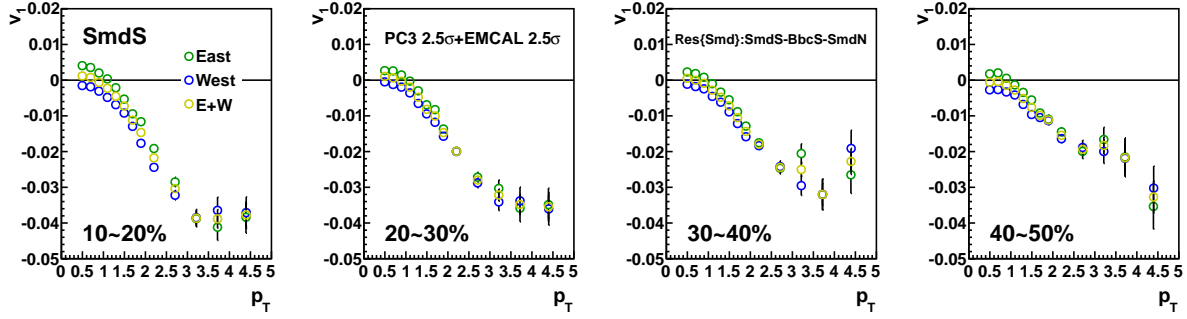


Figure 3.33: v_1 as a function of p_T with East, West and East and West combined central arms for different centrality bins

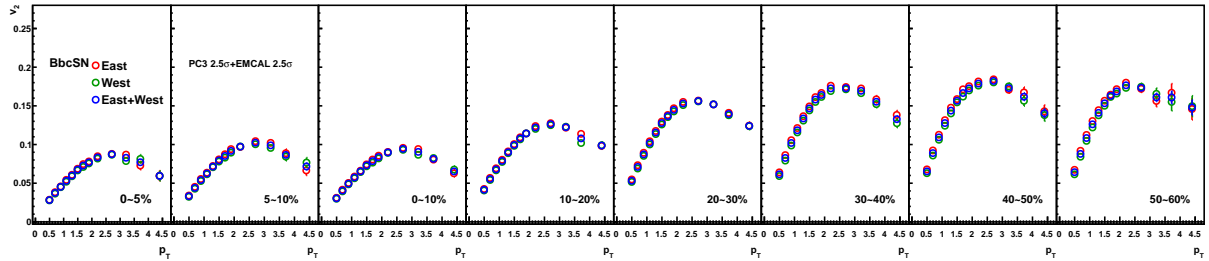


Figure 3.34: v_2 as a function of p_T with East, West and East and West combined central arms for different centrality bins

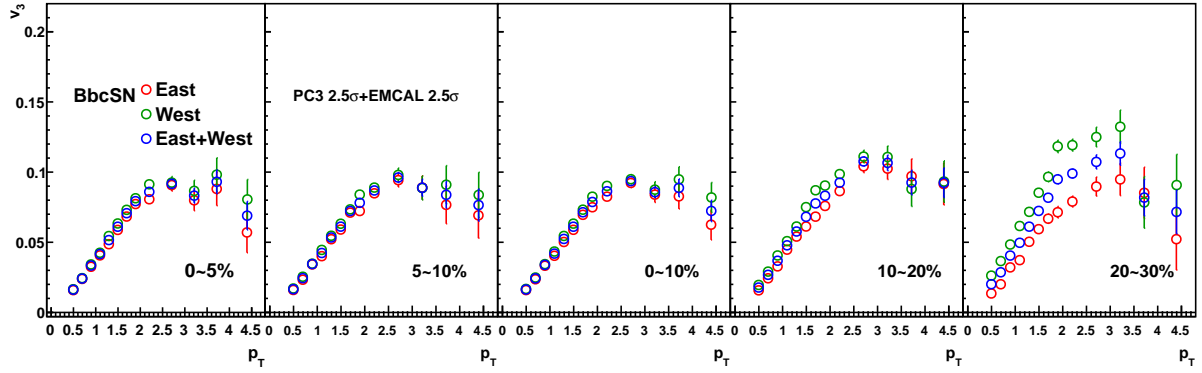


Figure 3.35: v_3 as a function of p_T with East, West and East and West combined central arms for different centrality bins

- 1.5 σ with 2 σ veto
- 2 σ with 2 σ veto
- 2.5 σ with 2 σ veto

3.9.2 Systematic Uncertainties of forward/backward v_n measurements

Sources of the systematic uncertainties of the forward/backward-rapidity v_n are following

- Event plane determination (experimental data)
- p_T spectra(simulation data)
- $dN/d\eta$ distribution (simulation data)
- p_T dependence of v_n (simulation data)
- η dependence of v_n (simulation data)

Uncertainty from Event plane determination

For the η dependence of v_2 and v_3 measurements, the uncertainties from event plane determination are included in systematic uncertainties. The systematic uncertainties from event plane measurements are obtained by comparing the v_2 and v_3 measured with respect to BbcS and BbcN in Cu+Cu and Cu+Au collisions. In Au+Au collisions, the measurements using RxnS and RxnN are also included since Rxn EP is available. Fig. 3.36 and 3.37 show the v_2 and v_3 measured with respect to Bbc, Cnt and Rxn in Au+Au collisions separately as a function of p_T for different centrality bins.

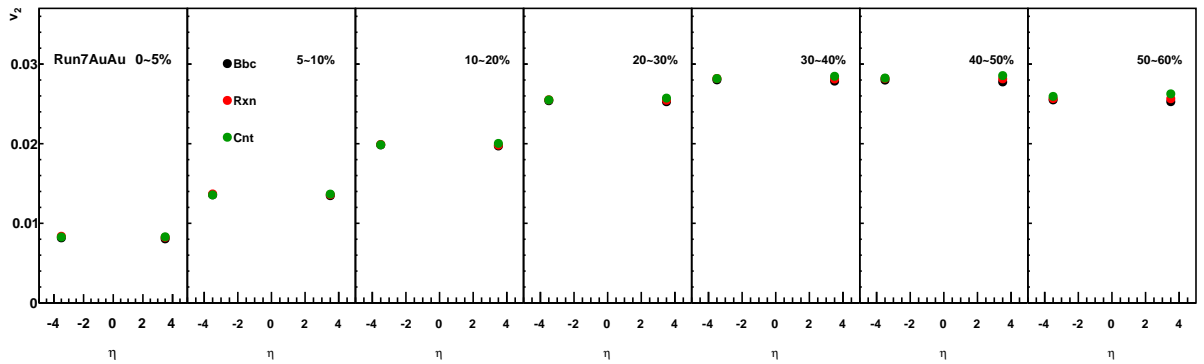


Figure 3.36: Integrated $p_T v_2$ as a function of η for different event plane selections in Au+Au collisions at $\sqrt{s_{NN}} = 200\text{GeV}$

Uncertainty from Input p_T spectra in Single particle simulation

The systematic uncertainties for p_T spectra are estimated by comparing three inverse slope parameters T of p_T spectra. The tested three inverse slope parameters T are 235, 300 and 150 MeV. The p_T spectra for π^\pm and π_0 in Au+Au 200 GeV are measured by BRAHMS experiment and parameterized using the $p_T \exp(-p_T/T)$ [36]. In the Ref. [36], the inverse slope parameters are extracted from fit to the spectra and are between 230 to 240 MeV.

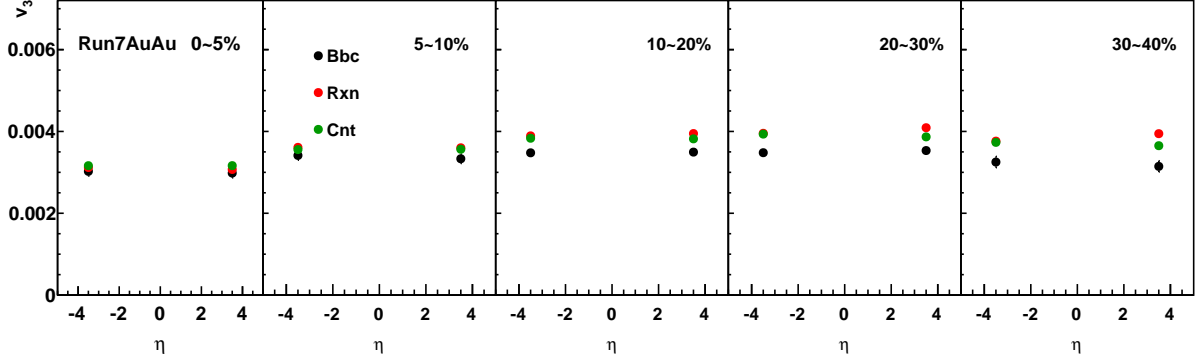


Figure 3.37: Integrated $p_T v_3$ as a function of η for different event plane selections in Au+Au collisions at $\sqrt{s_{NN}} = 200\text{GeV}$

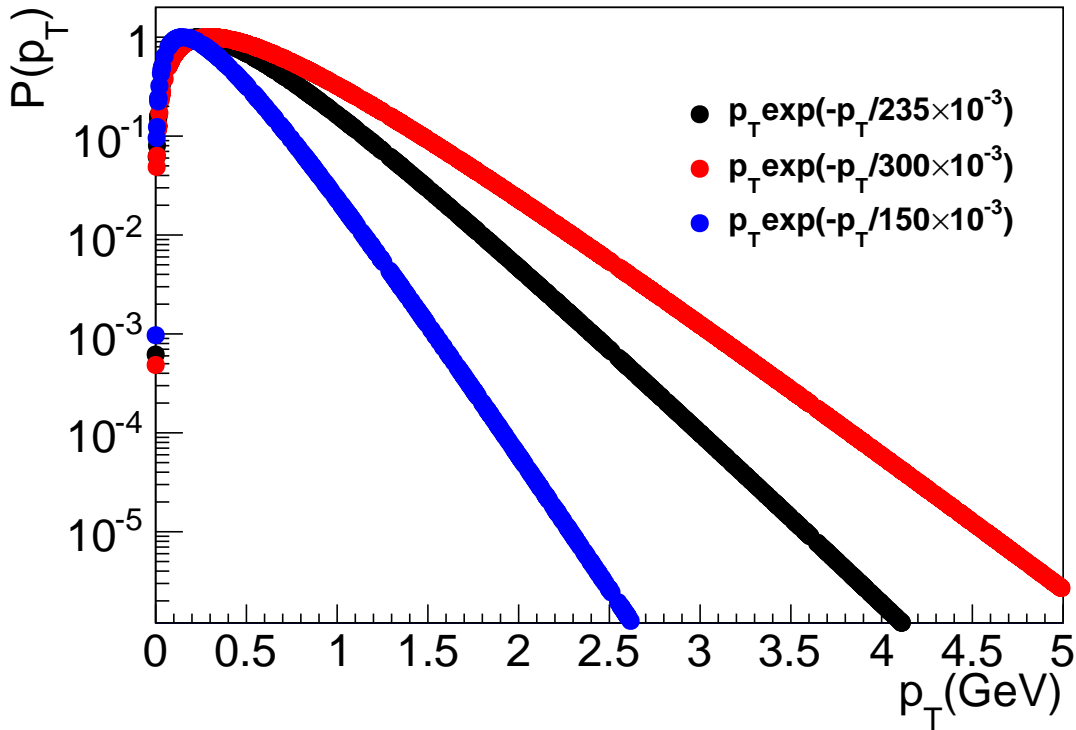


Figure 3.38: Input p_T spectra for three inverse parameters

Uncertainty from input η probability distribution in Single particle simulation

The systematic uncertainties from single particle pseudorapidity distributions are obtained by comparing two different probability distributions $P(\eta)$ shown in Fig. 3.39. The two η probability distributions are selected from most central Au+Au collision and most peripheral Cu+Cu collision [37]. The probability distributions in central collision case and peripheral collision case

are described as follows,

$$P(\eta) = \begin{cases} 0.3\eta + 1.6 & (\eta < -2) \\ 1 & (-2 \leq \eta \leq 2) \\ -0.3\eta + 1.6 & (\eta > 2) \end{cases} \quad (3.48)$$

$$P(\eta) = \begin{cases} 0.2\eta + 1.4 & (\eta < -2) \\ 1 & (-2 \leq \eta \leq 2) \\ -0.2\eta + 1.4 & (\eta > 2) \end{cases} \quad (3.49)$$

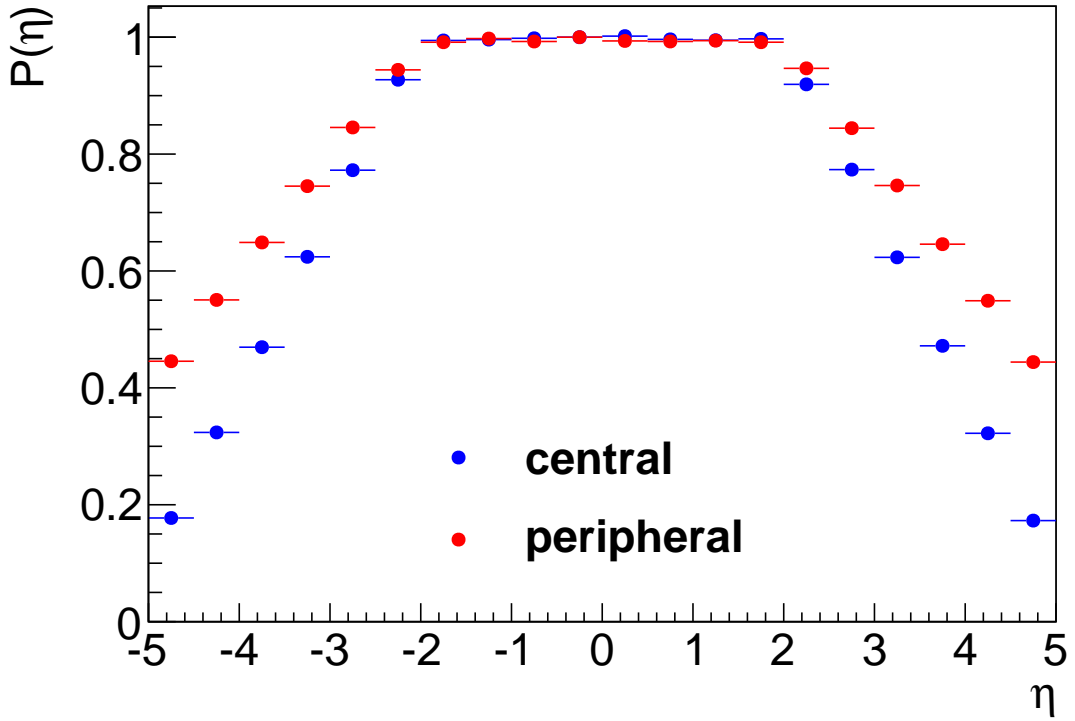


Figure 3.39: Input η probability distribution. The blue data points represent central Au+Au collisions case and the red data points corresponds to peripheral Cu+Cu collisions case.

Uncertainty from input $v_n(\eta)$ shape in Single particle simulation

The simulated shape of η dependence of v_n might influence the measured v_n . In our simulation study, four type of slope of $v_n(\eta)$ at $|\eta| > 2$ are tested. Since the PHOBOS experiment measured η dependence of v_2 in 200GeV Au+Au collisions[25], [39], the slope for central Au+Au collision(3-15%) case is used as the default setting and the slopes for and peripheral collision case(25-50%)

is included in the systematic uncertainties in our simulation. For the v_3 simulation, the same slope parameters as used in the v_2 study are used. The two input v_n are expressed using the slope parameters respectively.

$$P(v_n(\eta)) = \begin{cases} \frac{1}{6}\eta + \frac{7}{6} & (\eta < -1) \\ 1 & (-1 \leq \eta \leq 1) \\ -\frac{1}{6}\eta + \frac{7}{6} & (\eta < -1) \end{cases} \quad (3.50)$$

$$P(v_n(\eta)) = \begin{cases} \frac{1}{8}\eta + \frac{9}{8} & (\eta < -1) \\ 1 & (-1 \leq \eta \leq 1) \\ -\frac{1}{8}\eta + \frac{9}{8} & (\eta < -1) \end{cases} \quad (3.51)$$

Additionally, the asymmetric η dependence of v_n are tested and included in the systematic uncertainties because the η dependence of v_n are asymmetric distribution in heavy ion generator study. Fig. 3.40 shows the input η dependence of v_n for the four slopes. In the Fig.3.40, the type1 represents the slope for

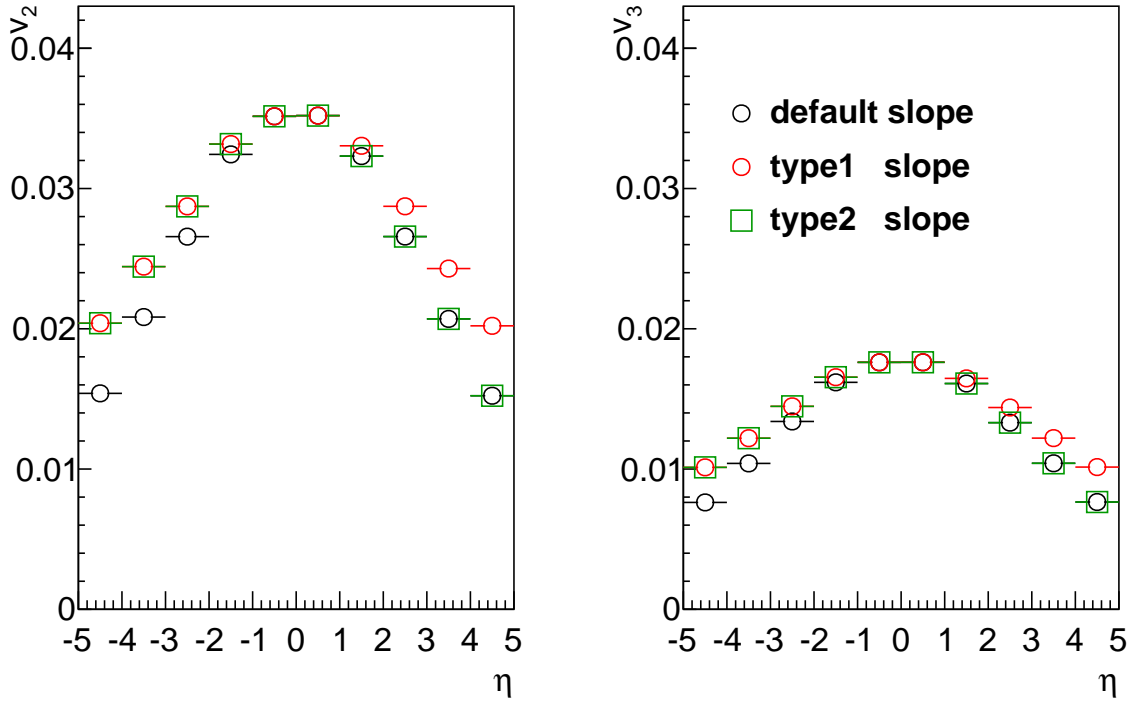


Figure 3.40: Input v_n as a function of η for four type slopes

Uncertainty from magnitude of $v_n(p_T)$

Since the magnitude of v_n widely vary with centrality class, the systematic uncertainties of the magnitude of v_n are obtained by comparing the central, mid-central and peripheral collision cases. Fig. 3.41 shows the input v_2 and v_3 as a function of p_T at mid-rapidity and forward-rapidity. In our simulation study, the p_T dependence of v_n at mid-rapidity are referred from the PHENIX v_n results [21] as the input. At forward rapidity, the maximum p_T dependence of v_n is determined by the slope of default η dependence of v_n . In the Fig. 3.41, the default setting represents mid-central collision case, the type1 corresponds to central collision case and the type2 is peripheral collision case. Fig. 3.42 shows the input η dependence of v_2 and v_3 for the default,

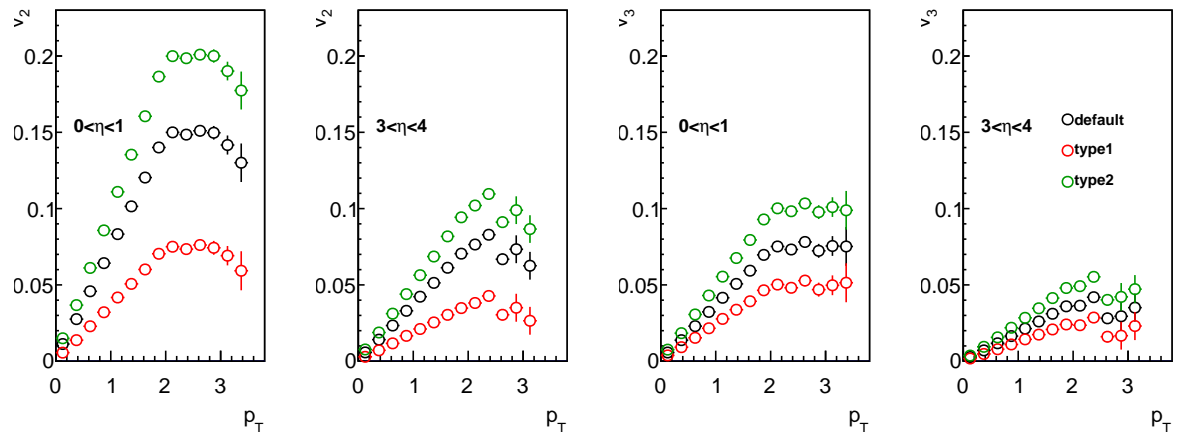
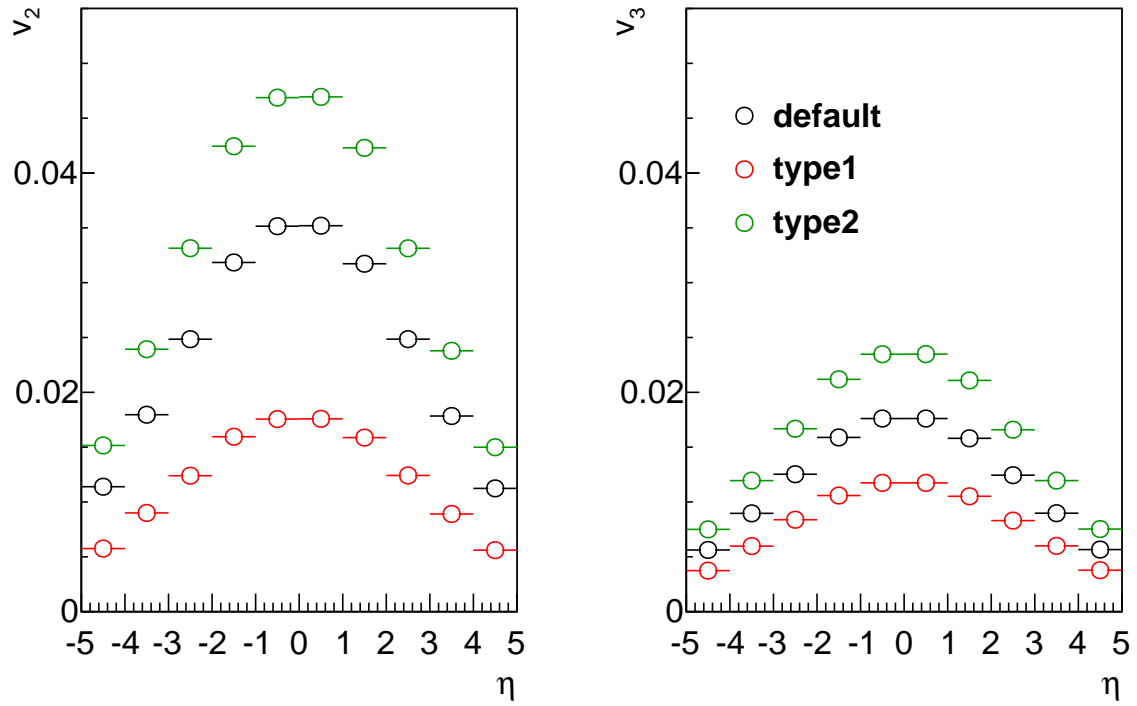
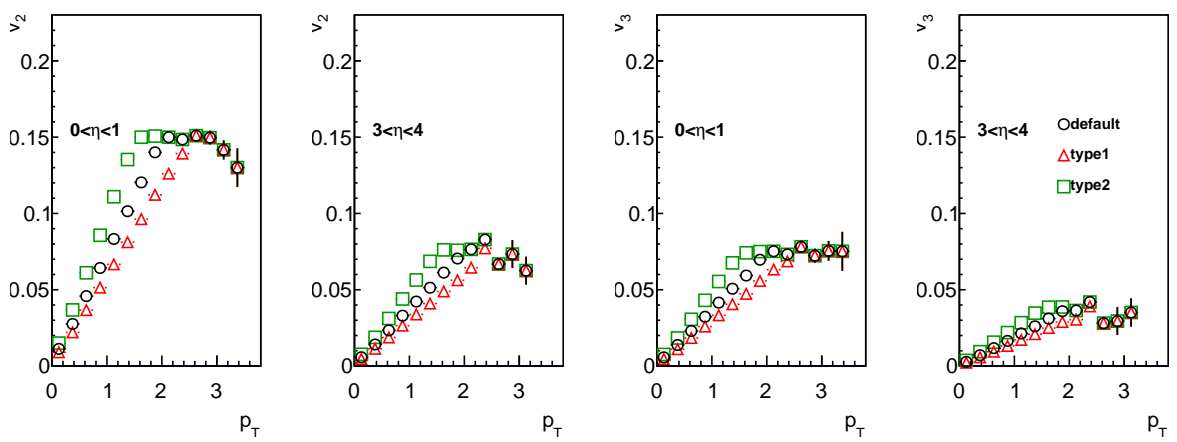


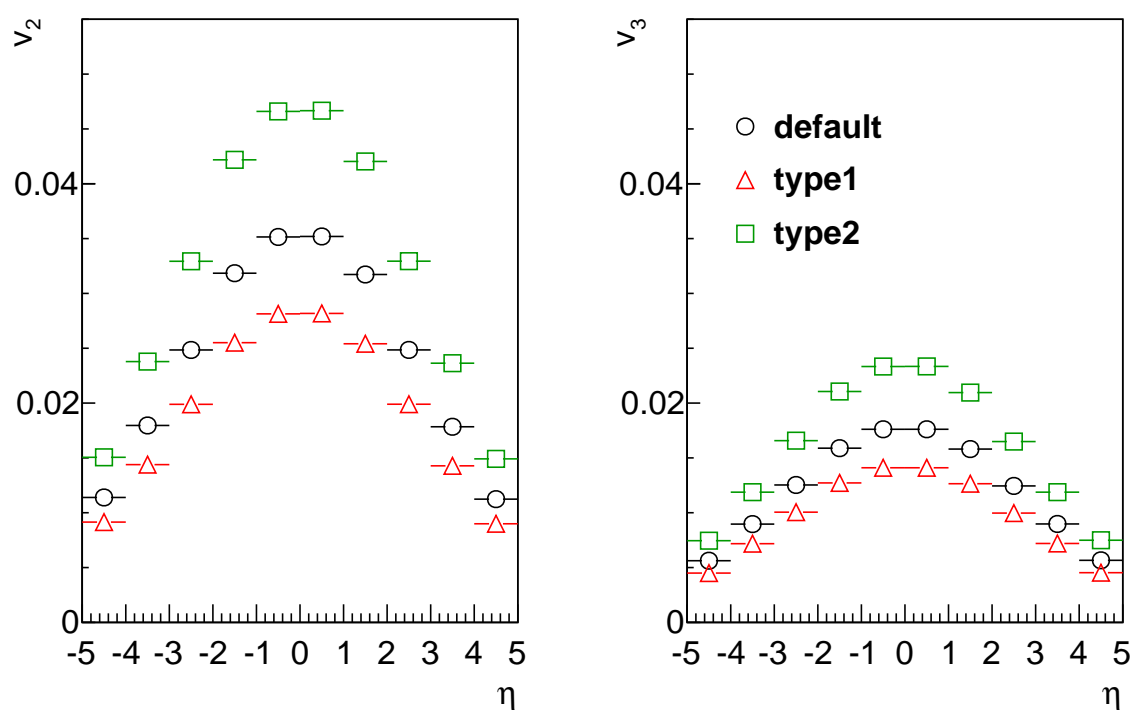
Figure 3.41: Input $v_n(\eta)$ probability distribution

type1 and type2.

Uncertainty from the shape of $v_n(p_T)$

Additionally, we studied the influence of the shape of p_T dependence of v_n . The systematic uncertainties are estimated by varying the p_T bin for the maximum value of p_T dependence of v_n . In the default setting, the p_T bin for the maximum value of v_n is 2 GeV. For the systematic study, we test 1.5 GeV and 2.5 GeV case as shown in Fig. 3.43. In the Fig. 3.43, default means the maximum value of v_n is at 2 GeV, type1 is 2.5 GeV and type2 is 1.5 GeV case. In Fig. 3.44, the input η dependence of v_n for the p_T bin cases are shown.

Figure 3.42: Input $v_n(\eta)$ probability distributionFigure 3.43: Input $v_n(\eta)$ probability distribution

Figure 3.44: Input $v_n(\eta)$ probability distribution

3.9.3 Systematic Uncertainties of forward/backward $dN_{ch}/d\eta$ measurements

Since the correction factor for charge particle multiplicity $dN/d\eta$ is obtained from the same simulation run in the v_n measurements, the systematic sources are same as the v_n measurements except for the p_T and η dependences of v_n distributions. Sources of the systematic uncertainties of the forward/backward $dN_{ch}/d\eta$ measurements are following,

- p_T spectra (simulation data)
- $dN/d\eta$ distribution (simulation data)

For the systematic uncertainty from the different p_T spectra, the input p_T spectra is shown in 3.38. As described in the previous section, the probability function for the p_T distribution is given by the $p_T * \exp(-p_T/T)$. The single particle is generated according to that function with the three inverse slope parameters T 235, 300 and 150 MeV.

The systematic uncertainty for $dN/d\eta$ distribution is also same as the v_n measurements. The input $dN/d\eta$ is shown in Fig. 3.39.

3.9.4 Summary of systematic uncertainties

Here are the tables for systematic uncertainties of the mid-rapidity and the forward/backward-rapidity v_n and the forward/backward-rapidity $dN/d\eta$.

Table 3.3: Systematic uncertainties in the v_1 measurements at mid rapidity

Centrality class	Event-plane	Background (absolute value)	Acceptance (absolute value)
10%-20%	24%	4×10^{-5}	3×10^{-3}
20%-30%	12%	5×10^{-5}	2×10^{-3}
30%-40%	10%	6×10^{-5}	2×10^{-3}
40%-50%	13%	6×10^{-5}	2×10^{-3}

Table 3.4: Systematic uncertainties given in percent on the v_2 measurements at mid rapidity

Centrality class	Event-plane	Background	Acceptance
0%–5%	3%	$3 \times 10^{-1}\%$	2%
5%–10%	2%	$2 \times 10^{-1}\%$	2%
0%–10%	2%	$2 \times 10^{-1}\%$	2%
10%–20%	1%	$1 \times 10^{-1}\%$	2%
20%–30%	1%	$1 \times 10^{-1}\%$	2%
30%–40%	2%	$2 \times 10^{-1}\%$	3%
40%–50%	2%	$2 \times 10^{-1}\%$	3%
50%–60%	4%	$4 \times 10^{-1}\%$	3%

Table 3.5: Systematic uncertainties given in percent on the v_3 measurements at mid rapidity

Centrality class	Event-plane	Background	Acceptance
0%–5%	1%	1%	3%
5%–10%	3%	1%	3%
0%–10%	2%	1%	3%
10%–20%	4%	1%	8%
20%–30%	7%	1%	22%

Table 3.6: Systematic uncertainties in the measured v_1 for identified particles at mid rapidity

species	$p_T \leq 2 \text{ GeV}/c$	$p_T \geq 2 \text{ GeV}/c$
pion (absolute value)	1×10^{-3}	2×10^{-3}
kaon (absolute value)	1×10^{-3}	3×10^{-3}
proton (absolute value)	1×10^{-3}	3×10^{-3}

Table 3.7: Systematic uncertainties in percent on the measured v_2 and v_3 for identified particles at mid rapidity

species	$p_T \leq 2 \text{ GeV}/c$	$p_T \geq 2 \text{ GeV}/c$
pion	3%	5%
kaon	3%	10%
proton	3%	5%

Table 3.8: Event Plane systematic uncertainties given in percent on the v_2 measurements at forward/backward rapidity.

South/North	Au+Au	Cu+Au	Cu+Cu
0%–5%			
South	1%	$4 \times 10^{-1}\%$	1%
North	2%	$4 \times 10^{-1}\%$	3%
5%–10%			
South	1%	2%	$3 \times 10^{-1}\%$
North	1%	1%	2%
10%–20%			
South	$2 \times 10^{-1}\%$	2%	$1 \times 10^{-1}\%$
North	1%	1%	2%
20%–30%			
South	$3 \times 10^{-1}\%$	2%	1%
North	1%	1%	$5 \times 10^{-1}\%$
30%–40%			
South	$4 \times 10^{-1}\%$	2%	$1 \times 10^{-1}\%$
North	2%	1%	$1 \times 10^{-1}\%$
40%–50%			
South	1%	2%	$2 \times 10^{-1}\%$
North	2%	2%	$2 \times 10^{-1}\%$
50%–60%			
South	1%	1%	2%
North	3%	3%	$4 \times 10^{-1}\%$

Table 3.9: Event Plane systematic uncertainties given in percent on the v_3 measurements at forward/backward rapidity.

South/North	Au+Au	Cu+Au
0%–5%		
South	3%	$5 \times 10^{-1}\%$
North	5%	1%
5%–10%		
South	3%	$1 \times 10^{-1}\%$
North	5%	1%
10%–20%		
South	7%	1%
North	6%	$1 \times 10^{-1}\%$
20%–30%		
South	8%	4%
North	7%	3%

Table 3.10: Correction factors and Systematic uncertainties given in percent on the simulated v_n ($n=2,3$) at forward/backward rapidity

South/North	Correction factor	Systematic uncertainty
v_2		
South	74%	4%
North	74%	3%
v_3		
South	67%	4%
North	66%	4%

Table 3.11: Correction factors and Systematic uncertainties given in percent on the simulated $dN_{ch}/d\eta$ at forward/backward rapidity

South/North	Correction factor	Systematic uncertainty
$dN_{ch}/d\eta$		
South	49%	7.4%
North	49%	7.6%

Chapter 4

Results

4.1 Charged hadron v_n at mid-rapidity

The final result of charged hadron v_n at mid-rapidity in Cu+Au $\sqrt{s_{NN}} = 200$ GeV with event plane technique is obtained. The charged hadron v_n as a function of p_T in different centrality classes are shown in Fig. 4.1, 4.2 and 4.3. The red solid symbols represent the v_n data and the shaded boxes are the systematic uncertainties. In Fig. 4.1, the v_1 measurements are shown. The v_1 measurements are performed with respect to the Ψ_1 event plane determined by the Au spectator neutrons. Since spectator neutrons going positive rapidity region have been used as reference axis for v_1 measurements in previous conventions. To align with the previous conventions, the sign of v_1 is flipped so that effectively the v_1 is measured with respect to the first order event plane determined by spectator neutrons from the Cu nucleus. In all centrality classes, the absolute values of v_1 are consistent with zero within the systematic uncertainties below $p_T = 1$ GeV/c and increases with p_T . The negative values of v_1 at high p_T region indicate the high p_T particles at mid-rapidity are emitted towards Cu hemisphere side. Although in low p_T regions, the more particles are expected to move towards the opposite direction of high p_T particles emission due to the momentum conservation effect, the values of v_1 at low p_T region can not be distinguished whether the signals are positive values or negative values beyond the large systematic uncertainties. From the central to the peripheral collisions, the absolute value decrease since the participant zone become the symmetric shape in peripheral collisions.

For the v_2 and v_3 measurements shown in Fig. 4.2 and 4.3, the v_2 and v_3 values are positive and increase with p_T for all centrality classes. The v_2 show strong centrality dependence where the values increase from the most central 0-10 % and the mid-central 30-40 % centrality classes. This trend is considered to be originated from the initial spatial ellipticity of participant nucleons ε_2 because the initial spatial ellipticity shown in Fig. 3.26 increases in the peripheral collisions. Unlike the v_2 measurements, the v_3 components show weak centrality dependence as seen in those in symmetric collisions. In the symmetric collisions, the triangular flow is driven by the event by event initial spatial fluctuation of participant nucleons. In Cu+Au collisions, the event by event spatial fluctuation are also the origin of the triangular flow.

In all three Fourier harmonics, the values of these coefficients increase with p_T up to about 3 GeV/c. Except for the v_1 measurements, the signal decrease with p_T above around 3 GeV/c.

This trend might indicate a change of particle production mechanism for example high p_T particle emission with fewer interactions. It is interesting to look system size dependence of the charged

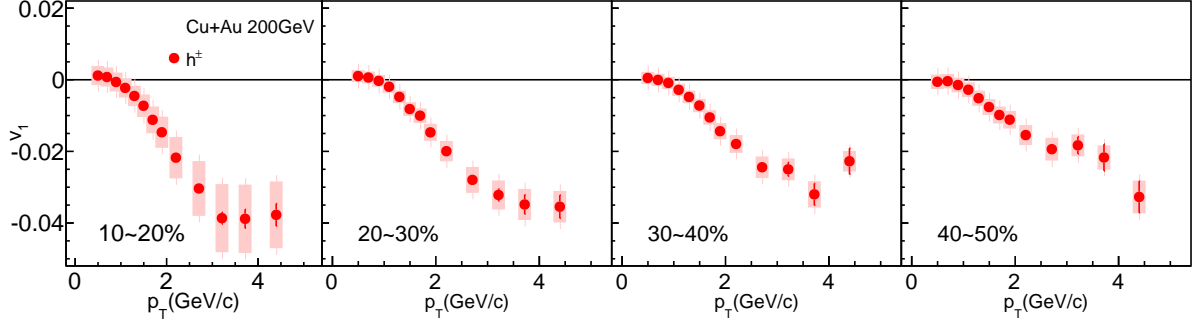


Figure 4.1: Charged hadron v_1 at mid-rapidity ($|\eta| < 0.35$) as a function of p_T in Cu+Au collisions

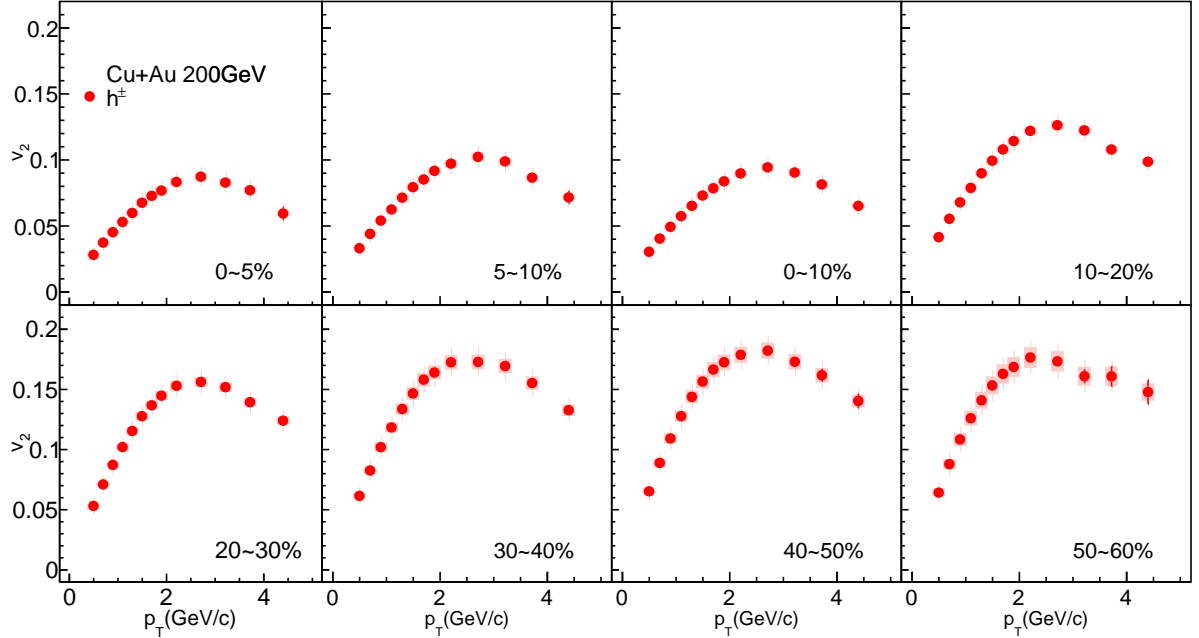


Figure 4.2: Charged hadron v_2 at mid-rapidity ($|\eta| < 0.35$) as a function of p_T in Cu+Au collisions

hadron v_n at the same center of mass energy measured by the PHENIX Collaboration. In early study, the PHENIX experiment has measured azimuthal anisotropic flow in Au+Au and Cu+Cu collisions at $\sqrt{s_{NN}} = 200\text{GeV}$. By comparing v_n in different collision systems and centralities, one can study the influence of the initial spatial anisotropy on the measured azimuthal anisotropy.

Fig. 4.4 shows the v_2 values as a function of p_T in Au+Au, Cu+Au and Cu+Cu collisions for different centrality classes. In each centrality class, we observe the v_2 coefficients in Cu+Au are

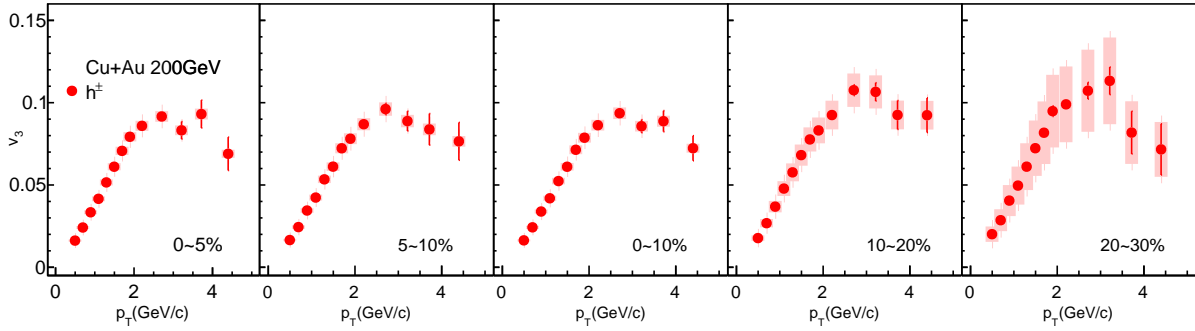


Figure 4.3: Charged hadron v_3 at mid-rapidity ($|\eta| < 0.35$) as a function of p_T in Cu+Au collisions

between those in Cu+Cu and Au+Au collisions. Except for central 0 to 10% class, the observed v_2 values are not ordered according to the magnitude of initial ellipticity in different systems obtained in Monte Carlo Glauber model shown in the left side of Fig. 3.26. In Fig. 4.5, the charged hadron v_3 coefficients as a function of p_T in Au+Au and Cu+Au collisions for three different centrality classes are compared. Since the measurements of v_3 in Cu+Cu collisions have not been performed, the data points of v_3 measurements in Cu+Cu collisions are not shown. Unlike the v_2 coefficients, the v_3 in Cu+Au collisions shows larger values than Au+Au collisions. This ordering of the v_3 values are same as the initial triangularities shown in the right side of Fig. 3.26. Although the $v_n(p_T)$ values in the different collision systems are compared at same centrality bins, it is difficult to conclude that the difference of the $v_n(p_T)$ values among the collision systems is caused by the initial geometry. Because at each centrality class, the number of participants N_{part} or the number of produced particles $dN/d\eta$ which are related to v_n values depend on collision systems.

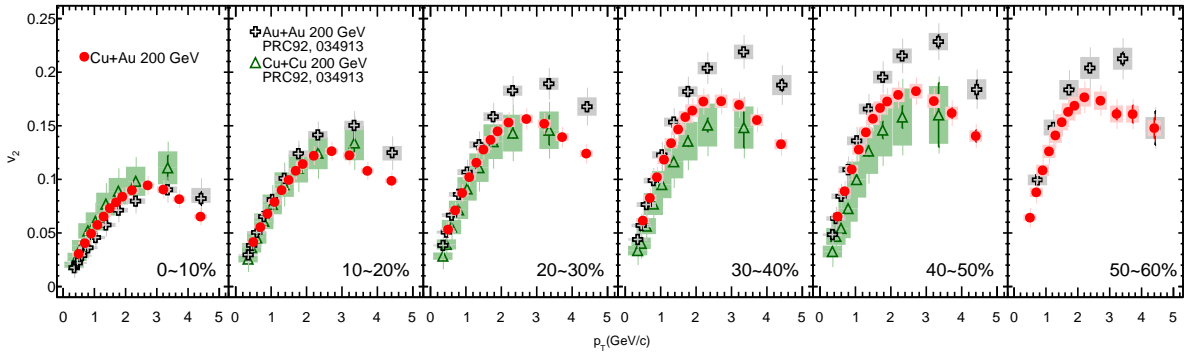


Figure 4.4: Charged hadron v_2 at mid-rapidity ($|\eta| < 0.35$) as a function of p_T in Au+Au, Cu+Au and Cu+Cu collisions for different centrality classes

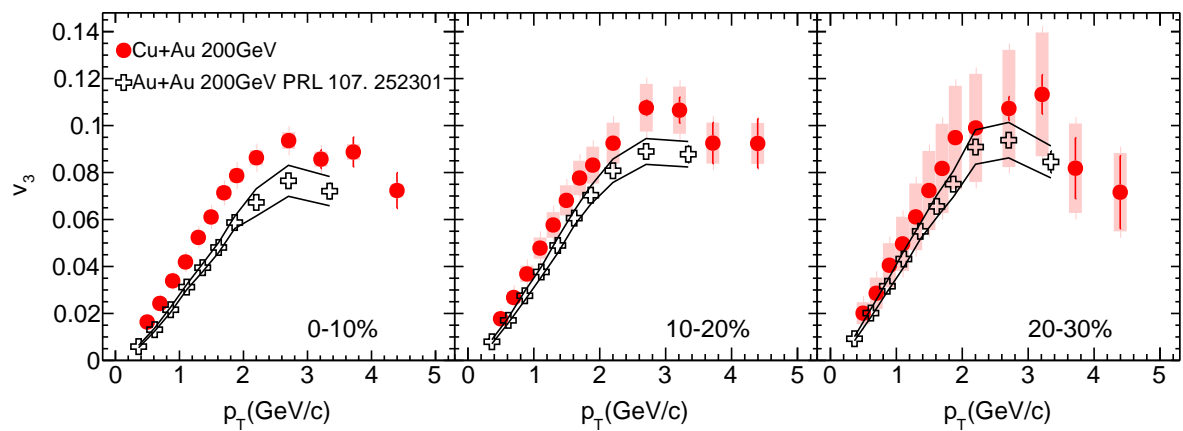


Figure 4.5: Charged hadron v_3 at mid-rapidity ($|\eta| < 0.35$) as a function of p_T in Au+Au and Cu+Au collisions for different centrality classes

For studying the effect of initial geometry on v_n coefficients by comparing different collision systems, the measurements of p_T integrated v_n as a function of N_{part} or $dN/d\eta$ are commonly used because the difference of $\langle v_n \rangle$ values among the collision systems at a given N_{part} or $dN/d\eta$ bin is considered to be caused by the initial geometry. p_T integrated v_n is calculated

$$\langle v_n \rangle = \frac{\int dp_T dN/dp_T v_n(p_T)}{\int dp_T dN/dp_T} = \frac{\sum_i dN_i/dp_T v_{n,i}(p_T)}{\sum_i dN_i/dp_T}, \quad (4.1)$$

where dN/dp_T is the transverse momentum distribution, and $v_n(p_T)$ is the v_n as a function of p_T . They are obtained by fitting functions to the experimental data. At low p_T region where there are no experimental data points, dN/dp_T and v_n are estimated by extrapolating the fitting results. In our $\langle v_n \rangle$ measurements, we integrate p_T from 0 to 3 GeV/c.

Fig. 4.6 and 4.7 show v_n with 3_{rd} polynomial functions as a function of p_T in Au+Au, Cu+Au and Cu+Cu collisions. The v_n in the three collision systems are parameterized by the fitting functions.

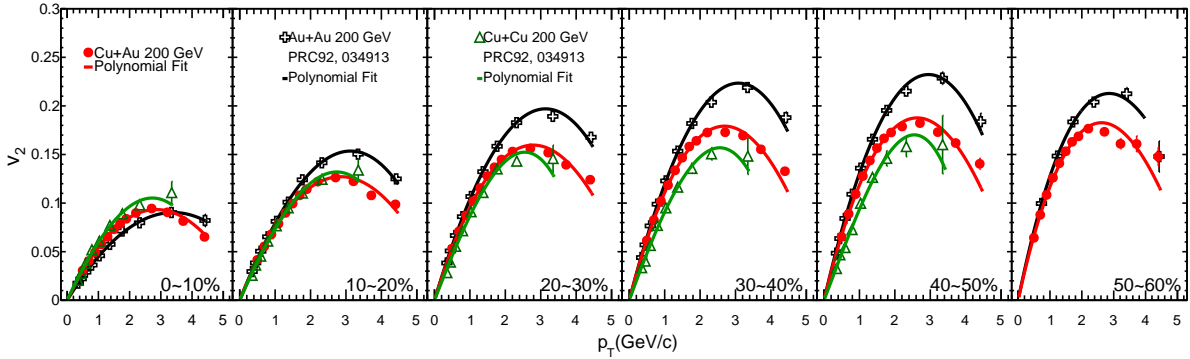


Figure 4.6: Charged hadron v_2 with polynomial fitting functions at mid rapidity in Au+Au, Cu+Au and Cu+Cu collisions

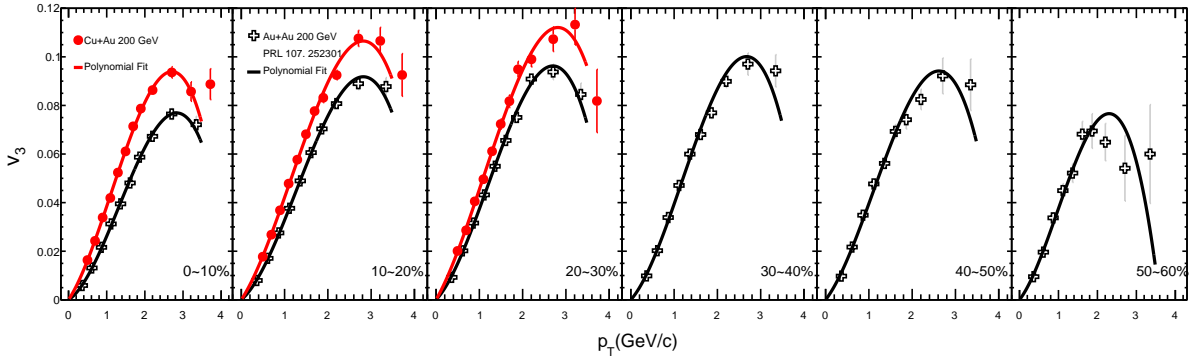


Figure 4.7: Charged hadron v_3 with polynomial fitting functions at mid rapidity in Au+Au and Cu+Au collisions

In Fig. 4.8, the transverse distribution at mid rapidity in Au+Au collisions measured by

PHENIX[16] is shown. To parameterize these p_T spectra, the following function is used,

$$f(p_T) = A \frac{p_0}{p_0 + p_T}^n \quad (4.2)$$

where A , p_0 and n are free parameters. These parameters are obtained by fitting procedure. Since PHENIX have not measured p_T spectra in Cu+Au and Cu+Cu collisions, we estimate p_T

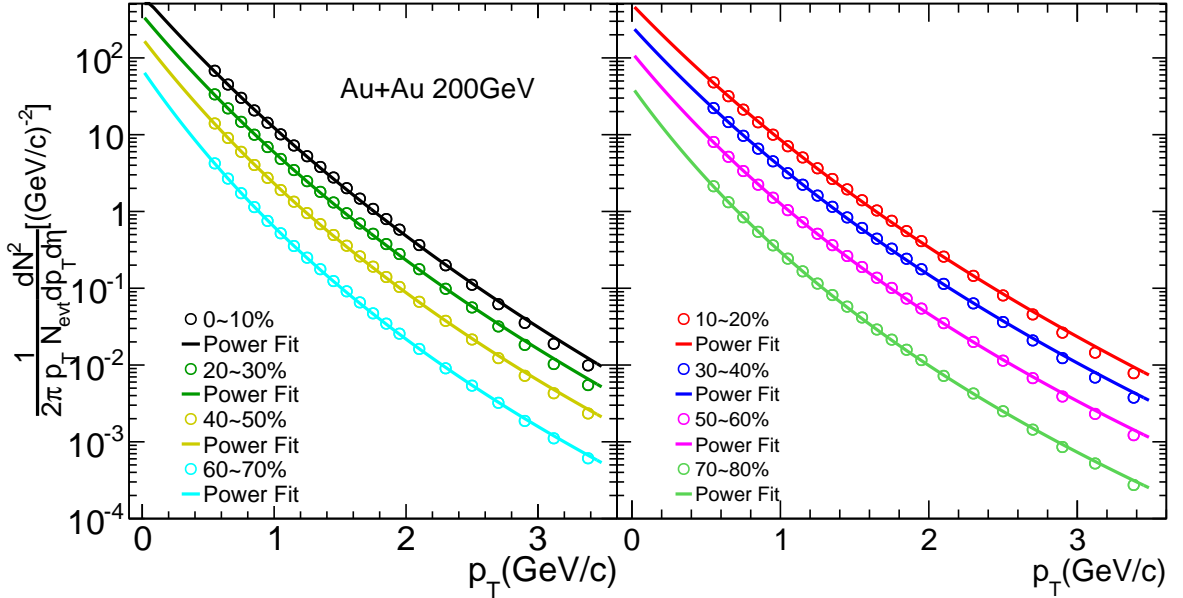


Figure 4.8: Charged hadron p_T spectra at mid rapidity in Au+Au collisions [16]

distributions for Cu+Cu and Cu+Au collisions using the fitting results of Au+Au p_T spectra based on the fact that $dN/d\eta$ and $\langle p_T \rangle$ do not depend on collision system but N_{part} [47],[18]. Fig. 4.9 shows the free parameters as a function of N_{part} for Au+Au p_T spectra obtained by the fitting results in Fig. 4.8. In Fig. 4.9, we fit A , p_0 and n with polynomial functions to extract their values at corresponding N_{part} for Cu+Au and Cu+Cu collisions. Then we make the p_T distributions for Cu+Cu and Cu+Au.

$$f(p_T, \text{Cu} + \text{Cu}) = A(N_{\text{part,Cu+Cu}}) \left(\frac{p_0(N_{\text{part,Cu+Cu}})}{p_0(N_{\text{part,Cu+Cu}}) + p_T} \right)^{n(N_{\text{part,Cu+Cu}})} \quad (4.3)$$

$$f(p_T, \text{Au} + \text{Au}) = A(N_{\text{part,Au+Au}}) \left(\frac{p_0(N_{\text{part,Au+Au}})}{p_0(N_{\text{part,Au+Au}}) + p_T} \right)^{n(N_{\text{part,Au+Au}})} \quad (4.4)$$

Figure 4.10 shows the p_T integrated v_2 ($0 < p_T < 3 \text{ GeV}$) as a function of N_{part} in Au+Au, Cu+Au and Cu+Cu collisions. Since the data points of v_2 in Au+Au and Cu+Cu measured by the PHOBOS ($|\eta| < 1, p_T > 0 \text{ GeV}$) are available, the our data points of v_2 are compared to PHOBOS's results. In all collision systems, the p_T integrated v_2 increase from the central to the peripheral collisions. Although p_T and η ranges are different between PHENIX and PHOBOS, the p_T integrated v_2 from the two experiments are good agreement within the systematic uncertainties.

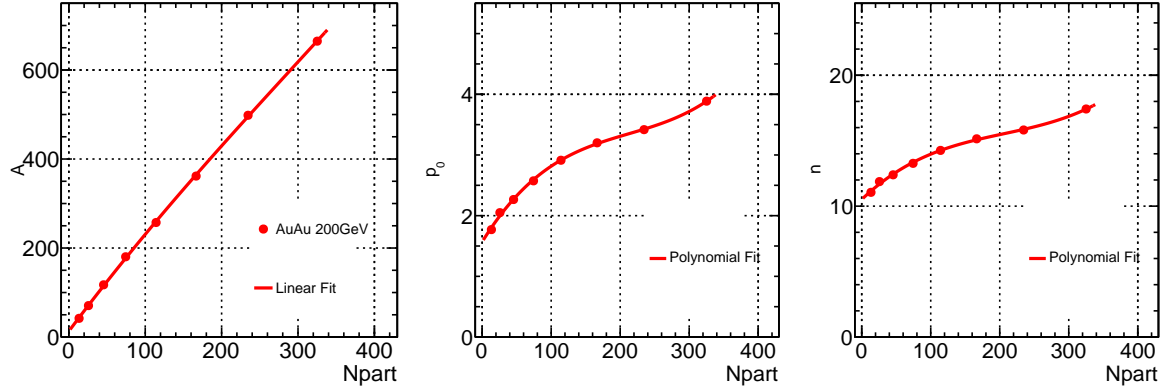


Figure 4.9: Parameters A , p_0 and n of fitting function $f(p_T) = A \frac{p_0}{p_0 + p_T}^n$ for charged hadron p_T spectra at mid rapidity in Au+Au collisions [16]

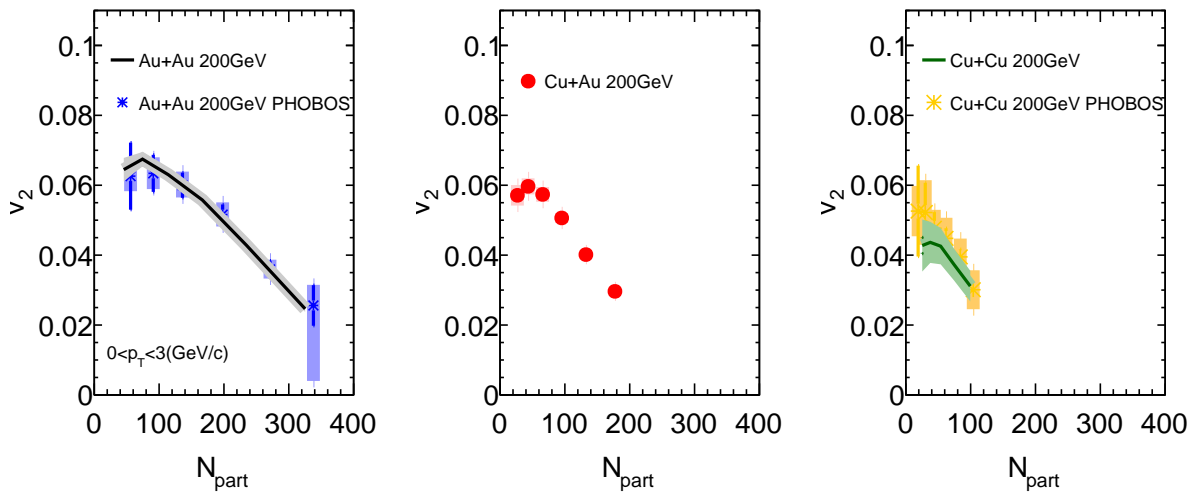


Figure 4.10: p_T integrated v_2 ($0 < p_T < 3 \text{ GeV/c}$) at mid rapidity Au+Au, Cu+Cu and Cu+Au collisions

4.2 π^\pm, K^\pm, p and \bar{p} v_n results

Figure 4.11, 4.12 and 4.13 show the final results of particle species dependence of v_n at mid-rapidity in Cu+Au $\sqrt{s_{NN}}=200$ GeV collisions. The results presented in the Fig.s are charge combined π^\pm, K^\pm, p and \bar{p} . The red solid circles represent π^\pm , the open squares represent K^\pm and the open cross symbols represent p and \bar{p} . The shaded boxes are the systematic uncertainties from the hadron misidentification based on the PID purity. In the systematic uncertainties, the other systematic uncertainties such as the event plane determination and the acceptance difference are not shown since these uncertainties are common for π^\pm, K^\pm, p and p^\pm . To improve the statistical uncertainties for the v_1 and v_3 , we have merged centrality classes into a single centrality class. For the v_2 and v_3 measurements, there are two trend. In low p_T region, the v_n for the lightest hadron is the largest and those for the heaviest hadron is the smallest. Hydrodynamical theory predict same mass dependence in low p_T caused by radial flow effect that makes all particles move in the same velocity. Above mid- p_T region, this particle mass trend is reversed, such that the anisotropy for baryons is larger than that for mesons. This baryon and meson dependence at the high p_T , namely valence quark number dependence, is associated with the partonic flow at the QGP phase and subsequent hadronization by quark coalescence. These two trends for PID v_n measurements have been seen in the symmetric collision systems at RHIC and LHC. However the PID v_1 measurements show mass ordering at the mid p_T region and do not show baryon and meson splitting at the high p_T . Although the values of PID v_1 are positive at the low p_T region, if the full systematic uncertainty is taken into account, the sign of the bulk directed flow can not be concluded.

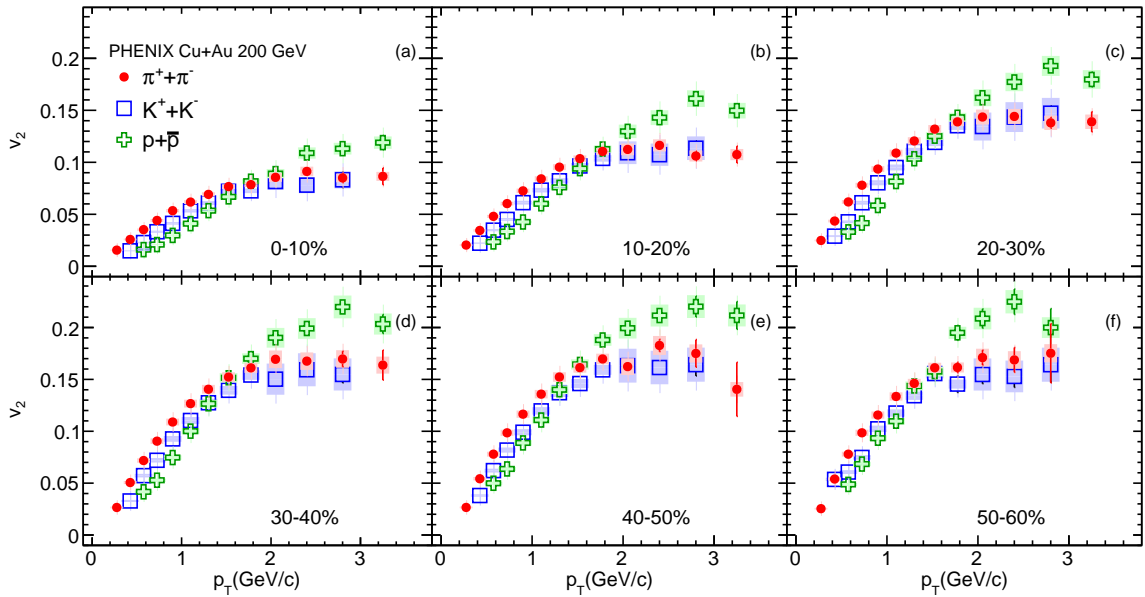


Figure 4.11: PID v_2 as a function of p_T in Cu+Au collisions

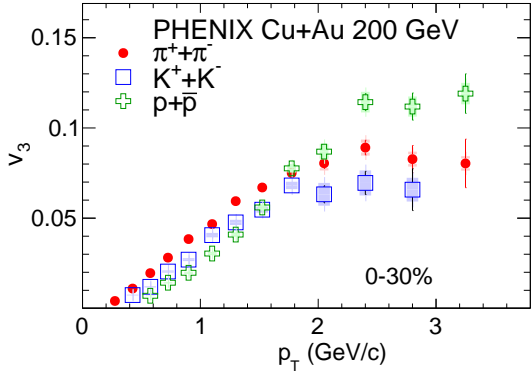


Figure 4.12: PID v_3 as a function of p_T in Cu+Au collisions for different centrality bins

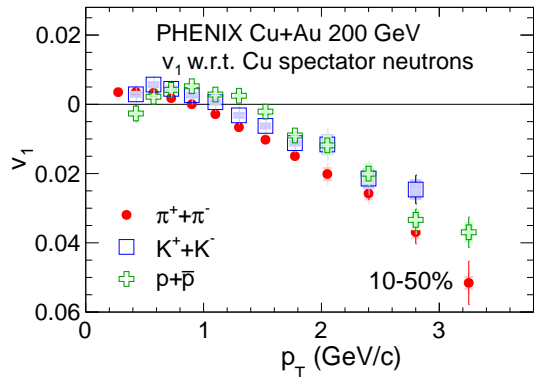


Figure 4.13: PID v_1 as a function of p_T in Cu+Au collisions

4.3 Charged hadron v_n at forward/backward rapidity

The measurements of the η dependence of v_2 in Au+Au and Cu+Cu collisions are compared to the PHOBOS Au+Au and Cu+Cu collisions [25, 38, 39] in Fig. 4.14 and 4.15. The v_2 shown in Fig. 4.14 and 4.15 are corrected with the correction factors R_n estimated by the full Geant based Monte Carlo simulation described in the previous analysis section. The v_2 measurements in Au+Au and Cu+Cu collisions show the highest values at mid-rapidity and the lower values at forward/backward-rapidity. The PHENIX results for Au+Au and Cu+Cu collisions corresponds to the open cross and the open triangle. and the PHOBOS results are the open circles. Good agreements between the PHENIX results and the PHOBOS results are seen at the three rapidity regions for Au+Au and Cu+Cu collisions, which indicate the correction factor R is estimated correctly.

The final results of v_2 and v_3 at forward/backward-rapidity in Cu+Au collisions at $\sqrt{s_{NN}} = 200$ GeV are obtained. The results presented in Fig. 4.16 and 4.18 are the v_2 and v_3 as a function of η in Au+Au, Cu+Au and Cu+Cu collisions at $\sqrt{s_{NN}} = 200$ GeV. Both of the v_2 and v_3 measurements are corrected for background effect. Since the v_3 measurements in Cu+Cu collisions have not been performed, the data points in Cu+Cu collisions are not shown. The solid symbols represent the data points and the shaded boxes are the systematic uncertainties. The dashed straight lines are drawn to look the slope between the data points. In all collision systems, the values of v_2 at forward/backward-rapidity are smaller than those at mid-rapidity. In symmetric Au+Au and Cu+Cu collisions, the η dependence of v_n is η symmetric distribution. On the other hand, a difference of the v_2 values in Au-going side (negative η side) and Cu-going side (positive η side) is seen in mid-central collision classes. The v_2 measurements at forward/backward-rapidity in all collision systems have the centrality dependence as seen at mid-rapidity. From central to peripheral, the value of v_2 increases in all collision systems. The forward/backward asymmetry of v_2 in Cu+Au collisions becomes small in the most central and the peripheral collision class.

In the left side of Fig. 4.17, the v_2 at forward/backward rapidity as a function of N_{part} in

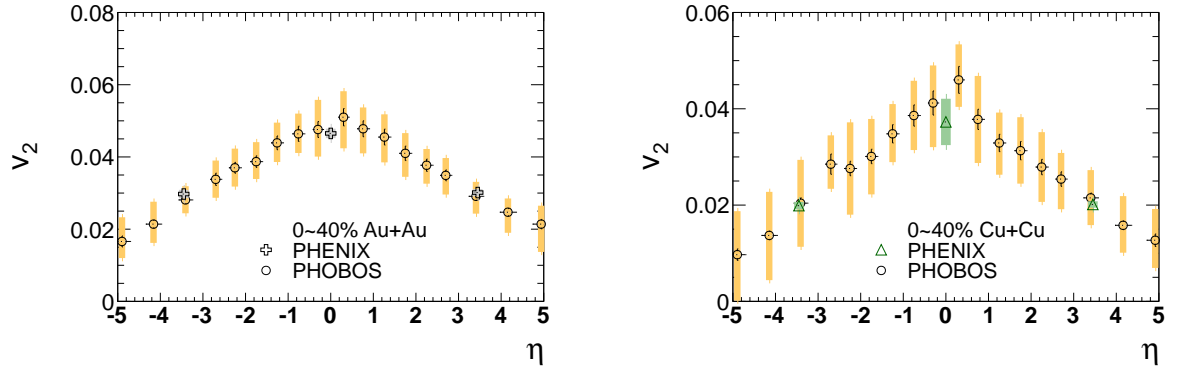


Figure 4.14: The v_2 measurements for $0 \sim 40\%$ centrality class in Au+Au and Cu+Cu compared to the PHOBOS results

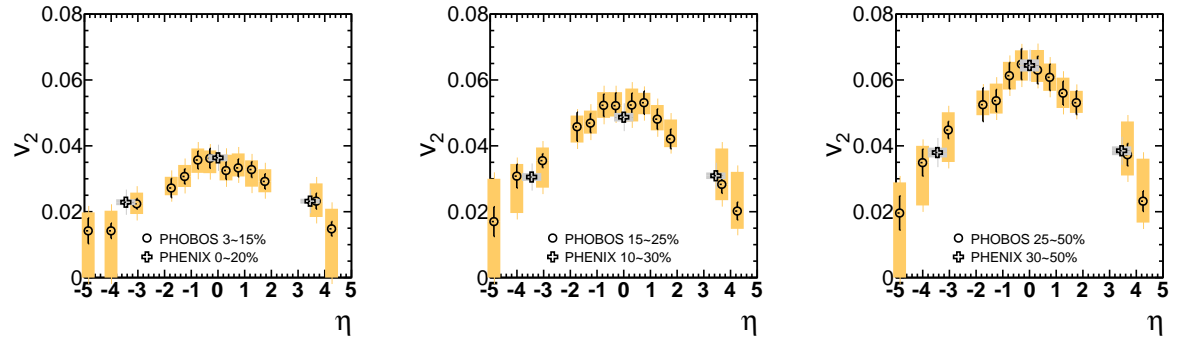


Figure 4.15: The v_2 measurements for different centrality classes in Au+Au and Cu+Cu compared to the PHOBOS results

Au+Au, Cu+Au and Cu+Cu collisions are shown. In Au+Au and Cu+Cu collisions, the data points shown in Fig. 4.17 are averages of v_2 values at forward and backward rapidities because rapidity dependence of v_2 in symmetric collision systems is symmetric. In Cu+Au collisions, the v_2 values at Au-going rapidity ($-3.9 < \eta < -3$) and these at Cu-going rapidity ($3 < \eta < 3.9$) are shown with blue and red circles, respectively. Like the v_2 measurements at mid-rapidity, the system size dependence of v_2 holds at forward/backward rapidity. In Cu+Au collisions, the v_2 for Au-going side shows larger values than that for Cu-going side except for the most central and peripheral collisions. This N_{part} dependence is predicted by the ε_2 shown in the right side of Fig. 4.17. In Fig. 4.17, we add Cu+Au $\varepsilon_{2,A(B)}$ which are $\varepsilon_{2,Au}$ estimated from Au participant nucleons and $\varepsilon_{2,Cu}$ estimated from Cu participant nucleons. The red open circles represent $\varepsilon_{2,Cu+Au}$ given by all participant nucleons in Cu and Au nuclei. In both ε , the common

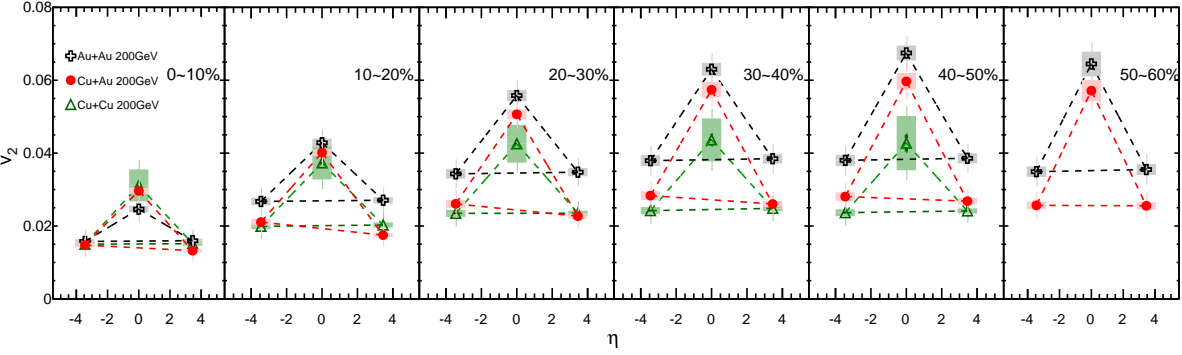


Figure 4.16: v_2 at BBC rapidity in the three collision systems for different centrality classes

participant plane estimated from all participant nucleons in Au and Cu nuclei are used.

$$\varepsilon_{n,Au} = \frac{\langle r^n \cos(n[\phi_{Au} - \Psi_{n,PP,Cu+Au}]) \rangle}{\langle r^n \rangle} \quad (4.5)$$

$$\varepsilon_{n,Cu} = \frac{\langle r^n \cos(n[\phi_{Cu} - \Psi_{n,PP,Cu+Au}]) \rangle}{\langle r^n \rangle} \quad (4.6)$$

where n is harmonics order and ϕ_{Au} and ϕ_{Cu} are azimuthal angle of participant Au and Cu nucleon positions respectively. $\Psi_{n,PP,Cu+Au}$ is the participant plane for n harmonics given by combined Au and Cu participant nucleons. The $\varepsilon_{2,Au}$ values are generally higher than the $\varepsilon_{2,Cu}$ values. However the difference of $\varepsilon_{2,Au}$ and $\varepsilon_{2,Cu}$ at the most central and the peripheral bins become small.

For the v_3 measurements shown in Fig. 4.18, the v_3 in Au+Au collisions is symmetric distribution and the v_3 in Cu+Au collisions is asymmetric distribution. Unlike the mid-rapidity v_3 measurements, the centrality dependence of v_3 in Cu+Au collisions decrease from central to peripheral collision class. The values of v_3 in Au-going side are always higher than those in Cu-going side.

For the v_3 measurements at the forward/backward rapidity, the forward/backward asymmetry of v_3 in Cu+Au collisions is seen in Fig. 4.18 and the left figure of Fig. 4.19. From the peripheral to the central collisions, the v_3 values in Au+Au and Cu+Au collisions increase. In Fig. 4.19, the v_3 values for Au going side are always larger than those for Cu going side in Cu+Au collisions. Surprisingly the v_3 values at Au-going side in Cu+Au collisions have the larger values than that in Au+Au collisions. This trend is not seen in the initial spatial triangularity shown in the right side figure of Fig. 4.19.

4.4 Charged hadron $dN/d\eta$

Figure 4.20 shows the $dN/d\eta$ at $3 < |\eta| < 3.9$ for charged hadrons in Au+Au and Cu+Cu collisions at $\sqrt{s_{NN}} = 200\text{GeV}$ in comparison to the results in PHOBOS [12, 53]. Our measurements presented in Fig. 4.20 are corrected from Bbc charge sum to number of charged particles

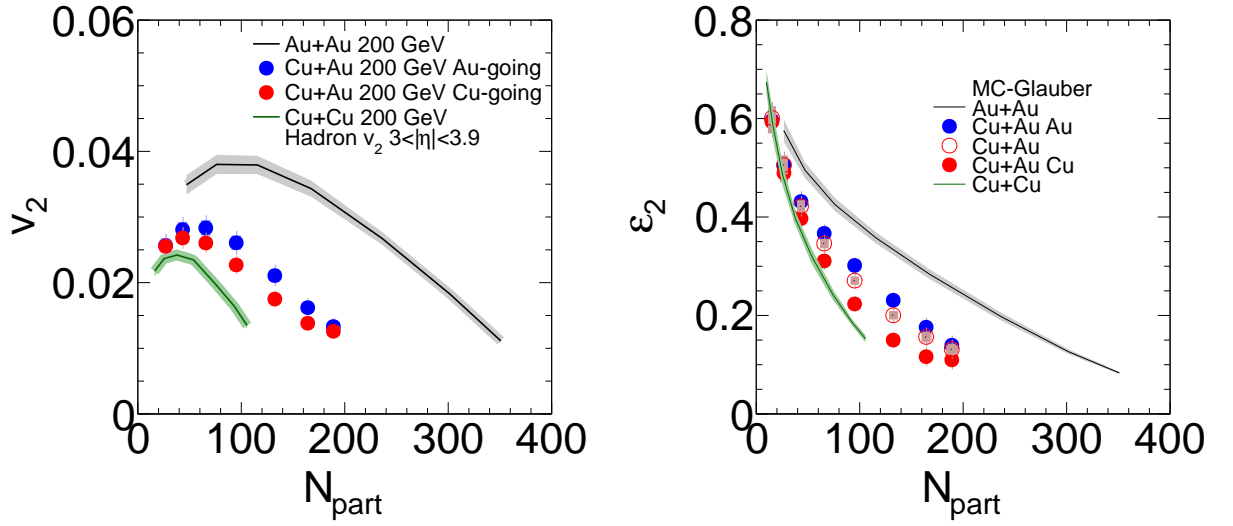


Figure 4.17: Left: p_T integrated v_2 as a function of N_{part} at forward/backward rapidity in Au+Au, Cu+Au and Cu+Cu collisions at $\sqrt{s_{NN}} = 200$ GeV. Right: ε_2 in Monte Carlo Glauber model as a function of N_{part} in Au+Au, Cu+Au and Cu+Cu collisions

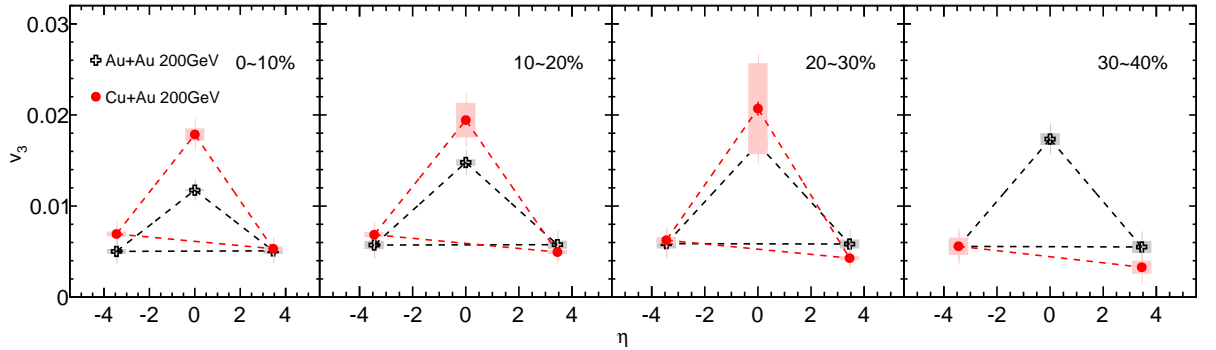


Figure 4.18: v_3 at BBC rapidity in the two collision systems for different centrality classes

by the correction factors estimated from the full Geant based Monte Carlo simulation. A good agreement between our measurements and PHOBOS results in both of Au+Au and Cu+Cu collisions. Figure 4.21 shows the measurements of rapidity dependence of $dN/d\eta$ in Au+Au, Cu+Au and Cu+Cu collisions for different centrality bins. The mid-rapidity data points are obtained from the previous PHENIX publication [47]. Like v_n measurements, $dN/d\eta$ at forward/backward rapidity is smaller than that at mid-rapidity in all collision systems. Au+Au collisions show the largest values of $dN/d\eta$ at mid, forward/backward-rapidities for all centrality bins, while Cu+Cu collisions show the smallest values in the three collision systems. The measurements of $dN/d\eta$ in Cu+Au collisions are always between those in Au+Au and Cu+Cu collisions. This system dependence of $dN/d\eta$ is supposed to arise from the system dependence of number of participants. In Cu+Au collisions, Au-going side have the larger values of $dN/d\eta$ than Cu-going side except

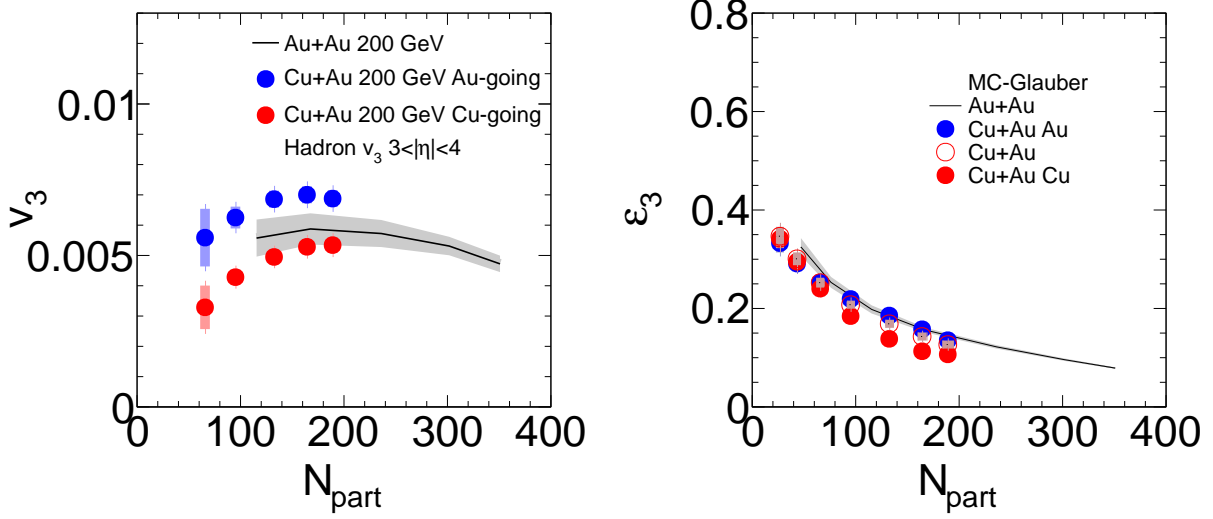


Figure 4.19: Left: p_T integrated v_3 as a function of N_{part} at forward/backward rapidity in Au+Au and Cu+Au collisions at $\sqrt{s_{NN}} = 200$ GeV. Right: ω^3 in Monte Carlo Glauber model as a function of N_{part} in Au+Au and Cu+Au collisions at $\sqrt{s_{NN}} = 200$ GeV

for peripheral collisions. In peripheral collisions, the difference of $dN/d\eta$ in Au-going side and Cu-going side becomes small, because the number of participants in Au nucleus and Cu nucleus would become similar.

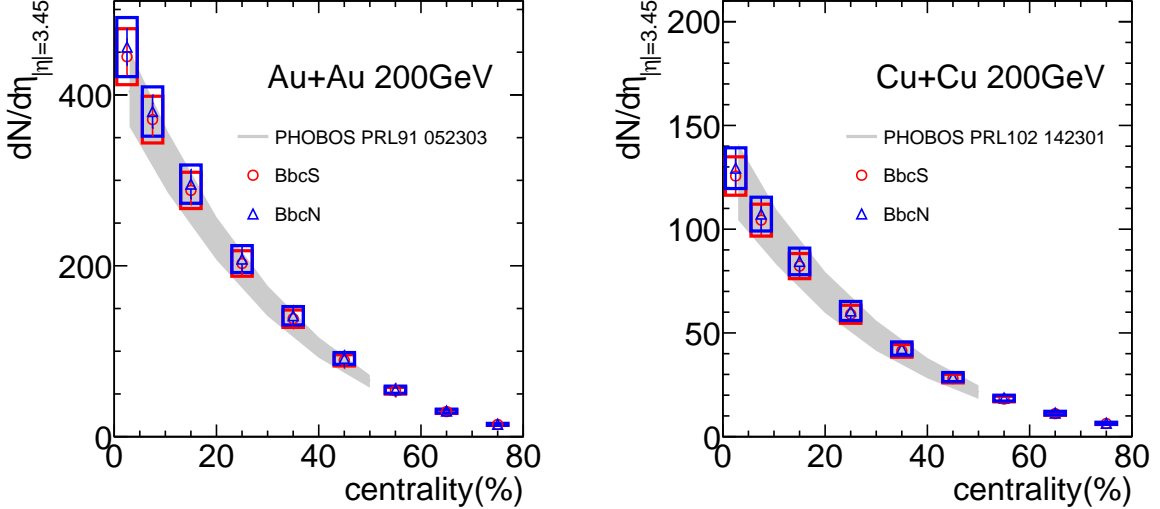


Figure 4.20: The measurements of charged particle multiplicity $dN/d\eta$ at $3 < |\eta| < 3.9$ in Au+Au and Cu+Cu collisions at $\sqrt{s_{NN}} = 200$ GeV in comparison to PHOBOS results[12],[53]

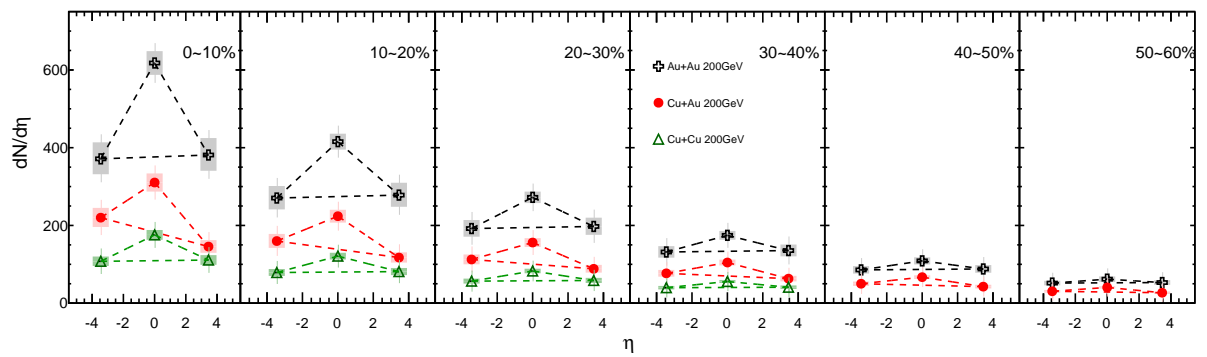


Figure 4.21: Charged particle multiplicity $dN/d\eta$ as a function of η in Au+Au, Cu+Au and Cu+Cu collisions at $\sqrt{s_{NN}} = 200\text{GeV}$

Chapter 5

Discussions

5.1 Interpretation of sign of $v_1(p_T)$

5.1.1 Approach with Monte Carlo Glauber model

In asymmetric collisions, the sign of mid-rapidity v_1 value reveals the direction of azimuthal angle where the density gradient becomes largest. Since particles are pushed to high p_T by radial flow, the high p_T particles move along the direction of the largest density gradient, while the low p_T particles move the opposite direction due to momentum conservation effect Ref. [34, 40].

Figure 5.1 shows the nucleon participant distribution in Cu+Au collisions for 20-30 % centrality class. In this figure, positive x direction is toward the Cu nucleus. This participant distribution is re-plotted with respect to the x-y position of center of mass. The red area denotes the larger number of participants, and the blue area denotes the lower number of participants. Although it looks symmetric distribution, the width of green and yellow bands is narrower in negative x direction (Au nucleus side) than that in positive x direction (Cu nucleus side), which indicates the larger density gradient in Au nucleus side. For the further study, the number of participant and density gradient in x direction are shown in Fig. 5.2. The number of participant distribution in x direction looks almost symmetric shape. In the density gradient distribution, the value of the density gradient is lower at the center and the surface of the participant zone and become higher at the middle of the participant zone. The Au side show the higher value of maximum density gradient than the Cu side. Figure 5.3 show the correlation of the participant plane for 1st harmonic $\Psi_{1,PP}$, which indicates the highest number density direction with r^3 weighting, with respect to the impact parameter Ψ_{imp} , $\langle \cos(\Psi_{1,PP} - \Psi_{imp}) \rangle$, as a function of centrality. In our calculation, we treat Ψ_{imp} as Cu nucleus side. Therefore positive and negative sign indicates the highest density gradient is Cu and Au side, respectively. In Fig. 5.3, the correlation shows the negative values, and the absolute value of the correlation increase from 0 to 30% centrality and decrease from 30 to 80 % centrality. In our measurements of directed flow (Fig. 4.1), the maximum absolute value decreases from 10-20 % to 40-50 % centrality. Thus the centrality dependence of directed flow measurements is consistent with the participant plane correlation from Monte Carlo Glauber model.

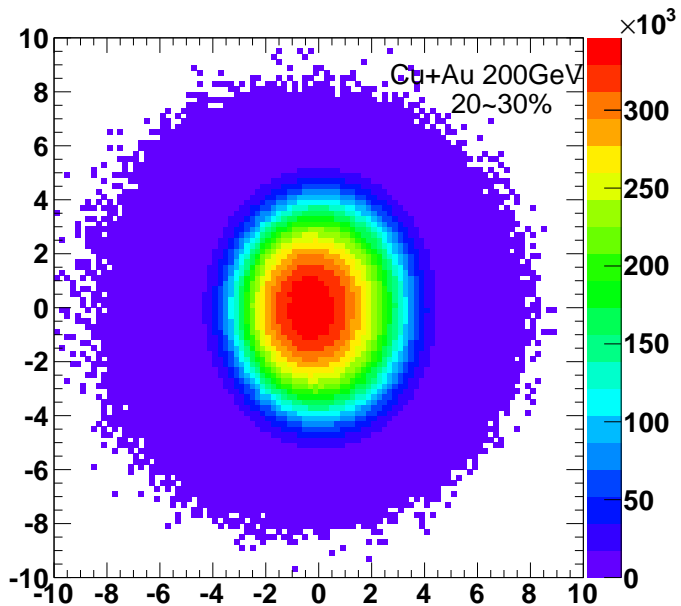


Figure 5.1: Participant nucleon distribution in Cu+Au collisions for 20-30 % centrality class

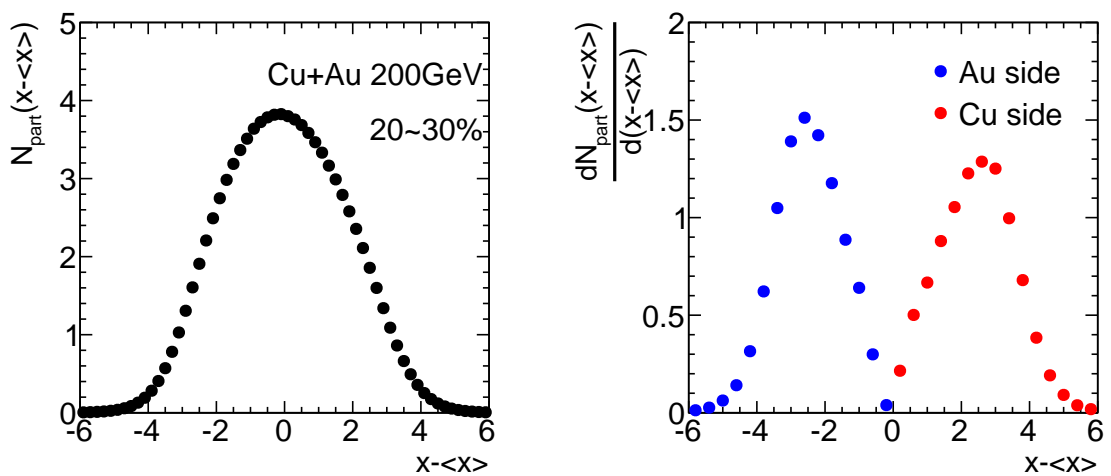


Figure 5.2: Number of participant distribution and density gradient distribution in x direction in Cu+Au collisions for 20-30% centrality class. Left: Number of participant distribution. Right: Density gradient distribution

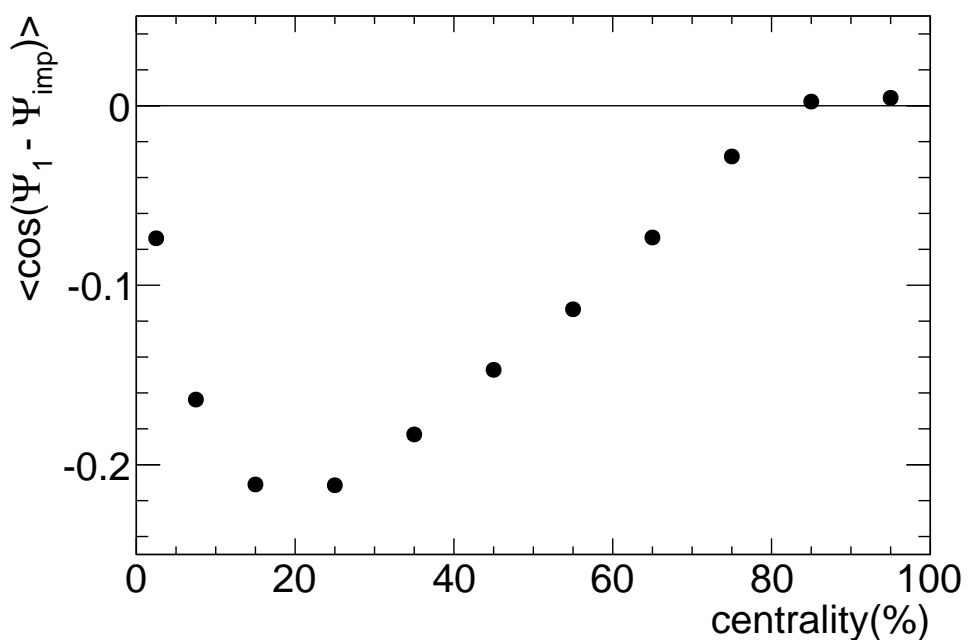


Figure 5.3: Azimuthal correlation between 1st order participant plane $\Psi_{1,PP}$ and impact parameter Ψ_{imp} . Negative sign indicates the highest density gradient is Au nucleus side.

5.1.2 Approach with Blast wave model

In order to study the direction of larger pressure gradient in Cu+Au collisions, we apply the Blast wave model to the directed flow results at mid-rapidity. The Blast wave model is commonly used in the study of the property of the medium at the freeze-out stage with its freeze-out temperature T_f and its integrated ϕ maximal flow velocity in radial direction ρ_0 . In our study, the extended Blast wave model which incorporate the azimuthal anisotropy of radial velocity ρ_n and spatial density s_n for nth harmonics defined as the coefficients in the Fourier expansion of the empirically introduced quantities $\rho(n, m, \phi, r) = \rho_0[1 + 2\rho_n \cos(n\phi)]r/R^{\max}$ and $S(n, m, \phi) = 1 + 2s_n \cos(n\phi)$ [24]. The charged hadron transverse momentum spectra and azimuthal anisotropy at the freeze-out of the medium are predicted by the following formulas,

$$\frac{dN}{p_T dp_T} \propto \int_{R^{\min}}^{R^{\max}} r dr \int d\phi m_T I_0(\alpha_t) K_1(\beta_t), \quad (5.1)$$

$$v_n = \frac{\int_{R^{\min}}^{R^{\max}} r dr \int d\phi \cos(n\phi) I_n(\alpha_t) K_1(\beta_t) S(n, m, \phi)}{\int_{R^{\min}}^{R^{\max}} r dr \int d\phi I_0(\alpha_t) K_1(\beta_t) S(n, m, \phi)}, \quad (5.2)$$

where I_n and K_1 are modified Bessel functions of the first and second kinds, α_t and β_t are $(p_T/T_f) \sinh(\rho(n, m, \phi, r))$ and $(m_T/T_f) \cosh(\rho(n, m, \phi, r))$, respectively. In above formulas, the Blast wave model parameters T_f, ρ_0, ρ_n and s_n are determined simultaneously by fitting single particle transverse momentum p_T spectra and azimuthal anisotropy $v_n(p_T)$ for π^\pm, K^\pm and $p + \bar{p}$ with minimizing χ^2/NDF . T_f and ρ_0 are mainly determined by the single particle spectra, whereas anisotropy parameters ρ_n and s_n are primarily determined by v_n .

Since the π^\pm, K^\pm and $p + \bar{p}$ single particle spectra in Cu+Au collisions at $\sqrt{s_{NN}} = 200$ GeV have not been measured at PHENIX, we utilize the T_f and ρ_0 parameters which are estimated in Au+Au collision at same energy by PHENIX [24]. The T_f and ρ_0 for lowest $N_{part, \text{AuAu}} \sim 94$ bin are selected to be similar $N_{part, \text{CuAu}} \sim 84$ bin corresponding to 10 – 50% centrality class. The fitting ranges of directed flow for π^{pm}, K^\pm and $p + \bar{p}$ are $0.5 < p_T < 1.1$ GeV/ c , $0.4 < p_T < 1.3$ GeV/ c and $0.6 < p_T < 1.7$ GeV/ c , respectively. These fitting ranges are same as it is done for the determination of the T_f and ρ_0 in Au+Au collisions [24].

In Fig. 5.4, the identified π^\pm, K^\pm and $p + \bar{p}$ v_1 as a function of p_T for 10 50% centrality class fitted with the Blast wave model is shown. The experimental data points are shown as markers and the smooth curves are the Blast wave fitting functions. The fitting functions for the fitting ranges are shown as bold line. The Blast wave model well reproduce the experimental data at the each fitting range. The Blast wave model parameters of freeze-out temperature T_f , radially integrated flow velocity $\langle \rho \rangle = \int \rho_0 [r/R^{\max}] r dr / \int r dr$, directed anisotropy of radial velocity ρ_1 and directed anisotropy of spatial density s_1 for 10 - 50 % centrality class are shown in Fig. 5.5. The T_f and $\langle \rho \rangle$ are same values in the PHENIX publication. The anisotropy parameter ρ_1 and s_1 are extrapolated from the fitting results. The ρ_1 shows the negative value, while the s_1 has the positive value. Since the v_1 measurements performed with respect to the Cu nucleus side, the negative ρ_1 indicates stronger radial flow in Au nucleus side, which is predicted by the previous Glauber Monte Carlo model approach. On the other hand, the positive s_1 indicates more particles are emitted toward Cu nucleus side.

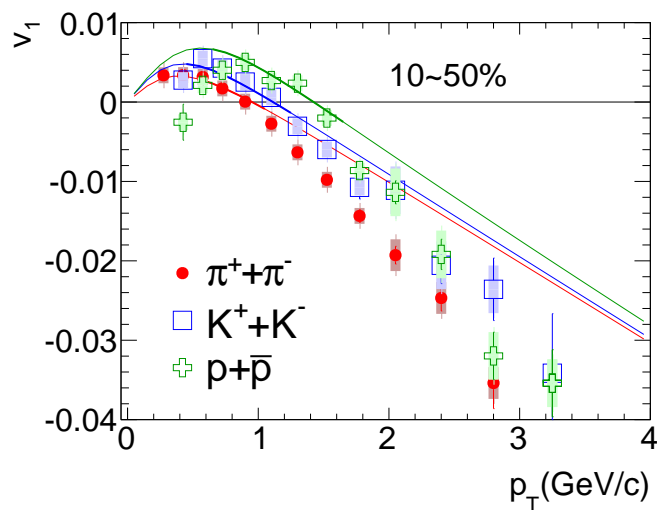


Figure 5.4: Identified charged hadron v_1 at mid-rapidity fitted with the Blast wave model for 10-50 % centrality class in Cu+Au collisions

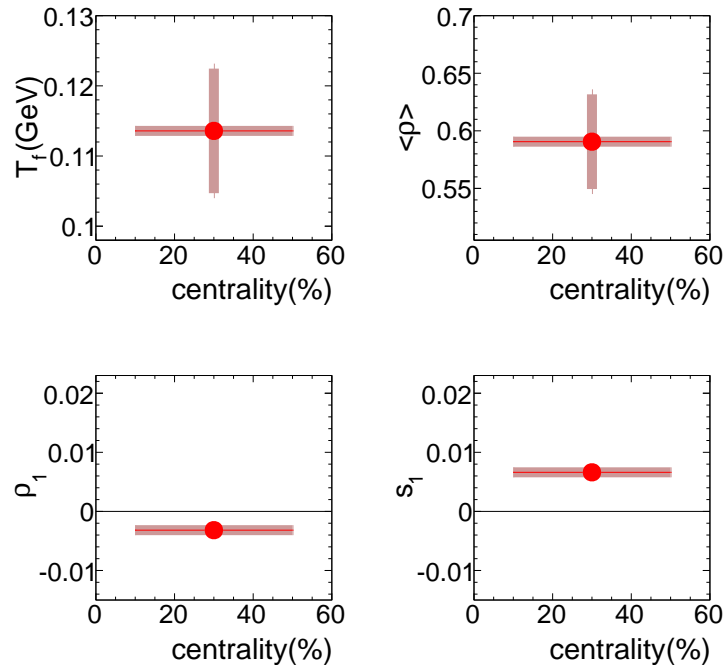


Figure 5.5: The Blast wave model parameters for identified charged hadron v_1 at mid-rapidity for 10-50 % centrality class in Cu+Au collisions. Top left: Freeze-out temperature T_f , Top right: Averaged radial velocity $\langle \rho \rangle$, Bottom left:Directed anisotropy of radial velocity ρ_1 , Bottom right:Directed anisotropy of spatial density s_1 . The parameters T_f and $\langle \rho \rangle$ are obtained from the PHENIX Au+Au publication [24]. The anisotropy parameters ρ_1 and s_1 are extrapolated from the fitting.

5.2 Interpretation of forward/backward asymmetry of $dN_{ch}/d\eta$ with Monte Carlo Glauber model

Wounded nucleon model

In the collision dynamics, the number of produced particles is related to the amount of the released the degree of freedom. In the 1970s, experimentally it was found that the number of produced charged particles in nucleon-nucleus collisions was proportional to the number of participants [46],

$$N_{ch} \propto N_{part,pA} = N_{part,A} + 1, \quad (5.3)$$

where $N_{part,pA}$ is the total number of participants, $N_{part,A}$ is the number of participants in A nucleus and 1 is the projectile nucleon. Surprisingly this experimental feature also holds in nucleus-nucleus collisions at RHIC energy. Figure 5.6 shows the charged particle multiplicity per participant nucleon in Au+Au collisions at several collision energies measured by PHOBOS collaboration [48]. From the central to the peripheral collisions, the normalized charged particle multiplicities at the three energies are almost constants, which indicates the charged particle production is determined by the number of participants, $N_{ch} \propto \langle N_{part}/2 \rangle$ or one nucleon produces same charged particles. Since participant nucleon is also called "wounded nucleon", this experimental fact is called "wounded nucleon model".

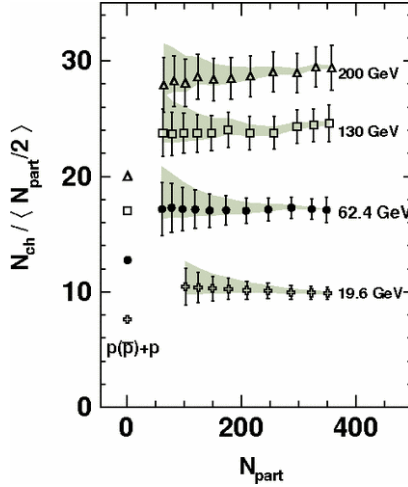


Figure 5.6: Total charged particle multiplicity per participant nucleon in Au+Au collisions at $\sqrt{s_{NN}} = 200, 130, 62.4$ and 19.6 GeV measured by PHOBOS [48]

Weighted N_{part} scaling based on wounded nucleon model

As it is seen in Fig. 4.21, the number of charged particles $dN_{ch}/d\eta$ in Cu+Au collisions shows the forward/backward asymmetry. The forward/backward asymmetry of charged particle production is considered to arise from the different number of participants in Au nucleus and Cu nucleus. In order to investigate the contributions of the Au participants, $N_{part,Au}$, and the Cu participants, $N_{part,Cu}$, to the particle production at forward/backward rapidity, we introduce the weighted N_{part} with $N_{part,Au}$ and $N_{part,Cu}$ based on wounded nucleon model. The weighted

5.2. INTERPRETATION OF FORWARD/BACKWARD ASYMMETRY OF $dN_{ch}/d\eta$ WITH MONTE CARLO

N_{part} for Au-going and Cu-going side in Cu+Au collisions is defined as the following formulas,

$$N_{part,Au-going} = w_{Au-going} N_{part,Au} + (2 - w_{Au-going}) N_{part,Cu} \quad (5.4)$$

$$N_{part,Cu-going} = w_{Cu-going} N_{part,Au} + (2 - w_{Cu-going}) N_{part,Cu}, \quad (5.5)$$

where $w_{Au-going}$ and $w_{Cu-going}$ are weights for the Au-going and the Cu-going sides, respectively. Since the weight is defined to change from 0 to 1, the weighed N_{part} ranges from $2N_{part,Cu}$ to $2N_{part,Au}$, $2N_{part,Cu} \leq N_{part,Cu-going}, N_{part,Au-going} \leq 2N_{part,Au}$.

Weighted ε_n scaling based on wounded nucleon model

Like the $dN_{ch}/d\eta$ measurements at forward/backward-rapidity, the forward/backward asymmetry of charged particle v_n in Cu+Au collisions is seen in Fig. 4.16 and 4.18. Based on wounded nucleon model, the weighted initial spatial anisotropy ε_n with the Au nucleus $\varepsilon_{n,Au}$ and Cu nucleus $\varepsilon_{n,Cu}$ is introduced for studying the influence of Au and Cu geometries on the forward/backward v_n .

$$\varepsilon_n = w\varepsilon_{n,Au} + (1 - w)\varepsilon_{n,Cu} \quad (5.6)$$

where w is the weights changing from 0 to 1 ($\varepsilon_{n,Cu} < \varepsilon_n < \varepsilon_{n,Au}$). This model is used in the next section for studying the initial geometry at the forward/backward-rapidity.

The charged particle multiplicity distributions $dN_{ch}/d\eta$ as a function of weighted N_{part} at Cu-going and Au-going side in Cu+Au collisions are compared to those in Au+Au and Cu+Cu collisions shown in Fig. 5.7 and 5.8. The values of $dN_{ch}/d\eta$ in all collision systems increase from the peripheral to the central collisions. The almost linear relation between $dN_{ch}/d\eta$ and N_{part} is seen, whose feature is described by the wounded nucleon model. In all panels, the values of $dN_{ch}/d\eta$ in the Au+Au and the Cu+Cu collisions are common. From the left to the right panel, both of the Au-going and the Cu-going side N_{part} range from $2N_{part,Cu}$ to $2N_{part,Au}$, $2N_{part,Cu} \leq N_{part,Cu-going}, N_{part,Au-going} \leq 2N_{part,Au}$. In the left side panels of Fig. 5.7, a good agreement among Au+Au, Cu+Au and Cu+Cu collisions is seen. However, the discrepancy between the symmetric Au+Au and Cu+Cu collisions and the Cu+Au collisions become larger with increasing the fraction of the $N_{part,Au}$ as in the right panels in Fig. 5.7. In Fig. 5.8, the Au-going side $dN_{ch}/d\eta$ in Cu+Au collisions become slightly close to the symmetric Au+Au and Cu+Cu results from the left to the right panel. For $1.5N_{part,Au} + 0.5N_{part,Cu}$ in Cu+Au collisions, the Cu+Au result is closest to the symmetric collision systems. Compared to the Cu-going results, $dN_{ch}/d\eta$ at Au-going side needs larger opposite beam participant ($N_{part,Cu}$) contribution. In Fig. 5.9, the χ^2/NDF as a function of the weight for the difference of $dN_{ch}/d\eta$ between the symmetric Au+Au and Cu+Cu collisions and the Cu+Au collisions is shown. In the left side panel, χ^2/NDF for Au-going side is shown. For the Au-going side, the χ^2/NDF decreases from the lower to larger weight. The lowest χ^2/NDF is expected to be between $w = 1 \sim 1.5$, which indicates the $dN_{ch}/d\eta$ at Au-going side is originated from not only $N_{part,Au}$ but also the $N_{part,Cu}$. On the other hand, the χ^2/NDF for Cu-going side becomes smaller at the larger weight of $N_{part,Cu}$. Thus the $dN_{ch}/d\eta$ at Cu-going side is described by the almost pure $N_{part,Cu}$ contribution.

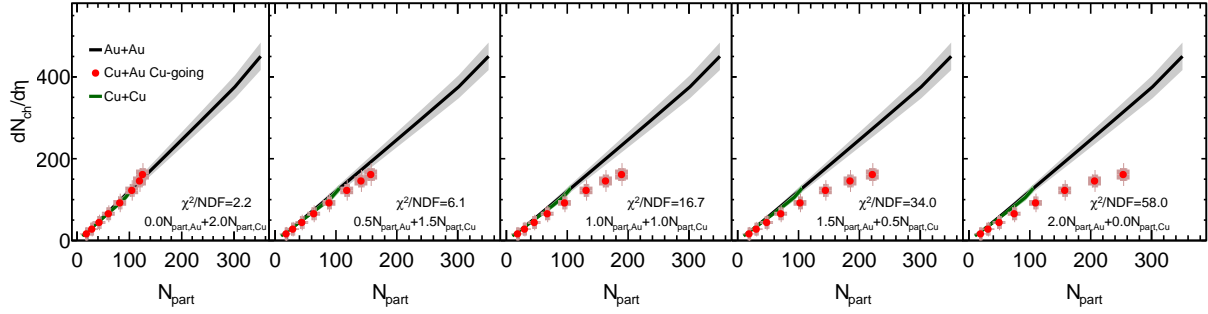


Figure 5.7: The comparison of the charged particle multiplicity distributions $dN_{ch}/d\eta$ among Au+Au, Cu+Au(Cu-going) and Cu+Cu collisions collisions

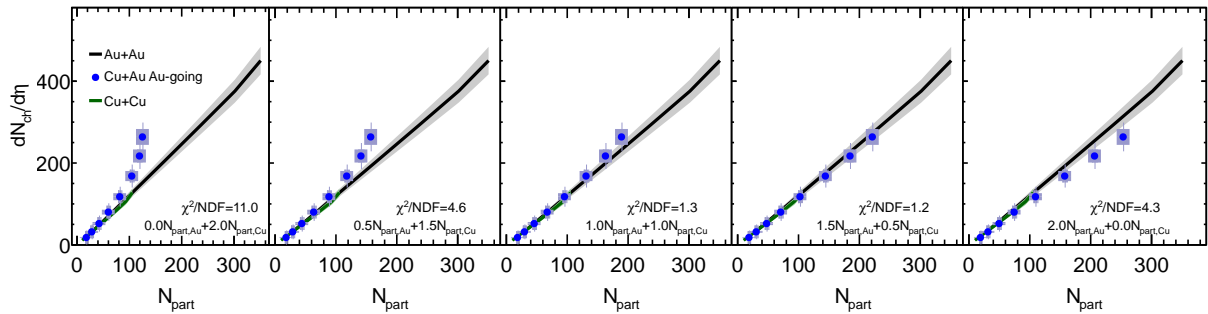


Figure 5.8: The comparison of the charged particle multiplicity distributions $dN_{ch}/d\eta$ among Au+Au, Cu+Au(Au-going) and Cu+Cu collisions collisions

5.2. INTERPRETATION OF FORWARD/BACKWARD ASYMMETRY OF $dN_{ch}/d\eta$ WITH MONTE CARLO

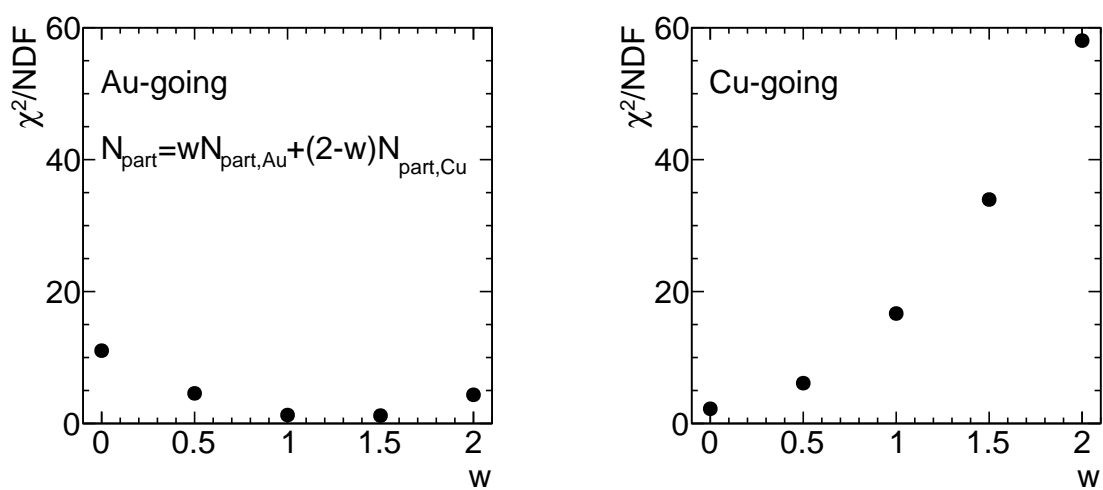


Figure 5.9: The χ^2/NDF distributions for the comparison of $dN_{ch}/d\eta$ among Au+Au, Cu+Au and Cu+Cu collisions

5.3 Eccentricity scaling of v_n

5.3.1 Mid-rapidity v_n/ε_n

In order to study the effect of initial geometry on azimuthal anisotropies, eccentricity scaling v_n/ε_n is commonly used, because v_n coefficients are mostly driven originally from ε_n . In this section, various eccentricity scalings of v_n mid, forward and backward rapidities are discussed to study the initial geometry effect. Especially the forward/backward asymmetry of v_n in Cu+Au collisions is discussed.

In Fig. 5.10, the average $\langle v_2 \rangle$ coefficients ($0 < p_T < 3\text{GeV}/c$) as a function of number of participants, N_{part} for Au+Au, Cu+Au and Cu+Cu collisions are shown. At all N_{part} bins, the v_2 coefficients in Au+Au collisions are the largest and those in Cu+Cu collisions are smallest in the three collision systems. The v_2 values increase from the large N_{part} (central collision) to the small N_{part} (peripheral collision). These system size dependence and N_{part} dependence are expected from the initial geometry in Monte Carlo Glauber model for the three collision systems shown in Fig. 5.10. From the central to peripheral collisions, the nuclei overlap region become more elliptical shape. In the earlier studies [38], [41] and [42], PHOBOS, PHENIX and STAR experiments compared the scaled v_2 values in Au+Au and Cu+Cu collisions at 200 GeV with their 2_{nd} participant eccentricity ε_2 to study the initial geometry and the collective response. In this comparison, the scaled v_2/ε_2 values in the two symmetric collision systems show a universal behavior. This trend indicates that the relation between v_2 and ε_2 is not linear and the collective responses depend on the N_{part} of the symmetric heavy ion collisions. We add the results from the asymmetric Cu+Au data to this comparison in Fig. 5.11. The Cu+Au collisions are in good agreement with the symmetric collision systems. All scaled v_2 increase from small N_{part} to large N_{part} . Namely, the strength of elliptic flow is mainly determined from initial geometry shape and system size.

For the $\langle v_3 \rangle$ measurements, the $\langle v_3 \rangle$ values in Au+Au and Cu+Au collisions as a function of N_{part} are shown in Fig. 5.12. Unlike the $\langle v_2 \rangle$ measurements, the Cu+Au v_3 is consistent with the Au+Au v_3 within the systematic uncertainties. This is not predicted by the simple Glauber model as shown in Fig. 5.12. Although both of v_3 and ε_3 do not have same system size trend, we scale v_3 in Au+Au and Cu+Au with their ε_3 shown in 5.13. Except for most central bin, the scaled v_3 values in Au+Au and Cu+Au collisions are consistent within error. Compared to the scaled v_2 values, the scaled v_3 values are smaller, which means that the conversion from ε_3 to v_3 through collective expansion is smaller than that from ε_2 to v_2 .

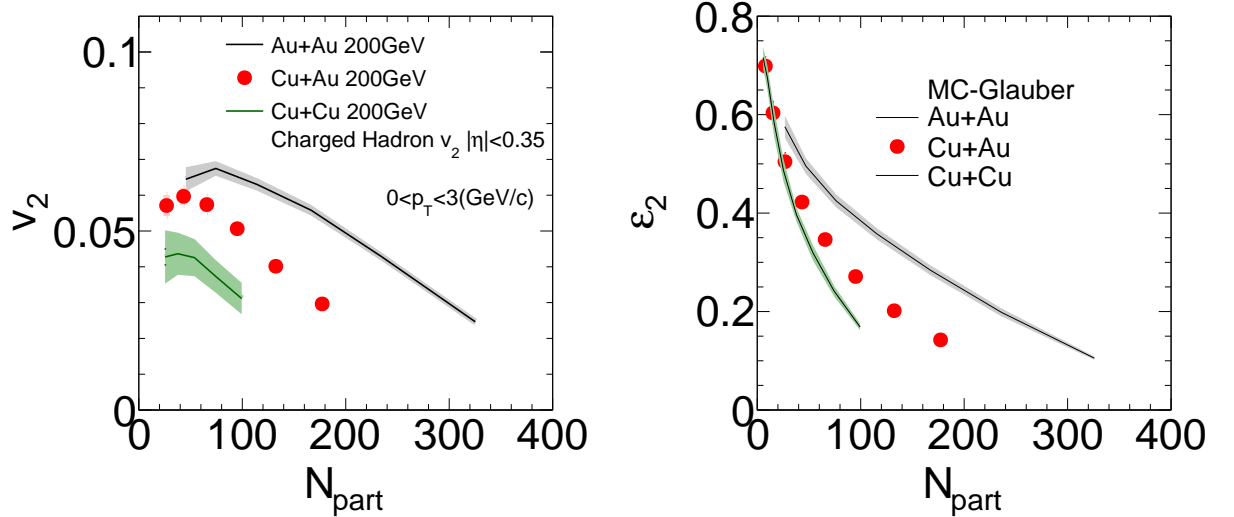


Figure 5.10: Left: p_T integrated v_2 as a function of N_{part} at mid-rapidity in Au+Au, Cu+Au and Cu+Cu collisions at $\sqrt{s_{NN}} = 200 \text{ GeV}$. The integrated p_T range is from 0 to 3 GeV. Right: ε_2 in Monte Carlo Glauber model as a function of N_{part} in Au+Au, Cu+Au and Cu+Cu collisions

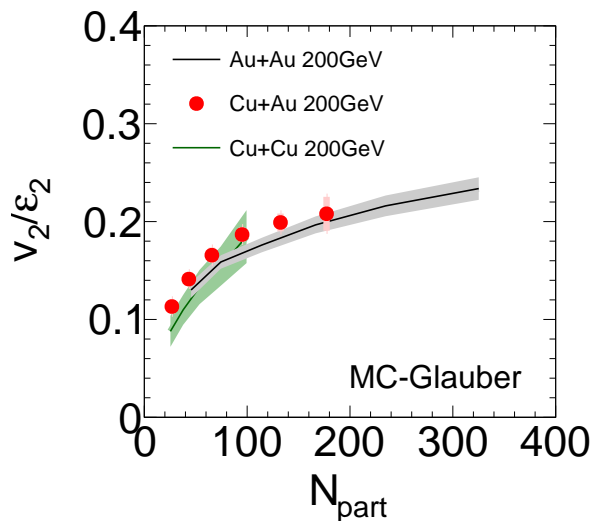


Figure 5.11: v_2/ε_2 at mid-rapidity as a function of N_{part} in Au+Au, Cu+Au and Cu+Cu collisions

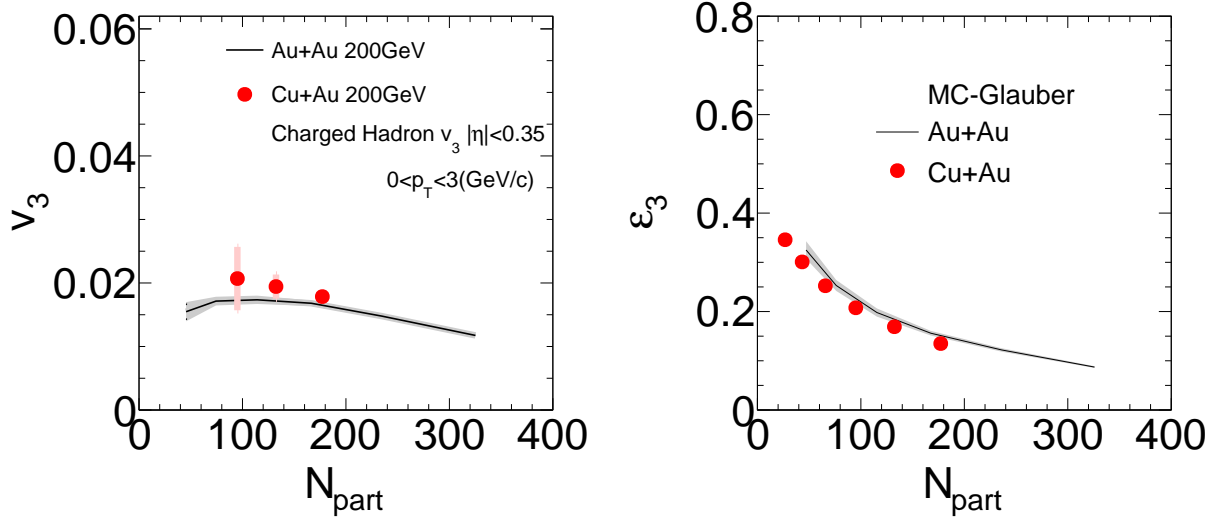


Figure 5.12: Left: p_T integrated v_3 as a function of N_{part} at mid-rapidity in Au+Au and Cu+Au collisions at $\sqrt{s_{NN}} = 200 \text{ GeV}$. The integrated p_T range is from 0 to 3 GeV. Right: ε_3 in Monte Carlo Glauber model as a function of N_{part} in Au+Au and Cu+Au collisions

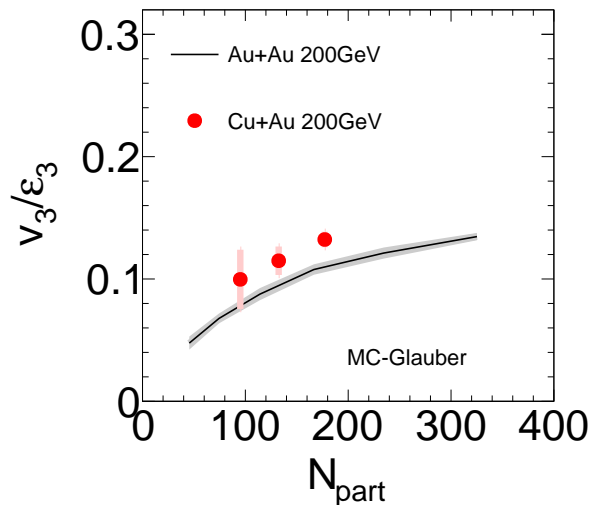


Figure 5.13: v_3/ε_3 as a function of N_{part} in Au+Au and Cu+Au collisions

5.3.2 Forward/Backward-rapidity v_n/ε_n

We also perform the eccentricity scaling of v_n at forward/backward-rapidity. As it is seen in the above study of the eccentricity scaling of mid-rapidity v_n , the magnitude of v_n is described by not only initial geometry but also N_{part} , which is related to the initial energy density and the volume of formed matter. In Cu+Au collisions, the forward/backward asymmetry of $dN/d\eta$ is observed in Fig. 4.21. Since the $dN/d\eta$ is proportional to N_{part} , this rapidity asymmetry of $dN/d\eta$ in Cu+Au collisions also could lead to the rapidity asymmetry of v_n . By taking this asymmetry of $dN/d\eta$ into account, we measure the v_n and the scaled v_n as a function of $dN/d\eta$ measured at the forward/backward-rapidity.

Figure 5.14 shows the v_2 measurements as a function of the forward/backward $dN/d\eta$ in Au+Au, Cu+Au and Cu+Cu collisions at the forward/backward-rapidity. In all collision systems, the v_2 increase from the central to the peripheral collisions. The v_2 in Au+Au collisions shows the largest values and the Cu+Cu v_2 is lowest value at entire measured $dN/d\eta$ region. The v_2 values in Cu+Au are always between those in Au+Au and Cu+Cu collisions. In Cu+Au collisions, the v_2 at Au-going side is higher than that at Cu-going side. This system size dependence is expected from the $\varepsilon_{2,A+B}$ shown in Fig. 5.15. In Fig. 5.15, the $\varepsilon_{2,A(B)}$, $\varepsilon_{2,A+B}$ and $\varepsilon_{2,B(A)}$ in Au+Au, Cu+Au and Cu+Cu collisions as a function of the forward/backward $dN/d\eta$ are shown. For the system size dependence of $\varepsilon_{2,A(B)}$, the $\varepsilon_{2,Cu}$ in Cu+Au collisions is same as the $\varepsilon_{2,Cu+Cu}$. This consistency is not seen in the v_2 measurements and indicates the initial geometry for the Cu-going side v_2 is not described by the $\varepsilon_{2,Cu}$ alone. Figure 5.16 shows the eccentricity scaling of v_2 with the ε_2 . In the three panels, each of the $\varepsilon_{2,Au+Au}$ and $\varepsilon_{2,Cu+Cu}$ uses common values. Therefore the scaled v_2 in Au+Au and Cu+Cu collisions is not changed in the three panels. For the Cu+Au collisions, the values of ε_2 are different in the three panels. In the left side panel, the $\varepsilon_{2,Au}$ and $\varepsilon_{2,Cu}$ are used to Au-going and Cu-going side v_2 , respectively. In the middle panel, the common $\varepsilon_{2,Cu+Au}$ is used to the both of side. In the right side panel, the $\varepsilon_{2,Cu}$ and $\varepsilon_{2,Au}$ are used to Au-going side and Cu-going side, respectively, which is the opposite combination of v_2 and ε_2 compared to the combination in the left side panel. Like the mid-rapidity scaled v_2 , the scaled v_2 at forward/backward-rapidity increase from the peripheral to the central in the three panels. From the left side to the right side panels, the scaled Au-going side v_2 increase, while the scaled Cu-going side of v_2 decrease. In the right and left side panels, the discrepancies between the Au going side and Cu going side are observed. The eccentricity scaling with independent eccentricity definitions fails in the v_2 measurements. In the middle of panel, a good agreement between Au going side and Cu going side is observed, and a universal behavior is seen except for the central Cu+Au collisions, which indicates that the forward/backward asymmetry of v_n is caused by the forward/backward asymmetry of $dN/d\eta$ with a common eccentricity $\varepsilon_{2,A+B}$. To confirm the results that the forward/backward asymmetry of v_2 in Cu+Au collisions is canceled with the common eccentricity, the scaled v_2 with the weighted eccentricity which is already introduced in the description about wounded nucleon model Sec. 5.2. We defined the eccentricity as following formula,

$$\varepsilon_{2,Au-going} = w_{Au-going}\varepsilon_{2,Au} + (1 - w_{Au-going})\varepsilon_{2,Cu} \quad (5.7)$$

$$\varepsilon_{2,Cu-going} = w_{Cu-going}\varepsilon_{2,Au} + (1 - w_{Cu-going})\varepsilon_{2,Cu} \quad (5.8)$$

where $w_{\text{Au-going}}$ and $w_{\text{Cu-going}}$ are the weights changing from 0 to 1 ($\varepsilon_{2,\text{Cu}} < w_{\text{Au-going}}, w_{\text{Cu-going}} < \varepsilon_{2,\text{Au}}$), which means the weighted eccentricity range from the the $\varepsilon_{2,\text{Cu}}$ to the $\varepsilon_{2,\text{Au}}$. In Fig. 5.17, the row from the bottom to the top corresponds to the weight for Au-going side $w_{\text{Au-going}}$ from 0 to 1 and the column from the left to the right corresponds to the weight for Cu-going side $w_{\text{Cu-going}}$ from 0 to 1. Namely, the $\varepsilon_{2,\text{Au}}$ ($\varepsilon_{2,\text{Cu}}$) contribution in $\varepsilon_{2,\text{Au-going}}$ increases (decreases) from the bottom to the top row, and the $\varepsilon_{2,\text{Au}}$ ($\varepsilon_{2,\text{Cu}}$) contribution in $\varepsilon_{2,\text{Cu-going}}$ increases (decreases) from the left to the right column. Thus the scaled Au-going side v_2 decreases from the bottom to the top row and the scaled Cu-going side v_2 decreases from the left to the right column. On the top left side and the bottom right side panels, there are the deviations between Au-going and Cu-going sides are seen. Around middle of row and column, a good agreement between the scaled Au-going and Cu-going v_2 is observed. An agreement between the Cu+Au and Au+Au collisions is also observed. Fig. 5.18 shows the χ^2/NDF contour distributions for $w_{\text{Au-going}}$ vs $w_{\text{Cu-going}}$. In Fig. 5.18, the χ^2/NDF is estimated from the difference between the scaled Au-going side and Cu-going side v_2 in Cu+Au collisions. The χ^2/NDF increase at the top left and the bottom right. The lower χ^2/NDF distribution is seen at around $w_{\text{Au}} \sim w_{\text{Cu}}$ band. In Fig. 5.19, the χ^2/NDF map is shown as a function of the weight w for ε , where χ^2/NDF is defined by the difference between each of the scaled Au-going and Cu-going side v_2 in Cu+Au collisions and that in Au+Au collisions. For both of Au-going and Cu-going side, the χ^2/NDF become large at $w = 1$ and $w = 0$, and the lowest χ^2/NDF is found to be between 0.25 and 0.5. For the forward/backward v_2 measurements in Cu+Au collisions, the almost same ε_2 is expected to be the initial geometry at forward/backward rapidity and the forward/backward asymmetry of the v_2 arise from the forward/backward asymmetry of the $dN/d\eta$ which is supposed to be originated from the initial energy density that later driving the strength of the collective expansion.

To confirm this indication, the v_3 as a function of $dN/d\eta$ is scaled as well. In Fig. 5.20, the forward/backward v_3 as a function of the forward/backward $dN/d\eta$ in Au+Au and Cu+Au collisions is shown. Figure 5.21, show the $\varepsilon_{3,\text{A(B)}}$, $\varepsilon_{3,\text{A+B}}$ and $\varepsilon_{3,\text{B(A)}}$ as a function of $dN/d\eta$. All ε_3 cases, does not describe the system size difference of v_3 . However we perform the eccentricity scaling of v_3 in the same way as done in the v_2 . In Fig. 5.22, the scaled v_3 values in Au+Au and Cu+Au collisions are compared. Like the mid-rapidity v_3 , the scaled v_3 at forward/backward-rapidity in both of Au+Au and Cu+Au collisions increase from the peripheral to the central collisions. The scaled Au+Au v_3 is common in all panels. The v_3 in Cu+Au collisions is scaled by the different ε_3 . In the left panel, the Cu+Au v_3 at Au-going and Cu-going side are scaled with the $\varepsilon_{3,\text{Au}}$ and the $\varepsilon_{3,\text{Cu}}$ respectively. The Au-going side v_3 in Cu+Au collisions is consistent with that in Au+Au collisions within the error, while the Cu-going side v_3 in Cu+Au collisions is larger than that in Au+Au collisions. The discrepancy between the Au-going and the Cu-going side is observed. In the middle panel, the common $\varepsilon_{3,\text{Cu+Au}}$ which is the average of the $\varepsilon_{3,\text{Au}}$ and the $\varepsilon_{3,\text{Cu}}$ is used for both of the Au-going and the Cu-going v_3 in Cu+Au collisions. The consistency between the Au-going and Cu-going side in Cu+Au collisions is seen as seen in the forward/backward v_2 measurements. The both of Au-going and Cu-going side is not consistent with Au+Au collisions. In the right side panel, the $\varepsilon_{3,\text{Cu}}$ and the $\varepsilon_{3,\text{Au}}$ in Cu+Au collisions are used for the Au-going and the Cu-going side v_3 respectively. The discrepancy among the Au-going and the Cu-going and Au+Au collisions is seen. From the left to the right panel, the Au-going side v_3 increase and the Cu-going side v_3 decreases. This is because the ε_3 for the Au-going and decreases and the ε_3 for the Cu-going side increases from the left to the right side panel. Like the

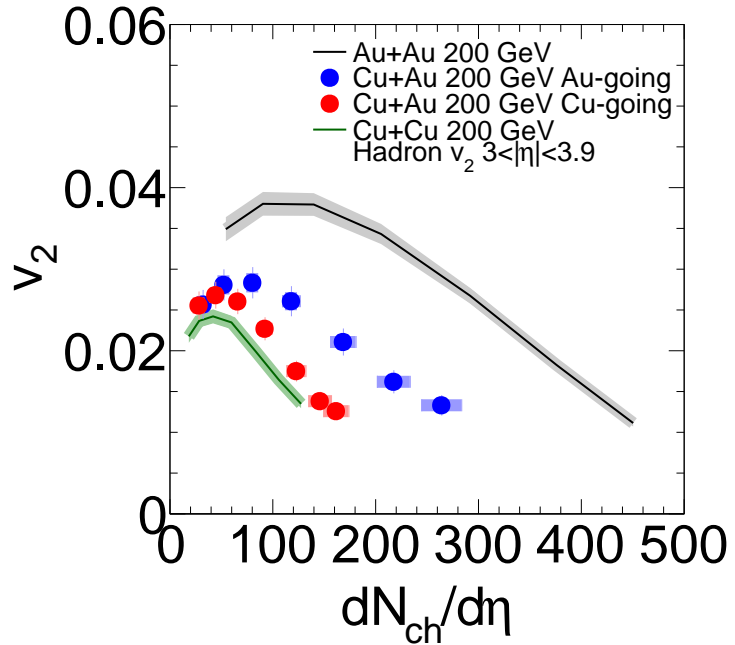


Figure 5.14: Forward/backward-rapidity v_2 for charged hadrons as a function of $dN_{ch}/d\eta$ measured at forward/backward rapidity($3 < |\eta| < 3.9$) in Au+Au, Cu+Au and Cu+Cu collisions.

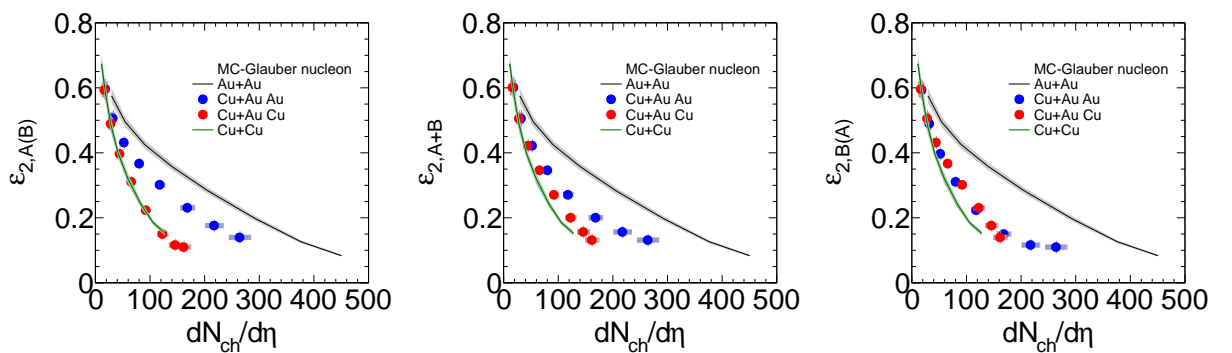


Figure 5.15: $\varepsilon_{2,A(B)}$, $\varepsilon_{2,A+B}$ and $\varepsilon_{2,B(A)}$ as a function of forward/backward $dN_{ch}/d\eta$ at $\sqrt{s_{NN}} = 200$ GeV in Au+Au, Cu+Au and Cu+Cu collisions.

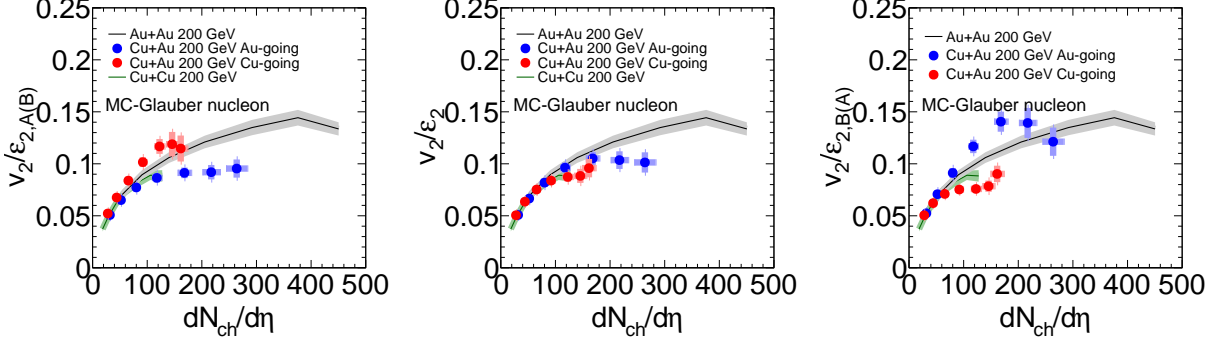


Figure 5.16: $v_2/\varepsilon_{2,A(B)}$ (Left), $v_2/\varepsilon_{2,A+B}$ (Middle) $v_2/\varepsilon_{2,B(A)}$ (Right) as a function of $dN/d\eta$ at forward/backward rapidity($3 < |\eta| < 3.9$) in Au+Au, Cu+Au and Cu+Cu collisions at $\sqrt{s_{NN}} = 200\text{GeV}$.

v_2 measurements, the forward/backward asymmetry of v_3 in Cu+Au collisions is scaled with the common eccentricity. We also test the scaling of the forward/backward v_3 with the eccentricity ranging from $\varepsilon_{3,Cu}$ to $\varepsilon_{3,Au}$, ($\varepsilon_{3,Cu} \leq \varepsilon_{3,Au-going}, \varepsilon_{3,Cu-going} \leq \varepsilon_{3,Au}$). In Fig. 5.23, the scaled v_3 values in Au+Au and Cu+Au collisions are shown. In all panel, the scaled v_3 in Au+Au and Cu+Au collisions increase from the peripheral to the central collisions. The values of the scaled v_3 in Au+Au collisions are common in all panels. For the Cu+Au collisions, the $\varepsilon_{3,Au-going}$ varies from the $\varepsilon_{3,Cu}$ to the $\varepsilon_{3,Au}$ from the bottom to the top row and the $\varepsilon_{3,Cu-going}$ varies from the $\varepsilon_{3,Cu}$ to the $\varepsilon_{3,Au}$ from the left to the right column. Thus the scaled $v_{3,Au-going}$ decreases from the bottom to the top row and the $v_{3,Cu-going}$ decreases from the left to the right column. From the bottom right to the top left, the ordering of the scaled v_3 magnitudes at Au-going and Cu-going sides is reversed. In the middle of panels, the good agreements between the Au-going and Cu-going sides are seen as seen the v_2 measurements. However, the discrepancy between Au+Au and Cu+Au collisions is seen except for the top right panel where the eccentricities for Au-going and Cu-going are $\varepsilon_{3,Au}$. In Fig. 5.24, the χ^2/NDF contour distributions for $w_{Au-going}$ vs $w_{Cu-going}$ are shown. The χ^2/NDF is estimated for evaluating the difference between the Au-going and the Cu-going side v_3/ε_3 . The χ^2/NDF increases at the top left and bottom right. The lower values of the χ^2/NDF are around $w_{Au} \sim w_{Cu}$ range as seen in the v_2 measurements. Fig. 5.25 shows the χ^2/NDF contour distributions given by the difference between Au+Au and Cu+Au collisions. The χ^2/NDF for the Au-going and Cu-going sides are shown in the left side panel and the right side panel, respectively. In both panel, the values of χ^2/NDF decrease from the low to the large weight. Unlike the χ^2/NDF for the v_2 measurements, a minimum point is not seen in both of panels, which might indicates the Glauber Monte Carlo model is not favored for the third order eccentricity.

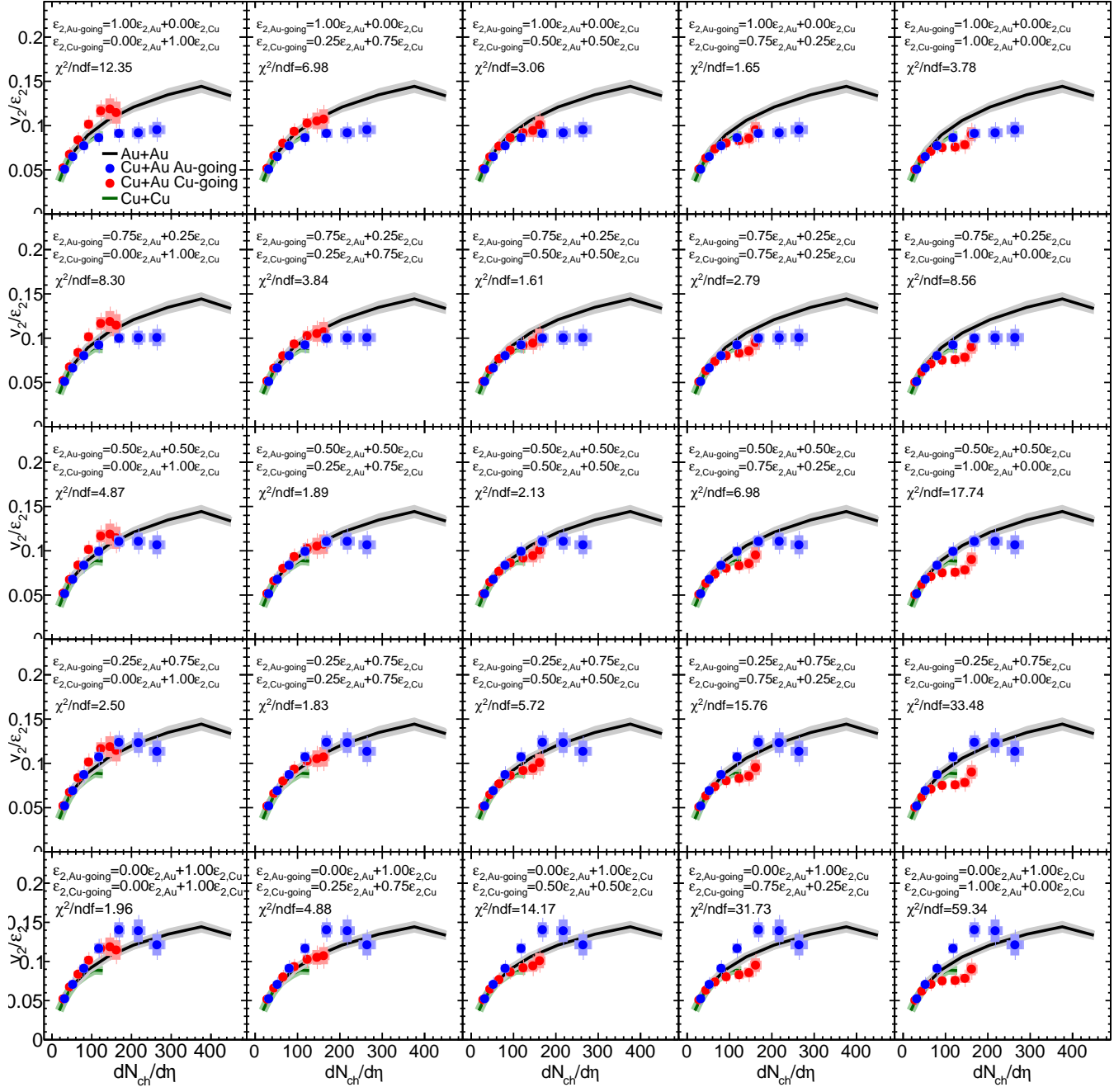


Figure 5.17: v_2/ε_2 as a function of $dN_{ch}/d\eta$ at measured rapidity region ($3 < |dN_{ch}/d\eta| < 3.9$) in Au+Au, Cu+Au(Cu-going, Au-going) and Cu+Cu collisions. ε_2 for Cu+Au collisions is defined as $\varepsilon_{2,Au(Cu)-going} = w_{Au(Cu)-going}\varepsilon_{2,Au} + (1 - w_{Au(Cu)-going})\varepsilon_{2,Cu}$

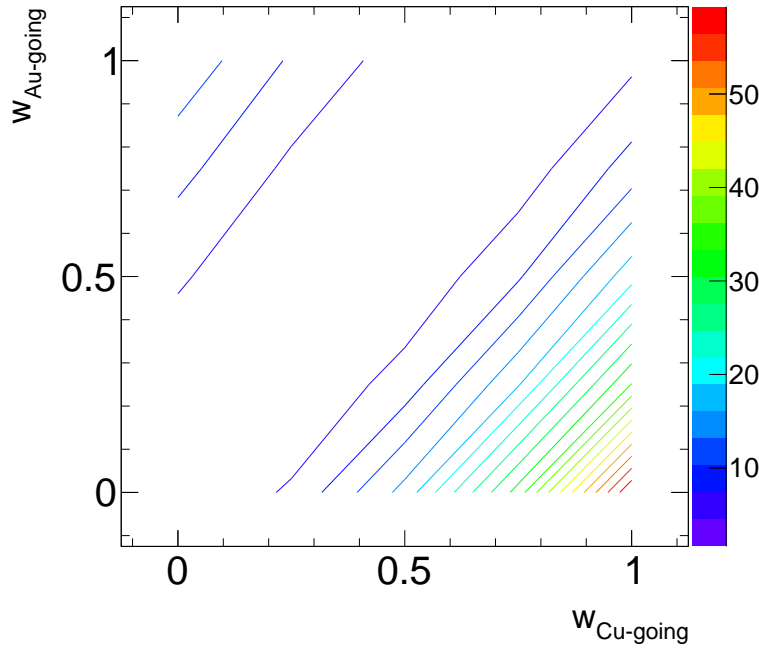


Figure 5.18: χ^2/NDF contour distribution for $w_{\text{Cu-going}}$ vs $w_{\text{Au-going}}$. χ^2/NDF is obtained from the difference between the Cu-going and the Au-going side v_2 .

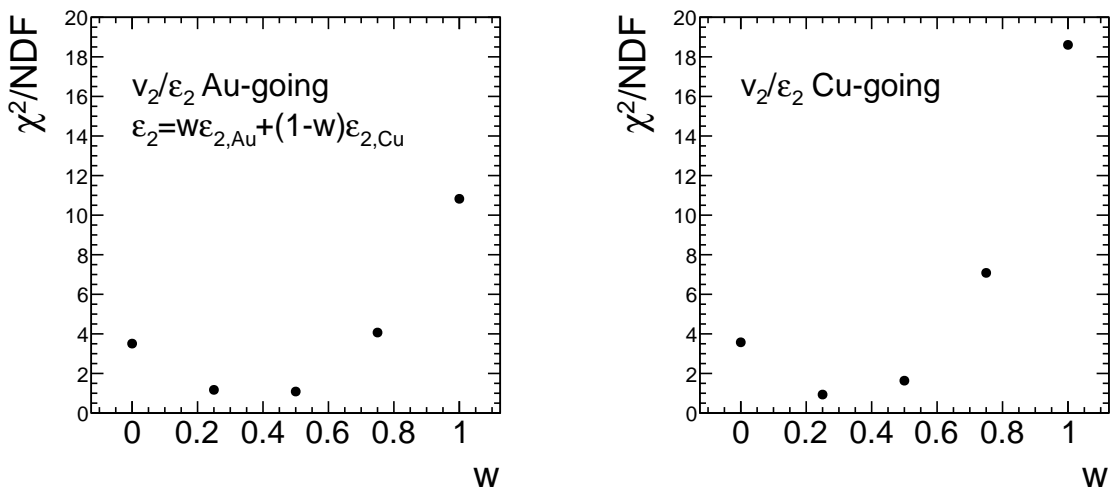


Figure 5.19: χ^2/NDF as a function of weight for the Au-going and the Cu-going side. χ^2/NDF is obtained from the difference between Cu+Au and Au+Au collisions

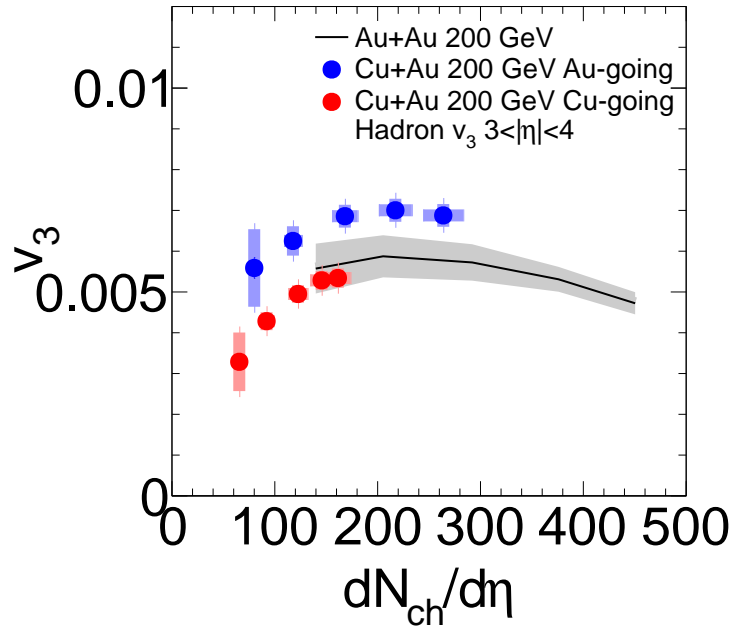


Figure 5.20: Forward/backward-rapidity v_3 for charged hadrons as a function of $dN_{ch}/d\eta$ measured at forward/backward rapidity ($3 < |\eta| < 3.9$) in Au+Au and Cu+Au collisions.

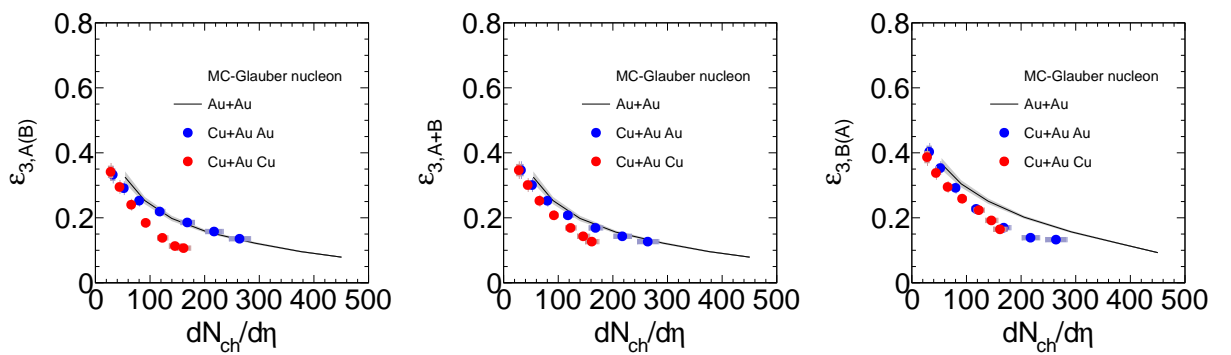


Figure 5.21: $\varepsilon_{3,A(B)}$, $\varepsilon_{3,A+B}$ and $\varepsilon_{3,B(A)}$ as a function of forward/backward $dN_{ch}/d\eta$ at $\sqrt{s_{NN}} = 200$ GeV in Au+Au and Cu+Au collisions.

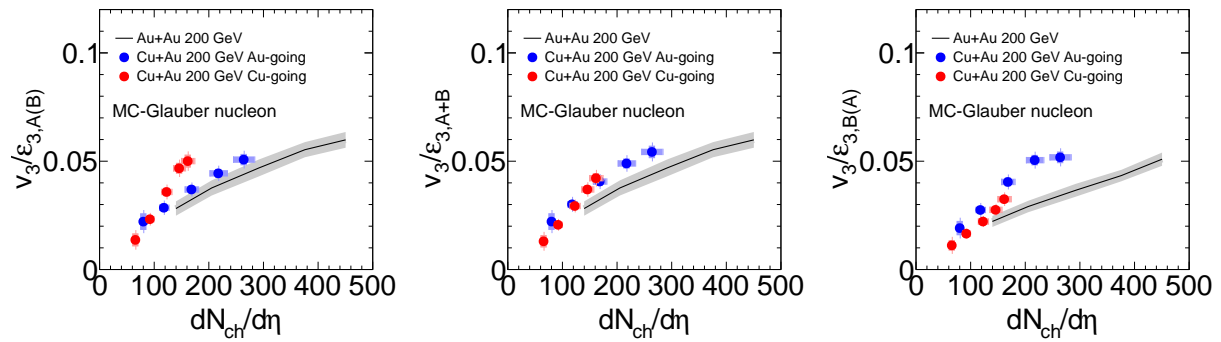


Figure 5.22: $v_3/\varepsilon_{3,A(B)}$ (Left), $v_3/\varepsilon_{3,A+B}$ (Middle) $v_3/\varepsilon_{3,B(A)}$ (Right) as a function of $dN/d\eta$ at forward/backward rapidity ($3 < |\eta| < 3.9$) in Au+Au, Cu+Au and Cu+Cu collisions at $\sqrt{s_{NN}} = 200$ GeV.

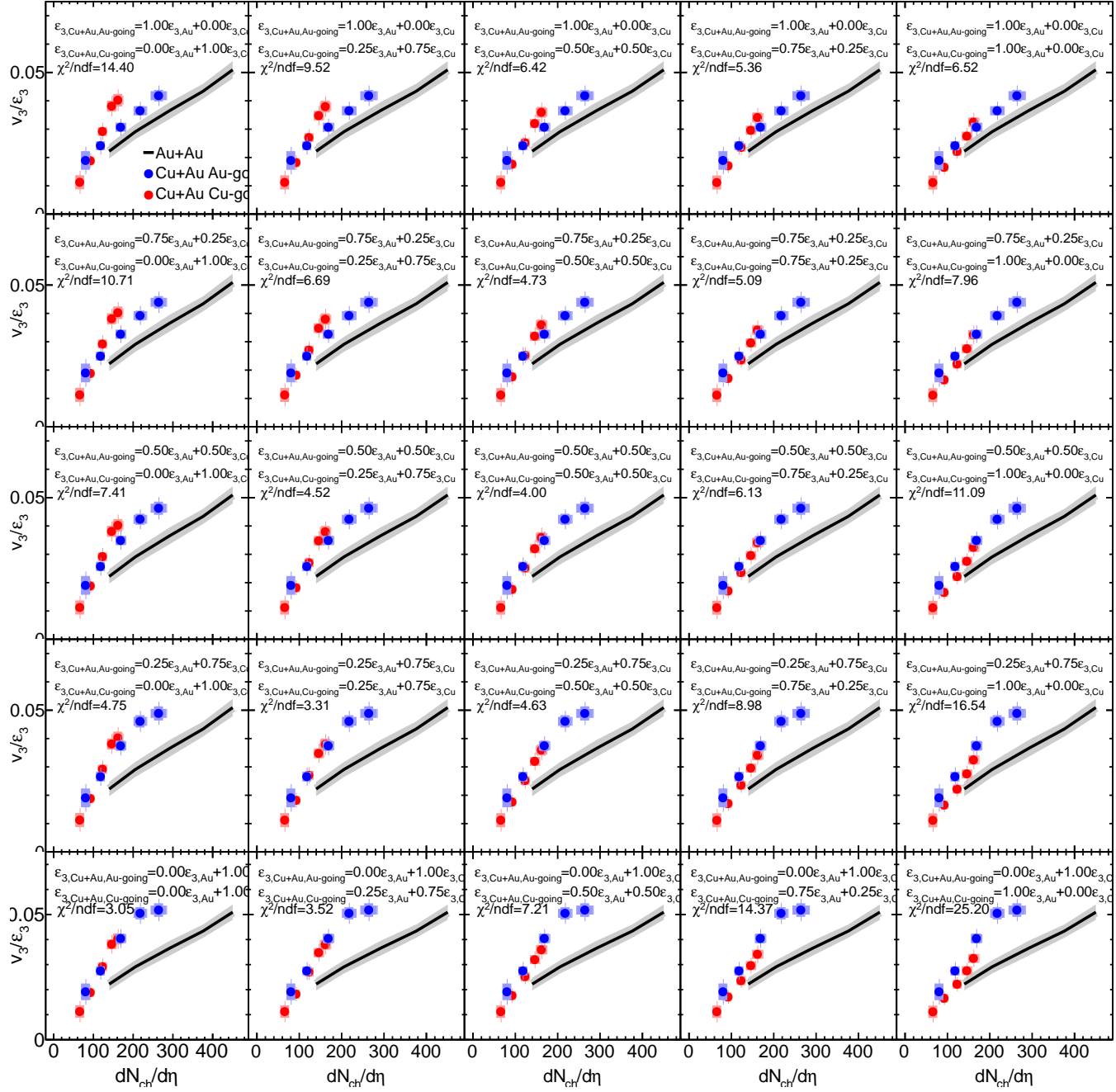


Figure 5.23: v_3/ϵ_3 as a function of $dN_{ch}/d\eta$ at measured rapidity region ($3 < |dN_{ch}/d\eta| < 3.9$) in Au+Au and Cu+Au (Cu-going, Au-going) collisions. ϵ_3 for Cu+Au collisions is defined as $\epsilon_{3,Cu(Au)-going} = w_{Au(Cu)-going}\epsilon_{3,Au} + (1 - w_{Au(Cu)-going})\epsilon_{3,Cu}$

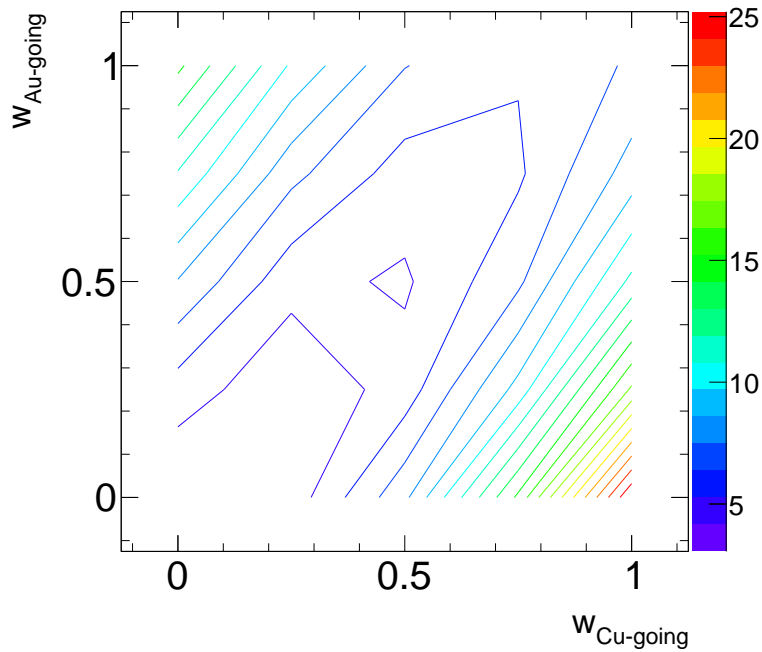


Figure 5.24: χ^2/NDF contour distribution for $w_{\text{Cu-going}}$ vs $w_{\text{Au-going}}$. χ^2/NDF is obtained from the consistency between the Cu-going and the Au-going side v_3

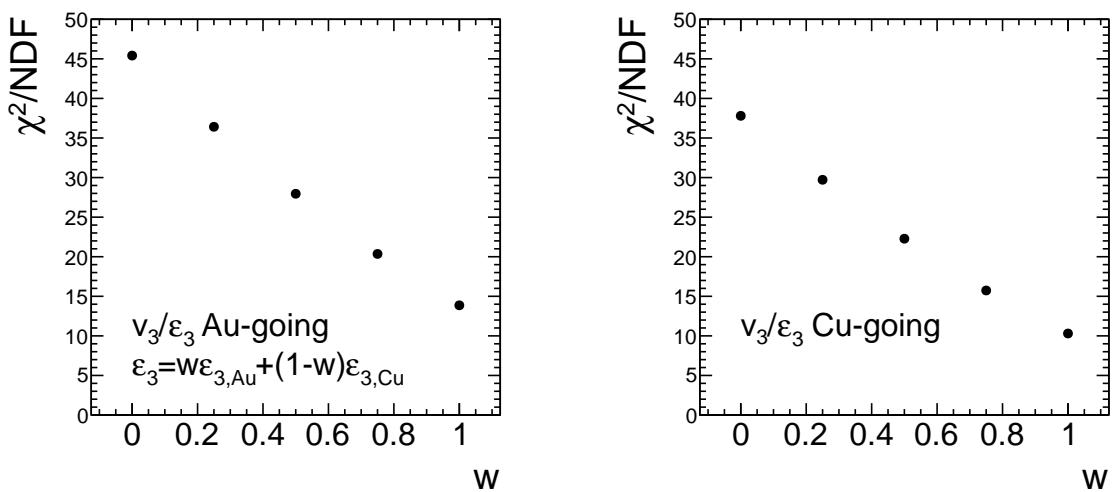


Figure 5.25: χ^2/NDF as a function of weight for the Au-going and the Cu-going side. χ^2/NDF is obtained from the consistency between Cu+Au and Au+Au collisions

5.4 Theory comparison

-A Multiphase Transport Model(AMPT)

For the study of azimuthal anisotropy in relativistic heavy ion collisions, the A-Multiphase-Transport Model(AMPT) generator[50] is a useful simulation tool. In the AMPT model, initial partonic interaction and final hadronic interaction are included. For the initial condition, the AMPT model uses the heavy ion jet interaction generator(HIJING) to produce the minijet(hard process) and excited strings(soft process). The excited strings are melted into partons. After the partons are generated in the nucleus-nucleus collisions, Zhang's parton cascade(ZPC) to describe multiple-interaction of partons, which is followed by a quark coalescence model in which hadrons are formed from quarks that are closest in phase space for a hadronization process. In the AMPT models, the parton cascade stage corresponds to the hydrodynamic stage in hydrodynamic model. After hadronization from partons, a relativistic transport(ART) is employed as describing scattering among the formed hadrons. In Fig. 5.26, the interaction process and the models used in AMPT is summarized.

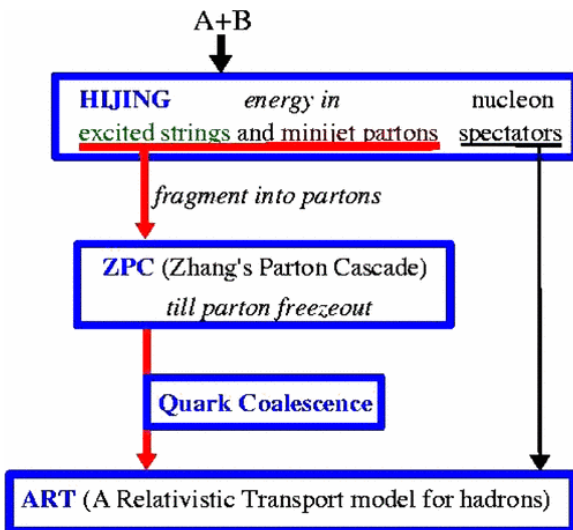


Figure 5.26: Structure of AMPT model

-Event by event hydrodynamic calculation

For v_n measurements in Cu+Au collisions at $\sqrt{s_{NN}} = 200\text{GeV}$, event by event hydrodynamic calculations are available[51],[52]. In [51], on event by event Monte Carlo Glauber model generates the initial energy density and then hydrodynamic expansion with shear viscosity is followed until a freeze-out temperature. This model does not use hadronic cascade model which cause hadronic re-scattering after the hydrodynamic expansion. In [52], ideal hydrodynamics approach is employed in the QGP phase after initial geometry is generated from Monte Carlo Glauber model in each event. As an afterburner, hadronic cascade model, JAM is used for hadronic re-scattering.

Theory comparison for mid – rapidity $v_n(p_T)$

At low p_T region, the two hydrodynamic models predict directed flow is in Cu hemisphere side,

while at high p_T the two models predict directed flow is in Au hemisphere side in Fig. 5.27. In the theory comparison, the viscous hydrodynamic calculation with $\eta/s = 0.08$ [51] predicts stronger directed flow compared to the prediction from the ideal hydrodynamic calculation [52]. But basically, ideal hydrodynamics predict larger magnitude of azimuthal anisotropies than viscous hydrodynamics. However, the difference of the two theory calculations are not only viscous correction but also model composition such as whether hadronic cascade is turned on or not. Thus we can not conclude that the viscous correction make stronger directed flow signal. On the other hand, the AMPT shows the opposite p_T dependence of v_1 predicted by the hydrodynamic calculations. The AMPT predicts directed flow is in Au hemisphere side at low p_T and in Cu hemisphere side at high p_T . The $v_1(p_T)$ values are well reproduced by the ideal hydrodynamic calculation. However the v_1 measurement shows the large systematic uncertainties and small values at low p_T . Therefore we can not conclude whether many particle move to Cu hemisphere side or Au hemisphere side.

Theory comparison for $v_n(p_T)$ at mid – rapidity

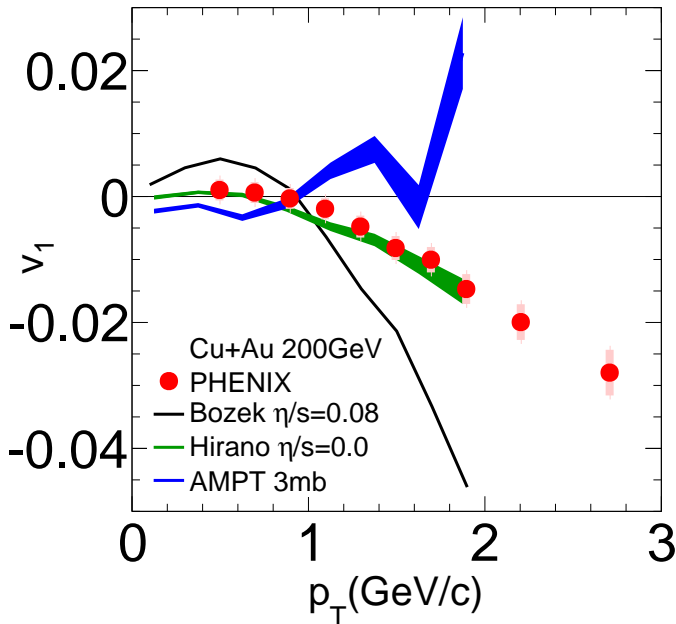


Figure 5.27: Charged hadron $v_1(p_T)$ measured at mid-rapidity in Cu+Au collisions at $\sqrt{s_{NN}} = 200\text{GeV}$ in comparison to theory calculations for 20-30% centrality class. The theory calculations shown in this figure are viscous hydrodynamic calculation with $\eta/s = 0.08$ (Bozek et al[51]), ideal hydrodynamic calculation(Hirano et al[52]) and AMPT model with $\sigma = 3\text{mb}$ parton cross section[50]

In Fig.5.28 and 5.29, the ideal hydrodynamic calculation [52] and the AMPT model with the values of parton cross section $\sigma = 3.0\text{mb}$ are compared to the experimental results. The ideal hydrodynamic calculation reproduce the experimental results for $p_T < 1\text{GeV}/c$. The v_n values from the ideal hydrodynamic increase with p_T due to no viscous correction. The AMPT

model well reproduce the v_2 values for $p_T < 1.5\text{GeV}/c$ except for 50-60% and the v_3 values for $p_T < 2\text{GeV}/c$.

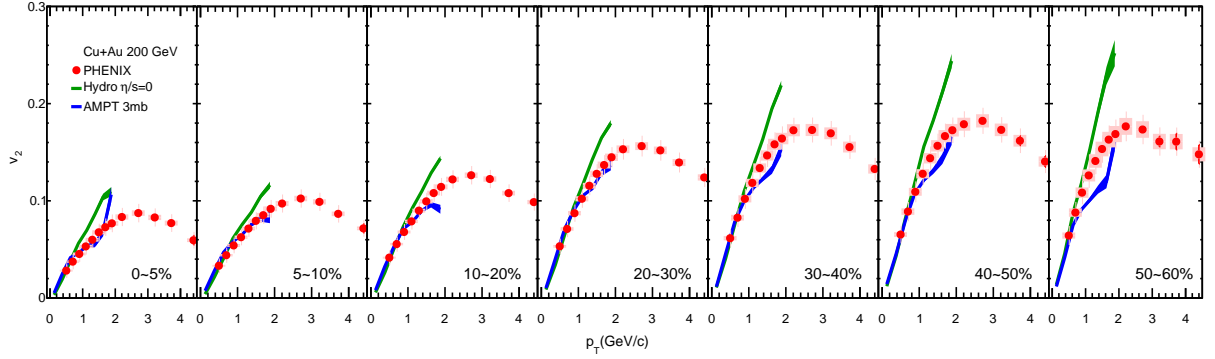


Figure 5.28: Charged hadron $v_2(p_T)$ measured at mid-rapidity in Cu+Au collisions at $\sqrt{s_{NN}} = 200\text{GeV}$ in comparison to theory calculations for different % centrality classes. The theory calculations shown in this figure are the ideal hydrodynamic calculation(Hirano et al[52]) and the AMPT model with $\sigma = 3\text{mb}$ parton cross section[50].

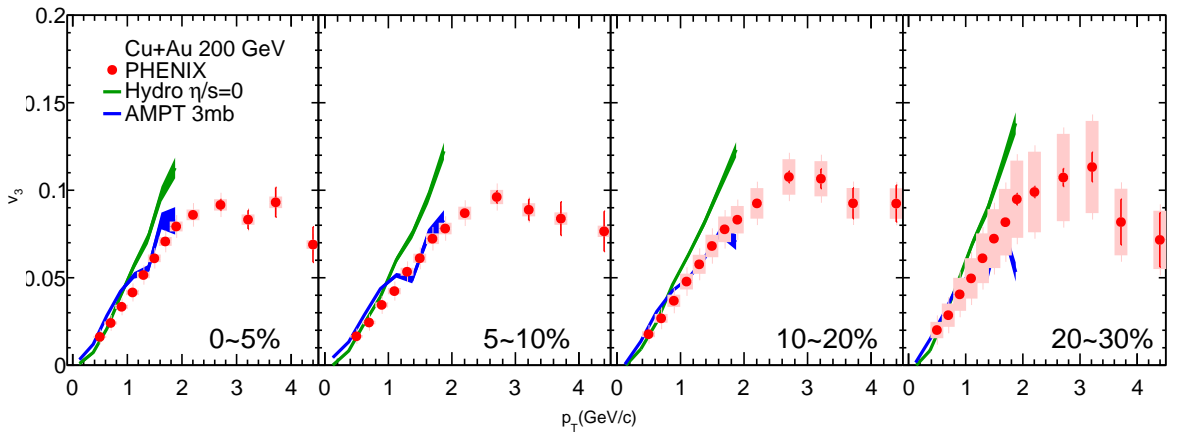


Figure 5.29: Charged hadron $v_3(p_T)$ measured at mid-rapidity in Cu+Au collisions at $\sqrt{s_{NN}} = 200\text{GeV}$ in comparison to theory calculations for different % centrality classes. The theory calculations shown in this figure are the ideal hydrodynamic calculation(Hirano et al[52]) and the AMPT model with $\sigma = 3\text{mb}$ parton cross section[50].

The $v_2(p_T)$ and $v_3(p_T)$ values are well predicted by the viscous hydrodynamic calculation[51] shown in Fig. 5.30 and Fig. 5.31. The viscous hydrodynamic calculation with the two different values of shear viscosity $\eta/s = 0.08, 0.16$ are shown. In 20-30% centrality class, viscous hydrodynamics with both of values reproduce v_n well. In the 0-5% centrality class, hydrodynamics with

$\eta/s = 0.08$ is closer to the experimental data.

Theory comparison for $v_n(\eta)$

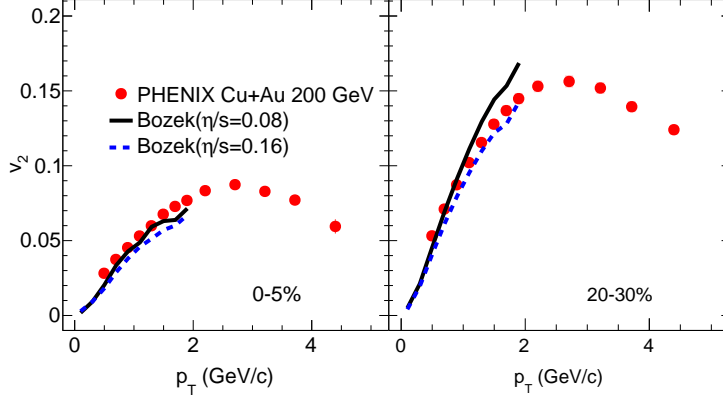


Figure 5.30: Charged hadron $v_2(p_T)$ measured at mid-rapidity in Cu+Au collisions at $\sqrt{s_{NN}} = 200\text{GeV}$ in comparison to theory calculation for 0-5% and 20-30% centrality classes. The theory calculation shown in this figure is the viscous hydrodynamic calculation(Bozek et al[51])

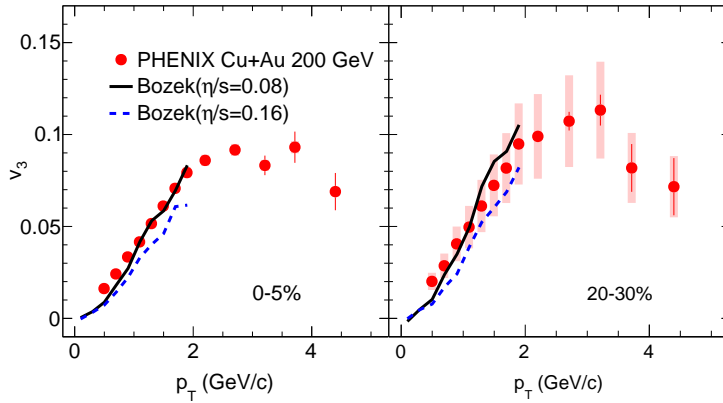


Figure 5.31: Charged hadron $v_3(p_T)$ measured at mid-rapidity in Cu+Au collisions at $\sqrt{s_{NN}} = 200\text{GeV}$ in comparison to theory calculation for 0-5% and 20-30% centrality classes. The theory calculation shown in this figure is the viscous hydrodynamic calculation(Bozek et al[51])

In Fig.5.32 and 5.33, the $v_2(\eta)$ and $v_3(\eta)$ results are compared to the predictions from the ideal hydrodynamic calculation and the AMPT model with $\sigma = 3\text{mb}$. The ideal hydrodynamic calculation show the larger values of v_n due to no viscous correction. The AMPT model reproduce well in terms of forward/backward asymmetry in v_n . In Fig. 5.34 and 5.35, the ratios of Au-going v_n and Cu-going v_n as a function of centrality are shown and compared to the ideal hydrodynamic and the AMPT model calculations are shown. For the v_2 measurement, the maximum value of the ratio is around 20% at mid-central collisions, and the ratio becomes small at central and

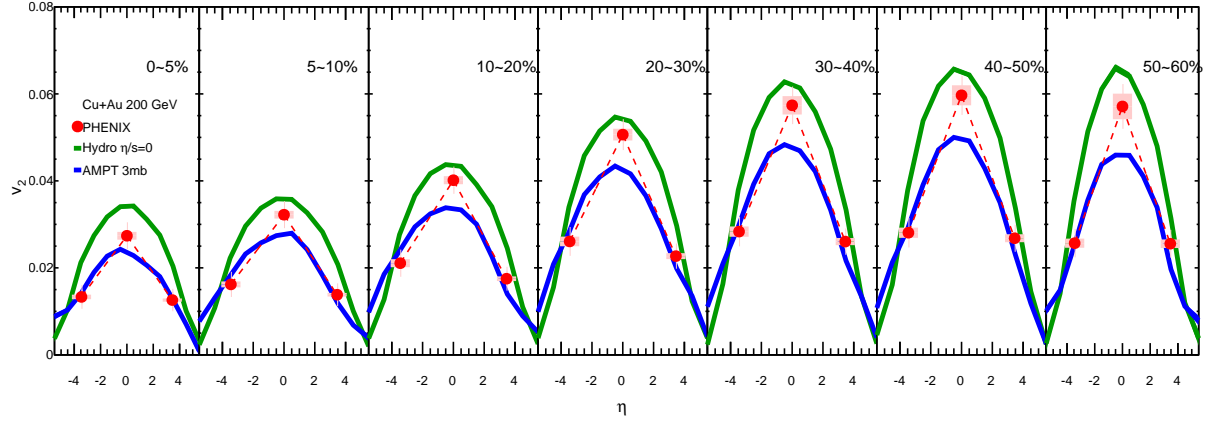


Figure 5.32: Charged hadron $v_2(\eta)$ measured in Cu+Au collisions at $\sqrt{s_{NN}} = 200\text{GeV}$ in comparison to theory calculations for different % centrality classes. The theory calculations shown in this figure are ideal hydrodynamic calculation(Hirano et al[52]) and AMPT model with $\sigma = 3\text{mb}$ parton cross section[50].

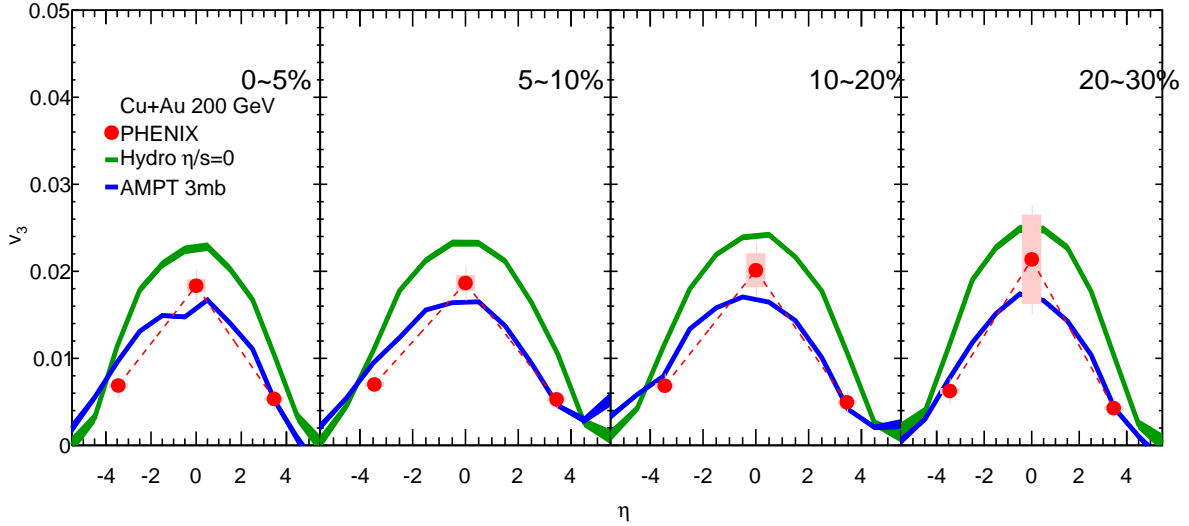


Figure 5.33: Charged hadron $v_3(\eta)$ measured in Cu+Au collisions at $\sqrt{s_{NN}} = 200\text{GeV}$ in comparison to theory calculations for different % centrality classes. The theory calculations shown in this figure are ideal hydrodynamic calculation(Hirano et al[52]) and AMPT model with $\sigma = 3\text{mb}$ parton cross section[50].

peripheral collisions. The ideal hydrodynamic calculation show similar values as seen in the experimental data. However the forward and backward asymmetry is still remained at peripheral collisions with flatter centrality dependence. The AMPT model predict larger values of forward and backward asymmetry except for central collisions. Like the ideal hydrodynamic calculation,

the large forward and backward asymmetry is still remained at peripheral collisions in the AMPT calculation. For the v_3 measurements, the value of the ratio of forward and backward v_3 slightly increase from central to mid-central collisions. The ideal hydrodynamic calculation underpredicts the values of v_3 ratio. On the other hand, the AMPT model calculation overpredicts the values of the ratio.

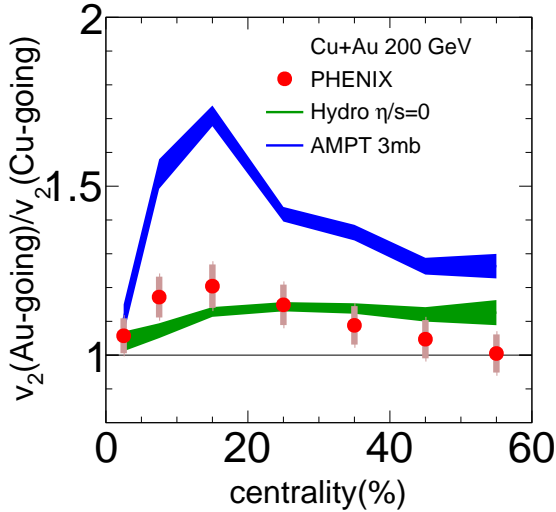


Figure 5.34: The ratio of forward/backward v_2 values as a function of centrality in Cu+Au collisions at $\sqrt{s_{NN}} = 200\text{GeV}$ in comparison to the theory calculations. The theory calculations shown in this figure are ideal hydrodynamic calculation(Hirano et al[52]) and AMPT model with $\sigma = 3\text{mb}$ parton cross section[50].

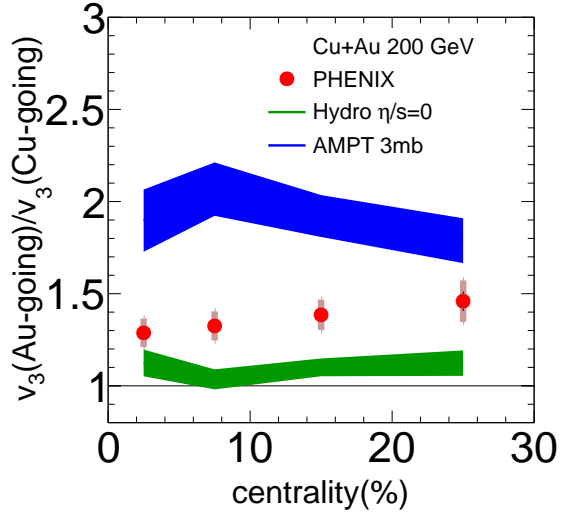


Figure 5.35: The ratio of forward/backward v_3 values as a function of centrality in Cu+Au collisions at $\sqrt{s_{NN}} = 200\text{GeV}$ in comparison to the theory calculations. The theory calculations shown in this figure are ideal hydrodynamic calculation(Hirano et al[52]) and AMPT model with $\sigma = 3\text{mb}$ parton cross section[50].

Chapter 6

Conclusion

We have measured the directed flow v_1 , elliptic flow v_2 , and triangular flow v_3 for charged hadrons, pions, kaons and protons at mid-rapidity ($|\eta| < 0.35$) in Cu+Au collisions at $\sqrt{s_{NN}} = 200\text{GeV}$ and the v_2 and v_3 for charged hadrons at forward and backward-rapidity ($3 < |\eta| < 3.9$) in Au+Au, Cu+Au and Cu+Cu collisions at $\sqrt{s_{NN}} = 200\text{GeV}$ by the PHENIX experiment at RHIC using event plane techniques.

At mid-rapidity, the measurements of charged hadron v_1 , v_2 and v_3 in Cu+Au collisions were performed as a function of transverse momentum p_T over a wide range of collision centralities. p_T integrated v_2 and v_3 were also measured as a function of the number of participants N_{part} . We found the following features of charged hadron v_n in Cu+Au collisions,

- The negative v_1 is observed at high p_T , which means the more number of high p_T particles are emitted toward the Au spectator side.
- The v_2 and v_3 have similar p_T dependence, centrality and N_{part} dependence as seen in Au+Au and Cu+Cu collisions
- The v_2 is always between Au+Au and Cu+Cu results
- The v_3 is similar to the Au+Au results

We also measured particle identified, π , K and p , v_n ($n = 1 \sim 3$) at mid-rapidity in Cu+Au collisions. In the identified particle measurements, particle mass ordering was observed for all three harmonics at low p_T as predicted by hydrodynamics. Baryon/mass splitting was also observed for 2nd and 3rd harmonics, but not observed for first harmonic. By studying with Monte Carlo Glauber model and Blast wave model for interpreting the negative v_1 at high p_T , we found the larger pressure gradient is Au nucleus side, which push more particles to high p_T region. We performed the eccentricity scaling of v_n with Monte Carlo Glauber model, v_n/ε_n , to study the initial spatial geometry. At mid-rapidity, the consistency of the scaled v_2 among Au+Au, Cu+Au and Cu+Cu collisions is seen. On the other hand, the eccentricity scaling of v_3 shows the discrepancy between Au+Au and Cu+Au collisions.

At forward/backward-rapidity, the measurements of the charged hadron v_2 in Au+Au, Cu+Au and Cu+Cu collisions and v_3 in Au+Au and Cu+Au collisions were performed. Charged particle multiplicity $dN/d\eta$ at in Au+Au, Cu+Au and Cu+Cu collisions were also measured. The

charged hadron v_2 and v_3 were plotted as a function of pseudo-rapidity η over a wide range of collision centralities and as a function of the $dN_{\text{ch}}/d\eta$. In Cu+Au collisions, the main features of v_n and $dN_{\text{ch}}/d\eta$ are following,

- The v_2 at Au-going side is larger than that at Cu-going for mid-central collisions, $v_{2,\text{Cu-going}} < v_{2,\text{Au-going}}$
- The v_2 at Au-going side becomes similar to that at Cu-going for most-central and peripheral collisions, $v_{2,\text{Cu-going}} \sim v_{2,\text{Au-going}}$
- Both of Au-going and Cu-going side v_2 are between those in Au+Au and Cu+Cu collisions, $v_{2,\text{Cu+Cu}} < v_{2,\text{Cu-going}}, v_{2,\text{Au-going}} < v_{2,\text{Au+Au}}$
- The v_3 at Au-going side is larger than that at Cu-going, $v_{3,\text{Cu-going}} < v_{3,\text{Au-going}}$
- Compared to the Au+Au collision results, the Au-going side v_3 is larger and the Cu-going side v_3 is smaller, $v_{3,\text{Cu-going}} < v_{3,\text{Au+Au}} < v_{3,\text{Au-going}}$
- The $dN_{\text{ch}}/d\eta$ at Au-going side is larger than that at Cu-going side $dN/d\eta(\text{Cu-going}) < dN/d\eta(\text{Au-going})$

For studying of the forward/backward asymmetry of v_n and $dN/d\eta$, we introduced weighted N_{part} scaling for $dN_{\text{ch}}/d\eta$ and weighted ε_n scaling for v_n are tested based on the Glauber Monte Carlo, where the weighted average of N_{part} and ε_n are calculated with Cu-participants and Au-participants with varying the relative contributions between Cu and Au nuclei. By performing the weighted N_{part} scaling, we found that the $dN_{\text{ch}}/d\eta$ at Au-going side is described by both of $N_{\text{part,Au}}$ and $N_{\text{part,Cu}}$ and the $dN_{\text{ch}}/d\eta$ at Cu-going side is mainly determined $N_{\text{part,Cu}}$. From the weighted ε_n scaling, we found that the forward/backward asymmetry of v_n in Cu+Au collisions mainly arises from the forward/backward asymmetry of $dN/d\eta$ which is supposed to be proportional to the initial energy density, and the forward/backward rapidity v_n is originated from the common initial spatial anisotropy ε_n .

The measurements of inclusive charged hadron v_n were compared to theoretical predictions. In the measurements of v_1 at mid-rapidity, the negative v_1 values at high p_T are observed with Cu beam spectator defining the sign of v_1 . The negative values of v_1 indicate that more particles are emitted in transverse plane preferentially toward the spectators from Au nucleus. The event by event ideal and viscous hydrodynamic calculations predict the positive values of v_1 at low p_T and the negative values of v_1 at high p_T as observed in the experimental data. Although the AMPT transport model reproduces the similar magnitude of the measured v_1 signals, the sign of v_1 is opposite compared with the experimental data. At low p_T , the AMPT models with parton cross section $\sigma = 3\text{mb}$ reproduces the elliptic flow and triangular flow at mid-rapidity in Cu+Au collisions. The event by event viscous hydrodynamic calculations with shear viscosity $\eta/s = 0.08 - 0.16$ also reproduce the measured v_2 and v_3 values at mid-rapidity in Cu+Au collisions. In case of the v_n measurements at forward/backward-rapidity for Cu+Au collisions, the event by event ideal hydrodynamic calculation reproduce the magnitude of forward/backward-rapidity v_2 and the forward/backward ratio of v_2 , but fails to explain the magnitude of the v_3 . Compared to the hydrodynamics, the magnitudes of v_2 and v_3 are better described by the AMPT.

Appendix A

intrinsic triangularity

A.1 $v_3(\Psi_1)$ at mid-rapidity

In Cu+Au collisions, the intrinsic triangularity which does not only come from the geometrical fluctuations but also from the shape of the overlap region is expected to provide the non zero value of $v_3(\Psi_1)$ at mid-rapidity. Figure A.1 shows the nucleon participant distributions in Au+Au and Cu+Au collisions for the impact parameter range $4 < b < 5$ fm. In Fig. A.1, the density of participant nucleons decrease from the center to the surface, the red area represent higher density and the blue area is lowest density. The black dashed circles represent the radii of Au nucleus ($R_{Au} = 6.38$) and Cu nucleus ($R_{Cu} = 4.2$). In the Au+Au collisions case, the overlap area is the symmetric elliptic shape. On the other hand, the overlap area in the Cu+Au collisions is the sideward asymmetric triangular shape. Thus in Cu+Au collisions, the initial triangular overlap shape will be converted into the triangular flow.

In order to measure the triangular flow driven by the triangular overlap region in Cu+Au collisions, the measurement of v_3 with respect to 1st order event plane determined from spectator neutrons is useful. If the $v_3(\Psi_1)$ shows non-zero values, the triangular overlap region leads to the triangular flow. Figure A.2 shows the azimuthal angle correlation between 3rd order participant plane $\Psi_{3,PP}$ and the angle of impact parameter $\Psi_{1,imp}$ which points toward Cu side as a function of centrality in Au+Au and Cu+Au collisions at $\sqrt{s_{NN}} = 200$ GeV simulated by Monte Carlo Glauber model. The values of the participant event plane correlation in Au+Au collision are zero due to the sideward symmetric overlap region. In Cu+Au collisions, the correlation shows positive values and have centrality dependence. The values of the azimuthal correlation in Cu+Au collisions increase from the central to the mid-central collisions and then decrease with increasing with centrality. In Fig. A.3, the $v_3(\Psi_{1,Imp})$ at mid-rapidity as a function of p_T for different centrality classes in Cu+Au collisions calculated from the ideal hydrodynamics [52] and the combined parton cascade and hadron cascade model (AMPT) [50] are shown. In both of calculations, Glauber Monte Carlo simulation are used as the initial condition. Like the participant correlation shown in Fig. A.2, the ideal hydrodynamic calculation shows the positive values. The value of $v_3(\Psi_{1,Imp})$ from the ideal hydrodynamics increase with p_T , which is seen in the v_2 and v_3 p_T dependence. However AMPT does not show finite values. In Fig. A.4, $v_3(\Psi_{1,Imp})$ as a function of p_T measured without the resolution correction at mid-rapidity ($|\eta| < 0.35$) in

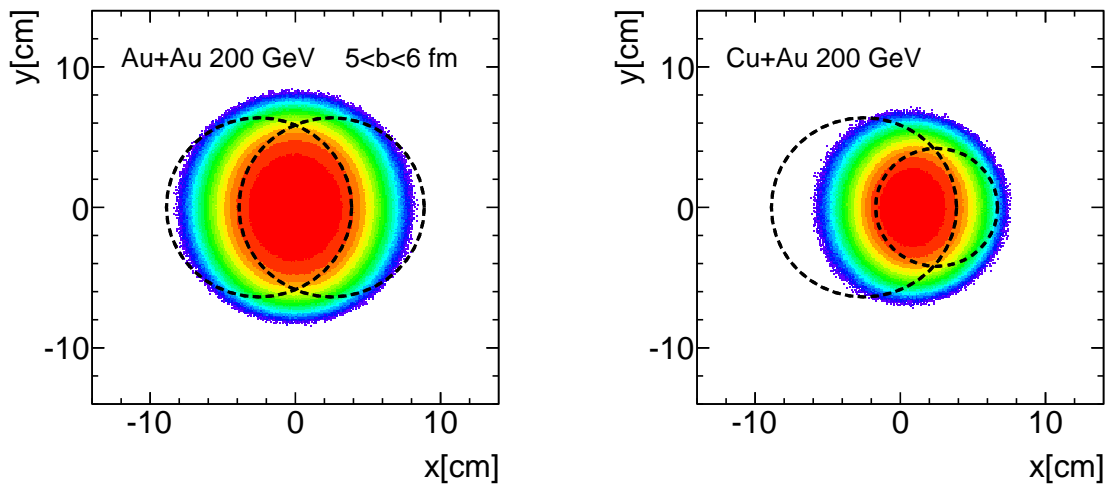


Figure A.1: Participant nucleon distributions for the impact parameter range $4 < b < 5$ in Au+Au and Cu+Au collisions at $\sqrt{s_{NN}} = 200$ GeV simulated by Monte Carlo Glauber model

Cu+Au collisions at $\sqrt{s_{NN}} = 200$ GeV. The values of the measured $v_3(\Psi_{1,\text{Imp}})$ are consistent with zero within the error.

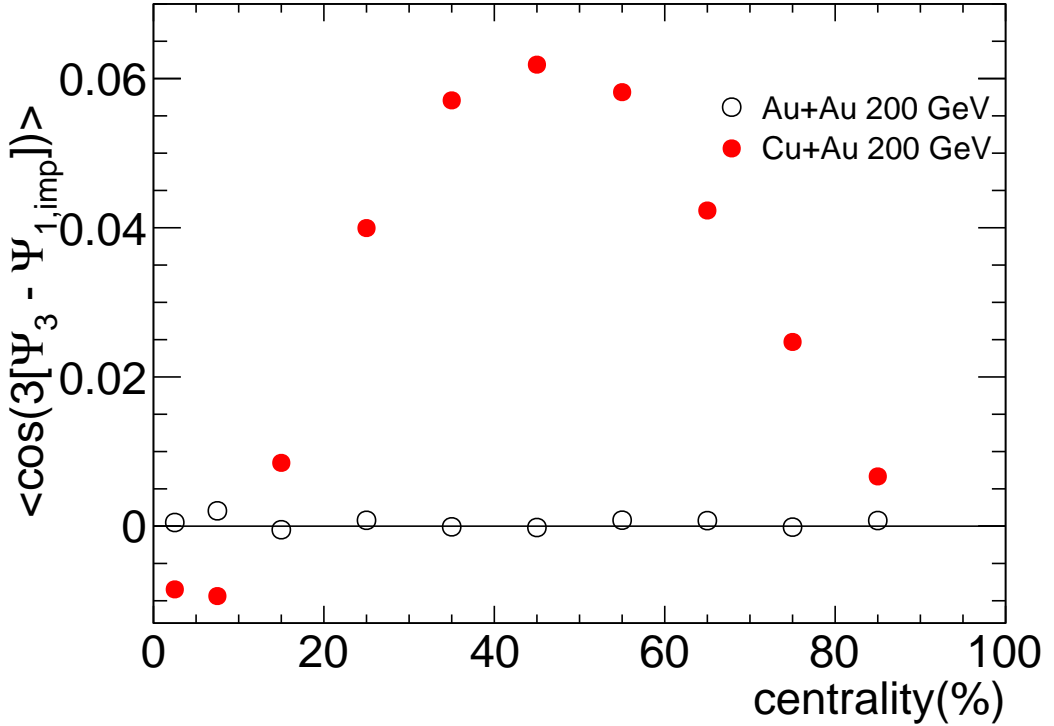


Figure A.2: Participant plane correlations between $\Psi_{3,PP}$ and the impact parameter $\Psi_{1,imp}$ in Au+Au and Cu+Au collisions

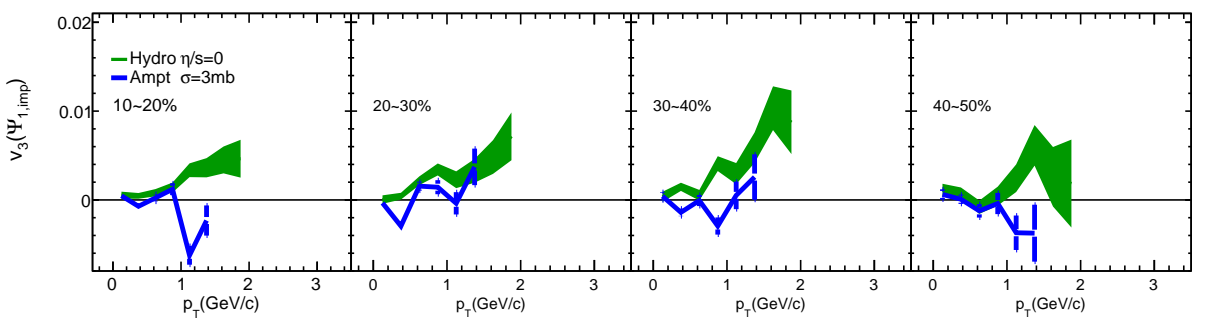


Figure A.3: $v_3(\Psi_{1,Imp})$ at mid-rapidity as a function of p_T in Au+Au and Cu+Au collisions at $\sqrt{s_{NN}} = 200\text{GeV}$ calculated from the ideal hydrodynamics and the AMPT.

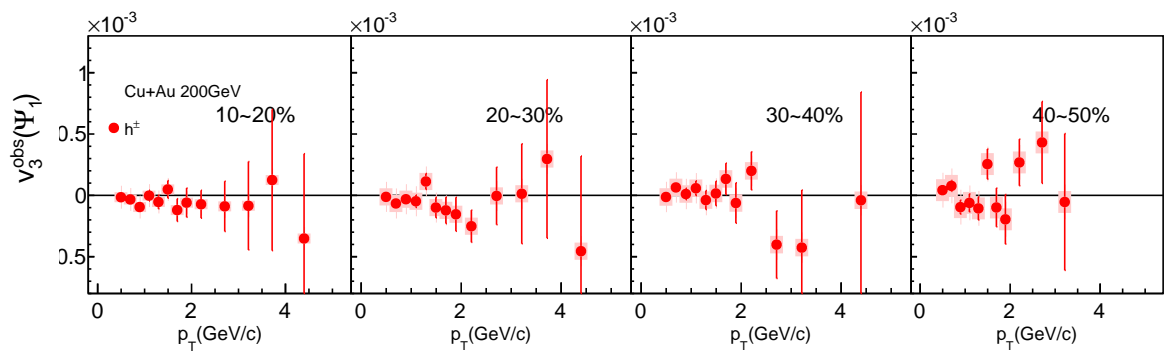


Figure A.4: $v_3(\Psi_1, \text{SMDs})$ as a function of p_T measured without the resolution correction at mid-rapidity ($|\eta| < 0.35$) in Au+Au and Cu+Au collisions at $\sqrt{s_{\text{NN}}} = 200\text{GeV}$

Appendix B

Initial geometry model

B.1 Initial geometry model dependence

One of the uncertainties in theory model calculation of relativistic heavy ion collision reaction is the initial geometry condition. Since azimuthal anisotropies are strongly affected by initial spatial geometry of nucleus-nucleus collisions, eccentricity scaling of v_n with different initial geometry models can provide further insights and hints for understanding initial geometry models. Historically, Monte Carlo Glauber model which describes initial spatial geometry with nucleon positions has been used as initial geometry. In our study, we compare nucleon base Monte Carlo Glauber model, quark base Monte Carlo Glauber model and IPGlasma model.

–Monte Carlo Glauber model : quark base

In $dN_{ch}/d\eta$ measurements, PHOBOS $dN_{ch}/d\eta$ data at mid-rapidity in Au+Au collisions at $\sqrt{s_{NN}} = 130$ and 200GeV are better described charged particle multiplicity at mid-rapidity in Au+Au collisions by scaling with number of participant constituent quarks, N_{qp} than number of participant nucleons, N_{part} [43]. Additionally, PHOBOS data are extended down to 62.4 and 19.6GeV and concluded the scaling with N_{qp} works well in the lower energies[45]. In PHENIX experiment, $dN_{ch}/d\eta$ at midrapidity is measured in various collision systems and energies[44],[47]. In Ref. [44] and [47], PHENIX verified the scaling with N_{qp} holds for Au+Au collisions from 200 to 7.7GeV, for Cu+Au 200GeV and for Cu+Cu collisions at 200 and 62.4 GeV.

In our study, the number of participant constituent quarks is estimated using a modified Monte Carlo Glauber model that treats multiple quark-quark collisions instead of multiple nucleon-nucleon collisions. First, the nuclei are assembled by the nucleons distributed according to a WoodsSaxon distribution. Second, the three constituent quarks are distributed around the center of each nucleon. The constituent quarks are distributed radially by an empirical function[47],

$$f(r) = r^2 \exp -4.27r(1.21466 - 1.888r + 2.03r^2)(1 + 1/r - 0.03/r^2)(1 + 0.15r) \quad (B.1)$$

where r is the radial distance of constituent quark in fm. Randomly the transverse positions of three constituent quarks in each nucleon are assigned to become a spherically symmetric distribution. Lastly, the center of mass of three constituent quarks in each nucleon is shifted to be the center of the nucleon position. The above empirical quark distribution is chosen

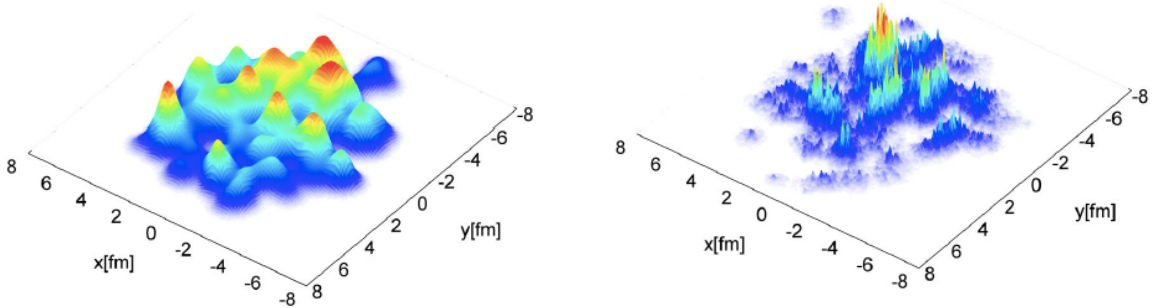


Figure B.1: Initial energy density in transverse plane for nucleon base Monte Carlo Glauber model and IPGlasma model. Left:nucleon base Monte Carlo Glauber model. Right:IPGlasma model [55]

to reproduce the measured the Fourier transform of the proton form factor in electron-proton elastic scattering[49]. If the distance between two centers of quarks in transverse plane is less than $\sqrt{\sigma_{\text{qq}}^{\text{inel}}/\pi}$ quark-quark collisions will occur.

$$d < \sqrt{\frac{\sigma_{\text{qq}}^{\text{inel}}}{\pi}} \quad (\text{B.2})$$

where $\sigma_{\text{qq}}^{\text{inel}} = 8.17\text{mb}$ is the inelastic quark-quark cross section. The $\sigma_{\text{qq}}^{\text{inel}}$ value is chosen to reproduce the inelastic nucleon nucleon cross section $\sigma_{\text{nn}} = 42\text{mb}$ at $\sqrt{s_{\text{NN}}} = 200\text{GeV}$.

-IPGlasma model : gluon base

The values of eccentricity in Au+Au and Cu+Au collisions in IPGlasma model which is a gluon base model are available[54]. At relativistic high energy, the density of gluons inside nucleus increase greatly. Both of nucleon base and quark base Monte Carlo Glauber models do not take into account this phenomena. Although quark base Monte Carlo Glauber model include fluctuations in nucleon and quark distributions, there are fluctuations in nucleon, auark gluon distributions in IPGlasma model. In Fig.B.1, initial energy density distributions in transverse plane for nucleon base Monte Carlo Glauber model and IPGlasma model are shown. The IPGlasma model have finner stuructures relative to the nucleon base Monte Carlo Glauber model. The quark base Monte Carlo Glauber model is considered to be in between the two models.

In Fig. B.2 and Fig. B.3, ϵ_n as a function of N_{part} for Au+Au, Cu+Au and Cu+Cu collisions at 200GeV in nucleon base Glauber Monte Carlo, quark base Glauber Monte Carlo and IPGlasma models are compared. In Au+Au collisions, ϵ_2 is largest in IPGlasma model and smallest in nucleon base Monte Carlo Glauber. Quark base Monte Carlo Glauber is always between them. In Cu+Au collisions, there is no significant difference between the three models. Because IPGlasma data points for Cu+Cu collisions are not available, we compare only the two Glauber Monte Carlo model. Like Cu+Au collisions, no model dependence is seen. For ϵ_3 , the model dependence is reversed. In Au+Au and Cu+Au collisions, nucleon base Monte Carlo Glauber shows the highest values of ϵ_3 , and IPGlasma shows the lowest values of ϵ_3 except for central collisions.

Fig. B.4 shows the scaled v_2 with ϵ_2 in nucleon base Monte Carlo Glauber, quark base Monte Carlo Glauber and IPGlasma models. In both of nucleon and quark base Glauber Monte Carlo

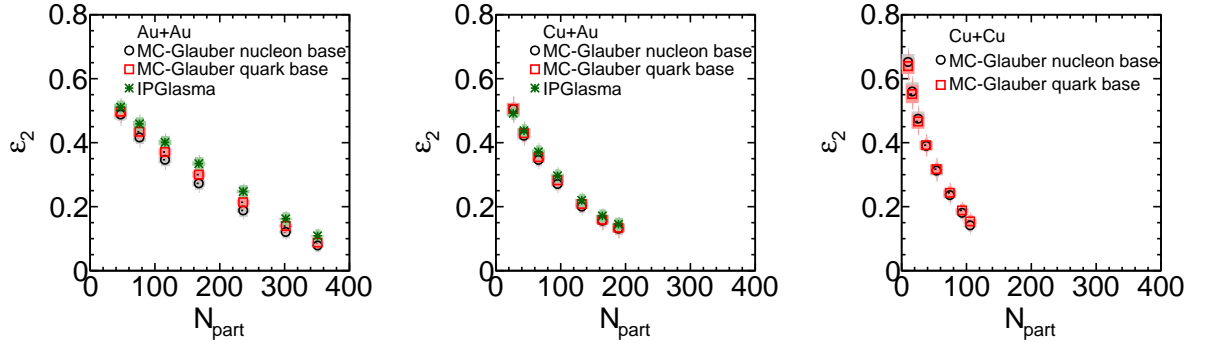


Figure B.2: ϵ_2 for Au+Au, Cu+Au and Cu+Cu collisions at 200GeV in nucleon base Glauber Monte Carlo, quark base Glauber Monte Carlo and IPGlasma models

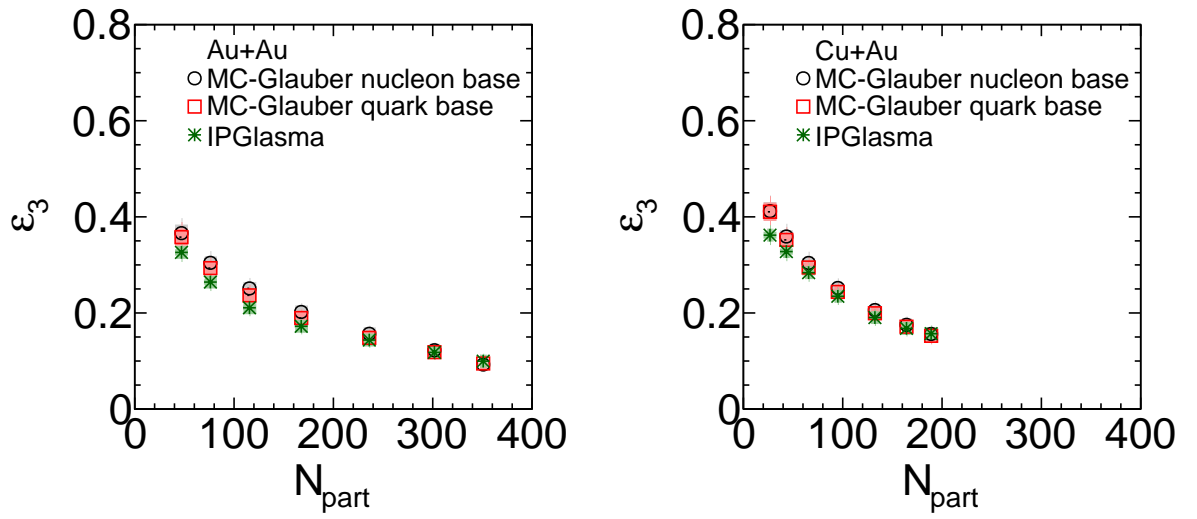


Figure B.3: ϵ_3 for Au+Au and Cu+Au collisions at 200GeV in nucleon base Glauber Monte Carlo, quark base Glauber Monte Carlo and IPGlasma models

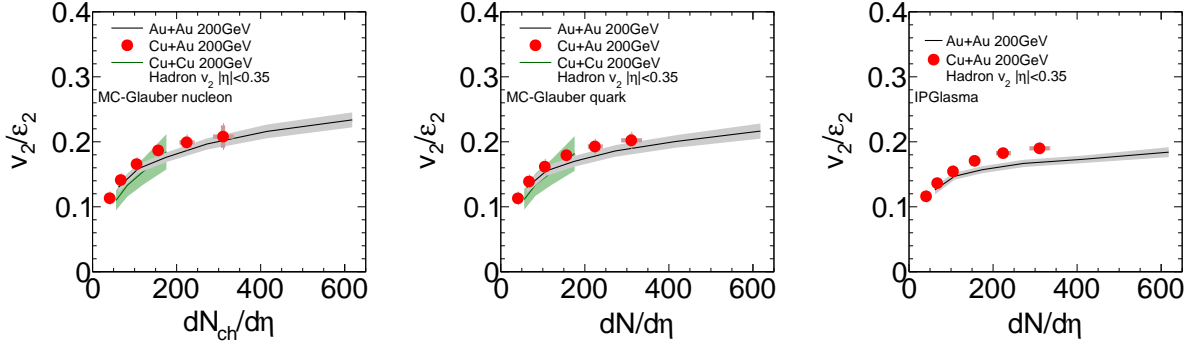


Figure B.4: Scaled v_2 for charged hadrons at mid-rapidity with ϵ_2 estimated in the three initial condition models in Au+Au, Cu+Au and Cu+Cu collisions at $\sqrt{s_{NN}} = 200\text{GeV}$. Left:Nucleon base Monte Carlo Glauber model, Middle:Quark base Monte Carlo Glauber model and Right:IPGlasma model

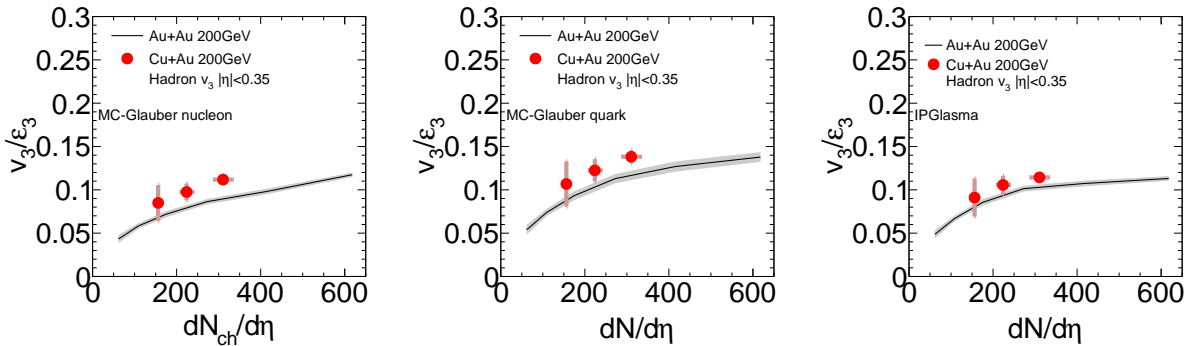


Figure B.5: Scaled v_3 for charged hadrons at mid-rapidity with ϵ_3 estimated in the three initial condition models in Au+Au and Cu+Au collisions at $\sqrt{s_{NN}} = 200\text{GeV}$. Left:Nucleon base Monte Carlo Glauber model, Middle:Quark base Monte Carlo Glauber model and Right:IPGlasma mode

models, a good agreement between all collision systems is seen. Conversely, the discrepancy between Au+Au and Cu+Au is seen in IPGlasma model.

In Fig. B.5, the scaled v_3 at mid-rapidity with ϵ_3 estimated from nucleon base Monte Carlo Glauber, quark base Monte Carlo Glauber and IPGlasma models in Au+Au and Cu+Au collisions at $\sqrt{s_{NN}} = 200\text{GeV}$. For the peripheral point in Cu+Au collisions, the scaled v_3 values in Cu+Au collisions are consistent with those in Au+Au collisions in all initial condition models. In IPGlasma model, the scaled v_3 values in central Cu+Au collisions are closer to those in Au+Au collisions compared to the results in the two Monte Carlo Glauber models.

We perform the eccentricity scaling of v_n at forward/backward rapidity. Fig. B.6 shows the scaled v_2 at forward/backward-rapidity with the $\epsilon_{2,A+B}$ in the three initial condition models. In all initial condition models, the forward and backward scaled v_2 with $\epsilon_{2,A+B}$ are consistent. For system size comparison, the scaled Cu-going v_2 in Cu+Au collisions is consistent with those in the symmetric collision systems for whole centrality classes in the three initial condition models. Although the Au-going v_2 is scaled well with the three initial condition models in mid-central and

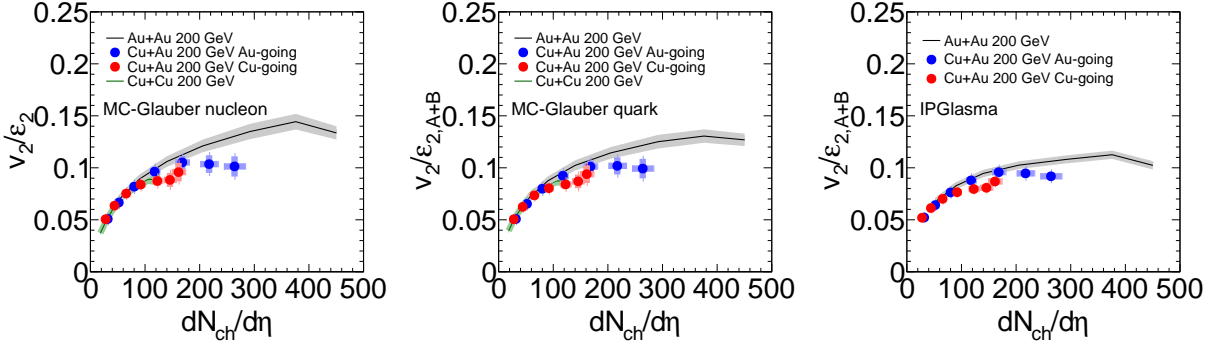


Figure B.6: Scaled v_2 for charged hadrons at forward/backward-rapidity with ϵ_2 estimated in the three initial condition models in Au+Au, Cu+Au and Cu+Cu collisions at $\sqrt{s_{NN}} = 200\text{GeV}$. Left:Nucleon base Monte Carlo Glauber model, Middle:Quark base Monte Carlo Glauber model and Right:IPGlasma mode

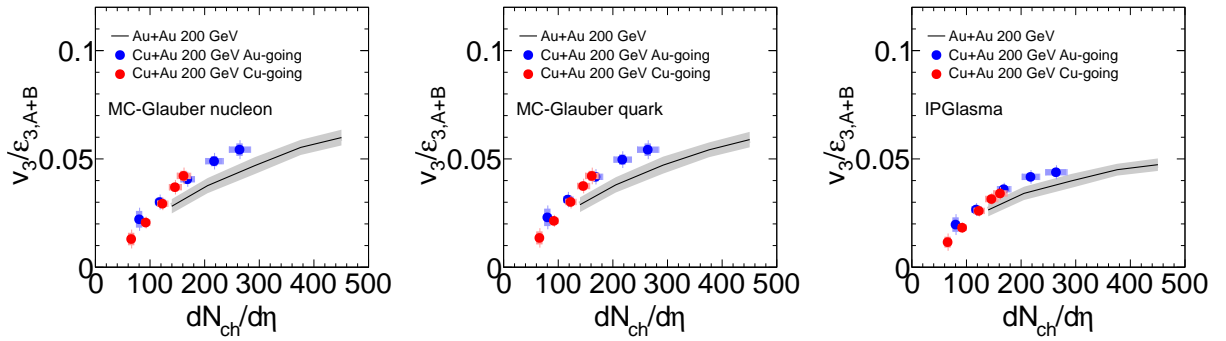


Figure B.7: Scaled v_3 for charged hadrons at forward/backward-rapidity with ϵ_3 estimated in the three initial condition models in Au+Au and Cu+Au collisions at $\sqrt{s_{NN}} = 200\text{GeV}$. Left:Nucleon base Monte Carlo Glauber model, Middle:Quark base Monte Carlo Glauber model and Right:IPGlasma mode

peripheral collisions, the scaled Au-going v_2 is somewhat worse in central collisions. However, the central Au-going $v_2/\epsilon_{2,A+B}$ with IPGlasma models in Cu+Au collisions is close to that in Au+Au collisions compared to the scaled v_2 in the other two models.

In Fig. B.7, the scaled v_3 at forward/backward-rapidity with ϵ_3 in nucleon base Monte Carlo Glauber model, quark base Monte Carlo Glauber model and IPGlasma model. Like the scaled v_2 results, a good agreement between Au-going and Cu-going v_3/ϵ_3 is seen in all initial condition models, and the colliding system difference is seen in mid-central and central collisions. However the scaled v_3 with $\epsilon_{3,A+B}$ in IPGlasma model in Cu+Au collisions is closer to that in Au+Au collisions for mid-central and central collisions compared to the other initial condition models.

Appendix C

Eccentricity and N_{part} scaling

C.1 Weighted eccentricity and N_{part} scaling of forward/backward v_n

In this section, we show the weighted eccentricity scaling of v_n as a function of weighted N_{part} at forward/backward-rapidity in Cu+Au collisions. In Fig. C.1, C.2, C.3 and C.4, the scaled v_n for Au-going side and Cu-going side are compared to the symmetric collision systems. In all figures, the weighted ε_n changes from $\varepsilon_{n,Cu}$ to $\varepsilon_{n,Au}$ and the weighted N_{part} changes from $2N_{part,Cu}$ to $2N_{part,Au}$ from the left to the right column.

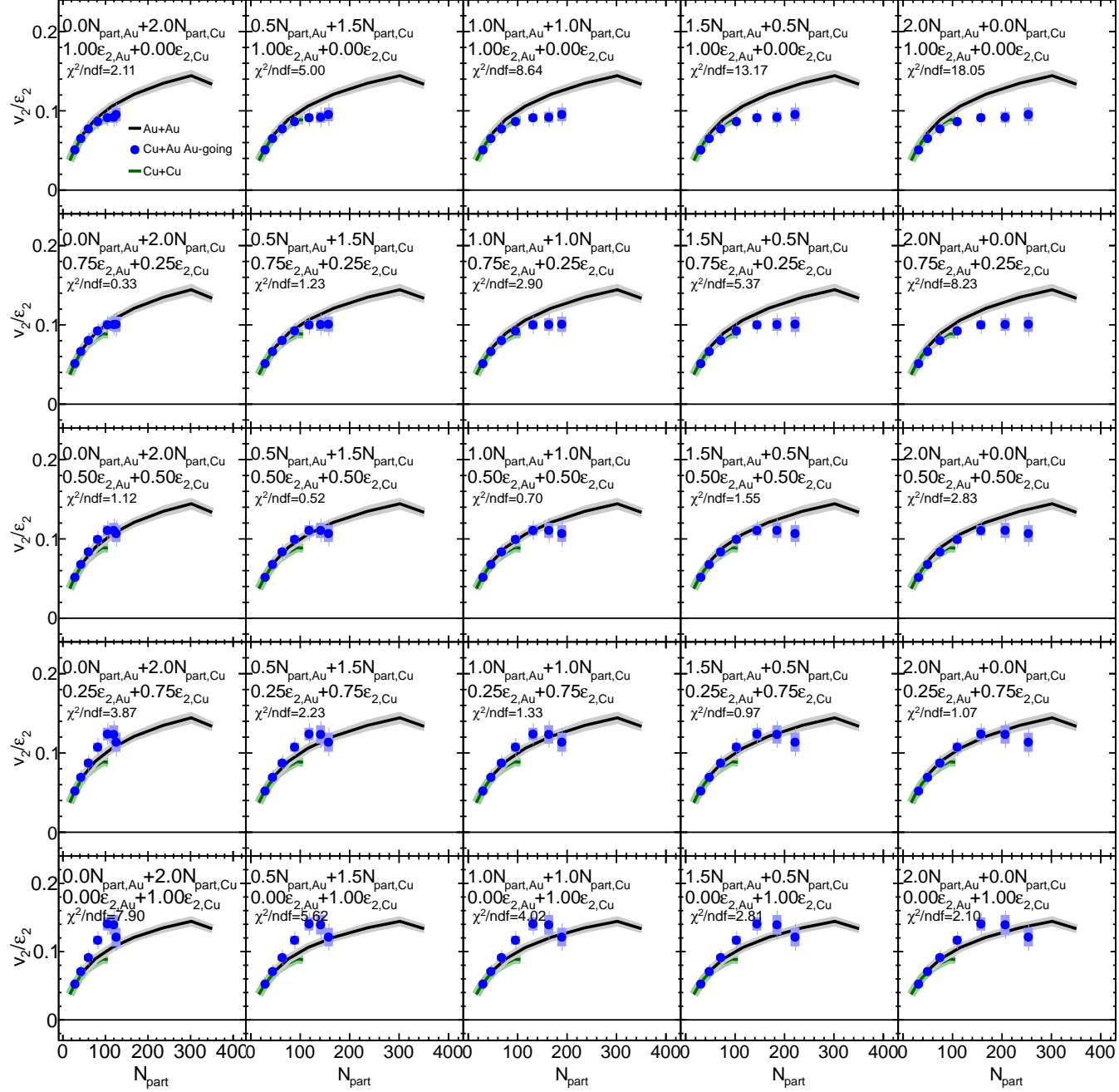


Figure C.1: Weighted eccentricity scaling of v_2 as a function of weighted N_{part} for Au-going side in Cu+Au collisions compared to the Au+Au and Cu+Cu results.

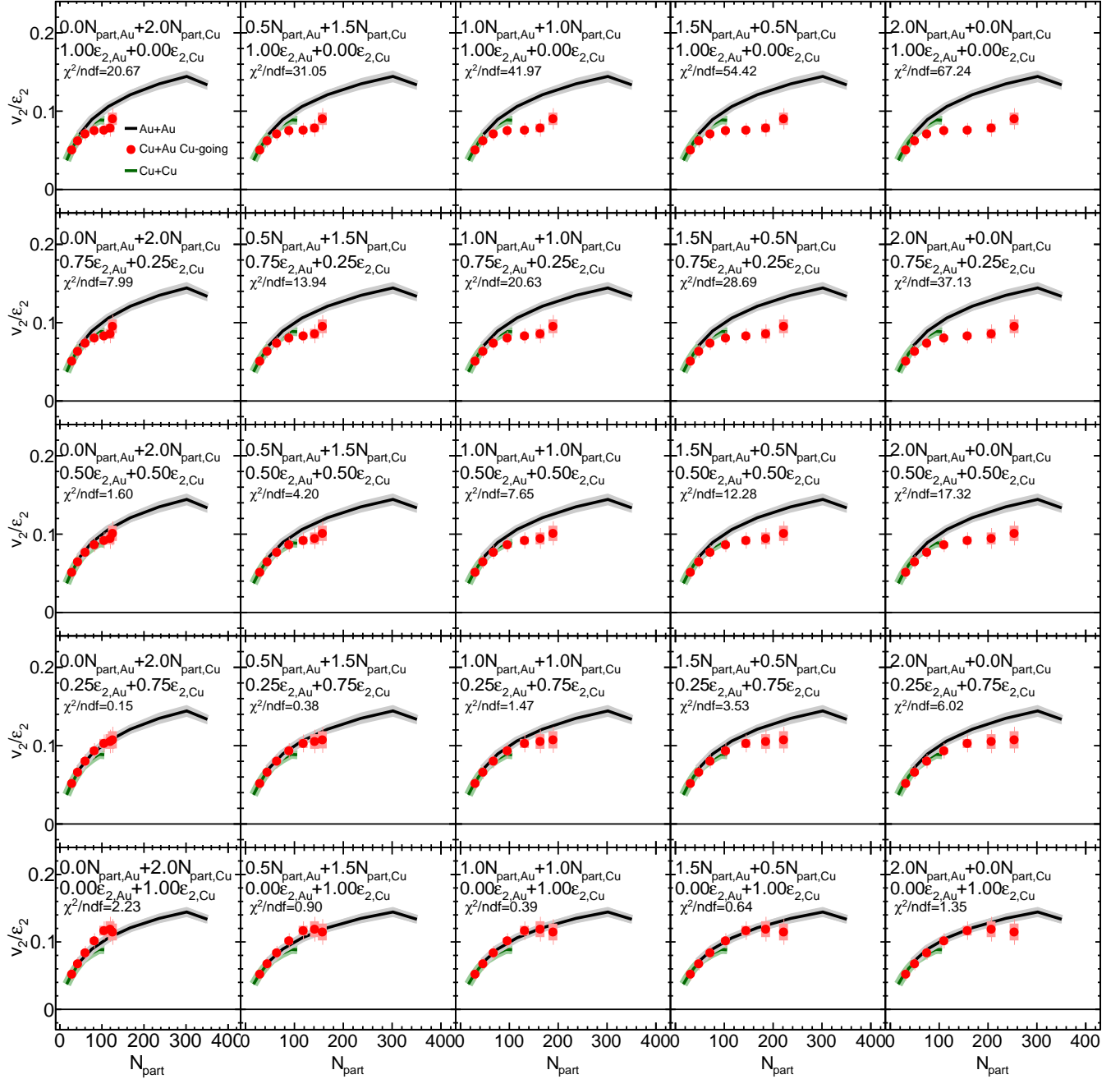


Figure C.2: Weighted eccentricity scaling of v_2 as a function of weighted N_{part} for Cu-going side in Cu+Au collisions compared to the Au+Au and Cu+Cu results.

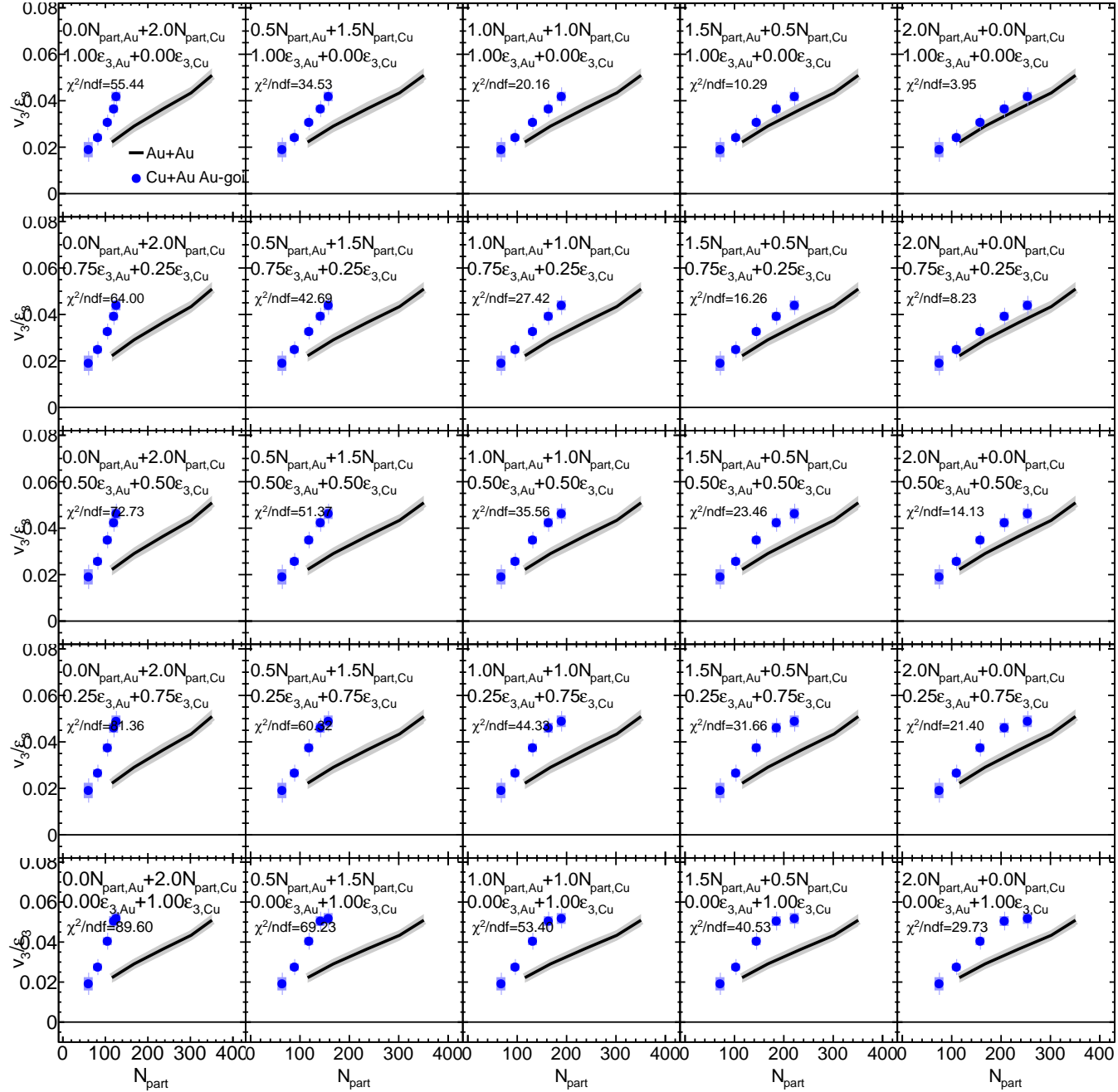


Figure C.3: Weighted eccentricity scaling of v_3 as a function of weighted N_{part} for Au-going side in Cu+Au collisions compared to the Au+Au result.

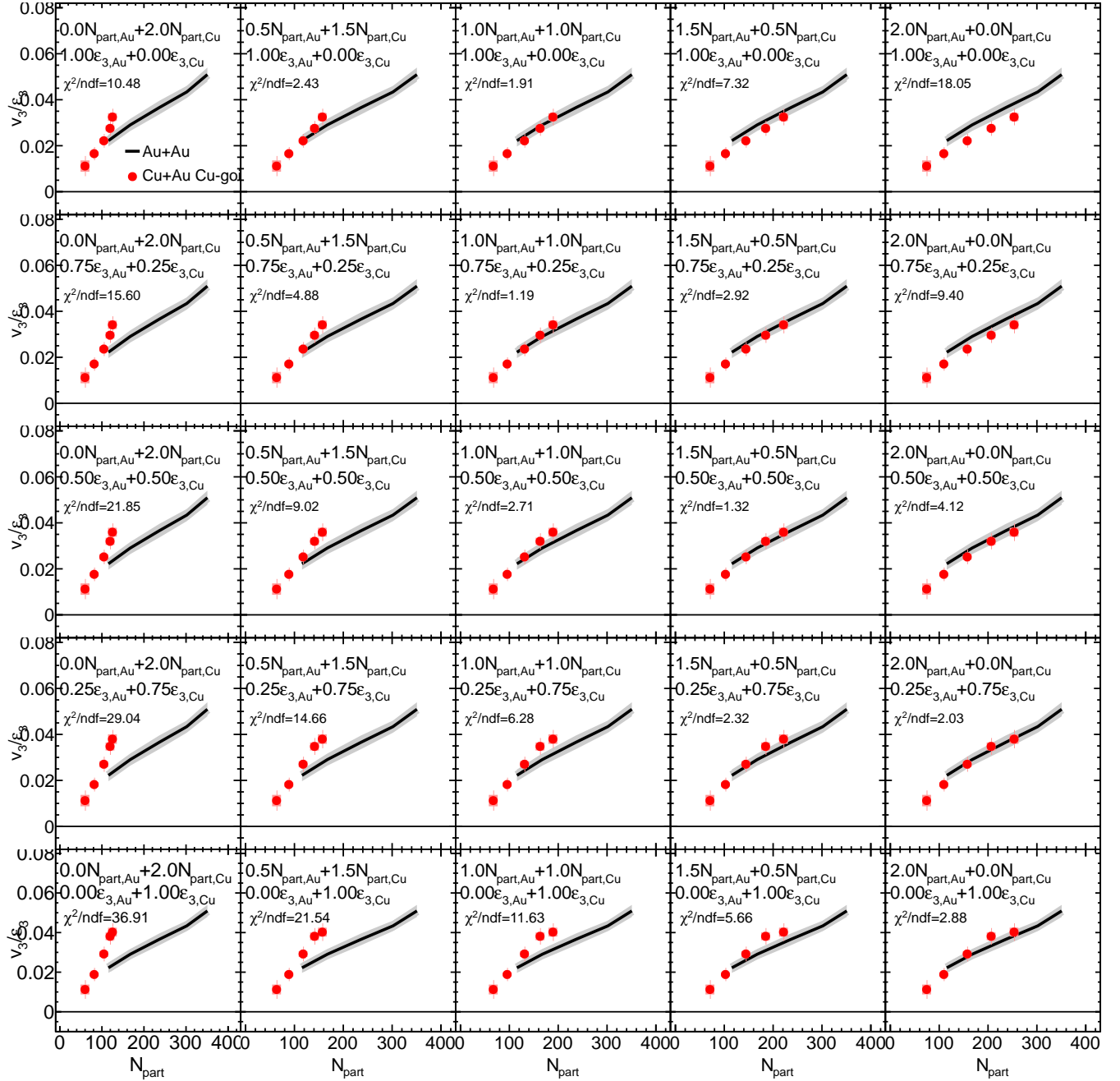


Figure C.4: Weighted eccentricity scaling of v_3 as a function of weighted N_{part} for Cu-going side in Cu+Au collisions compared to the Au+Au result.

Bibliography

- [1] D. J. Gross and F. Wilczek "Ultraviolet Behavior of Non-Abelian Gauge Theories" Phys. Rev. Lett. **30** 1343 (1973)
- [2] H. D. Politzer "Reliable Perturbative Results for Strong Interactions?" Phys. Rev. Lett. **30** 1343 (1973)
- [3] K. G. Wilson "Confinement of quarks" Phys. Rev. D **10** 2445
- [4] Particle Data Group "REVIEW OF PARTICLE PHYSICS", Phys. Rev. D **86**.010001
- [5] A. Aoki et al(PACS-CS Collaboration). "2+1 flavor lattice QCD toward the physical point", Phys. Rev. D **79**.034503
- [6] A. Bavozov et al(HotQCD Collaboration)"Equation of state in (2+1)-flavor QCD" Phys. Rev. D **90**.094503
- [7] M.L. Miller, K. Rygers, S.J. Standers, P. Steinberg, "Glauber Modeling in High Energy Nuclear Collisions", Ann.Rev.Nucl.Part.Sci.57:205-243,2007
- [8] J. D. Bjorken "Highly relativistic nucleus-nucleus collisions: The central rapidity region" Phys. Rev. D **27** 140 (1983)
- [9] S. S. Adler et al, (PHENIX Collaboration) "Systematic studies of the centrality and $\sqrt{s_{NN}}$ dependence of the $dE_T/d\eta$ in heavy ion collisions at midrapidity" Phys. Rev. C **71**, 034908(2005)
- [10] I. G. Bearden et al(BRAHMS Collaboration), "Nuclear Stopping in Au+Au Collisions at $\sqrt{s_{NN}} = 200\text{GeV}$ " Phys. Rev. Lett. **93** 102301
- [11] I. Arsene et al(BRAHMS Collaboration) "Quark Gluon Plasma and Color Glass Condensate at RHIC? The perspective from the BRAHMS experiment." Nucl. Phys. A **757** 1-27 (2005)
- [12] B.B. Back et al,(PHOBOS Collaboration) "Significance of the Fragmentation Region in Ultrarelativistic Heavy-Ion Collisions", Phys. Rev. Lett. **91**, 052303
- [13] B.B. Back et al,(PHOBOS Collaboration) "Charged Particle Pseudorapidity Distributions in Au+Au collisions at $\sqrt{s_{NN}} = 62.4\text{GeV}$ " Phys. Rev. C **74**, 021901 (2006)
- [14] B. Alver, G. Roland "Collision-geometry fluctuations and triangular flow in heavy-ion collisions", Phys. Rev. C **81** 054905(2010)

- [15] K. Guettler et al, "INCLUSIVE PRODUCTION OF LOW-MOMENTUM CHARGED PIONS AT $x = 0$ AT THE CERN INTERSECTING STORANGE RINGS" Phys. Lett B **64** 111-116
- [16] A. S. Adler et al, (PHENIX Collaboration) "High- p_T charged hadron suppression in Au+Au collisions at $\sqrt{s_{NN}} = 200\text{GeV}$ " Phys. Rev. C **69** 034910 (2004)
- [17] I. G. Bearden et al. (NA44 Collaboration), "Collective Expansion in High Energy Heavy Ion Collisions" Phys. Rev. Lett. **78** 2080 (1997)
- [18] S. S. Adler et al, (PHENIX Collaboration) "Identified Charged Particle Spectra and Yields in Au + Au Collisions at $\sqrt{s_{NN}} = 200\text{GeV}$ " Phys. Rev. C **69** 034909
- [19] P.F. Kolb and U.W. Heinz, " Hydrodynamic description of ultrarelativistic heavy-ion collisions", arXiv:nucl-th/0305084 154, 163, 166
- [20] B. Zhang, M. Gyulassy and C.M. Ko, "Elliptic flow from a parton cascade", Phys. Lett. B **455**, 45 (1999)
- [21] A. Adare et al (PHENIX Collaboration), "Measurements of Higher Order Flow Harmonics in Au + Au Collisions at $\sqrt{s_{NN}} = 200\text{GeV}$ " Phys. Rev. Lett. **107**, 252301(2011)
- [22] G. Aad et al (ALTAS Collaboration), "Measurement of the azimuthal anisotropy for charged particle production in $\sqrt{s_{NN}} = 2.76\text{TeV}$ Phys. Rev. Lett. **86**. 014907 (2012)
- [23] B. Abelev et al. (ALICE Collaboration) "Directed Flow of Charged Particles at Midrapidity Relative to the Spectator Plane in Pb-Pb Collisions at $\sqrt{s_{NN}} = 2.76\text{TeV}$ " Phys. Rev. Lett. **111**, 232302 (2013)
- [24] A. Adare et al. "Measurement of the higher-order anisotropic flow coefficients for identified hadrons in Au+Au collisions at $\sqrt{s_{NN}} = 200\text{GeV}$ Phys. Rev. C. **93**.051902 (2016)
- [25] B. B. Back et al. (PHOBOS Collaboration), "Centrality and pseudorapidity dependence of elliptic flow for charged hadrons in Au+Au collisions at $\sqrt{s_{NN}} = 200\text{GeV}$ ", Phys. Rev. C **72**, 051901 (2005)
- [26] L. Adamczyk et al. (STAR Collaboration), "Third harmonic flow of charged particles in Au+Au collisions at $\sqrt{s_{NN}} = 200\text{GeV}$ ", Phys. Rev. C **88**, 014904 (2013)
- [27] B. B. Back et al. (PHOBOS Collaboration) "Forward-backward multiplicity correlations in $\sqrt{s_{NN}} = 200\text{GeV}$ " Phys. Rev. C **74**, 011901
- [28] B. I. Abelev et al. (STAR Collaboration) "Growth of Long Range Forward-Backward Multiplicity Correlations with Centrality in Au+Au Collisions at $\sqrt{s_{NN}} = 200\text{GeV}$ " Phys. Rev. Lett. **103**, 172301
- [29] J. Jia and P. Huo "Forward-backward eccentricity and participant-plane angle fluctuations and their influences on longitudinal dynamics of collective flow" Phys. Rev. C **70**. 034915 (2014)

- [30] ALESSI, J. et al, "ELECTRON BEAM ION SOURCE PREINJECTOR PROJECT (EBIS) CONCEPTUAL DESIGN REPORT" BNL-73700-2005-IR-R1
- [31] J. T. Mitchel et al., "Event Reconstruction in the PHENIX Central Arm Spectrometers", Nuclear Instruments and Methods in Physics Research A **482** (2002) 498
- [32] T.C.Awes et al. "High Energy Beam Test of the PHENIX Lead-Scintillator EM Calorimeter" arXiv:nucl-ex/0202009
- [33] "Nuclear Inst. and Methods in Physics Research", A 636 (2011) pp. 99-107
- [34] D. Teaney, L. Yan "Triangularity and dipole asymmetry in relativistic heavy ion collisions" Phys. Rev. C **83** 064904
- [35] B.Alver, M.Baker, C.Loizides, P.Steinberg "The PHOBOS Glauber Monte Carlo" arXiv:0805.4411
- [36] Oana Ristea et al, "Identified particle production in nuclear collisions at Relativistic energies", Romanian Reports in Physics, Vol. 65, No.2, 411-419 2013
- [37] B. Alver et al(PHOBOS Collaboration), "Charged-particle multiplicity and pseudorapidity distributions measured with the PHOBOS detector in Au+Au, Cu+Cu, d+Au, and p+p collisions at ultrarelativistic energies", Phys. Rev. C 83, 024913
- [38] B. Alver et al(PHOBOS Collaboration), "System Size, Energy, Pseudorapidity, and Centrality Dependence of Elliptic Flow" Phys. Rev. Lett. **98** 242302(2007)
- [39] B. B. Back et al,(PHOBOS Collaboration) "Energy dependence of elliptic flow over a large pseudorapidity range in Au+Au collisions at RHIC" Phys. Rev. Lett. **94**, 122303 (2005)
- [40] S. A. Voloshin and T. Niida "Ultrarelativistic nuclear collisions: Direction of spectator flow" Phys. Rev. C **94**, 021901 (2016)
- [41] "Systematic Study of Azimuthal Anisotropy in Cu+Cu and Au+Au Collisions at $\sqrt{s_{NN}} = 62.4\text{GeV}$ and 200 GeV" Phys. Rev. C **92** 034913(2015)
- [42] "Energy and system size dependence of charged particle elliptic flow and v_2/ϵ_2 scaling" J.Phys.G34:S883-886,2007
- [43] A. Eremin and S. Voloshin "Nucleon participants or quark participants?" Phys. Rev. C **67**, 064905(2003)
- [44] S. S. Adare, et al,(PHENIX Collaboration) "Transverse-energy distributions at midrapidity in p+p, d+Au and Au+Au collisions at $\sqrt{s_{NN}} = 62.4-200\text{GeV}$ and implications for particle-production models" Phys. Rev. C **89**, 044905(2014)
- [45] R. Nouicer"Charged particle multiplicities in A+A and p+p collisions in the constituent quarks framework" Eur. Phys. J. C **49**,281-286(2007)
- [46] W. Busza et al, "Charged-Particle Multiplicity in π^- -Nucleus Interactions at 100 and 175 GeV/c" Phys. Rev. Lett. **34** 13 (1975)

- [47] A. Adare, et al,(PHENIX Collaboration) "Transverse energy production and charged-particle multiplicity at midrapidity in various systems from $\sqrt{s_{NN}}=7.7$ to 200GeV"
- [48] B. B. Back "Charged-Particle Pseudorapidity Distributions in Au+Au Collisions at $\sqrt{s_{NN}} = 62.4$ GeV" Phys. Rev. C **74** 021901 (2006)
- [49] R. Hofstadter "Electron Scattering and Nuclear Structure" Rev. Mod. Phys. **28**, 214
- [50] Zi-Wei Lin, Che Ming Ko, Bao-An Li, Bin Zhang, Subrata Pal. "Multiphase transport model for relativistic heavy ion collisions" Phys. Rev. C **72**, 064901(2005)
- [51] Piotr Bozek "Event-by-event viscous hydrodynamics for Cu-Au collisions at $\sqrt{s_{NN}} = 200$ GeV" PLB **717**, 287(2012)
- [52] T. Hirano, P. Huovinen, K. Murase and Y. Nara "Integrated Dynamical Approach to Relativistic Heavy Ion Collisions" Prog.Part.Nucl.Phys. **70** (2013) 108-158
- [53] B. Alver(PHOBOS Collaboration) "System Size, Energy and Centrality Dependence of Pseudorapidity Distributions of Charged Particles in Relativistic Heavy Ion Collisions" Phys. Rev. Lett. **102** 142301
- [54] B. Schenke, P. Tribedy and R. Venugopalan "Initial-state geometry and fluctuations in Au+Au, Cu+Au, and U+U collisions at energies available at the BNL Relativistic Heavy Ion Collider" Phys. Rev. C **89**, 064908(2014)
- [55] B. Schenke, P. Tribedy and R. Venugopalan "Fluctuating Glasma Initial Conditions and Flow in Heavy Ion Collisions" Phys. Rev. Lett. **108**, 252301